



**HAL**  
open science

**Cyclodextrin: a versatile supramolecular tool to extend  
lithium-based batteries lifespan: a versatile  
supramolecular tool to extend lithium-based batteries  
lifespan**

Fanny Betermier

► **To cite this version:**

Fanny Betermier. Cyclodextrin: a versatile supramolecular tool to extend lithium-based batteries lifespan: a versatile supramolecular tool to extend lithium-based batteries lifespan. Material chemistry. Université Paris-Saclay, 2021. English. NNT: 2021UPASF046 . tel-03578938

**HAL Id: tel-03578938**

**<https://theses.hal.science/tel-03578938>**

Submitted on 17 Feb 2022

**HAL** is a multi-disciplinary open access archive for the deposit and dissemination of scientific research documents, whether they are published or not. The documents may come from teaching and research institutions in France or abroad, or from public or private research centers.

L'archive ouverte pluridisciplinaire **HAL**, est destinée au dépôt et à la diffusion de documents scientifiques de niveau recherche, publiés ou non, émanant des établissements d'enseignement et de recherche français ou étrangers, des laboratoires publics ou privés.

Cyclodextrin : a versatile supramolecular tool  
to extend lithium-based batteries lifespan  
*Utilisations de la cyclodextrine pour prolonger la  
durée de vie des batteries au lithium*

**Thèse de doctorat de l'université Paris-Saclay**

École doctorale n°571 Sciences chimiques : Molécules, matériaux,  
instrumentation et biosystèmes, 2MIB  
Spécialité de doctorat : Chimie  
Réfèrent : Université d'Evry Val d'Essonne

Unité de recherche : Université Paris-Saclay, Univ Evry, CNRS, LAMBE, 91025 Evry-  
Courcouronnes, France  
Collège de France, Chaire de Chimie du Solide et de l'Energie

**Thèse présentée et soutenue au Collège de France, le  
16/12/2021**

**Fanny BÉTERMIER**

**Composition du Jury**

<b>Sophie FOURMENTIN</b> Professeur, Université Littoral Côte d'Opale - UCEIV	Présidente
<b>Robert DOMINKO</b> Professeur, National Institute of Chemistry, Ljubljana	Rapporteur
<b>Guy SCHLATTER</b> Professeur, Université de Strasbourg - ICPEES	Rapporteur
<b>Marc DESCHAMPS</b> Docteur, Responsable Electrochimie, BlueSolutions	Examineur
<b>Dominique LARCHER</b> Professeur, Université de Picardie Jules Verne - LRCS	Examineur
<b>Juan PELTA</b> Professeur, Université Paris Saclay, Univ Evry - LAMBE	Examineur

**Direction de la thèse**

<b>Nathalie JARROUX</b> Professeur, Université Paris Saclay, Univ Evry - LAMBE	Directrice de thèse
<b>Jean-Marie TARASCON</b> Professeur, Collège de France - CSE	Directeur de thèse



*Even a blind squirrel will someday find a nut,*



# Acknowledgements

As this long and challenging journey is coming to an end, the time has come to thank all the people whose paths I have crossed. I consider myself very fortunate to have worked in an extraordinary scientific environment under the direction of Nathalie Jarroux and Jean-Marie Tarascon. First, I am very grateful to Nathalie for having me embarked on this adventure and for transmitting me her scientific knowledge and passion about supramolecular chemistry. You are a model of energy and your dedication to our "3<sup>rd</sup> floor synthesis team" has always impressed me. Then I would like to warmly thank Jean-Marie with whom I have tremendously learnt through his passion to chemistry, his scientific curiosity, his incredible availability, his practical nature, his legendary competitive spirit and above all his energy at work. I still cannot figure out how you get so much energy ! Thank you for trusting me and being increasingly demanding.

This PhD work has benefited from strong collaborations that deserve to be acknowledged. My first thanks go to the 4 Post-Docs I have had the great opportunity to work with successively, and who have shared both tips and expertise. Thanks to Boris Mirvaux for introducing me to the CSE lab lifestyle, to Benjamin Cressiot for his guidance and positive feedbacks, to Laura Coustan for her wise counsel and finally to Nour Daher with who I have made a fantastic pair to make Si anodes binders work. I also sincerely acknowledge Juan Pelta and Laurent Bacri (LAMBE) for their scientific enthusiasm and great availability as well as Giovanni di Muccio, Blasco Morozzo della Rocca and Mauro Chinappi, our collaborators from Tor Vergata University (Roma), who carried out some simulations for us. Some characterizations presented in this manuscript would have not been possible without the help of Carine van Heijenoort (RMN, ICSN), Olek Maciejak (RMN, LAMBE), Dominique Larcher (pycnometric densities, LRCS), Mathieu Courty (TGA, LRCS), William Buchman (MS, LAMBE), Ronan Chometon and Tunçay Koç (SEM, CSE), Julie Brun and Alba Marcellan (mechanical testing, SIMM). I have also really appreciated to work with Laura Alberio Blanquer (CSE), Henrique Trevisan (CSE-C3M) and Jason Richard (LCMCP). I would finally like to thank Christel Laberty (LCMCP) and Joanne Xie (PPSM) for their time and support during our annual "comité de suivi de thèse" meetings.

I would like to acknowledge both Robert Dominko and Guy Schlatter for accepting the role of referee of this thesis and Sophie Fourmentin, Dominique Larcher, Marc Deschamps and Juan Pelta for accepting to be part of my jury.

I am grateful to the RS2E research network and the DIM RESPORE for funding this thesis. I sincerely thank those who work hard to keep these dynamic networks running, especially through the meetings that I have always had a great pleasure to attend.

Of course I am extending my acknowledgements to the LAMBE lab members with whom I have shared a part of these 3 years. Thank you to Julia who has always taken care of me since I started in Evry. I particularly thank Inès, Salma, Izadora, Lorenzo, Roggerio, Hervé, Paolo and Dorian, *-who has freshly joined-*, for their daily kindness and discussions. I am also really grateful to Emmanuelle Léon for offering me the opportunity to teach. Next, I would like to acknowledge all the amazing people from CSE that I have met over my three years here. I am so lucky to have been part of such an innovative, kind, multicultural and inspiring research group ! I am immensely grateful to Thomas, Léa, Pierre, Nour, Nicolas, Benjamin, Laura and Gwen, *-my welcoming office mate-*, for all the pleasant moments we have shared together and of course to the running CSE team for our noon (and less frequent sunrise) sessions along the Seine. Special thanks go to Ketty Fixot, Frédérique Augougnon and Jessica Duvoisin for their administrative support.

Finally, I am very grateful to my family and friends for their positive and cheerful support along these three years. Of course, I wish to extend a very special thank you to Alexis for keeping me motivated, for his understanding and unconditional support !

# Table of Contents

<b>Acknowledgements .....</b>	<b>5</b>
<b>Table of Contents.....</b>	<b>7</b>
<b>General introduction and thesis outline .....</b>	<b>11</b>
1. Global warming promoting the emergence of batteries.....	11
2. Supramolecular prospects to improve battery cycling life .....	14
3. Thesis outline .....	15
<b>Chapter I: Prospects for cyclodextrins supramolecular chemistry in Li-based batteries.....</b>	<b>17</b>
1. Cyclodextrin <i>host-guest</i> supramolecular chemistry .....	17
a. Structure and properties of cyclodextrins (CDs).....	17
b. From molecular recognition to macroscopic molecular recognition .....	19
c. <i>Smart</i> properties induced by CD macroscopic molecular recognition .....	24
2. Cyclodextrin architectures enabling Li-based batteries improvements .....	27
a. Tailoring Li-ion batteries electrolytes .....	29
b. Designing Si anode binders .....	32
c. Preventing the solubilization of red-ox active species .....	35
3. Conclusion and thesis prospects.....	37
<b>Chapter II: Cyclodextrin <i>host-guest</i> chemistry to address the Li-S battery polysulfides red-ox shuttle</b>	<b>39</b>
1. Background and motivation.....	39
a. Li-S batteries and polysulfides red-ox shuttle characterization.....	39
b. Nanopore sequencing technology.....	40
c. Our strategy to implement nanopore sensing via CD <i>host-guest</i> interaction.....	42
2. CD supramolecular recognition towards aqueous polysulfides .....	43
a. <i>Host-guest</i> complexation between CDs and polysulfides .....	44
b. Influence of the polysulfides length.....	47
c. A reversible complexation equilibrium .....	50
3. Aqueous polysulfides detection and discrimination by nanopore .....	54
a. $\beta$ -CD interaction with the $\alpha$ -hemolysin ( $\alpha$ -HL) nanopore channel.....	54
b. Polysulfides detection.....	56
c. Polysulfides chain length discrimination.....	58
4. Conclusions and discussions.....	60
a. Extension towards organic polysulfides .....	60
b. Future for nanopores as new powerful electrolyte sensors.....	63



<b>Chapter III: Novel elastic deformable mechanically interlocked architectures synthesized from <math>\alpha</math>-cyclodextrins based polyrotaxanes .....</b>	<b>67</b>
1. Background and motivation.....	67
a. Si anode volume changes being addressed through the design of binders.....	68
b. Mechanically interlocked architectures inducing enhanced mechanical properties .....	70
c. Synthesis strategy of our binders.....	74
2. $\alpha$ -CDs based polyrotaxanes (PRs) synthesis .....	77
a. PR synthesis pathway.....	77
b. Characterization of PR10K.....	81
c. Characterization of PR35K and PR100K.....	90
3. PR-PAA network synthesis .....	93
a. PR-PAA synthesis pathway .....	93
b. Thermal properties investigation .....	99
c. Mechanical properties evaluation.....	104
4. Conclusions and discussions.....	110
<b>Chapter IV: Understanding the electrochemical performances of Si anodes incorporating mechanically interlocked binders prepared from <math>\alpha</math>-cyclodextrins based polyrotaxanes.....</b>	<b>113</b>
1. Background and motivation.....	113
2. Development of reference Si composite electrodes .....	114
a. Si particles choice .....	114
b. Si composite electrodes preparation.....	116
c. Battery assembling and cycling performances .....	118
3. Evaluation of the cycling performances of PR-PAA binders.....	125
a. Electrochemical stability.....	126
b. Aqueous formulation .....	129
c. Ethanol-based formulation.....	134
4. Conclusions and discussions.....	138
<b>General conclusion and perspectives .....</b>	<b>141</b>
<b>Bibliography .....</b>	<b>145</b>
<b>Supporting Information for Chapter II.....</b>	<b>157</b>
1. Materials & Methods .....	157
2. Supporting Figures: Polysulfides characterization.....	161
3. Supporting Figures: CD/polysulfide interaction by $^1\text{H}$ NMR.....	163
4. Supporting Figures: CD/polysulfide interaction by Molecular Docking calculations .....	168
5. Supporting Figures: Nanopore detection .....	170

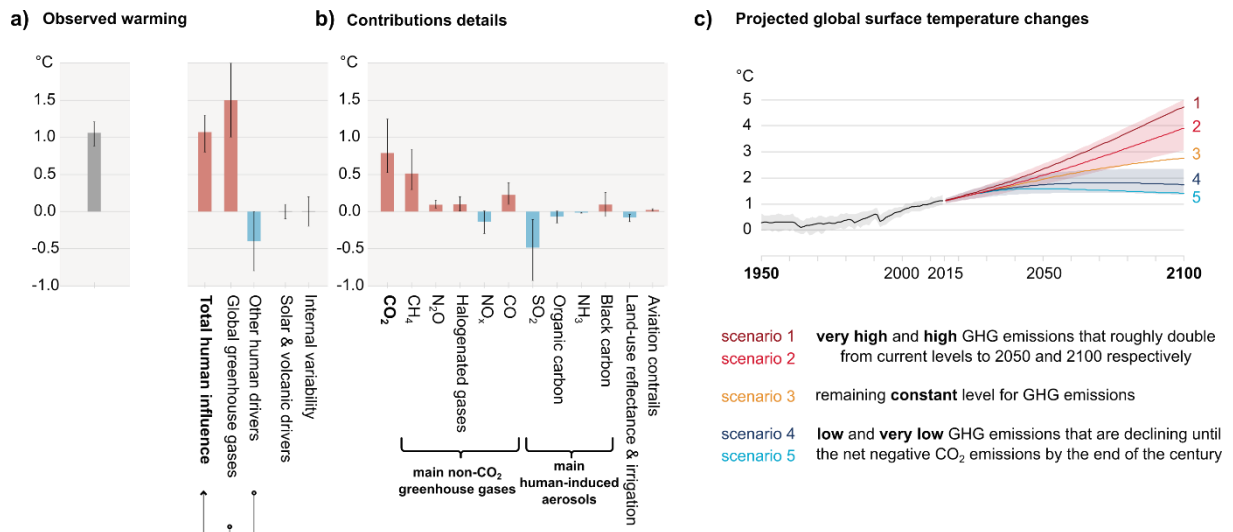
<b>Supporting Information for Chapter III .....</b>	<b>175</b>
1. Materials & Methods .....	175
2. Supporting Figures: PEO end-chains methacrylation .....	180
3. Supporting Figures: PPRs characterization.....	191
4. Supporting Figures: PRs characterization .....	195
5. Supporting Figures: PR-PAA network characterization .....	209
<b>Supporting Information for Chapter IV .....</b>	<b>223</b>
1. Materials & Methods .....	223
2. Supporting Figures: reference Si/PAA electrodes.....	225
3. Supporting Figures: Si/PR-PAA electrodes.....	229
<b>Glossary .....</b>	<b>235</b>
<b>Résumé détaillé.....</b>	<b>239</b>



# General introduction and thesis outline

## 1. Global warming promoting the emergence of batteries

Global warming turns out to be the major self-induced challenge the humanity must cope with during the 21<sup>st</sup> century. It is mainly caused by CO<sub>2</sub> emissions that represent 75% of global greenhouse gas (GHG) emissions (Figure 1.a.b). The IPCC report<sup>1</sup>, that was published on August 9<sup>th</sup>, 2021, dramatically emphasizes the influence of human activities on the global temperature rise and subsequent devastating environmental changes that have been observed during the past decades. The situation has gotten so critical that some world policies are being launched, as witnessed by the Paris Agreement<sup>2</sup> that was adopted by 196 parties on December 12<sup>th</sup>, 2015. The different scenarios envisioned show that a strong reduction of GHG emissions is necessary to maintain a “reasonable” global surface temperature rise to 1.5°C by the end of the century (Figure 1.c, scenarios 4 & 5).

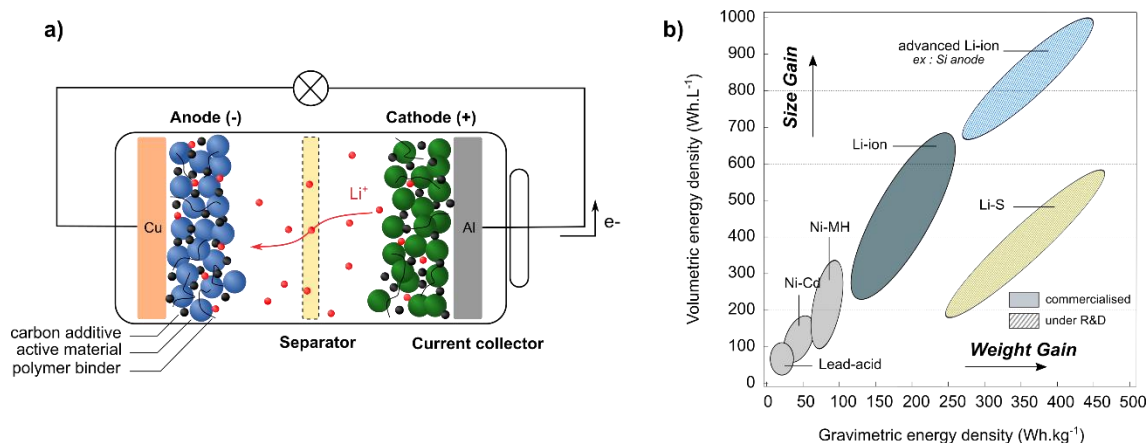


**Figure 1: Assessed contributions to global warming: a human-induced phenomenon, adapted from ref<sup>1</sup>.** Observations were made between 2010 and 2019. **a)** Observed increase in the global surface temperature. **b)** Details of the contributions to global warming. **c)** Projections for the five emissions scenarios of the global surface temperature changes in °C described by the IPCC. Historical values are included in the graph to provide context for the projected future changes.

Therefore, great efforts must be pursued to decarbonate our economy. In this sense, the energy sector currently undergoes a significant mutation with (i) the integration of renewables in the energy supply, -they are intrinsically intermittent energy sources-, (ii) the improvement of efficiency and the reduction of energy consumption of our energy systems, (iii) the electrification of our transport facilities and (iv) the development of carbon capture, storage and utilization technologies. The French Environmental and Energy Management Agency (ADEME), has foreseen such a transformation of our methods of energy production to almost halve the French global energy demand, by 2050 (-47%)<sup>3</sup>.

To achieve these sustainability objectives, energy-storage devices, especially rechargeable batteries, have become crucial actors. In its basic configuration, a battery is an electrochemical cell composed of one positive (cathode) and one negative (anode) electrodes, separated by an ion-containing electrolyte solution. Electrodes are connected to an electrical circuit that allows the electrons flow while the ions flow is only possible through the electrolyte. Simultaneous electrochemical reactions occur at the two electrodes, leading to the charge (energy storage) and the discharge of the battery (energy delivering), depending on the electrons flow direction (Figure 2.a). The kinetics and reversibility of these electrochemical processes are intimately linked to the rate capability and cyclability respectively. The cell voltage (V) is defined as the potential difference between the two electrodes while the extent of the reaction determines the cell capacity (Ah). The energy (Wh) stored by the battery is calculated as the product of the cell voltage and the cell capacity (Ah).

Several requirements are desired in a good rechargeable battery: high gravimetric and volumetric energy densities ( $\text{Wh.kg}^{-1}$  &  $\text{Wh.L}^{-1}$ ), low cost, long cycle lifetime, high energy efficiency and high-power density ( $\text{W.kg}^{-1}$ ) which is correlated to rate capability. Consequently, in the past decades, scientists have mainly worked to increase energy densities by developing extreme voltages electrode materials or switching to other chemistries inducing higher intrinsic capacities.



**Figure 2: Overview of Li-based batteries.** a) Working principle of a rechargeable Li-based battery during charge. The movements of  $\text{Li}^+$  and  $e^-$  are inverted during discharge. b) Roadmap of the different rechargeable battery technologies in terms of volumetric ( $\text{Wh.L}^{-1}$ ) and gravimetric ( $\text{Wh.kg}^{-1}$ ) energy densities, highlighting the Li-based technologies envisioned in this thesis : Li-S (yellow) and Si anode (blue). Figure adapted from ref<sup>4</sup> and *PhD thesis from Gaurav Assat, 2018*.

Because of their improved energy densities, high efficiency, and cost-competitiveness, Li-ion batteries have ousted their predecessors (Pb-acid, Ni-Cd and Ni-MH) and stand out as the key technology ( $< \$100/\text{kWh}$ ) (Figure 2.b). They are ubiquitous in consumer electronics and are currently deployed for the massive development of electric vehicles encouraged by the government's policies. They are also being considered for larger scale grid-applications and stationary storage. The massive research in material science coupled with engineering efforts, which have led to the growth of manufacturing volumes of Li-ion batteries, allow us to expect an optimistic future for the next-generation batteries that are classified into two categories: *advanced Li-ion* and *post Lithium-ion* technologies<sup>5</sup>.

*Advanced Li-ion* consists in innovation in material (anode, cathode) and electrolyte chemistry, electrode design, cell geometry to improve today Li-ion batteries performances while *post* Li-ion technology refers to other battery chemistries such as lithium-sulfur (Li-S), lithium-air or sodium-ion batteries. This thesis deals with both Li-S battery (*post-Li-ion* technology) and the development of silicon (Si) anode for *advanced Li-ion* battery, which suffer from inherent failure mechanisms that are preventing them to reach the commercialisation (Figure 2.b). The originality of our approach lies on the use of supramolecular chemistry to address these issues.

## 2. Supramolecular prospects to improve battery cycling life

In the context of sustainability, the rising challenge of this new decade is to reduce the carbon footprint of batteries, in addition to improve energy densities. The large-scale and long-term European initiative BATTERY 2030+, which has been launched to develop a neutral chemistry approach, is entirely dedicated to this problematic<sup>6</sup>. One of the main pillars of this program is to enhance the cycling life and reliability of batteries, resulting in a lower environmental impact. To do so, *smart* functionalities, **sensing** and **self-healing**, are integrated in batteries.

A large research work is carried out to monitor the batteries cycling life in real time from the inside<sup>7</sup>. Very sensitive sensing tools have been integrated in batteries to detect the degradation mechanisms responsible for their premature end of life. As illustrated in Figure 3, these failures are intimately associated to the loss of interactions between the electrode components during cycling. They are mostly correlated to some structural changes at the components level (pulverization, micro-cracking), some morphology changes (Li dendrites growth) or some electrode/electrolyte interfacial reactivities, such as the uncontrolled formation of passivating layers (solid electrolyte interphase, SEI) or dissolution processes (chemical cross-talks, red-ox shuttle).

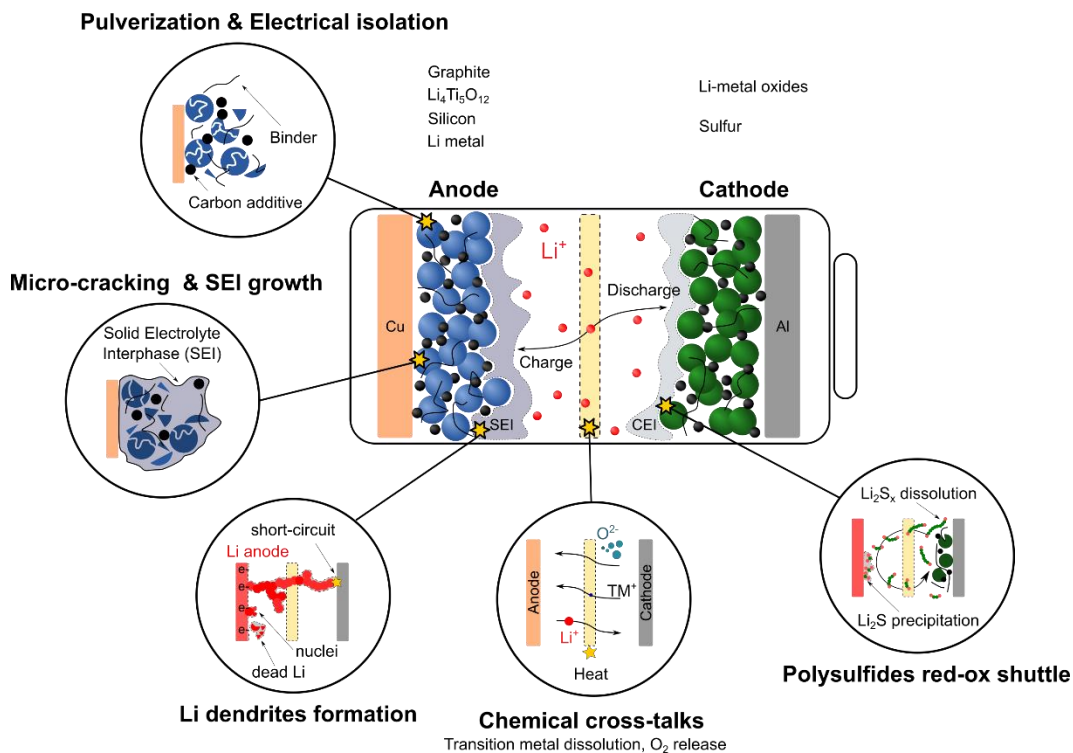


Figure 3: Overview of the degradation mechanisms occurring in Li-based batteries.

Once the diagnostic of these degradation mechanisms is completed, some curing strategies need to be developed to repair the damages, hence extending the batteries lifetime. Notably, life sciences have inspired the development of batteries embedded with some self-healing functionalities. Thus, a unique opportunity is offered for supramolecular chemistry to design adaptive systems that can respond to the local structure changes and restore the battery components configuration.

Supramolecular chemistry deals with spontaneous reversible non-covalent interactions, including hydrogen bonding, Van der Waals forces,  $\pi$ - $\pi$  stacking, ion-ion, ion-dipole, hydrophobic and *host-guest* interactions. Such supramolecular interactions play a fundamental role in biological systems to preserve their integrity or ensure their functions. For instance, the double helix structure of DNA, the reaction antigen-antibody or the ribosome's translation of DNA information can be realized by the means of these non-covalent interactions. Equipping battery components with smart supramolecular materials enables self-healing functionalities and addresses the challenge to develop more sustainable batteries with longer cycle life.

### 3. Thesis outline

This thesis aims to contribute to the improvement of Li-based batteries performances by using the knowledge of supramolecular chemistry. More specifically, the focus is made on cyclodextrins (CDs) which are bio-sourced cage molecules that can give reversible supramolecular *host-guest* interactions with a large variety of molecules. Inspired from the nature processes, we target the underlying origins of capacity fading of two different high-energy density electrode materials, namely the sulfur (S) cathode and the silicon (Si) anode, using CD as a "swiss army knife".

This thesis is structured in the following four chapters:

**Chapter I** begins with a brief introduction of the CD *host-guest* supramolecular chemistry. The large panel of *smart* architectures made of CDs is then described to underline the promising properties such materials can offer to the battery field. Finally, this chapter provides a review of the recent works in which the CD *host-guest* interaction has been successfully exploited to enhance Li-based batteries performances.



**Chapter II** addresses the main issue from which lithium-sulfur (Li-S) batteries suffer : the so-called “polysulfide red-ox shuttle” associated to the undesirable dissolution of active red-ox intermediates (lithium polysulfides) in the electrolyte. The demonstration of the *host-guest* interaction between polysulfides and CDs outlines a novel chemical approach to trap polysulfides. It also allowed the successful discrimination of polysulfides with a single sulfur atom resolution by nanopore, which is a characterization tool borrowed from biology, hence opening new ways for the design of new powerful batteries electrolytes sensors.

**Chapter III** presents the synthesis and characterization of mechanically interlocked architectures prepared from CDs-based polyrotaxanes, consisting of the supramolecular assembly of CDs on a threading polymer. The sliding motion of CDs provides these architectures with enhanced mechanical properties. A systematic synthesis strategy is adopted to investigate structure-properties relationships, with the ultimate goal for these polymer networks to serve as Si anode binders.

**Chapter IV** explores the electrochemical performances of the mechanically interlocked architectures disclosed in Chapter III, when used as Si anode binders. This investigation aims to unveil the origin of the performances' improvement of this new class of binders compared to traditional binders. The influence of the structural parameters of such architectures on the cyclability of Si anodes is finally discussed.

The general conclusion summarizes the main achievements of the thesis along with the remaining questions. We hope this work will help in a wider acceptance of considering supramolecular chemistry as a useful tool for the battery community. Some opening future directions for further studying the role that CDs can play to improve Li-based batteries performances are also presented. The thesis is then closed by my personal opinion about the exciting research that can be conducted at the interface of several different scientific fields.

# Chapter I: Prospects for cyclodextrins supramolecular chemistry in Li-based batteries

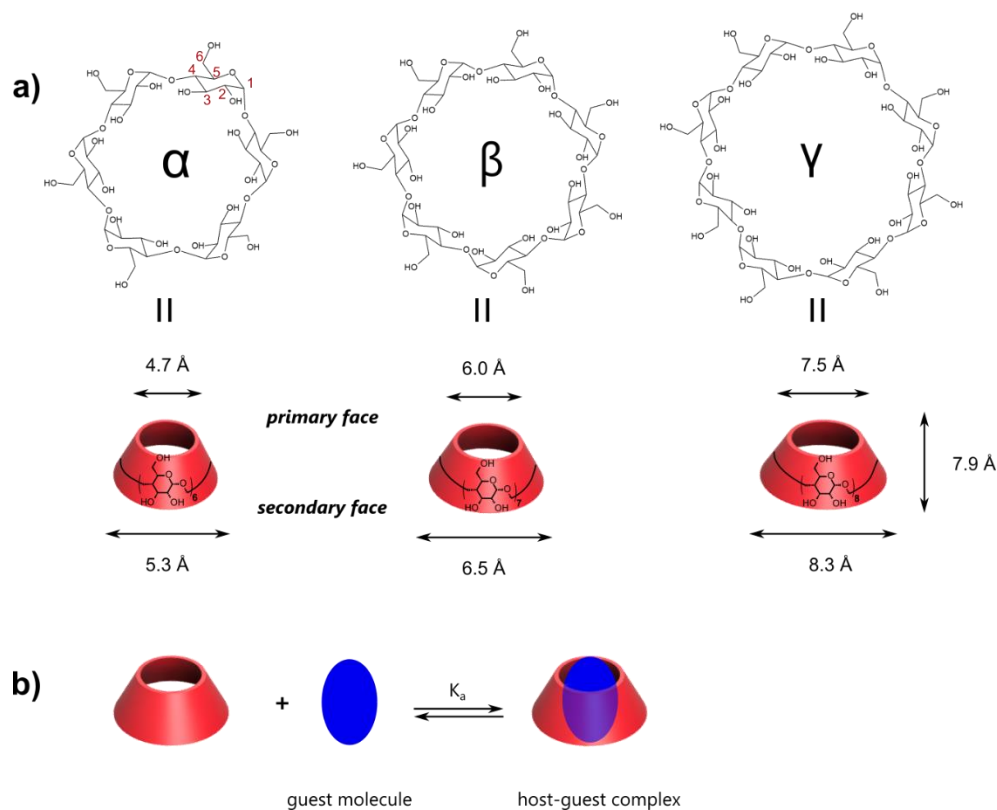
Beyond traditional molecular chemistry that involves the formation of covalent bonds by the sharing of electron pairs between two atoms, supramolecular chemistry deals with weak, reversible non-covalent interactions between molecules. In this thesis, cyclodextrins (CDs) are emerging as versatile supramolecular building blocks in the design of *smart* materials for batteries applications. Indeed, they are well-defined cyclic oligosaccharides which can form *host-guest* complexes with a large panel of compounds, from small molecules to polymers. The CD-based *host-guest* inclusion complexation and the different classes of adaptive materials made of CDs are presented next, followed by a brief overview of the already successful utilisations of CD supramolecular chemistry in enhancing Li-based batteries performances.

## 1. Cyclodextrin *host-guest* supramolecular chemistry

### a. Structure and properties of cyclodextrins (CDs)

Cyclodextrins (CDs) are cyclic oligosaccharides naturally occurring from enzymatic starch degradation. They are non-toxic and biodegradable. Three main types of CDs have been isolated so far :  $\alpha$ -CD is composed of six glucopyranose units in chair conformation, linked by  $\alpha$ -1,4 glycosidic bonds, whereas  $\beta$ -CD and  $\gamma$ -CD consist of seven and eight units respectively (Figure I.1.a.). They can adopt a truncated cone shape with a 7.9 Å depth cavity. The secondary hydroxyl groups are orientated towards the wide rim of the cone (secondary face) and the narrow rim (primary face) is decorated with the primary alcohols, hence making them soluble in water. The interior of the cavity is lined with glycosidic oxygens and rows of CH groups coming from C3 and C5, which provide some non-polar and rather hydrophobic properties.  $\alpha$ -CD,  $\beta$ -CD and  $\gamma$ -CD differ from the diameters of their primary and secondary faces: 4.7 Å and 5.3 Å for  $\alpha$ -CD, 6.0 Å and 6.5 Å for  $\beta$ -CD and 7.5 Å and 8.3 Å for  $\gamma$ -CD<sup>8</sup> (Figure I.1.a.) Moreover, they exhibit disparate solubilities in water that are often correlated to the presence of intramolecular hydrogen bonds between primary alcohols ( $s_\alpha = 145 \text{ g.L}^{-1}$ ,  $s_\beta = 18.5$  and  $s_\gamma = 232 \text{ g.L}^{-1}$ )<sup>9</sup>.

The possession of this cavity makes CDs attractive since they can form *host-guest* inclusion complexes with a large panel of rather hydrophobic *guest* molecules (Figure I.1.b.). Since their discovery by Villiers in 1891, this molecular recognition property has raised intensive research and CDs-based materials have been successfully developed for many emerging applications such as drug delivery, tissue engineering, diagnostics and therapies, smart coatings, foods, cosmetic, textile, or pollutant removal to cite only a few<sup>9,10</sup>. For these applications, the major advantage lies in the water solubilization of rather hydrophobic *guest* molecules by the means of CD complexation.



**Figure I.1: Cyclodextrins.** a) Representations of  $\alpha$ -,  $\beta$ -, and  $\gamma$ -CDs, with the indication of the nomenclature used to identify the different protons and carbons of the glucopyranose units. b) CD *host-guest* complexation equilibrium.

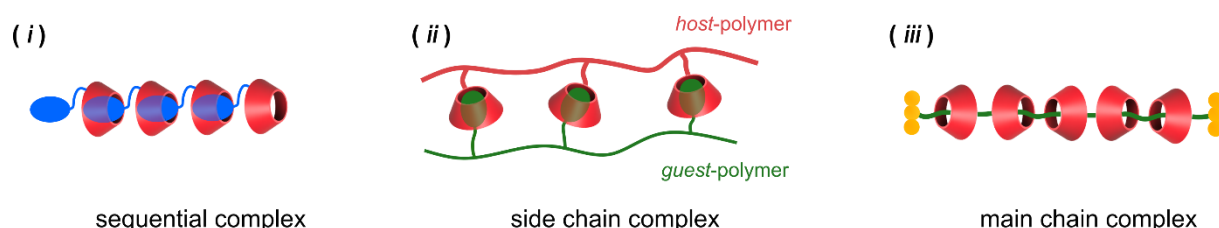
The inclusion complex forms through a reversible elementary reaction involving two partners, the *guest* molecule and the *host* molecule (here CD). The most commonly reported stoichiometric ratio is 1:1. Although the complex formation is spontaneous ( $\Delta G < 0$ ), inclusion complexes easily dissociate under mild conditions (dilution or temperature rise) because of the reversible nature of the supramolecular interactions that hold the structure. Thus, the stability of a complex is expressed through its association or binding constant  $K_a$ , ( $\Delta G = -RT \ln K_a = \Delta H - T\Delta S$ ). A wide number of analytical methods are available for the characterization of inclusion complexes in solution: spectroscopic, chromatographic or calorimetric methods are the more generally used<sup>11,12</sup>.

We will succinctly review the supramolecular interactions that participate in the CD *host-guest* interaction<sup>8,13</sup>. In aqueous medium, the encapsulation of a *guest* molecule by the CD cavity is mainly supported by **hydrophobic effect**. Indeed, the inclusion complex formation is favoured by the poor interactions existing between water molecules and both, the CD cavity and the surface of the *guest* molecule. The expulsion of water molecules from the cavity constitutes the main complexation driving force that is correlated to an exothermic contribution ( $\Delta H$ ). The self-reorganization of these released molecules through H-bonding mainly composes the entropy contribution ( $\Delta S$ ). **Van der Waals interactions** also participate by stabilizing the complex and they can even monitor the orientation of the *guest* molecule. Additionally, **size-** and **shape-matching** between host and *guest* play a role in the binding strength. Finally, **hydrogen bonding** with the CD hydroxyl groups implies a greater complexation strength for *guest* molecules embedded with H-bonds donor or acceptor groups. So in short, we must remember that the complexation strength depends on the complementary between CD and the *guest* molecule (nature, size, conformation) as well as on the environment (solvent, temperature, pH).

The *host-guest* interaction of CD offers great opportunity to realize “macroscopic molecular recognition”. Indeed, CDs can participate in supramolecular assemblies involving macromolecular chains, either as supramolecular building blocks or via the functionalization of their hydroxyl groups. The resulting architectures provide design opportunities that are exposed in the following section.

### b. From molecular recognition to macroscopic molecular recognition

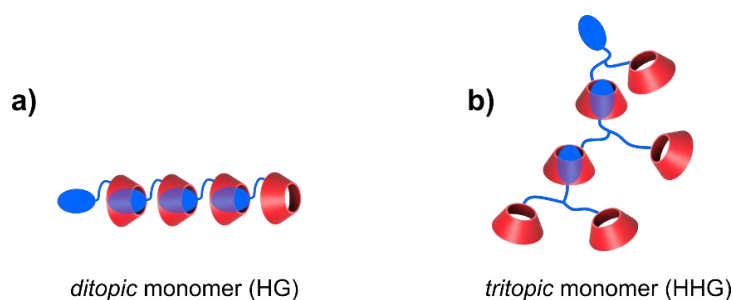
The CD molecular recognition can be exploited to form (i) sequential, (ii) side chain or (iii) main chain complexes, hence categorising three main types of architectures<sup>14</sup> (Figure I.2). This section is dedicated to the description of these different structures from the synthesis point of view.



**Figure I.2: Three types of macromolecular complexes based on CD *host-guest* interaction.**

### Sequential complexes

Sequential complexation leads to the formation of supramolecular polymers (SMP) under equilibrium conditions. They are self-assembled macromolecules constituted of monomers that interact to each other through non-covalent reversible and directional interactions. Lehn *et al* first demonstrated this concept by introducing H-bonding self-assembled polymers<sup>15</sup>. CDs also appear as suitable monomers to synthesise SMP held by *host-guest* interactions, because they can be easily functionalized through their hydroxyl functions<sup>16,17</sup>. Different types of architectures can be obtained: *ditopic* monomers form linear or cyclic SMP (Figure I.3.a.), while *multitopic* monomers can reach ramified architectures (Figure I.3.b)<sup>18</sup>.



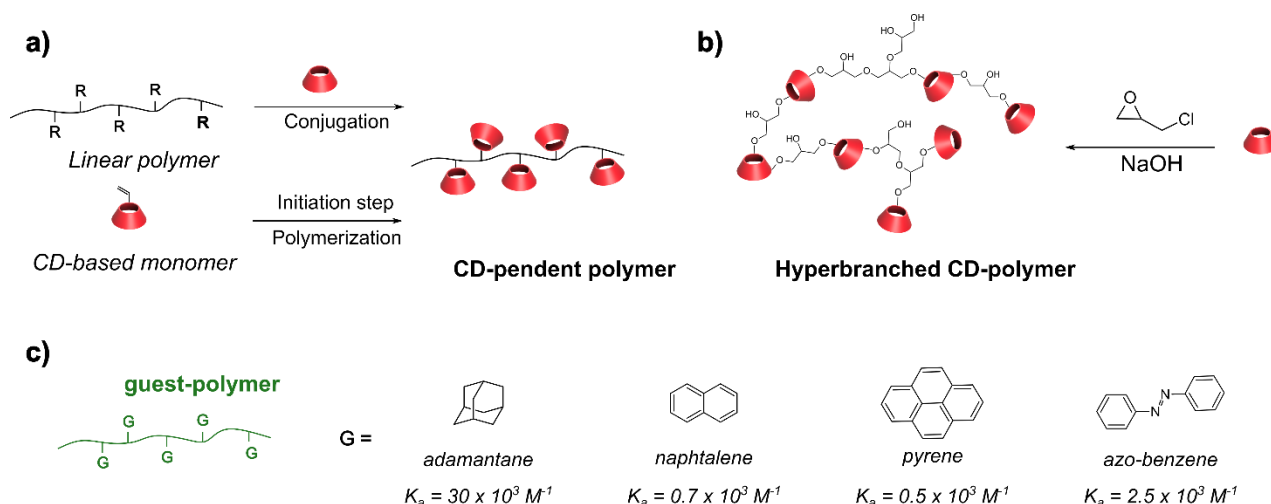
**Figure I.3: Examples of SMP obtained from CDs-based monomers.** To designate the monomer, H and G stand for the CD *host* and the *guest* molecule moieties respectively. **a)** Linear SMP made of a (HG) *ditopic* monomer. **b)** Ramified architecture made of a (HHG) *tritopic* monomer.

Despite the great variety of architectures that can be fabricated, the reversible nature of the *host-guest* interaction leads to the poor stability of these dynamic systems either in temperature or in solution. Furthermore, the development of CDs-based SMP requires a sophisticated organic chemistry to selectively functionalize CD hydroxyl groups. Therefore, for practicability issues this thesis focuses on the side chain and main chain complexes that involve macromolecular chains of polymer, hence ensuring a better stability control.

### Side chain complexes

The high reactivity of hydroxyl functions offers opportunities for CDs to be incorporated as pendent units of a desired polymer. Such architectures, called *host-polymers*, are obtained either by the polymerization of CD-based monomers or by the *post*-functionalisation of CDs on the polymer chain<sup>19</sup> (Figure I.4.a.). On the one hand, CD-based monomers are commonly embedded with acrylamide functions to undergo a conventional radical polymerization<sup>20-27</sup>. On the other hand,

various conjugation chemistries can be used to react CD-based derivatives with side chains polymers: amidation<sup>28–32</sup> and Huisgen-type cycloaddition involving alkyne-pendent polymers and azide modified CDs<sup>33–35</sup> are the most prevalent synthetic routes. Other widespread *host*-polymer matrices are the commercialized hyperbranched CDs-polymers that are prepared from CDs cross-linked with epichlorohydrin<sup>36,37</sup>. Despite its easy implementation, the latter method falls short in controlling the architecture of the targeted network as well as the aforementioned strategies.



**Figure I.4: Side chain complexes of CDs.** Synthetic routes of host-polymers as **a)** CD-pendent polymers **b)** hyperbranched CDs-polymer. **c)** Example of the most common *guest* moieties used in the design of *guest*-polymers with the indication of their  $K_a$  towards  $\beta$ -CD (from ref<sup>8</sup>).

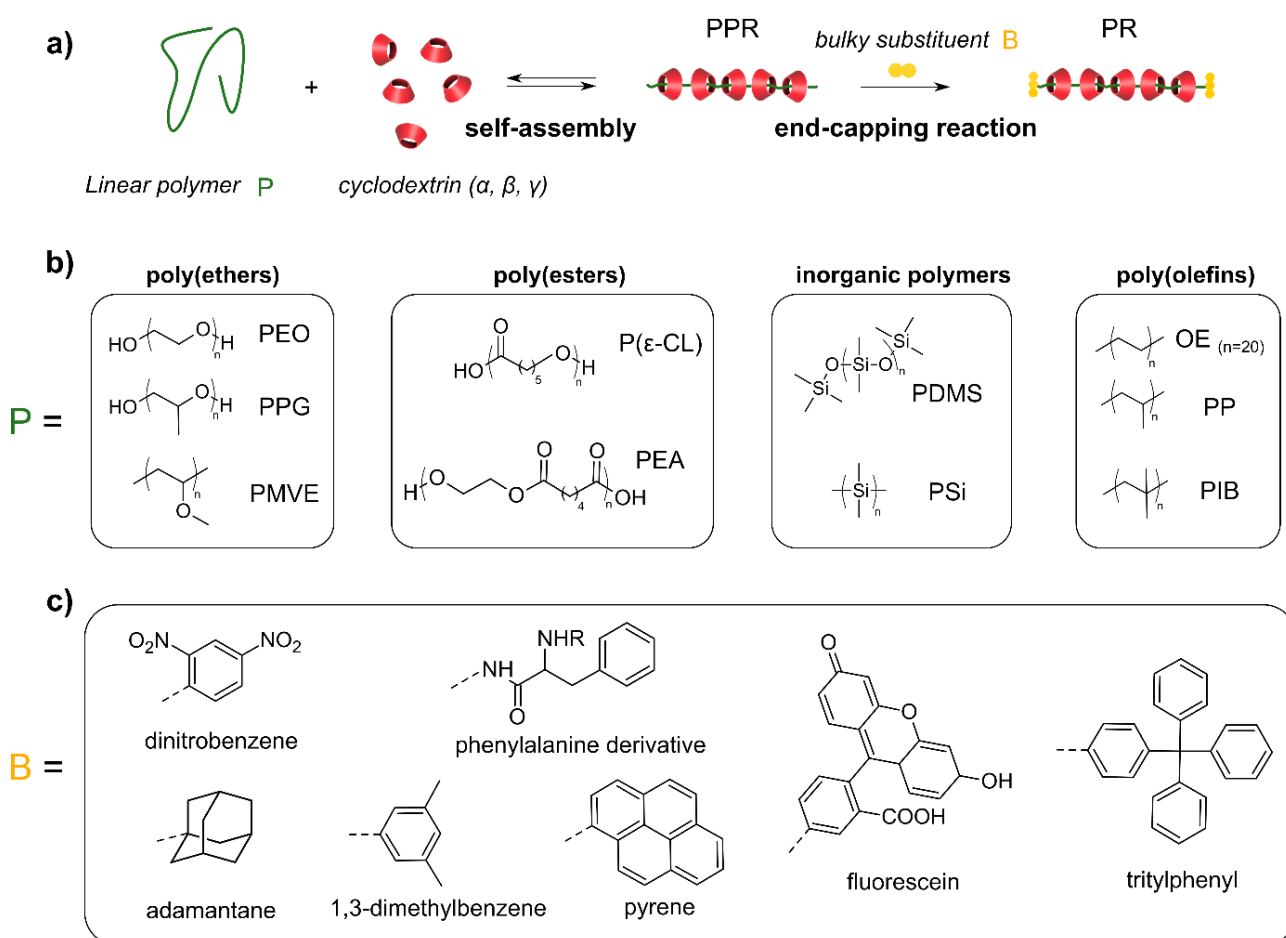
Simultaneously, some *guest*-polymers can be synthesised from adamantane<sup>28–30,35,36,38</sup>, azo-benzene<sup>23,25,37,39–41</sup>, naphthalene<sup>20,21,31</sup> or pyrene substituents<sup>21,22</sup> to cite only a few molecules known for being complexed by CDs (Figure I.4.b). Thus, the cooperative binding of *host*- and *guest* polymers though numerous interaction points is promoted by the side chain molecular recognition process which is very related to the antigen-antibody complex or the secondary structure of DNA or proteins. It enables the formation of a myriad of easily-processable adaptive materials that display some attractive functions that will be overviewed subsequently.

### Main chain complexes

CDs can also interact with polymer chain to form threaded molecular systems (Figure I.5.a.) as demonstrated by Harada *et al* through X-ray analysis and turbidity measurements<sup>42</sup>. The threading process of  $\alpha$ -CDs on poly(ethylene oxide) (PEO) leads to **pseudopolyrotaxane** (PPR). The major driving force for forming these tubular architectures lies on the supramolecular interactions between

the inner surface of the CD ring and the polymer units (see 1.a.). Moreover, the structure is strengthened by the hydrogen bonding between the hydroxyl groups of neighbouring CDs which preferentially arrange through head-to-head and tail-to-tail modes<sup>43,44</sup>.

A wide variety of PPR has been synthesized from linear polymers, the most common ones being poly(ethers), poly(esters), inorganic polymers or polyolefins<sup>18,45</sup> (Figure I.5.b). The adequation of the size of the CDs cavities with the cross-section of the threading polymer is needed to achieve a high yield PPR formation. This is well illustrated by the work of Harada *et al*, showing that  $\beta$ -CDs produce complexes with poly(propylene glycol) (PPG) whereas no PPR could be isolated with PEO<sup>46</sup>. A similar conclusion was drawn for  $\gamma$ -CDs from which PPR could be obtained with poly(methyl vinyl ether) (PMVE), while negligible complexation occurs with PPG<sup>47</sup>. Interestingly,  $\gamma$ -CDs does not include spontaneously PEO, but they can accommodate two PEO chains resulting in a double-stranded PPR<sup>48</sup>.



**Figure I.5: Various synthetic routes of CDs-based PRs.** **a)** Scheme of the two-step's PR synthesis. **b)** Examples of threading polymers: poly(ethylene oxide) (PEO), poly(propylene glycol) (PPG), poly(methyl vinyl ether) (PMVE), poly( $\epsilon$ -caprolactone) (P $\epsilon$ -CL), poly(alkylene adipate) (PEA), poly(dimethylsiloxane) (PDMS), poly(dimethylsilane) (PSi), oligoethylene (OE), poly(propylene) (PP), poly(isobutylene) (PIB). **c)** Examples of end-capping groups.

The poor stability of PPR in solution, mainly due to the nature of their constituting interactions, led researchers to synthesize **polyrotaxanes** (PR) via the attachment of bulky substituents at the end-chains of the threading polymer (Figure I.5.c). The end-capping groups must be sufficiently large to prevent CDs from dethreading, hence ensuring a “molecular necklace” architecture for the PR. Different synthetic pathways have been developed with a particular attention paid to the kinetics because there is a competition between the end-capping reaction and the PPR dissociation.

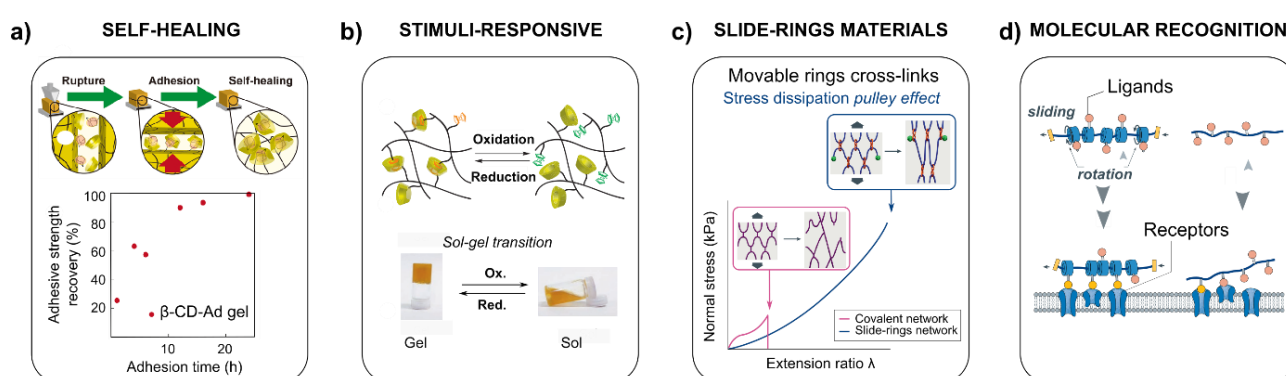
The first  $\alpha$ -CD based PR reported was prepared through the nucleophilic aromatic substitution of dinitrofluorobenzene (DNFB) which reacts with the terminal amino groups of a pre-functionalized PEO under homogeneous conditions. Despite the undesirable secondary reaction which can occur between DNFB and  $\alpha$ -CD hydroxyl groups, this route remains the most employed nowadays to synthesize  $\alpha$ -CD based PR<sup>49</sup>. Other grafting approaches have been pursued by reacting PEO terminal amino groups with phenylalanine<sup>50–52</sup>, fluorescein derivatives<sup>53,54</sup> or by introducing adamantane moieties to PEO end-chains pre-functionalized with amino<sup>55</sup> or carboxylic acids groups<sup>56</sup>. Moreover, impressive yields have been obtained through the reaction of pre-tosylated end-chains of PEO with dimethylphenol<sup>57</sup> or by the radical coupling reaction of terminal PEO methacrylate functions with pyrene moieties<sup>58</sup>. More recently, to overcome the dethreading phenomenon and achieve highly compact PR, some groups have taken advantage of isocyanate reactivity and have developed a solvent-free synthesis<sup>59</sup> and a one-pot PR synthesis<sup>60</sup> involving the grafting of a tritylphenyl and 1,3-dimethyl benzene derivatives respectively.

In addition to the various synthetic methods mentioned above, PRs can be precisely tailored using different types of CDs and any molecular weight for the threading polymer, by obtaining different PR ring coverage, *ie* the number of CDs threaded per polymer, by easily modifying the threaded CDs or synthesizing PR from block copolymers, brush, star or branched polymers<sup>45,61</sup>. The sliding of CDs along the polymer chain gives a dynamic feature, hence opening the feasibility of integrating these interlocked macromolecules into real systems.



### c. Smart properties induced by CD macroscopic molecular recognition

The dynamic nature of the CD *host-guest* interaction provides the above-described supramolecular materials with some *smart* attractive features. In the following section, we will report the most striking examples of CDs-based adaptive materials, stressing the role of the architecture design. The selective molecular recognition originating from the side chain complex approach has mainly been considered for self-healing and stimuli responsiveness. In contrast, main chain complexes are rather exploited to enhance mechanical properties or facilitate macromolecular recognition for biomaterials (Figure I.6).



**Figure I.6: Smart CDs-based adaptive materials categories.** **a)** Self-healing through  $\beta$ -CD/adamantane cooperative *host-guest* interaction, adapted from ref<sup>62</sup>. **b)** Red-ox responsive sol-gel switching through  $\beta$ -CD/ferrocene, adapted from ref<sup>63</sup>. **c)** Improved mechanical properties for slide-rings materials adapted from ref<sup>64</sup>. **d)** Multivalent binding molecular recognition, adapted from ref<sup>64</sup>. Yellow ligand indicates the successful ligand-receptor binding.

#### Self-healing properties

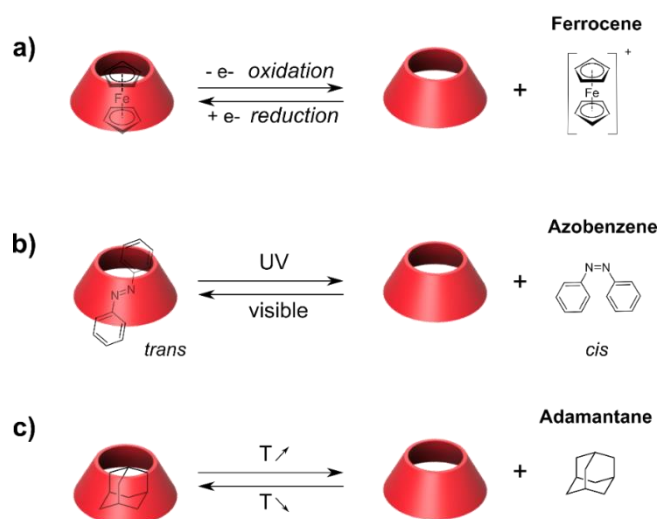
Self-healing is the ability that a material has to spontaneously repair the cracks or fractures. The repairing mechanism of CDs-based self-healing materials lies on the reversibility of *host-guest* interaction. Kakuta *et al* designed the first self-healable supramolecular hydrogel based on the selective  $\beta$ -CD/adamantane interaction, adopting the side chain complex approach (Figure I.6.a.). Furthermore, they compared two *guest*-hydrogels equipped with either adamantane or butyl groups and showed the self-healing efficiency is intimately linked to the *host-guest* binding strengths<sup>62</sup>. Many other self-healing CDs-based materials have arisen from this work and have been recently inventoried by Mohamadhoseini *et al*<sup>65</sup>.

Later, Kobayashi *et al* coupled the side chain and the main chain complexes approaches to prepare a supramolecular gel relying on the spontaneous interaction of a  $\beta$ -CDs-pendent polymer with

adamantane moieties grafted on an  $\alpha$ -CDs-based PR. The better healing rate of these gels was attributed to the enhanced flexibility originating from the sliding motion of  $\alpha$ -CD on the polymer chain<sup>66</sup>.

### Stimuli-responsive properties

The association and dissociation of *host-guest* complexes depend on the environmental conditions. Temperature, light or red-ox have been largely exploited to design stimuli-responsive materials. Ferrocene derivatives are used to embed the materials with **red-ox responsiveness** since the oxidation of ferrocene results in the dissociation of CD/ferrocene complex (Figure I.7.a.). Thus, some supramolecular sol-gel transition materials were fabricated from the side chain complex approach involving a  $\beta$ -CDs-pendent poly(acrylic acid) (PAA) (*host-polymer*) and PAA possessing ferrocene moieties (*guest-polymer*)<sup>63</sup> (Figure I.6.b).



**Figure I.7: Stimuli-responsive CD complexation.** a) Ferrocene red-ox, b) azobenzene light and c) adamantane temperature responsiveness towards CD complexation.

Light also appears as an interesting stimulus since it can be precisely applied both temporally and spatially. Azobenzene derivatives, which are efficiently accommodated in CDs cavities, are often chosen for the design of **light-responsive** materials. Indeed, under UV irradiation, they exhibit a reversible isomerization from the *trans* to *cis* conformation, inducing the dissociation of the *host-guest* complex. Visible light irradiation allows the conformation to go back from *cis* to *trans* and the re-complexation (Figure I.7.b). Therefore, sol-gel systems were successfully designed<sup>41,67</sup> and the

different affinities of  $\alpha$ -CD and  $\beta$ -CD towards the *trans*-azobenzene and *cis*-azobenzene were exploited to prepare of a photo-switchable gel assembly system ( $K_{\alpha-trans} = 2000 > K_{\beta-trans} = 770 M^{-1}$  vs  $K_{\alpha-cis} = 35 > K_{\beta-cis} = 280 M^{-1}$ )<sup>23</sup>. Moreover, systems containing  $\alpha$ -CD/azobenzene<sup>68</sup> and  $\beta$ -CD/ferrocene<sup>25</sup> *host-guest* interactions have shown promising results in realizing muscle-like movements as they can convert light or chemical red-ox stimuli respectively into mechanical energy (deformation, contraction, expansion).

Finally, CDs inclusion complexes display **reversible thermal properties** (Figure I.7.c). Due to their negative association enthalpy, they dissociate when increasing the temperature and form again at lower temperature<sup>8</sup>. A clear example is the colour change, from transparent to purple, of a hydrogel based on the *host-guest* interaction of  $\beta$ -CD and phenolphthalein (purple) that can be triggered by thermal (80°C) or electric (Joule effect) stimuli<sup>69</sup>. Low temperatures can also be used to boost the complexation strength as emphasized in Zheng's work<sup>70</sup>. At 5°C, benzyl gels self-assemble with  $\alpha$ -,  $\beta$ - and  $\gamma$ -CDs gels whereas at ambient temperature, the macroscopic self-assembly only occurs for  $\beta$ -CDs gels, which is consistent with the binding constant values ( $K_{\beta} \sim 10^2 M^{-1}$  vs  $K_{\alpha} \sim 10^1 M^{-1}$ ).

### **Mechanical properties**

Unusual degrees of freedom are ascribed to CDs that are constituting main chain PRs, such as rotating motions and sliding along the threading polymer. Inspired from the working principle of moving pulleys, PRs have been integrated in polymer networks to form slide-rings materials (Figure I.6.c). Owing to mobile interlocked cross-links, such polymer allows the stress dissipation in a cooperative manner inducing some impressive mechanical properties. The influence of this topological cross-linking is well-reported in the recent review of Hart *et al*, in terms of decline of Young's modulus decline, greater strain at break and better strain recovery than conventional fixed cross-linked polymers<sup>64</sup>. These novel materials have been developed for many industrial applications from the scratch-resistant coatings, vibration-proof insulating materials<sup>71</sup>, to stimuli-responsive hydrogels<sup>72,73</sup>. A more detailed overview of the structure-properties relationship of these interlocked architectures is provided in the introduction of Chapter III.

### **Molecular recognition for biomedical applications**

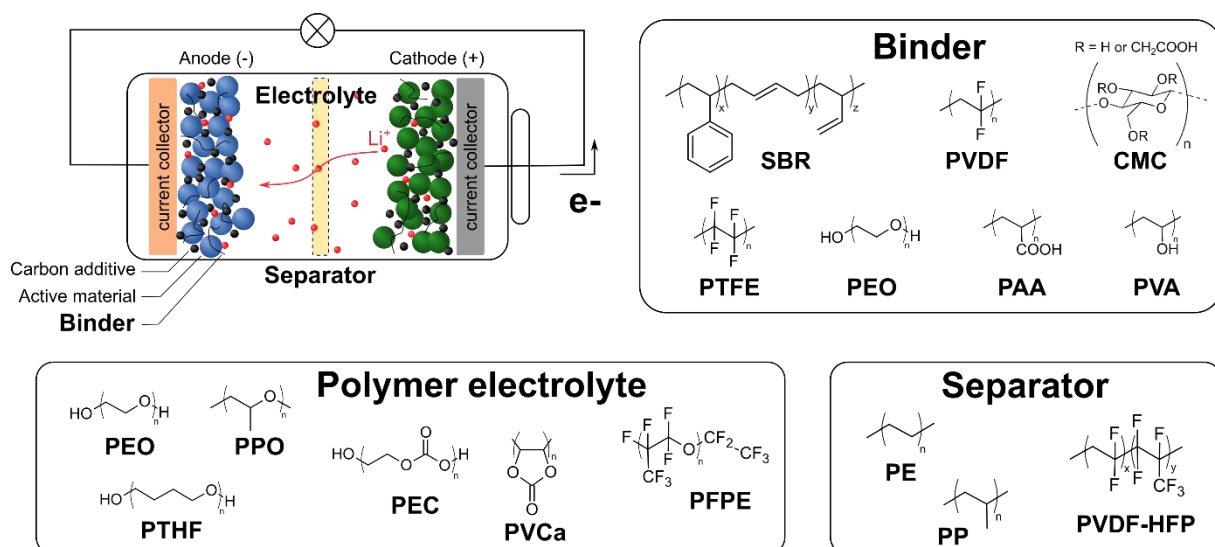
Eventually, the CD *host-guest* interaction has been exploited for biomedical applications owing to the hydrophilicity and biocompatibility of CDs. On the one hand, PRs have recently drawn particular

attention because they can be used as precursors for the synthesis of molecular tubes. Obtained by cross-linking adjacent CDs (mostly epichlorohydrin) and then cleaving the covalent bond between the threading polymer and the end-capping groups<sup>74,75</sup>, these molecular tubes exhibit some inclusion abilities<sup>76</sup>, which offer some great opportunity in the design of drug/gene delivery systems. On the other hand, the ring mobility (sliding and rotation) in PRs has also been used to enhance biological targeting of synthetic systems. Considering weak ligand-receptor interactions, biological ligands grafted on the threaded CDs achieve more efficient and adaptive multivalent interactions with the binding sites of their receptor proteins due to the mobility of CDs<sup>52,77,78</sup> (Figure I.6.d).

In conclusion, adaptive features result from the dynamic nature of the CD *host-guest* interaction. The research currently undergoes a turning point with the willingness to introduce these smart supramolecular systems into real applications. Clearly the biomedical field seems to be befitting but a significant attention has also been gained in the energy sector in the last decade, especially for electrochemical energy storage systems such as batteries. Indeed, equipping batteries components with *smart* CDs-based materials has already demonstrated some performances improvements while integrating into an eco-compatibility approach. The following part of this Chapter report and discuss the successful implementation of the CD *host-guest* interaction to enhance Li-based batteries performances.

## 2. Cyclodextrin architectures enabling Li-based batteries improvements

Recently, the increasing demand for higher performances batteries has led to the design of new functional organic polymers to improve the operation of existing materials or facilitate the development of next-generation batteries. Although most polymers are electrochemically inactive, they are ubiquitous in Li-based batteries either in liquid or solid state. They commonly operate as binders, separators, and solid electrolytes to provide mechanical stability, adhesion, and structural support to the devices<sup>79</sup>. In this context, CD supramolecular chemistry stands as an ideal engineering platform to introduce advanced functionalities to polymeric materials. To facilitate the understanding, we will briefly describe the role and structure of each aforementioned polymer-based battery component (Figure I.8).



**Figure I.8: Summary of the organic polymers mainly used in the Li-based batteries design.** The scheme shows the Li-based battery charging mode ( $\text{Li}^+$  moving from the cathode to the anode).

The basic role of a **binder** is to maintain the cohesion between the electrode components (*ie*, active material, conductive additive), while preserving a good adhesion to the current collector. Depending on the nature of the active material, different linear polymers have been used as conventional binders: poly(vinylidene fluoride) (PVDF), styrene butadiene rubber (SBR), poly(tetrafluoro ethylene) (PTFE), sodium carboxymethyl cellulose (CMC), poly(acrylic acid) (PAA), poly(vinyl alcohol) (PVA), or poly(ethylene oxide) (PEO).

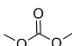
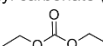
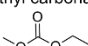
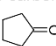
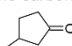
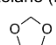
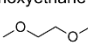
The simultaneous electrochemical reactions occurring at the battery electrodes induce an electrons flow in the external circuit and an ions flow through the electrolyte. In liquid-based batteries, the **separator** electrically isolates the two electrodes from each other, while allowing the ion conduction through its pores ( $\sim 30\text{-}100$  nm). Separators are generally made of poly(vinylidene fluoride-co-hexafluoropropylene) (PVDF-HFP) or polyolefins such as poly(ethylene) (PE), poly(propylene) (PP).

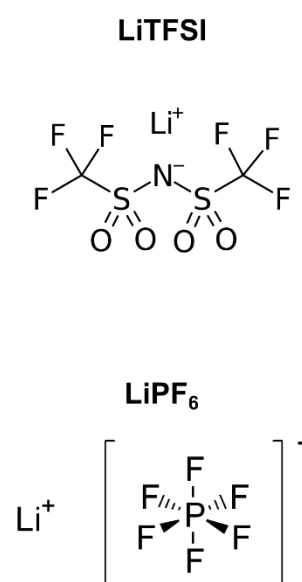
To enhance battery safety aspects, such as flammability of liquid electrolytes, some efforts have simultaneously been pursued to turn liquid Li-ion batteries into solid devices, implying the development of solid electrolytes. Polymers have been widely studied as solid polymer **electrolytes** (SPE), which consist of a polymer hosting dissolved Li-salts. Although PEO remains the most widely used, poly(propylene oxide) (PPO), poly(tetrahydrofuran) (PTHF), poly(ethylene carbonate) (PEC), poly(vinylene carbonate) (PVCa), perfluoropoly(ether) (PFPE) have also been utilized.

Interestingly, the CD *host-guest* interaction has been recently exploited to design new types of battery polymer-based components such as binders or customized electrolytes. Several desirable properties have been achieved such as (i) the tailoring of electrolytes (liquid or SPE) for *advanced* Li-ion batteries, (ii) the design of efficient Si anode binders and (iii) the molecular recognition of parasitic soluble red-ox species, as the so-called polysulfides that cause undesirable effect in Li-S batteries performances. In the following sections, we discuss the benefits of the CD *host-guest* chemistry in the above-mentioned realizations. For reason of clarity, for each case, some battery context is provided to highlight the inherent drawback that is targeted via the implementation of CDs-based materials.

### a. Tailoring Li-ion batteries electrolytes

The composition skeleton of Li-based electrolytes has not varied much since the first Li-ion cell was brought to the market in 1991 by Sony. Liquid electrolytes consist in a lithium (Li) salt that is solubilized in a mixture of organic solvents. Figure I.9 references the most generally used Li salts and carbonate and ether solvents.

Solvent	$T_m/T_b(^{\circ}\text{C})$	$\epsilon_R$	$\eta$ (mPa 25 $^{\circ}\text{C}$ )
Dimethyl carbonate (DMC) 	5 / 91	3.1	0.6
Diethyl carbonate (DEC) 	-74 / 126	2.8	0.8
Ethyl methyl carbonate (EMC) 	-53 / 110	2.9	0.7
Ethylene carbonate (EC) 	36 / 248	90	1.9 (40 $^{\circ}\text{C}$ )
Propylene carbonate (PC) 	-49 / 242	65	2.5
Dioxolane (DOL) 	-95 / 78	7.1	0.6
Dimethoxyethane (DME) 	-58 / 84	7.2	0.5

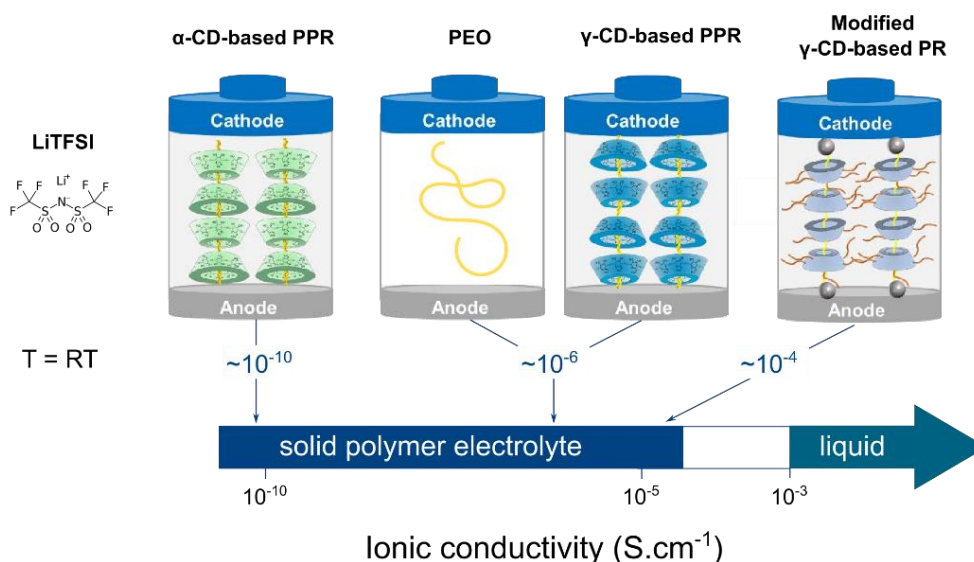


**Figure I.9: Main composition of liquid electrolyte for Li-based battery (from ref<sup>80</sup>).** LiTFSI and LiPF stands as lithium bis(trifluoromethanesulfonyl)imide and lithium hexafluorophosphate.<sup>6</sup>

Besides being stable over a wide range of potential ([0-4V]) and meeting the requirements of interfacial stability with both anode and cathode, the electrolytes key property is the ionic conductivity ( $\sigma$ ). It quantifies how mobile the ions are ( $\text{Li}^+$  for Li-based batteries), for participating in the electrochemical reactions at the electrodes. The Li transference number ( $t^+$ ) evaluates the contribution of  $\text{Li}^+$  to the total electrolyte conductivity. For liquid electrolytes, numerous interwoven factors affect the ionic conductivity, such as the solvent dielectric permittivity  $\epsilon_R$  (dissolution of salts), the viscosity  $\eta$ , the glass transition, melting and boiling temperatures (facilitating ion transport), as well as the interactions of both anions and solvent with  $\text{Li}^+$ . For SPE, the empirical Vogel-Tammann-Fulcher (VTF) model is often used to describe the ion transport, relying on the strong inter-relation between ionic conductivity and polymer chain motion<sup>81</sup>. In the context of this thesis, we have spotted two recent strategies benefiting from the CD *host-guest* interaction to design liquid of SPE electrolytes with enhanced Li transport properties. They are discussed hereafter.

The first approach tackles organic liquid-based electrolytes containing LiTFSI. Taking advantage of the CD *host-guest* interaction at the molecular level, Jeschke *et al* reported a new concept of capture of the TFSI anion, to reach a close to 1 Li transport number ( $t^+$ ). The principle is simple : if TFSI anion is immobilized, the  $\text{Li}^+$  contribution to the total ionic conductivity is enhanced. Overwhelmed evidence of TFSI encapsulation by randomly methylated  $\beta$ -CD (RM $\beta$ -CD) was obtained in organic solvent. However, the anticipated decrease in TFSI ion mobility was not successfully achieved owing to dynamic guest exchange in RM $\beta$ -CD/TFSI complexation. Therefore, this promising concept calls for a more efficient trapping of TFSI in RM $\beta$ -CD. According to the authors, both the chemical modification and the grafting of the *host* molecule on immobilized components of the batteries (such as separator) can be envisioned<sup>82</sup>.

The second strategy is part of the overall challenge facing SPES about finding the right balance between mechanical strength and ionic conductivity to enable the resulting solid-state polymer batteries at ambient temperature. A new class of SPEs prepared from CDs-based PPRs<sup>83</sup> or PRs<sup>84</sup> mixed with LiTFSI has been recently introduced by Winter's group. The main interest of considering these mechanically interlocked architectures lies on the numerous tailored structures that can be synthesized varying the CD cavity dimensions ( $\alpha$ -,  $\beta$ - to  $\gamma$ -CD) or the polymer backbone (nature, molecular weight) and functionalizing the threaded CDs (Figure I.10).



**Figure I.10: Polyrotaxanes as the new platform for tailored solid polymer electrolyte**, adapted from ref<sup>83,84</sup>.

First, the ionic conductivity of the most widely used SPE ( $\sim 10^{-6} S.cm^{-1}$  for PEO+LiTFSI at RT) was compared to the ones of (PPR+LiTFSI) SPE, that were obtained by a one-pot self-assembly process<sup>83</sup>. Although they are not competitive, they interestingly rise with the ring size of CDs ( $\sigma_{\alpha} \sim 10^{-10}$ ;  $\sigma_{\beta} \sim 10^{-8}$  &  $\sigma_{\gamma} \sim 10^{-6} S.cm^{-1}$  at RT). The authors attributed this finding to steric effect induced by the different diameters of CDs. We also assume that the different PR ring coverages may play a role in the resulting flexibility of the threading polymer. Next, PPRs were methylated to prevent H-bonding between neighbouring CDs to enhance flexibility. These modified PPR-based electrolyte exhibit the same trend in terms of ring size : they get more conductive ( $\times 10^{1.5}$ ) and the Li transport number ( $Li^{+}$ ) becomes three times higher than (PEO+LiTFSI) SPE<sup>83</sup>. An alternative modification route was carried out to simultaneously achieve PEO end-capping and graft poly( $\epsilon$ -caprolactone) flexible side chains on  $\gamma$ -CDs<sup>85</sup>. The corresponding PR-based SPE exhibits some impressive ionic conductivities ( $\sigma \sim 10^{-4} S.cm^{-1}$ ) as well as enables great cycling performances at  $40^{\circ}C$  while (PEO+LiTFSI) cannot be cycled at such temperature<sup>84</sup>.

In conclusion, both approaches have brought into the scene original concepts to tailor Li-based battery polymer or liquid electrolyte, by taking advantage of the CD-based supramolecular chemistry. However, real performances benefits are still awaiting to be proved. Indeed, the first example raises the question of the dynamic nature of the CD *host-guest* interaction equilibrium that complicates any efficient trapping strategy in bulk solution. Turning to the second, PPR and PR have been used as



highly flexible scaffold macromolecules to achieve tailored hyperbranched architectures by modifying the threaded CDs. It remains to determine if the channel-type architecture combined with the CD sliding motion have an influence on the electrolyte properties. An earlier study suggested that tubular structures may provide directional pathways for  $\text{Li}^+$  fast transport<sup>86</sup>, while preventing the access of anions by size exclusion. Molecular dynamics simulations confirmed the latter assumption but showed that  $\text{Li}^+$  were mostly distributed outside the channels<sup>83,84</sup>.

### b. Designing Si anode binders

Si stands among the most promising candidate for *advanced* Li-ion batteries anode materials, owing to its theoretical capacity of  $3600 \text{ mAh}\cdot\text{g}^{-1}$ , which is almost ten times higher than the commercialized graphite anodes ( $372 \text{ mAh}\cdot\text{g}^{-1}$ ). The interest in Si also stems from its abundance in nature, its low cost and low discharge voltage ( $< 0.5 \text{ V vs Li}^+/\text{Li}$ ). However, during the electrochemical alloying processes of lithiation (charge) and delithiation (discharge), Si experiences colossal volume fluctuations ( $\sim 300\%$ ) leading to the electrode structural collapse. Si electrode undergoes cracking and pulverization which contribute to its delamination and thus the electrical isolation of some Si domains. Moreover, a critical issue is the stability of the solid electrolyte interface (SEI), which is the layer composed of electrolyte reduction products, that forms at the electrode-electrolyte interface<sup>87</sup>. This layer constantly grows as some fresh Si surfaces are created (Figure I.11). Unsurprisingly, these main degradation mechanisms result in poor cycling performances of Si anodes<sup>88-91</sup>, hence the colossal amount of studies devoted to improving Si electrode cyclability<sup>87,92,93</sup>.

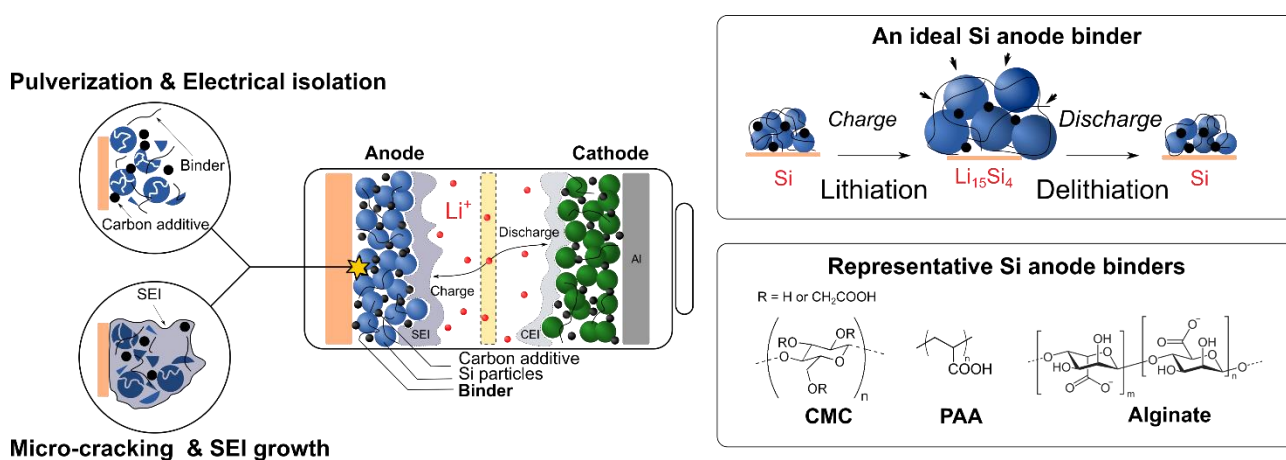
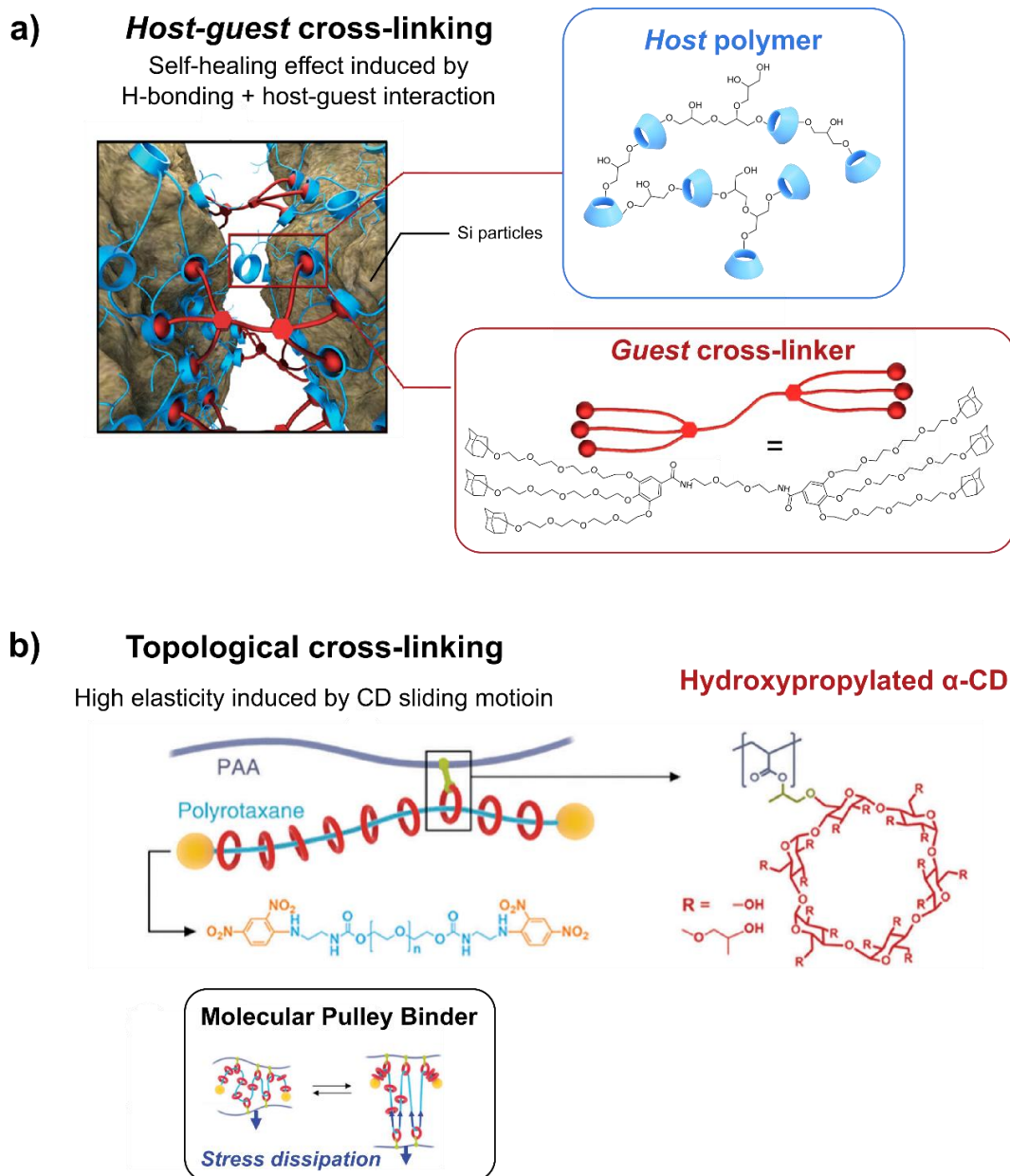


Figure I.11: Illustration of the desired working principle of a Si anode binder.

In this thesis, we focus here on the design of Si anode binders that can maintain the electrode structure and accommodate the mechanical stress along cycling<sup>94–96</sup>. Up to now, the most widely implemented Si anode binders are synthetic and bio-derived polymers containing carboxyl and hydroxyl groups, such as poly(acrylic acid) (PAA)<sup>97</sup>, sodium alginate<sup>98</sup> and sodium carboxymethylcellulose (CMC)<sup>99</sup> (Figure I.11). Their spontaneous interactions with the Si surface (Si-OH) through hydrogen bonding can reform if locally broken under stress, hence leading to self-healing effect. Other parameters such as polymers architectures, the type of cross-links (covalent, non-covalent) as well as the mechanical properties are known to play a role in the performances of Si anode binders. They will be discussed in detail in the introduction of Chapter III.

The chemical similarities between CD, PAA, CMC, alginate make it not farfetched to envision CDs-based binders (Figure I.11). The self-healing and mechanical properties imparted to the CD *host-guest* interaction have inspired the engineering of new Si anode binders that can mimic the “breathing” of Si electrodes upon cycling (*ie* expansions and contractions). Two main designs, relying on the (a) side chain and the (b) main chain complex approaches, have been proposed by the same research group<sup>100,101</sup> (Figure I.12).

The side chain complex approach relies on *host-guest* cross-linking between an hyperbranched polymer prepared from  $\beta$ -CDs (*host-polymer*) and a dendritic modified gallic acid, containing six adamantane moieties (*guest-crosslinker*)<sup>100</sup> (Figure I.12.a). If the  $\beta$ -CDs hyperbranched polymer 3D structure was already shown to reinforce the mechanical properties and facilitate the recovering of broken linkages (Si-binder and binder-binder interaction)<sup>102</sup>, the self-healing ability is even more promoted through the addition of the dynamic *host-guest* cross-linking. Finally, a very striking finding is that the greater binding strength of  $\beta$ -CD toward adamantane at the molecular level is directly translated in the cycling performances since poorer results were obtained with analogous  $\alpha$ - and  $\gamma$ -CDs hyperbranched polymers. Overall, such binder design has resulted in improving the cyclability of Si electrodes as compared to PAA, CMC or alginate binders.



**Figure I.12: Design variations of Si anode binders exploiting the CD *host-guest* interaction. a) *Host-guest* cross-linking inspired adapted from ref.<sup>100</sup> b) Topological cross-linking adapted from ref.<sup>101</sup>.**

The second example lies on the main chain complex approach and explores the CD *host-guest* interaction from a whole new side (Figure I.12.b). Getting inspiration from the working principle of moving pulleys, Choi *et al* introduced a novel topological cross-linking concept<sup>101</sup>. PAA is cross-linked to  $\alpha$ -CDs based PRs, resulting in a mechanically interlocked (PR-PAA) network equipped with movable cross-links. Tensile tests revealed that PR-PAA networks can sustain large strain (390%) while having better stress-strain recovery properties than PAA, owing to the sliding motion of CDs along the threading polymer. They can also resist to higher mechanical strength. Moreover, when

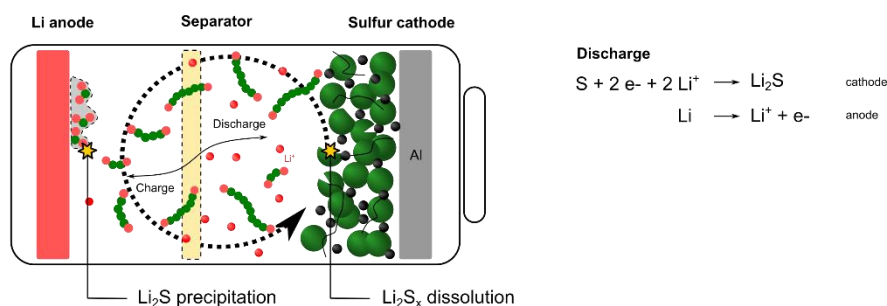
used as binder, they outperformed PAA in terms of capacity retention and microscopic analyses highlighted the presence of less cracks in the Si particles. These impressive capacities retentions have inspired several other works and this topological cross-linking concept was combined with boronic esters (reversible covalent bond) to provide both high elasticity and self-healing properties to the Si anode binder<sup>103</sup>. Recently, the use of PR-PAA was extended to silicon monoxide (SiO) electrodes<sup>104</sup> and carbon nanotubes, which are seen promising mechanically stable lithium hosts in the context of Li metal anode development<sup>105</sup>.

Although quite elegant and promising, the underlying science associated to these two approaches was not deeply scrutinized. If a systematic study was performed to rationalize the *host-guest* cross-linking binder (*a*) performances (CD type, the binder loading, the guest cross-linker nature), the influence of the structural parameters on the topological cross-linker (*b*) remains vague. This missing fundamental-applied link last remark invites us to move on to the following paragraph to examine some examples in which CDs intimately interact with active red-ox species (here Li-S batteries red-ox intermediates).

### c. Preventing the solubilization of red-ox active species

A typical Li-S battery consists of a Li metal anode associated to a sulfur (S) cathode. Li-S batteries have emerged as candidates for high-energy storage systems as their high theoretical specific energy (2600 Wh.kg<sup>-1</sup>) largely exceeds the energy delivered by conventional Li-ion batteries (~300 Wh.kg<sup>-1</sup>) composed of a transitional metal oxide cathode and a carbon-based anode. Despite the other considerable advantages of S which is an abundant, low cost and environmentally friendly element that can accept two electrons per atom, some technical obstacles have prevented the practical application of Li-S batteries. The major issue occurs during discharge when S is reversibly converted into Li<sub>2</sub>S through a multi-step red-ox process involving the formation of soluble lithium polysulfide intermediates with various chain lengths (Li<sub>2</sub>S<sub>x</sub> with x = 2-8). Part of the polysulfides migrate back and forth the electrodes, leading to the so-called "polysulfide red-ox shuttle". The entire reduction at the anode results in a poorly controlled Li/electrolyte interface since insoluble Li<sub>2</sub>S is deposited. The low utilisation of active material induces the poor electrochemical performances of Li-S batteries<sup>106</sup> (Figure I.13).

## Li-S battery and polysulfides red-ox shuttle



**Figure I.13 : Illustration of the polysulfide red-ox shuttle in Li-S battery.**

Much progress has been made to circumvent the persistent polysulfide migration by designing entangled separators (porosity, trapping, repulsive interactions)<sup>107</sup>, developing novel materials (electrolyte)<sup>108</sup> and new cell configurations. A special attention has been paid towards innovation of sulfur encapsulation techniques at the positive electrode to limit polysulfides dissolution via oxides surface adsorption<sup>109</sup>, mesoporous carbon confinement strategies or the development of “wrapping” binders. In this context, efficient CDs-based binders were reported<sup>110–112</sup>. The following section aims to evaluate the influence of the CD molecular recognition properties towards polysulfides in the efficiency of these reported CDs-based binders.

First, in comparison to the commonly used PVDF and PTFE, an oxidised  $\beta$ -CD derivative was identified as a viable aqueous binder. Its better cycling performances were attributed to its superior water solubility that offers a good surrounding of the S particles during the slurry process<sup>111</sup>. Later, placing a  $\beta$ -CD hyperbranched polymer (*cf* Figure I.4.b) in S-based cathode further improved the Li-S battery performances, owing to the good wrapping properties of such 3D polymer architecture<sup>112</sup>. Then, a polysulfides immobilization strategy was proposed by grafting some cationic moieties (quaternary ammonium cations) on the hydroxyl groups of  $\beta$ -CDs of such hyperbranched polymer. The authors ascribed the resulting improvements in cycling performances to the attractive electrostatic interactions between the negatively charged polysulfides and the cationic CDs-based binder.

Such use of CDs has been remaining empirical with no clear rationalization of the role played by CD cavities dimensions<sup>8</sup> with respect to the size of the polysulfides intermediates<sup>113</sup>. A *host-guest* interaction might be suggested. This observation triggers the way that my research thesis topic was initiated and pursued.

### 3. Conclusion and thesis prospects

In a nutshell, the first part of this Chapter provides a comprehensive review of the CD *host-guest* interaction and describes the *smart* properties resulting from its exploitation through the synthesis of a large panel of supramolecular architectures. The second part of the Chapter covers the recent adoption of CDs-based materials by the battery community. Although the field is still at its infancy, the embracement of this biomolecule has not only enabled the establishment of a sound engineering platform relying on *host-guest* supramolecular interactions, but it has also led to encouraging designs for electrolytes and Si anode binders as well as a new confinement strategy to tackle the polysulfide red-ox shuttle.

Among the three depicted examples, the customization of either liquid or polymer electrolytes appears as the less appropriate to take advantage of the CD *host-guest* interaction. On the one hand, despite the elegant TSI trapping concept, the sobering reality is that the intrinsic reversibility of the complexation phenomenon is responsible of the poor encapsulation efficiency. On the other hand, in the synthesis of SPEs, the interlocked macromolecules (PPR and PR) are used as synthesis platforms on which to graft ion conducting functions which is, in a certain sense, minimizing the underlying properties of such supramolecular architectures.

Nevertheless, more exciting perspectives are reflected in the development of novel Si anode binders relying on the dynamic nature of the CD *host-guest* interaction. The *host-guest* cross-linking binder (side chain approach) clearly showed CD/adamantane self-healing systems can also be successfully applied for battery applications. However, the underlying reasons for the impressive performances of the topologically cross-linked binder (main chain approach) remain unclear. From a synthesis point a view, this study has raised one major question: to what extent the structural parameters of this topologically cross-linked binder play a role its performances (PR ring coverage, polymer molecular weight, cross-linking, PR doping ratio compared to PAA)?

When it comes to mitigating the polysulfide red-ox shuttle effect, the assumption according to which CD cavities participate in the polysulfides immobilization, has drove us to push further the characterization of the interaction occurring between CDs and polysulfides. Interestingly, other

research groups have also committed to this task and new CDs-based binders that can efficiently trap polysulfides have been reported in the last two years<sup>114,115</sup>. As these works are concomitant with our findings, they will be discussed in the results part (Chapter II).

Finally, the stimuli-triggered responsiveness of CD complexation has not been envisioned yet, while it is expected to offer a large scope of possibilities for self-healing applications such on-demand trapping or control release of “curing” species. Therefore, the floor is entirely opened to new scientific contributions to extend our fundamental knowledge about the benefits CD can bring to the battery community and develop new viable CDs-based systems in batteries. This thesis aims to participate in this new research adventure and explore different directions to specifically answer to the abovementioned arising questions.

Along that line, Chapter II is dedicated to Li-S batteries and especially to the deep understanding at the molecular level of the *host-guest* complexation equilibrium between CDs and polysulfides. Chapters III and IV target the understanding of the structure/property relationships of the topologically cross-linked Si anode binders that were first reported by Choi *et al*<sup>101</sup>. Chapter III focuses on the synthesis of mechanically interlocked binders while Chapter IV concerns their electrochemical performances. For reasons of clarity, we decided to focus on the structure of CDs-based materials in this Chapter, prior to provide a more detailed battery-orientated section in the introduction of each following chapter.

# Chapter II: Cyclodextrin *host-guest* chemistry to address the Li-S battery polysulfides red-ox shuttle

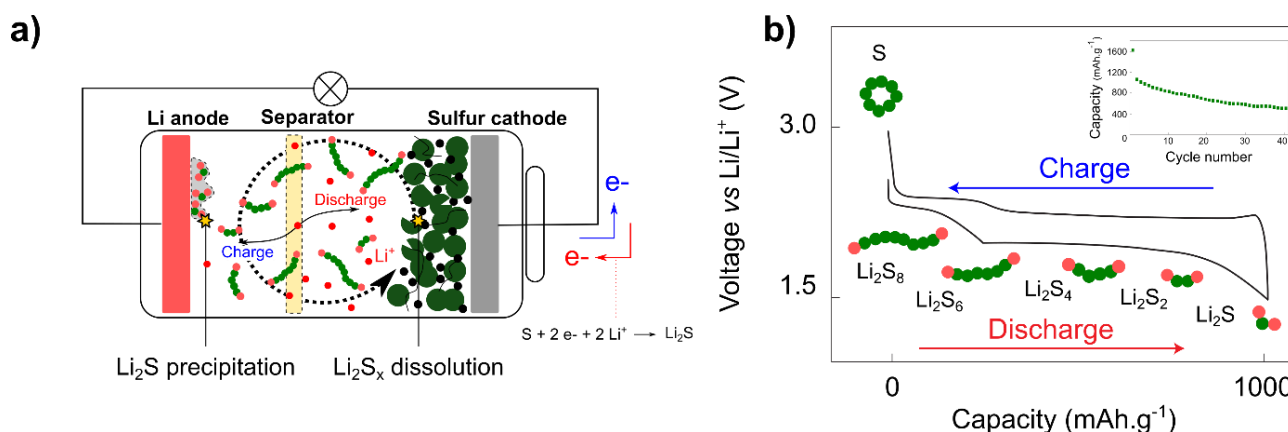
## 1. Background and motivation

This Chapter aims to evaluate the relevance of novel strategies, that rely on the CD supramolecular *host-guest* interaction, to address an inherent drawback of Li-S batteries that suffer from: the so-called polysulfide red-ox shuttle. The originality of our work lies on the implementation, for the first time in the energy field, of the nanopore sequencing approach to characterize this parasitic phenomenon resulting from the massive solubilization of red-ox polysulfide intermediate species. Consequently, for sake of clarity, a brief overview of this nano-sensing technique borrowed from biology is given in introduction. Then, we expose the strategy we adopted to demonstrate the benefits of the nanopore technology involving the CD *host-guest* interaction.

### a. Li-S batteries and polysulfides red-ox shuttle characterization

A liquid electrolyte-based Li-S battery is composed of a Li metal anode associated to a sulfur (S) cathode, that are immersed in an electrolyte, commonly made of 1M LiTFSI dissolved in a mixture of ether-based solvents, dioxolane (DOL) and dimethoxyethane (DME). Li-S batteries stand as *post* Li-ion technologies and have emerged as candidates for high-energy storage systems because of their high theoretical specific energy ( $2600 \text{ Wh.kg}^{-1}$ ), which largely exceeds the energy delivered by a conventional Li-ion battery ( $\sim 300 \text{ Wh.kg}^{-1}$ ). Additionally, as already mentioned, S is an abundant, low cost and environmentally friendly element that can accept two electrons per atom. Notwithstanding, some technical inherent issues induce poor cycling performances for Li-S batteries and have prevented their practical application so far<sup>106</sup>.





**Figure II.1: Li-S battery and polysulfides red-ox shuttle, adapted from ref<sup>106</sup>.** **a)** Schematic illustration of the working principle of liquid electrolyte Li-S battery exhibiting the parasitic polysulfide red-ox shuttle. **b)** First galvanostatic discharge and charge voltage profiles with the stepwise cathodic reduction of S involving the formation of the polysulfide intermediates, originating from the two plateaus. The inset presents which the capacity retention of Li-S battery.

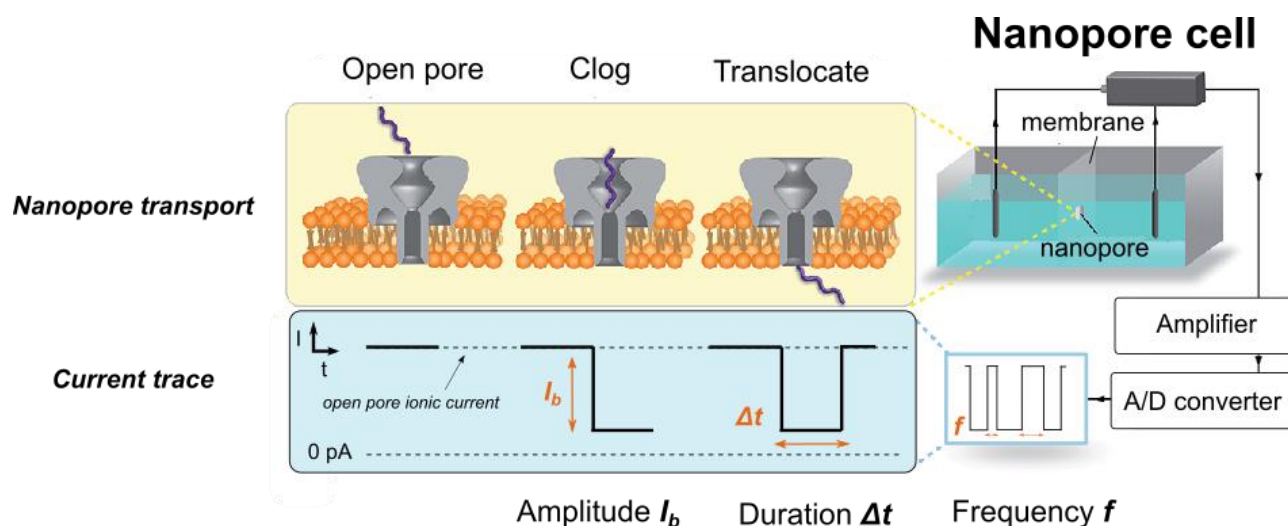
The Li-S battery operates on discharge by the reduction of elemental S at the cathode to be converted into Li<sub>2</sub>S. Lithium polysulfide intermediates, which exhibit various chain lengths (Li<sub>2</sub>S<sub>x</sub> with x = 2-8) are formed through a multi-step red-ox process (Figure II.1). These discharge products are soluble in the electrolyte, leading to their diffusion through the separator towards the Li anode where they are reduced to lower polysulfides that can migrate back to the cathode (red-ox shuttle). The entire reduction at the anode results in a poorly controlled Li/electrolyte interface since insoluble Li<sub>2</sub>S is deposited. Therefore, poor rechargeability of S electrode and a fast capacity decay emerge from the massive solubilization of polysulfides (inset Figure II.1.b).

Unfortunately, the strategies dealing with S cathode engineering, separator design or electrolyte tuning that were undertaken to address the persistent polysulfide dissolution and migration were only partially successful<sup>107,109</sup>. In this work, we propose to focus on the root of the problem by introducing a new characterization technique to sense polysulfides species : the nanopore sequencing technology.

## b. Nanopore sequencing technology

To further develop high-performance Li-S batteries, a clear understanding of the S red-ox chemistry and the polysulfides outcome are extremely important. Up to now, various advanced electrochemical characterization tools<sup>116</sup> and spectroscopic techniques<sup>117</sup>, have been developed to detect *in-situ*

polysulfide intermediates while Li-S battery is cycling. They rely on bulk measurements and cannot neither detect, nor sequence at the single molecule level these red-ox intermediates. Here, to increase the detection sensibility, we implement the highly-resolved nanopore technology for the characterization of these sulfide-based species (Figure II.2).



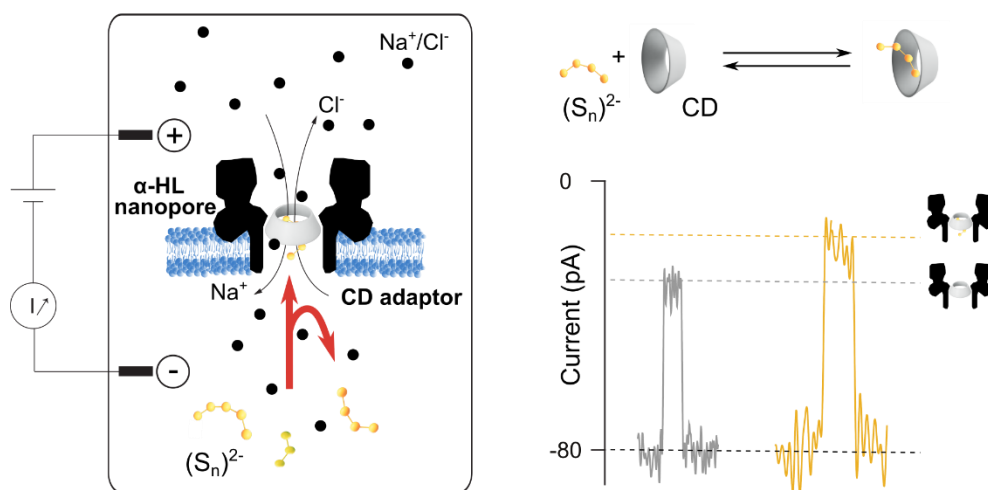
**Figure II.2: Illustration of the principle and experimental configuration of a nanopore sensor taking the example of a stranded molecule, adapted from ref<sup>118</sup>.**

The nanopore technology is a powerful single molecule technique, based on electrical detection, which has been inspired from biological voltage-gated ion channel<sup>119</sup>. With this approach, a nanopore is a nanometer-sized hole inserted into an insulating membrane that separates two electrolyte-filled compartments (Figure II.2). Applying a constant potential difference ( $< 1$  V) between the two electrodes on both sides of the nanopore enables the measurement of a stable ionic current flowing through the pore (open pore current, pA). As individual molecules clog the nanopore without translocating, or pass through it, a detectable decrease of the open pore ionic current is observed since ion transport is partially blocked. These blockages can be characterised by three parameters : blockage current amplitude ( $I_b$ ), blockage duration, *ie* dwell time ( $\Delta t$ ) and frequency ( $f$ ). They are specific of the molecule size, conformation, sequence, net charge, and geometry, hence allowing precise characterization of the studied molecules. Different types of nanopores have been reported enlisting protein ion channels inserted into lipid membranes<sup>118,120,121</sup>, solid state nanopores which are nano-holes drilled into a semiconductor membrane<sup>122</sup> or hybrid nanopores consisting in a biological channel supported by a solid state membrane<sup>123</sup>. The lifetime of an experiment ranges from a few hours, with a protein nanopore to several hours or a few days with solid-state or hybrid nanopores.

Such single molecule approach using protein nanopores has already been successfully implemented for the ultrafast sequencing of nucleic acids<sup>124</sup> together with the high-resolution size discrimination of biomolecules<sup>125,126</sup>, for biomarkers<sup>127,128</sup> or pathogenic agent detection<sup>129</sup>. These nanopore-based sensors are now employed for the detection of subtle chemical modifications<sup>130,131</sup> or to read the sequence of biomolecules<sup>121,132</sup>. Nanopores are also used to study protein conformational changes and transitions<sup>133,134</sup> and to detect of DNA methylations<sup>135,136</sup>. Further pushing this technique to its limits researchers have recently identified the twenty amino acids<sup>131</sup>, paving the way to protein sequencing. Thus, a burning question regards the implementation of this technique to the field of batteries.

### c. Our strategy to implement nanopore sensing via CD *host-guest* interaction

Herein, we have used Na-based polysulfide species  $\text{Na}_2\text{S}_n$  ( $n = 3, 4, 5$ ) in an aqueous medium that can be found as catholyte in aqueous Na-ion/polysulfide batteries<sup>137-139</sup>. Aqueous medium was chosen for stability considerations of the protein channel nanopore that we opted for. Moreover, we selected sodium rather than lithium polysulfides because they are more stable with less disproportionation<sup>141</sup>. Given the size of polysulfides<sup>113</sup> and the sulfur atom difference to be detected, the nanopore sensitivity is the key feature to demonstrate the feasibility of polysulfides sensing. Therefore,  $\alpha$ -hemolysin ( $\alpha$ -HL)<sup>140</sup> was chosen for its wide range of aqueous operating conditions<sup>142,143</sup>, as well as its high sensitivity that can be further enhanced by narrowing the  $\alpha$ -HL channel constriction through a CD lodging in it<sup>144</sup>. Thus, the lodged CD acts as a binding site and the polysulfides detection is then closely correlated to the polysulfide/CD interaction (Figure II.3). This is where our expectations about the CD affinity towards  $(\text{S}_n)^{2-}$ , that we discussed in Chapter I, come in.



**Figure II.3: Schematic of the ion-current measurement  $\alpha$ -HL nanopore set-up used to discriminate supramolecular complexes  $\beta$ -CD/  $\text{Na}_2\text{S}_x$ , with a single sulfur atom resolution.**

Following this introduction, the first results section of this Chapter concerns the careful description of the reversible complexation equilibrium resulting from the *host-guest* interaction between CDs and sodium polysulfides. In the second section, we report a protein channel nanopore,  $\alpha$ -HL, with a  $\beta$ -CD adaptor as a new powerful detection tool enabling the successful discrimination of polysulfides in their complexed form (Figure II.3). Eventually, some exciting perspectives enrich this *proof-of-concept* study.

## 2. CD supramolecular recognition towards aqueous polysulfides

In this section, the reversible complexation equilibrium between CDs and Na-based aqueous polysulfides ( $\text{Na}_2\text{S}_x$  with  $x = 3-5$ ) is thoroughly described by NMR spectroscopy. The resulting findings are completed by Molecular Docking calculations and Molecular Dynamics that were performed by our collaborators in the Tor Vergata University of Roma. For sake of clarity, the details of these calculations are mentioned in the Methods part of this Chapter (Supplementary Information for Chapter II).

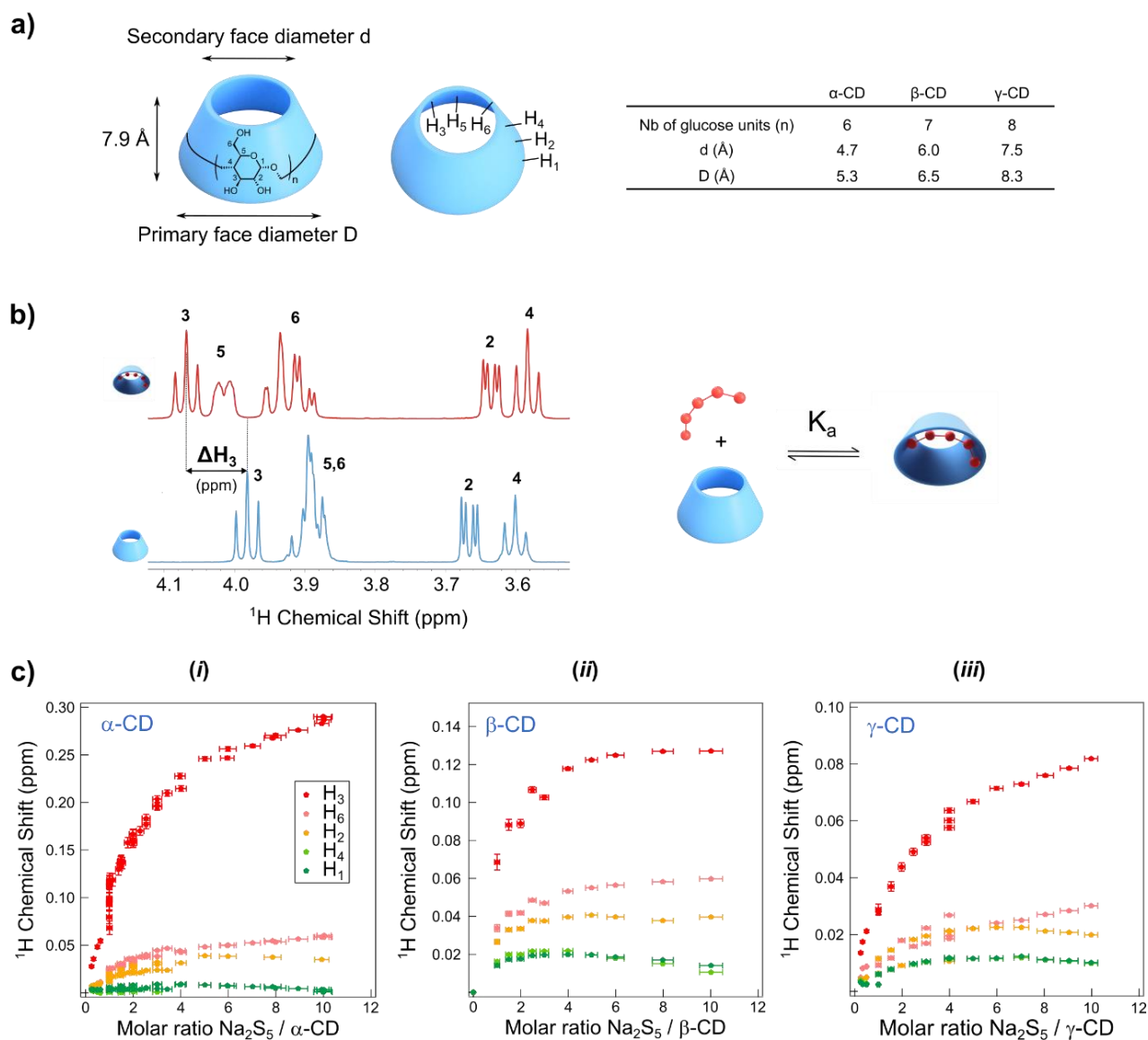
### a. *Host-guest* complexation between CDs and polysulfides

#### **Evidence of the complex formation**

Several aqueous polysulfides solutions, ( $\text{Na}_2\text{S}_x$  with  $x = 2-5$ ), were prepared via a solution process, by mixing  $\text{Na}_2\text{S}$  with  $\text{S}$  under Argon atmosphere in an aqueous buffer (25 mM  $\text{NaHCO}_3$ , pH 10)<sup>145</sup>. The sulfur chain lengths were varied by introducing the precursors in stoichiometric proportions. As previously reported, we characterized these coloured solutions by UV-vis spectroscopy<sup>141</sup>. The UV-vis spectra of the different aqueous polysulfides solutions exhibit two local maximum peaks  $\lambda = (300.2 ; 376.6 \text{ nm})$ , that we used to calculate the molar extinction coefficients of each polysulfides solution according to the Beer Lambert law (Figure SI.II.1).

We are aware of the inherently poor evidence such characterization method provides in terms of monodispersity of the as-prepared polysulfides solutions. Although some other characterization techniques such as cyclic voltammetry (Figure SI.II.2) were investigated, they also fell short in addressing this question. However, the results obtained by nanopore (see 3.c) undeniably confirm the most abundant species of the different polysulfides solutions has the targeted stoichiometry, even though the monodispersity of each solution cannot be ensured.

The interaction between polysulfides and the different  $\alpha$ -,  $\beta$ - and  $\gamma$ -CDs was determined by liquid  $^1\text{H}$  NMR, following the chemical shifts of the different protons of CDs, once dissolved in a polysulfides solution that was prepared from a deuterated buffer (25 mM  $\text{NaHCO}_3$  in  $\text{D}_2\text{O}$ ) (Figure II.4). Figure II.4.b shows the  $^1\text{H}$  NMR spectrum of  $\beta$ -CD and  $\text{Na}_2\text{S}_5$  in the deuterated buffer (red) with respect to the spectrum of  $\beta$ -CD alone in the same buffer (blue). 2D HSQC experiments were performed to finely attribute the signals to the different protons of CDs that are shifted (Figures SI.II.3-5). The chemical shifts differences undoubtedly indicate the existence of an interaction related to a complexation equilibrium. As the exchange rate of this equilibrium is very fast compared to the NMR time scale, the peaks assigned to free and complexed CD populations are merged and appear as the weight average chemical shift of both populations. Note that similar experiments with  $\alpha$ -CDs and  $\gamma$ -CDs confirmed the existence of an equilibrium complexation as well (not shown here).



**Figure II.4: Demonstration of the *host-guest* complexation between CDs and  $\text{Na}_2\text{S}_5$  by  $^1\text{H}$  NMR spectroscopy** **a)** Structure and geometric dimensions of  $\alpha$ -,  $\beta$ -, and  $\gamma$ -CDs with the indication of the nomenclature used to identify the different protons and carbons of the glucopyranose units<sup>8</sup>. **b)** Selected region of the  $^1\text{H}$  NMR spectra of native  $\beta$ -CD (10 mM, blue) and  $\beta$ -CD in presence of  $\text{Na}_2\text{S}_5$  (equimolar ratio 10 mM, red) (600 MHz, 298K, 25 mM  $\text{NaHCO}_3$  in  $\text{D}_2\text{O}$ ). For better readability,  $\text{Na}^+$  counter ions are not represented on the schematic representation of the *host-guest* interaction equilibrium between  $\beta$ -cyclodextrin and  $\text{Na}_2\text{S}_5$ . **c)** Variation of the CD protons chemical shifts of (i)  $\alpha$ -, (ii)  $\beta$ - and (iii)  $\gamma$ -CDs in presence of  $\text{Na}_2\text{S}_5$ , which concentration was increased from 10 mM to 100 mM, while CD concentration was maintained constant to 10 mM. The protons chemical shifts were compared to the initially recorded native CD references dissolved in the same deuterated buffer.

The shifting amplitudes of the  $\alpha$ -,  $\beta$ - and  $\gamma$ -CDs protons were reported as a function of the proportion of  $\text{Na}_2\text{S}_5$  introduced, keeping the concentration of CD constant (Figure II.4.c). Interestingly, CD protons are not affected in an equivalent manner and the most shifted protons turn out to be the ones pointing inside the cavity of the *host* molecule, such as  $\text{H}_3$ . Note that despite its large shift amplitude,  $\text{H}_5$  was not reported because of its superposition with  $\text{H}_6$  signal, which makes the chemical shift measurement not precise. These observations clearly side with the *host-guest* interaction between  $\text{Na}_2\text{S}_5$  and CDs and motivated the following quantitative analyses.

### Determination of the complex stoichiometry

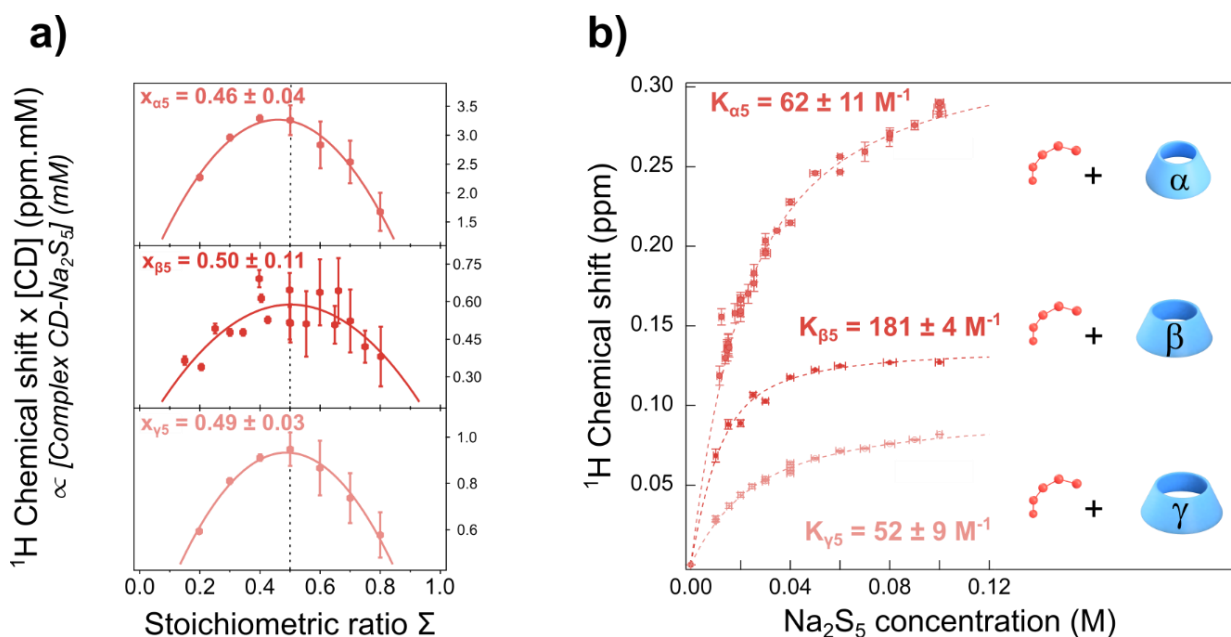
The continuous variation method, also known as Job's plot, was performed to determine the stoichiometry of the CD/polysulfide complexes, using NMR spectroscopy<sup>146</sup>. Figure II.5.a shows the Job's plot obtained for  $\alpha$ -,  $\beta$ - and  $\gamma$ -CDs with  $\text{Na}_2\text{S}_5$ . This method consists in varying the mole fraction of  $\text{Na}_2\text{S}_5$  while keeping the total concentration of *host* and *guest* molecules constant, respectively to 50 mM, 16 mM, and 50 mM for  $\alpha$ -,  $\beta$ - and  $\gamma$ -CDs. As they exhibit the greater shift, we mainly focused on  $\text{H}_3$  and we plotted the  $\text{H}_3$  chemical shift multiplied with the CD concentration (quantity proportional to the population of CD that is complexed) as a function of the stoichiometric ratio  $\Sigma$ , with  $\Sigma = [\text{Na}_2\text{S}_5] / [\text{CD}] + [\text{Na}_2\text{S}_5]$ . According to the Job's plot approach, the stoichiometry of the studied complex was obtained from the  $x$ -coordinate corresponding to the maximum of the curve that was fitted with a second order polynomial. Thus, stoichiometric ratios  $\Sigma$  of 0.5 were calculated, which corresponds to the (1:1) stoichiometry for the inclusion complexation.

In order to support these experimental findings, molecular docking calculations were also performed. As shown in Figure SI.II.8, docking results show that in all cases  $\text{Na}_2\text{S}_5$  binds inside the CDs cavities and Figure SI.II.9 emphasizes that there is room for only one *guest* molecule (here  $\text{Na}_2\text{S}_5$ ) per CD *host*. This is in full agreement with the NMR experiments, strongly hinting a (1:1) stoichiometry, that provided us with a 2-states thermodynamic equilibrium model, as illustrated in Figure II.4.

### Evaluation of the binding constant

Then we carried out  $^1\text{H}$  NMR titration experiments with the aim to calculate the different association constants  $K_a$  for the complexes formation of  $\text{Na}_2\text{S}_5$  with  $\alpha$ -,  $\beta$ -, and  $\gamma$ -CDs (Figure II.5.b). In presence of an increasing concentration of  $\text{Na}_2\text{S}_5$ , the  $\text{H}_3$  NMR chemical shifts were measured and fitted with the binding isotherm equation corresponding to the (1:1) stoichiometry inclusion complex (see

Methods section for further details). Comparable values to the previous reports were found<sup>8</sup>. Interestingly,  $\beta$ -CD turns out to have the best affinity towards  $\text{Na}_2\text{S}_5$  with an association constant of  $K_{\beta 5} = 181 \pm 4 \text{ M}^{-1}$ , almost three times larger than with  $\alpha$ -CD and  $\gamma$ -CD,  $K_{\alpha 5} = 62 \pm 11 \text{ M}^{-1}$  and  $K_{\gamma 5} = 52 \pm 9 \text{ M}^{-1}$ , respectively. The molecular docking affinity ranking over all the CD/ $\text{Na}_2\text{S}_5$  inclusion complexes led to the same result highlighting the stronger affinity for the  $\beta$ -CD (Figure SI.II.8). Hence our experimental and numerical results are consistent.



**Figure II.5: Influence of the CD nature on the *host-guest* interaction with  $\text{Na}_2\text{S}_5$**  a) Experimental Job's plot obtained monitoring the  $\text{H}_3$  chemical shift for  $\alpha$ -,  $\beta$ - and  $\gamma$ -CDs in presence of  $\text{Na}_2\text{S}_5$  (respectively, top-down). Second order polynomial fitting which maximum matches with the stoichiometry of the complex (x-coordinate). b)  $^1\text{H}$  NMR titration plots for the inclusion of  $\text{Na}_2\text{S}_5$  in the different CDs and fitted binding isotherms with indication of the resulting association constants  $K_{\alpha 5}$ ,  $K_{\beta 5}$ , and  $K_{\gamma 5}$ . The statistic error relative to the chemical shift measurement was obtained by the calculation of the standard deviation of 10 similar and independent points and is estimated to 9%. The plotted error bars were calculated considering the uncertainties propagation as explained in the Materials and Methods section (Supporting Information for Chapter II).

## b. Influence of the polysulfides length

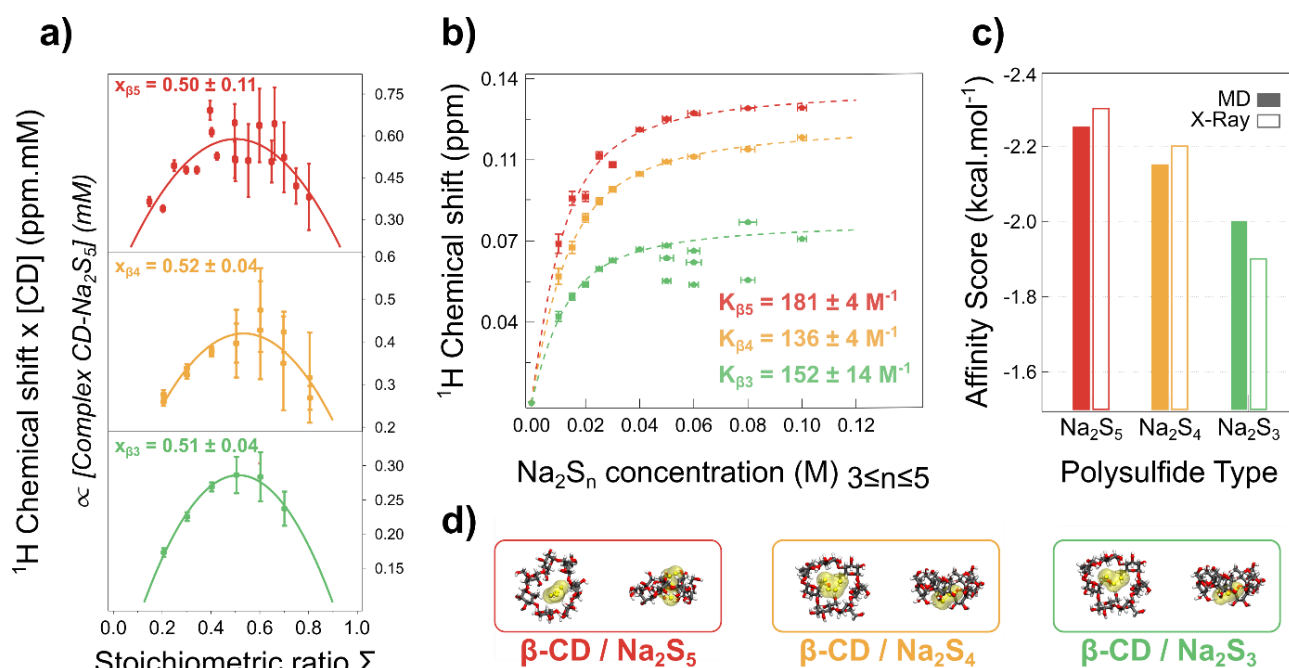
Tracking the most stable  $\beta$ -CD inclusion complexes, we investigated the influence of the polysulfides size by calculating the association constants of the different complexes prepared from  $\text{Na}_2\text{S}_5$ ,  $\text{Na}_2\text{S}_4$  and  $\text{Na}_2\text{S}_3$ . To do so, we coupled the above-mentioned NMR experiments (Job's plot & titration) with



molecular docking calculations. The Job's plots presented in Figure II.6.a are characteristic of the formation of (1:1) stoichiometry complexes. As shown in Figure II.6.b, we calculated the corresponding binding constants  $K_{\beta 5} = 181 \pm 4 \text{ M}^{-1}$ ,  $K_{\beta 4} = 136 \pm 4 \text{ M}^{-1}$  and  $K_{\beta 3} = 152 \pm 14 \text{ M}^{-1}$ .  $K_{\beta 3}$  could not be estimated with as high reliability as the previous ones because of the experimental noise resulting from the very small chemical shifts measured for H<sub>3</sub>.

As reported in Figure SI.II.6, we also determined these association constants considering the chemical shift of H<sub>6</sub>, another CD proton located at the secondary face (see Figure II.4.a) Although the constant values are different, quite a strong correlation is exhibited between the complexation strength and the length of the sulfur chain. The more sulfur atoms the polysulfide is made of, the greater the complexation strength is with  $\beta$ -CD. Therefore, the experimental noisy curve obtained for H<sub>3</sub> could be rationalized by the position of Na<sub>2</sub>S<sub>3</sub> in  $\beta$ -CD cavity which might tend to be located closer to the secondary face compared to the longer polysulfides (H<sub>6</sub> more affected than H<sub>3</sub>). Similar experiments were performed with  $\alpha$ -CD and they demonstrated the same influence of the polysulfide size on the association constant values (Figure SI.II.7).

The correlation observed between the binding capability and the polysulfide length is consistent with the similar trend obtained by calculations performed by docking the different polysulfides on CDs structures (Figure II.6.c). In all cases, the general trend is a (1:1) complex formation, with (S<sub>n</sub>)<sup>2-</sup> located inside the CD cavity (Figure II.6.d). The calculated affinity scores increase with the length of the polysulfide chain and thus confirm the weakest affinity for the  $\beta$ -CD/Na<sub>2</sub>S<sub>3</sub> complex. Therefore, these results indicate a non-specific complex formation but highlight a size-matching phenomenon (polysulfide's size dependence). Additionally, the  $\beta$ -CD selectivity suggests the trapping depends on the CD conformation that induces different strength of interactions.



**Figure II.6: Influence of the polysulfides length chain on  $\beta$ -CD complexation.** **a)** Experimental Job's plot obtained monitoring the  $H_3$  chemical shift of  $\beta$ -CD in presence of  $Na_2S_5$  (red),  $Na_2S_4$  (yellow) and  $Na_2S_3$  (green). Indication of the corresponding stoichiometric ratios  $\Sigma$ . **b)**  $^1H$  NMR titration plots for the inclusion complexes and fitted binding isotherms with indication of the resulting association constants  $K_{\beta_5}$ ,  $K_{\beta_4}$ , and  $K_{\beta_3}$ . The error bars were estimated similarly to Figure II.5. **c)** Best docking affinity scores ( $kcal.mol^{-1}$ ) for the  $\beta$ -CD inclusion complexes calculated from two types of CD structures (Molecular Dynamics simulations and crystallographic structures extracted from PDB<sup>147</sup>, see Supplementary Information). **d)** Corresponding best docking poses from the top and side views.  $\beta$ -CD is represented in sticks while a yellow space-fill representation is adopted for polysulfides.

In conclusion, these complexation results successfully provide a fundamental understanding of the polysulfide immobilization strategy induced by the utilisation of CD-based binders for S cathode (see Chapter I). Two contemporary works have also addressed the questions of both the nature and the mechanisms of the CD/polysulfide *host-guest* interaction<sup>115,148</sup>. Ni *et al* have managed to isolate  $\beta$ -CD/ $Na_2S_4$  complex in solid-state and have used spectroscopic methods (NMR and Raman) to qualitatively demonstrate the interaction<sup>148</sup>. Then, in either case, the analogous lithium polysulfide,  $Li_2S_4$ , prepared in an organic medium has been considered and its encapsulation by  $\beta$ -CD has also been exhibited, combining spectroscopic techniques (UV-*vis* and XPS) and molecular modelling (DFT). Both studies agree in demonstrating the formation of Li-O bonds between the lithium polysulfides and CD, but different oxygens atoms are assumed to play the binding role (OH<sup>115</sup> vs glycosidic O atom<sup>148</sup>). Interestingly, Ren *et al* have showed that  $\beta$ -CD had the strongest binding capability towards  $Li_2S_4$  compared to  $\alpha$ - and  $\gamma$ -CDs, which corroborates well with our results<sup>115</sup>.

Although our NMR experiments do not provide such interaction details, we successfully addressed the selectivity of this *host-guest* complexation towards the CD type and the polysulfides length, in a quantitative manner. As the *host-guest* interaction is governed by a complexation equilibrium, we found relevant to study how its reversibility, *ie* association/dissociation, could be triggered by an external stimulus. The following section tackles the influence of dilution and temperature on the complexation equilibrium of the already described complexes  $\alpha$ -CD/Na<sub>2</sub>S<sub>5</sub>,  $\beta$ -CD/Na<sub>2</sub>S<sub>5</sub> and  $\beta$ -CD/Na<sub>2</sub>S<sub>4</sub>.

### c. A reversible complexation equilibrium

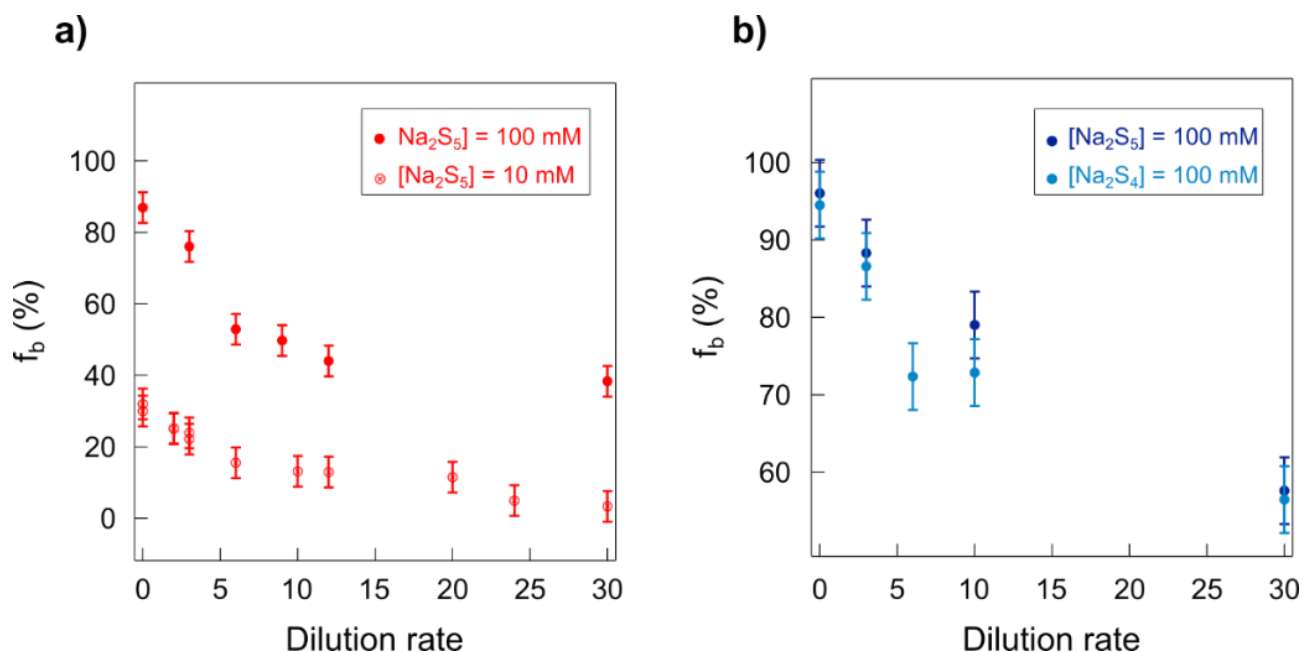
For each CD/polysulfide complex, the determination of the association constant  $K_a$ , from the binding isotherm equation, comes along with the calculation of  $\Delta_{max}$ , which represents the chemical shift that would be recorded if 100% of CDs were complexed (see Methods, Supplementary Information for Chapter II). Thus, the fraction of CD molecules that are complexed,  $f_b$ , is easily accessible as the ratio of the measured chemical shift  $\Delta$  over  $\Delta_{max}$ . Therefore, we studied the influence of the dilution rate and the temperature on the equilibrium complexation of CD/polysulfide by calculating  $f_b$ .

#### Role of dilution

CD/polysulfide complexes solutions were diluted with the same aqueous buffer at different dilution rates. First, we investigated the effect of dilution on two  $\alpha$ -CD/Na<sub>2</sub>S<sub>5</sub> complex solutions of different initial compositions (Figure II.7.a) In both cases, the  $\alpha$ -CD concentration was set to 10 mM while the concentration of Na<sub>2</sub>S<sub>5</sub> was either set to 10 mM or to 100 mM, resulting in initial  $f_b$  of  $87 \pm 4 \%$  and  $30 \pm 4 \%$  respectively.  $f_b$  decreases as diluting the complex solutions with a steeper slope at the beginning of the dilution process. Such behaviour was expected, since dilution induces a less frequent meeting of the *host* and *guest* molecules.

Then, the influence of the *guest* polysulfide type was examined (Figure II.7.b).  $\beta$ -CD/Na<sub>2</sub>S<sub>5</sub> and  $\beta$ -CD/Na<sub>2</sub>S<sub>4</sub> complex solutions were prepared by introducing 10 mM of  $\beta$ -CD and 100 mM of the corresponding polysulfide, leading to initial  $f_b$  of  $96 \pm 4 \%$  and  $94 \pm 4 \%$ , respectively. An almost identical declining trend is observed for both complexes. It is worth noticing that,  $\beta$ -CD/Na<sub>2</sub>S<sub>5</sub> complex is less sensitive to dilution compared to  $\alpha$ -CD/Na<sub>2</sub>S<sub>5</sub> ( $58 \pm 4 \%$ , Figure II.7.a vs  $38 \pm 4 \%$  Figure II.7.b, for a 30 dilution factor), which is consistent with their respective association constant

values (Figure II.5.b). Therefore, dilution definitely plays a role on the *host-guest* complexation equilibrium and can be used as an engineering tool to prepare some complex solutions with any desired composition.



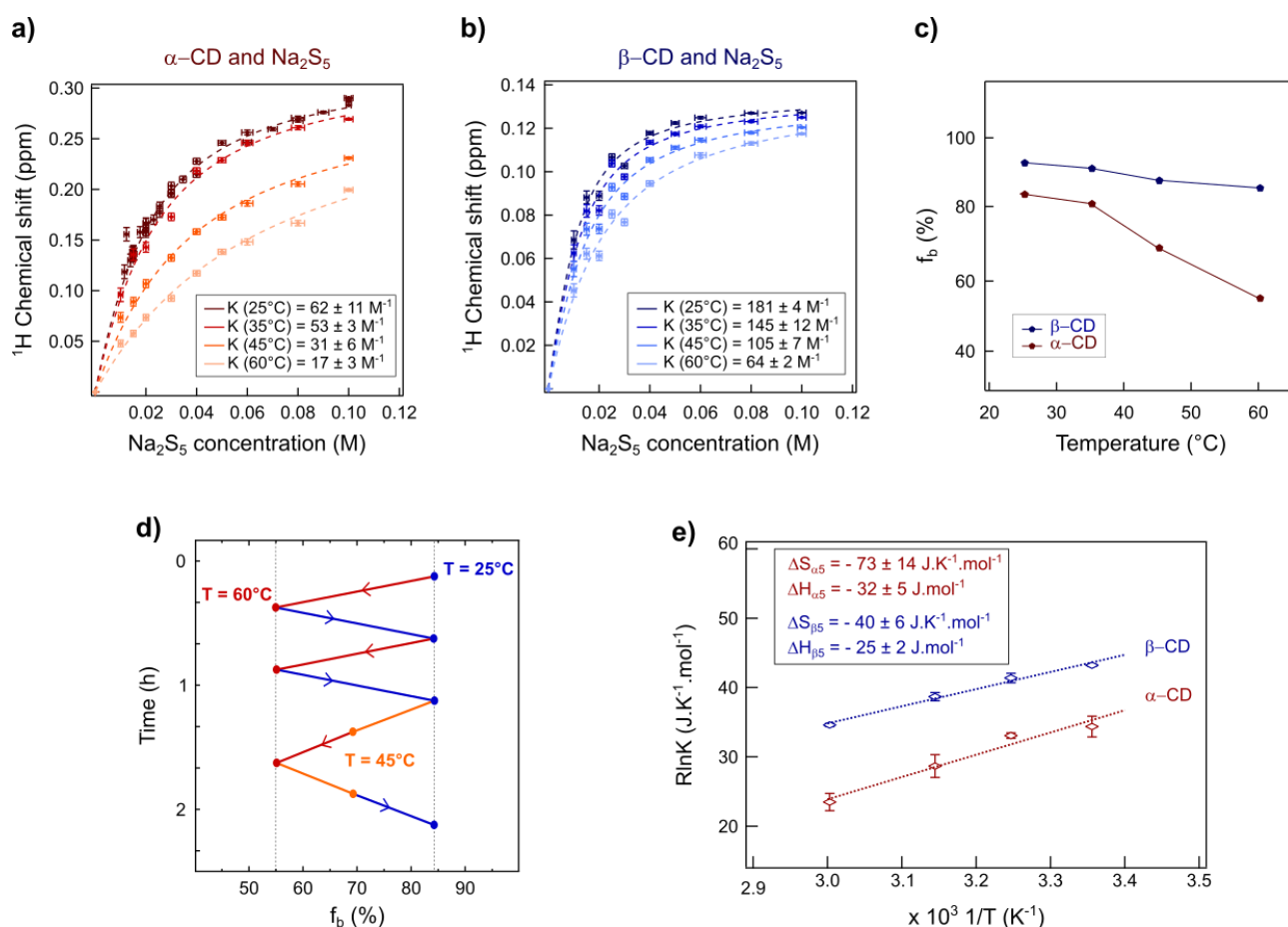
**Figure II.7: Influence of dilution on CD/polysulfide complexation equilibrium.** Concentration of CD remains constant to 10 mM. **a)** Influence of the initial composition of  $\alpha$ -CD/ $\text{Na}_2\text{S}_5$  complex solutions. Plain circle and ring markers correspond to a  $\text{Na}_2\text{S}_5$  concentration of 100 mM and 10 mM respectively. **b)** Influence of the polysulfide type whose initial concentration is set to 100 mM.  $\beta$ -CD/ $\text{Na}_2\text{S}_5$  (dark blue) and  $\beta$ -CD/ $\text{Na}_2\text{S}_4$  (light blue) complexes are investigated.

### Role of temperature

With respect to practicality, we investigated the thermal stability of CD/polysulfide complexes. The possibility to vary the temperature of the NMR probe allowed us to calculate the association constants of  $\beta$ -CD/ $\text{Na}_2\text{S}_5$  and  $\alpha$ -CD/ $\text{Na}_2\text{S}_5$  complexes for three higher temperatures than 25°C, *ie* 35, 45 and 60°C (Figures II.8.a & b). For both complexes, the binding constants decrease while rising the temperature. Figure II.8.c shows that  $f_b$  also declines as increasing the temperature, the slope being more pronounced for  $\alpha$ -CD than for  $\beta$ -CD complexes solutions of the same initial composition. In conclusion, the temperature effect is more stressed for the  $\alpha$ -CD complex which displays a global lower binding strength than the  $\beta$ -CD complex (Figure II.5.b).

Next, an *in-situ* temperature cycling experiment was carried out to monitor the fate of the  $\alpha$ -CD/ $\text{Na}_2\text{S}_5$  complex while varying the temperature (Figure II.8.d). We found that, by increasing and decreasing the temperature, the complex can dissociate and form back with a fast kinetic over a narrow temperature range ( $35^\circ\text{C}$ ) in a neatly reversible way. Because of technical restriction of the NMR probe, we could not go to higher temperature, but we expect an almost total dissociation of the complex being achieved further increasing the temperature. This suggests that temperature can be used as a stimulus to regulate the capture and release of polysulfide species by CD.

The elucidation of the temperature dependence of the association constants,  $K_a$ , allowed us to estimate the contributions of enthalpy  $\Delta H$  and entropy  $\Delta S$  associated to  $\alpha$ -CD/ $\text{Na}_2\text{S}_5$  and  $\beta$ -CD/ $\text{Na}_2\text{S}_5$  complexes formation ( $K_a = e^{-\frac{\Delta G}{RT}}$ ) (Figure II.8.d). Such observation comes as supporting evidence of the difference of binding strength observed for  $\alpha$ - and  $\beta$ -CD towards  $\text{Na}_2\text{S}_5$ . Linear Van't Hoff representations evidenced the exothermic nature of the *host-guest* interaction accompanied by rather unfavourable entropic contributions. Similar enthalpies are obtained for  $\alpha$ -CD/ $\text{Na}_2\text{S}_5$  and  $\beta$ -CD/ $\text{Na}_2\text{S}_5$  complexes, whereas the significant variation of the entropic terms indicates a less favourable complexation process for  $\alpha$ - than for  $\beta$ -CD. Thus, it suggests that  $\text{Na}_2\text{S}_5$  might be hampered to enter the  $\alpha$ -CD cavity or that there are less degrees of freedom for the complex conformation. This does not come as a surprise in light of the different dynamical conformations of  $\alpha$ - or  $\beta$ -CD in water, noted by our Molecular Dynamics simulations<sup>149</sup>, as well as the steric effect and "size-matching" feature to name only a few parameters.



**Figure II.8: Influence of temperature on CD/polysulfide complexation equilibrium.**  $^1\text{H}$  NMR spectra were recorded in the deuterated aqueous buffer (25 mM  $\text{NaHCO}_3$  in  $\text{D}_2\text{O}$ ). The tube was placed into the NMR probe 30 min before the acquisition (16 scans) to ensure a uniform temperature. Binding isotherms at four temperatures 25, 35, 45, and 60°C for the complexes **a)**  $\alpha$ -CD/ $\text{Na}_2\text{S}_5$  **b)**  $\beta$ -CD/ $\text{Na}_2\text{S}_5$ . **c)** Influence of temperature on  $f_b$  for two complexes solutions initially prepared from 10 mM  $\alpha$ - or  $\beta$ -CD and 100 mM  $\text{Na}_2\text{S}_5$ . **d)** In-situ temperature cycling experiments performed on the  $\alpha$ -CD/ $\text{Na}_2\text{S}_5$  complex solution.  $f_b$  is represented as a function of temperature during heating up (60 °C,  $55.1 \pm 0.1\%$ ) and cooling down (25 °C,  $84.3 \pm 0.1\%$ ) cycles, where confidence intervals are calculated as reported in “Methods” section. **e)** Linear Van’t Hoff representations with the indication of the resulting enthalpic ( $\Delta H$ ) and entropic ( $\Delta S$ ) contributions to the complexation process of  $\text{Na}_2\text{S}_5$  with respectively  $\alpha$ - and  $\beta$ -CDs.

Altogether, these experiments successfully characterize the *host-guest* interaction phenomena occurring between CDs and aqueous Na-based polysulfides.  $\beta$ -CD/polysulfide complexes have been highlighted as being the more thermodynamically stable inclusion complexes. We have gathered the essential parameters pertaining to the  $\beta$ -CD interactions with polysulfides that turn out to be the key to successfully implement our nanopore sensing technique.

### 3. Aqueous polysulfides detection and discrimination by nanopore

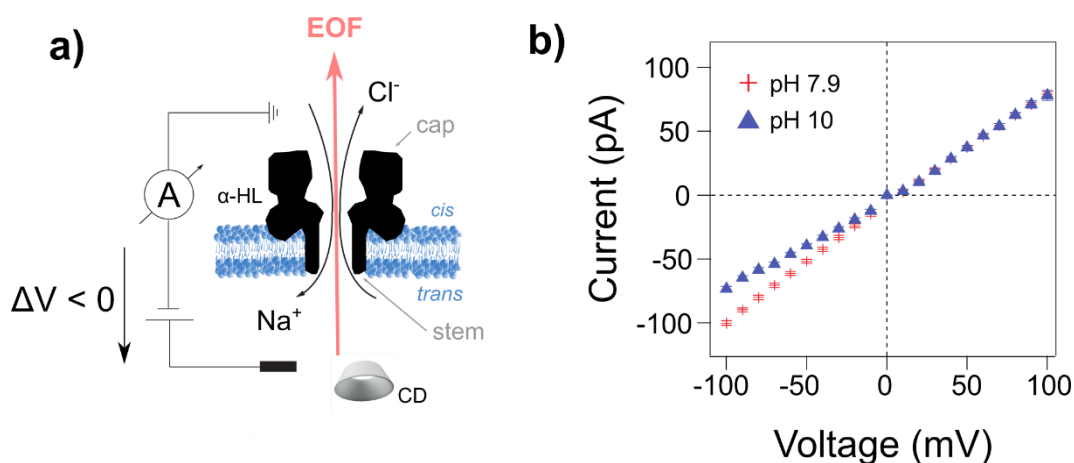
All the nanopore experiments presented hereafter were built on the recognize know-how of the LAMBE team members working preferentially on nanopore. The experiments were conducted by Benjamin Cressiot, with whom I collaborated with.

#### a. $\beta$ -CD interaction with the $\alpha$ -hemolysin ( $\alpha$ -HL) nanopore channel

In order to fine-tune the characterization of  $\beta$ -CD/polysulfide complexes, we used the nanopore approach to detect and discriminate at the single molecule level each species. We opted for the  $\alpha$ -hemolysin ( $\alpha$ -HL) nanopore, which is a mushroom-shape heptameric complex that spontaneously insert into lipid bilayer to form a transmembrane channel of 26 Å diameter<sup>140</sup> (Figure II.9.a). In the last years,  $\beta$ -CDs have been used to narrow the  $\alpha$ -HL pore constriction (stem part) to enhance the capability of the pore to discriminate nucleotides<sup>150</sup> and organic compounds<sup>144</sup>. We used this strategy to compare  $\beta$ -CD and  $\beta$ -CD/polysulfide complexes using an  $\alpha$ -HL pore. The electrical detection was undertaken in the basic buffer used to prepare aqueous polysulfides solutions (25 mM NaHCO<sub>3</sub>, pH 10), to which 1M NaCl was added. All the experiments were carried out in an Argon glovebox. The description of the nanopore formation process and the data acquisition are detailed in the Materials & Methods (Supporting Information for Chapter II).

Protein pores such as  $\alpha$ -HL are ion-selective, resulting in an unbalance between cation (Na<sup>+</sup> here) and anion (Cl<sup>-</sup> here) flows under any applied potential difference. This gives rise to a net motion of water molecules, hence creating an electro-osmotic flux (EOF).  $\alpha$ -HL is an anion selective channel and the resulting EOF is known to affect the entrance of the neutral  $\beta$ -CD through the stem of the nanopore and its lodging into the channel<sup>151</sup> (Figure II.9.a). The interaction of  $\beta$ -CD with  $\alpha$ -HL has already been studied as a function of a wide range of pH (5 to 11), transmembrane potentials (hundreds of mV) and nature of electrolyte salts, in order to control the entry and dwell times of CD into the nanopore<sup>142,143</sup>. A previous study<sup>152</sup> indicated that pH could affect the  $\alpha$ -HL selectivity, with an inversion observed between pH 7.5 (anion selective) and pH 11 (cation selective), which seems not surprising since pH might alter the protonation state of the exposed amino acids that are

constituting the  $\alpha$ -HL protein. Here, we work at pH10 where, to the best of our knowledge, no literature data provide any information about the  $\alpha$ -HL selectivity and the EOF direction.



**Figure II.9: Experimental  $\alpha$ -HL nanopore set up.** **a)** Principle of the electrical detection method showing the ions flowing through an  $\alpha$ -HL nanopore inserted in a lipid bilayer membrane according to the applied voltage sign. *Trans* refer to the stem side and *cis* to the cap. **b)** Current-potential curves in presence of 1M NaCl at pH 7.9 and pH 10 (25 mM NaCO<sub>3</sub>).

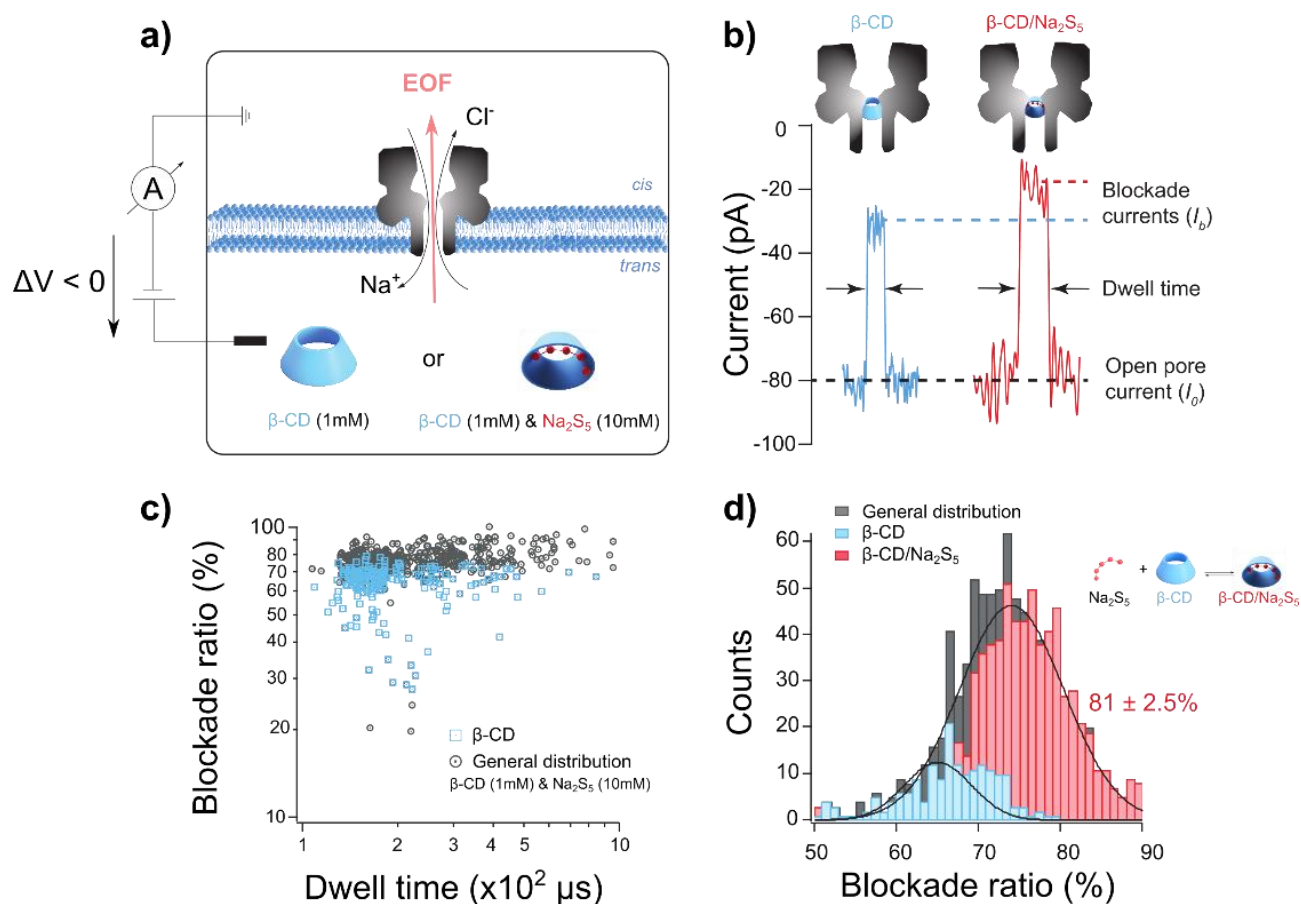
Therefore, we first tested the effect of our electrolyte (1M NaCl pH 10) by recording the current-voltage (I-V) curves of the  $\alpha$ -HL pore at pH 7.9 and pH 10 (Figure II.9.b). Similar currents as previously published were obtained<sup>143</sup>. Interestingly, the response of the pore to positive potentials is identical for pH 7.9 and pH 10 whereas at negative potentials, the conductance declines with decreasing the potential at pH 10, as shown by the I-V curve rectification change. In order to characterize the EOF, a computational analysis via all-atom Molecular Dynamics simulation was performed by our Italian colleagues. Two different plausible titration states of the amino acids constituting the  $\alpha$ -HL channel were considered at pH 10 (Figure SI.II.10). We explored transmembrane electric potentials ranging from  $-500$  mV to  $500$  mV and it was found that for both cases, the anion ( $\text{Cl}^-$ ) flow is much larger than the cation ( $\text{Na}^+$ ) flow and the EOF is directed as the anions (Figure SI.II.11). Hence the anion selectivity of the  $\alpha$ -HL is demonstrated (Figure II.9.a). These results suggested us to perform experiments at a negative applied voltage ( $-100$  mV) so that the direction of negative ions and of the EOF is from *trans* to *cis* compartment.



## b. Polysulfides detection

To show the feasibility of polysulfides detection by nanopore, preliminary experiments were carried out by adding  $\beta$ -CD (1 mM) into the *trans* compartment applying -100 mV (Figure II.10.a). Some partial transient ionic current blockades were detected due to interactions of  $\beta$ -CD with the  $\alpha$ -HL stem (Figure II.10.b, blue), confirming the already reported results<sup>143,152</sup>. In the same conditions, we then added a  $\beta$ -CD/ $\text{Na}_2\text{S}_5$  complex solution (1mM  $\beta$ -CD mixed with 10 mM  $\text{Na}_2\text{S}_5$ ) and we also detected ionic current blockades with some events showing a deeper blockage amplitude (Figure II.10.b, red). No total current blockade was achieved, indicating that  $\text{Na}^+$  and  $\text{Cl}^-$  are still transported through the  $\beta$ -CD/ $\text{Na}_2\text{S}_5$  complex lodged in the  $\alpha$ -HL while the complex cannot go through due to steric hindrance. In addition, we do not expect the polysulfides to cross the membrane via  $\beta$ -CD constriction as well. This is based on the size of the  $(\text{S}_n)^{2-}$  species<sup>113</sup>,  $\sim 9.1 \text{ \AA}$  ( $\text{S}_3$ )<sup>2-</sup> or  $\sim 11.7 \text{ \AA}$  ( $\text{S}_5$ )<sup>2-</sup>, which is greater than the narrowest diameter ( $\sim 6 \text{ \AA}$ ) of the cone-like shape of  $\beta$ -CD<sup>8</sup>. Nevertheless, when  $\beta$ -CD or  $\beta$ -CD/ $\text{Na}_2\text{S}_5$  complex was added to the *cis* compartment, no such current blockades were observed (data not shown). This result is indicative of an EOF from *trans* to *cis* compartment preventing molecules to enter the  $\alpha$ -HL.

A statistical analysis was performed on the current traces recorded for the  $\beta$ -CD and  $\beta$ -CD/ $\text{Na}_2\text{S}_5$  experiment. The blockade ratio, given by the relation  $I_0 - I_b/I_0$ , where  $I_0$  is the ionic open pore current and  $I_b$  is the blockade current, *versus* individual event dwell times scatter plot (Figure II.10.c) shows two distinct event populations for free  $\beta$ -CD compared to  $\beta$ -CD/ $\text{Na}_2\text{S}_5$  complex. While dwell times cannot be used as a parameter for discrimination (Figure SI.II.12), we found that the general distribution of current blockade ratios for  $\beta$ -CD/ $\text{Na}_2\text{S}_5$  complex solution could be deconvoluted (Figure II.10.d). Two populations centered in  $74.0 \pm 0.3\%$  and  $64 \pm 2\%$  were attributed to the  $\beta$ -CD/ $\text{Na}_2\text{S}_5$  complex ( $74.0 \pm 0.3\%$ ) and the free  $\beta$ -CD in solution ( $64 \pm 2\%$ ), respectively, which is consistent with the equilibrium governing the  $\beta$ -CD/ $\text{Na}_2\text{S}_5$  *host-guest* complexation. Interestingly, the ratio between the number of events associated to the  $\beta$ -CD/ $\text{Na}_2\text{S}_5$  complex (red distribution) and the total number of events (grey distribution) is  $81 \pm 2.5\%$ . This is in very good agreement with the NMR calculated proportion of complexed  $\beta$ -CD in the same conditions, namely  $f_b = 79 \pm 4\%$  (Figure SI.II.13). Therefore, bulk and single molecule characterization methods corroborate well.



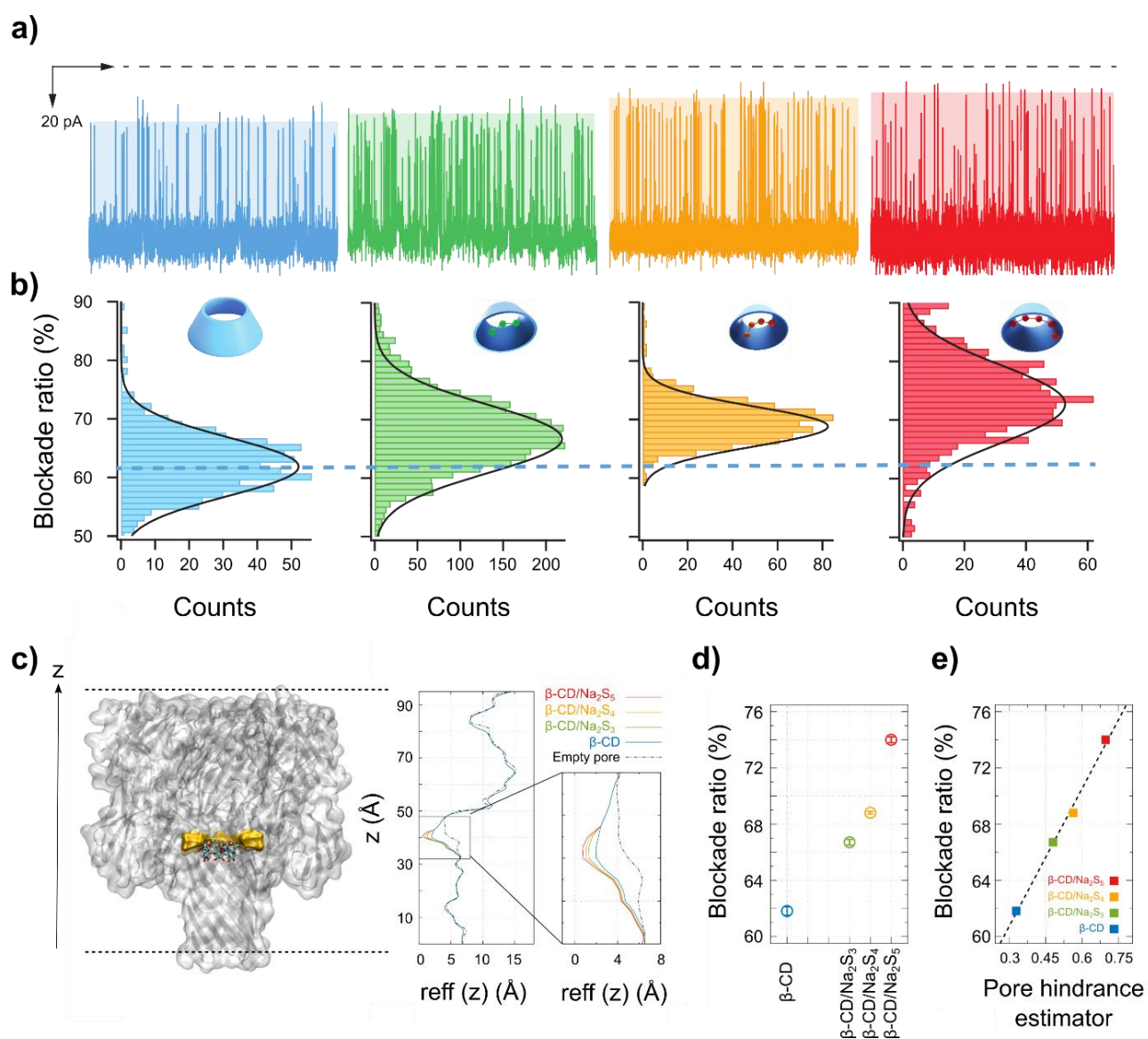
**Figure II.10: Discrimination of  $\beta$ -CD/ $\text{Na}_2\text{S}_5$  complex vs  $\beta$ -CD.** **a)** Schematic of the ion-current measurement  $\alpha$ -HL set-up. **b)** Detail of a part of current trace blockades arising from  $\beta$ -CD (blue) and  $\beta$ -CD/ $\text{Na}_2\text{S}_5$  complex (red) interaction with the pore at  $-100$  mV (1M NaCl, 25 mM  $\text{NaHCO}_3$ , pH 10). **c)** Scatter plots of blockade ratio versus the dwell time in presence of  $\beta$ -CD (blue, 225 events) and the  $\beta$ -CD/ $\text{Na}_2\text{S}_5$  complex solution (red, 761 events). (5 independent experiments). **d)** General distribution (grey) blockade ratio histogram in presence of the  $\beta$ -CD/ $\text{Na}_2\text{S}_5$  complex solution (945 events). Deconvolution of the general distribution showing two populations attributed to  $\beta$ -CD and  $\beta$ -CD/ $\text{Na}_2\text{S}_5$  complex centered in  $64 \pm 2\%$  and  $74.0 \pm 0.3\%$  respectively.

In conclusion, the electrical detection by nanopore allowed the successful distinction between  $\beta$ -CD and  $\beta$ -CD/ $\text{Na}_2\text{S}_5$  complex. Is this technique sensitive enough to discriminate different polysulfides chain lengths ?

### c. Polysulfides chain length discrimination

We then characterized  $\beta$ -CD/ $\text{Na}_2\text{S}_5$ ,  $\beta$ -CD/ $\text{Na}_2\text{S}_4$ ,  $\beta$ -CD/ $\text{Na}_2\text{S}_3$  complexes and compared our results to free  $\beta$ -CD molecules (Figure II.11). The current traces of each species show two kinds of current blockades associated with two types of events: (i) “bumping” events, characterized by brief low-level current blockades, which arise due to diffusion of molecules close to the pore; and (ii) interaction events, characterized by larger current blockades of longer duration. In order to characterize the interaction of  $\beta$ -CD and  $\beta$ -CD/ $\text{Na}_2\text{S}_x$  complexes with  $\alpha$ -HL, each current trace was statistically analysed to determine the event current amplitude and to separate bumping events from interaction events (see the Methods section in Supplementary Information, the reported data refer only to interaction events). We can observe a statistical decrease in the event current amplitudes correlated to a decrease of sulfur number for each complex (Figure II.11.a). We find  $74.0 \pm 0.3\%$ ,  $68.8 \pm 0.1\%$ ,  $66.7 \pm 0.2\%$  for  $\beta$ -CD/ $\text{Na}_2\text{S}_5$ ,  $\beta$ -CD/ $\text{Na}_2\text{S}_4$  and  $\beta$ -CD/ $\text{Na}_2\text{S}_3$  complexes, respectively. Therefore, each complex is well discriminated from free  $\beta$ -CD in solution with an average blockade ratio of  $61.8 \pm 0.3\%$  (Figure II.11.b). These results confirm that polysulfide species are docked inside the  $\beta$ -CD cavity and that we can discriminate each species at a single sulfur atom level.

In order to support this finding, our Italian collaborators calculated the nanopore hindrance estimator introduced as in a previous publication<sup>153</sup>. It reflects the steric hindrance of the pore channel corresponding to the volume occupied by  $\beta$ -CD and  $\beta$ -CD/ $\text{Na}_2\text{S}_x$  complexes. The calculation is based on an approximated quasi-1D continuum description of the nanopore electric resistance. As a first step, for each pore section, the effective area available to the electrolyte passage for both the open  $\alpha$ -HL and the  $\alpha$ -HL with the  $\beta$ -CD lodged in the pore stem (Figure II.11.c) was calculated from Molecular Dynamics simulations. Then, from the effective area of the  $\beta$ -CD case, a section corresponding to the occupancy of the different polysulfides was subtracted. As already discussed<sup>153</sup>, this method is based on several simplified assumptions not satisfied at the nanoscale, the main being: (i) it is a continuum method where atomistic details enter only via the effective area profile, (ii) it is a quasi-1D method that, in principle, is valid only for smoothly varying pore section and (iii) it neglects electrical double layer effects. Although it does not provide a quantitative estimation of the current blockades, it allows to catch their qualitative trends, as shown by the good correlation with the experimentally observed average current blocked (Figure II.11.d).



**Figure II.11: Discrimination of  $\beta$ -CD/ $\text{Na}_2\text{S}_x$  complexes.** **a)** Part of current versus time traces of an  $\alpha$ -HL pore at  $-100$  mV, in the presence of 1 mM  $\beta$ -CD (blue),  $\beta$ -CD/ $\text{Na}_2\text{S}_3$  (green),  $\beta$ -CD/ $\text{Na}_2\text{S}_4$  (yellow),  $\beta$ -CD/ $\text{Na}_2\text{S}_5$  (red). All experiments are independent (6 in total) and were performed in 1M NaCl, 25 mM  $\text{NaHCO}_3$  pH 10 in an Argon filled glovebox. **b)** Histograms of blockade ratio for  $\beta$ -CD (blue,  $61.8 \pm 0.3\%$ ),  $\beta$ -CD/ $\text{Na}_2\text{S}_3$  (green,  $66.7 \pm 0.2\%$ ),  $\beta$ -CD/ $\text{Na}_2\text{S}_4$  (yellow,  $68.8 \pm 0.1\%$ ),  $\beta$ -CD/ $\text{Na}_2\text{S}_5$  (red,  $74.0 \pm 0.3\%$ ). **c)** Accessible volume estimation from Molecular Dynamics simulations.  $\alpha$ -HL constriction is highlighted in yellow, while  $\beta$ -CD atoms are represented as balls-and-sticks. The plot reports the radius of the effective ( $r_{\text{eff}}$ ) pore section available for ion passage for  $\beta$ -CD,  $\beta$ -CD/ $\text{Na}_2\text{S}_3$ ,  $\beta$ -CD/ $\text{Na}_2\text{S}_4$  and  $\beta$ -CD/ $\text{Na}_2\text{S}_5$  complexes. **d)** Experimental current blockades. **e)** Experimental current blockades versus nanopore hindrance estimator calculated from atomistic model (see Methods in Supplementary Information for Chapter II).

Therefore, via the use of a protein nanopore sensor inserted into a lipid membrane we have demonstrated the feasibility to discriminate molecules that solely differ by a single sulfur atom. Indeed, the different  $\beta$ -CD/polysulfide complexes can be identified with great sensibility by a unique pattern of events in term of current blockade that increases with increasing the number of sulfur atoms, as intuitively expected.

## 4. Conclusions and discussions

In summary, a comprehensive multidisciplinary approach combining NMR spectroscopy, electrical nanosensing experiments and Molecular Dynamics simulations was adopted to understand deeply and at the molecular level the *host-guest* complexation equilibrium between CDs and polysulfides. Thus, an extension of this work with respect to the Li-S technology is imminent, involving the exploitation of CD molecular recognition towards organic polysulfides and the prospects for nanopore in the battery field.

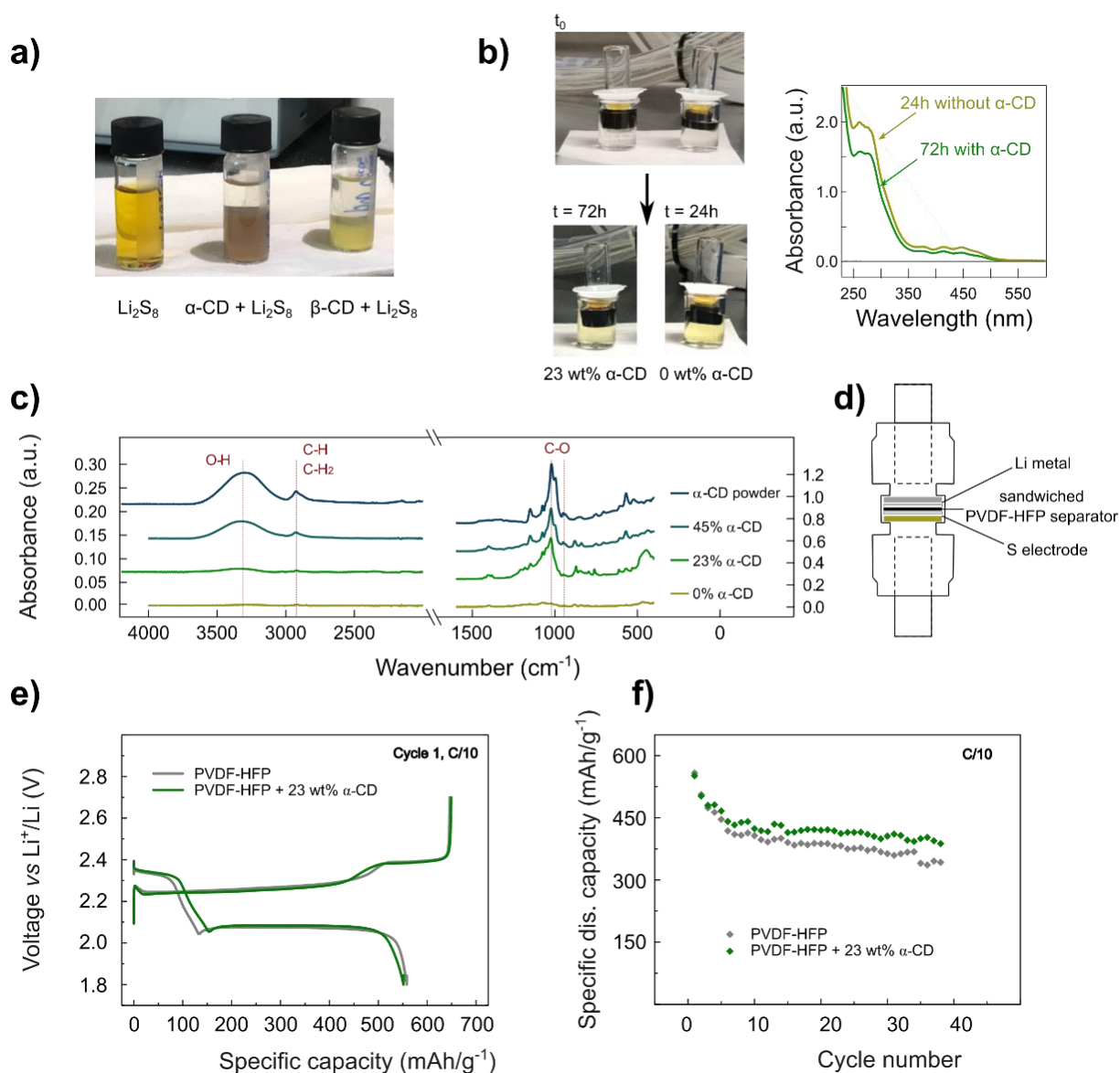
### a. Extension towards organic polysulfides

Some preliminary experiments were carried out to investigate this *host-guest* interaction in organic medium. Lithium polysulfides solutions were prepared via a solution process, by mixing  $\text{Li}_2\text{S}$  with S in organic solvent (DOL/DME, DME, PC and THF) for 24h in an argon glovebox.  $\alpha$ - and  $\beta$ -CD, which are not soluble in this kind of solvent, were vigorously mixed with  $\text{Li}_2\text{S}_8$  (2.5 mM in DOL-DME) to form an emulsion. After decantation, a brownish precipitate separates from the discolored electrolyte, showing the expected interaction. Therefore, CD is acting as a surfactant since it entails the polysulfides migration from the liquid organic phase to the solid phase by encapsulation. Such finding supports the usefulness of CD analogous in Li-S batteries in the set-up of a polysulfides immobilization strategy. Nevertheless, the precipitation of the complex does not allow us neither to calculate any association constant ( $K_a$ ), nor to assess the effect of the organic solvent on the binding thermodynamics (Figure II.12.a).

From our exposed study, the  $\beta$ -CD/polysulfide complexes formed in solution are specifically blocked by a nanopore embedded in a lipid membrane, while enabling the cation ( $\text{Na}^+$ ) and anion ( $\text{Cl}^-$ ) flows.

That led us to envision the design of CDs-based separators that could prevent the diffusion of polysulfides. We prepared PVDF-HFP separators according to the Bellcore process<sup>154</sup> and incorporated  $\alpha$ -CD, which exhibits a temperature sensitiveness greater than  $\beta$ -CD. FTIR spectra of the different  $\alpha$ -CD-based separators show the characteristic peaks of  $\alpha$ -CD, coming from the cyclic ether function and corresponding to the C-O stretching ( $910$  and  $1030\text{ cm}^{-1}$ ). The C-H/C-H<sub>2</sub> vibration ( $2900\text{ cm}^{-1}$ ) can also be observed in the mid-infrared region, as well as the O-H stretching vibration ( $3500\text{ cm}^{-1}$ ) (Figure II.12.c). Qualitative tests were performed to show the restraining ability of  $\alpha$ -CD-based separators on blocking the polysulfides migration (Figure II.12.b). A vial containing a polysulfide catholyte ( $\text{Li}_2\text{S}_8$  in PC) was dipped into polysulfide-free electrolyte contained in a bigger size beaker. PVDF-HFP separators (with and without CDs) were placed at the vial lids. We observed a progressive polysulfides diffusion, as witnessed by the coloration of the initially transparent electrolyte, which is quite slower for the beaker using a  $\alpha$ -CDs-based PVDF-HFP membrane. This indicates the trapping of polysulfide species by  $\alpha$ -CDs molecules pertaining to the separator membrane. Besides, the colour change was monitored by time through UV-vis spectroscopy to confirm our eye visualisation.

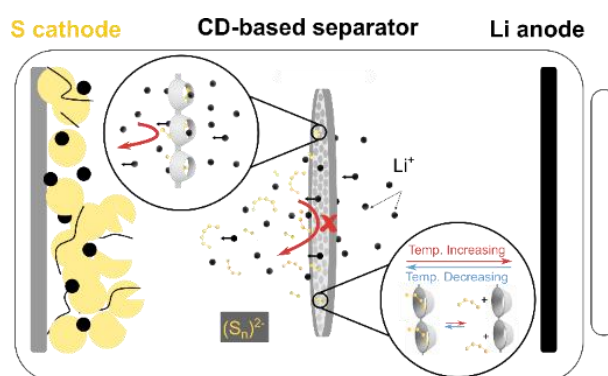
Then, galvanostatic experiments were carried out to assess the Li-S cells performances using  $\alpha$ -CDs-based PVDF-HFP separators. Sulfur composite electrodes were prepared from a sulfur impregnated carbon (60/40%<sub>wt</sub>) and PTFE (5%<sub>wt</sub>), through a self-standing method. Swagelock® cells were assembled using Li metal foil as the negative electrode and the tested separator was sandwiched between two layers of borosilicate glass microfibre membranes soaked with electrolyte (1M LiTFSI, 0.25M  $\text{LiNO}_3$  in DOL/DME) (Figure II.12.d). The electrochemical performances of the  $\alpha$ -CDs-based separator (green, 23%<sub>wt</sub>) and the control separator (grey, 0%<sub>wt</sub>) were compared. First initial galvanostatic discharge/charge profiles show the characteristic plateaux of Li-S red-ox processes and exhibit similar specific capacities<sup>106</sup> (Figure II.12.e). However, the cell with the  $\alpha$ -CDs-based separator (green) displays better cycling stability and higher specific capacity ( $388\text{ mAh.g}^{-1}$ ) than the one without CD (grey,  $342\text{ mAh.g}^{-1}$ ) after 38 cycles (Figure II.12.f). Although the Li-S cell equipped with the  $\alpha$ -CDs-based separator still shows obvious evidence of the persistence of redox shuttle (over charge capacity), these results confirm a positive effect of CD upon cycling, that will need to be further confirmed by improving the separator processing, investigating the most efficient CD type and adjusting the CD loading.



**Figure II.12: Exploitation of CD molecular recognition towards organic lithium polysulfides.** **a)** Discoloration of  $\text{Li}_2\text{S}_8$  solution (2.5 mM DOL/DME) before and after 10 h upon contact with  $\alpha$ -CD or  $\beta$ -CD (1:1). **b)** Restraining ability of the  $\alpha$ -CDs-based PVDF-HFP separator (23 wt%) on blocking the diffusion of polysulfides ( $\text{Li}_2\text{S}_8$ , 2.5 mM in PC). **c)** FTIR spectra of  $\alpha$ -CDs-based PVDF-HFP separators. **d)** Swagelok® cell configuration. **e)** First galvanostatic charge and discharge curves for Li-S equipped with the  $\alpha$ -CDs-based (23 wt%) (green) and the control (grey) PVDF-HFP separators. **f)** Capacity retention upon cycling.

The immobilization of polysulfides within the separator does not constitute a long-term solution since they become dead active material. That is where stimulus-responsive CD encapsulation, which has never been envisioned in batteries, may represent an added value in the design of thermo-responsive regenerative separators, that could regulate polysulfides on demand (Figure II.13). It would require a cooling step during discharge, hence preventing diffusion of polysulfides

intermediates towards the Li anode, while a heating-up step during charge would release the trapped polysulfides, letting them to participate again in the red-ox processes. Despite the seducing concept of thermal regeneration, we are aware of the inherent obstacles that prevent a straightforward application, such as the temperature influence on the electrochemical performances, the concentration of dissolved polysulfides, the CD orientation to control the spatial release and the complexation selectivity<sup>82</sup>. Thus, we must remain realistic on the prospects for stimulus-responsive polysulfides regenerative separators.



**Figure II.13: Conceptual illustration of a thermo-responsive cyclodextrin material as an efficient regenerative Li-S battery separator.**

In conclusion, CD molecular recognition towards aqueous polysulfides is well extended to organic polysulfides and it may offer some opportunities to synthesize stimuli-responsive CDs-based materials. What about the extension of the nanopore technology to organic Li-based polysulfides ?

#### b. Future for nanopores as new powerful electrolyte sensors

In light of our results, single-molecule nanopore detection stands as a powerful sensing tool to scrutinize at the molecular level the sulfur speciation of Na-based aqueous polysulfides. Hence, it may be envisioned as a novel *in-situ* probe of the unwanted polysulfide shuttle effect Li-S batteries suffer from, with a reliable identification of the intermediate species. However, we must admit that implementing our developed methodology to discriminate polysulfides in organic solvent would not be straightforward.



First, the encapsulation approach must be reconsidered because native CDs and CD/polysulfide complexes are not soluble in organic electrolyte. As chemical modification of CD triggers its solubility, we came up with a soluble randomly methylated  $\beta$ -CD (RM $\beta$ -CD) and tried to implement our NMR protocol to thoroughly study the corresponding CD/polysulfide complexation equilibrium in organic medium ( $^1\text{H}$  and  $^7\text{Li}$  NMR, data not shown). Unfortunately, the complex mostly precipitates, resulting in a very small proportion of soluble complex (not quantified). Although the translation of our previous strategy becomes then impossible, our successful *proof-of-concept* in aqueous media gives faith in the sensitivity that the nanopore technology benefits from. Therefore rethinking our approach is not regarded as an obstacle, but it rather represents the unique opportunity for the nanopore technology to strengthen its overall credibility and overcome the traditional characterization techniques.

Additionally, non-aqueous electrolytes are not ideal for both biological nanopores and lipid membranes. The alternative way to conduct nanopore sensing consists in switching to solid-state nanopores made of drilled polymers or semi-conductors membranes mimicking biological ionic channels<sup>122</sup>. We must admit that the precise control of the nanopore size constitutes a challenge for the small pore sizes required (< 5 nm). However, owing to their chemical stability, such tailored membranes offer a nice playground for molecule discrimination and for characterizing at the molecular level, any parasitic redox products, chemical cross-talks or degradation products resulting from the electrolyte reduction, such as alkyl carbonates<sup>155</sup>.

Independently to this organic *proof-of-concept* to be pursued, we should keep in mind that to be competitive with other non-invasive sensing tools that operate *in-situ* and the battery community has become more familiar with such as optical fibers<sup>156,157</sup>, nanopores must be integrated to the electrochemical device to monitor in real-time the electrolyte composition. This may come through the design of a microfluidic system collecting, analysing and reintroducing the electrolyte, but we must confess such integration strategy appears more elegant than practical for the moment.

In summary, we have successfully rationalized the *host-guest* interaction between CD and polysulfides, hence explaining the benefit to use CD in the design of S cathode binders. Then, we have thrivingly implemented the nanopore technology for the first time in the battery field, exploiting

this encapsulation property. This electrical detection tool borrowed from biology appears as a very promising high-resolution tool to discriminate polysulfides only differing from a single sulfur atom.

Nevertheless, our discussions have emphasized that further development is needed to pave the way towards smart regenerative Li-S batteries separators. Therefore, our willingness to implement CDs properties into real electrochemical systems has brought us to consider macromolecular synthesis of CDs-based architectures as well as to switch to another battery technology, *ie* the Si anodes for the next-generation Li-ion batteries. This is how we decided to dive in the understanding of the great performances induced by the use of mechanically interlocked architectures of CDs as Si anode binders<sup>101</sup>.



# Chapter III: Novel elastic deformable mechanically interlocked architectures synthesized from $\alpha$ -cyclodextrins based polyrotaxanes

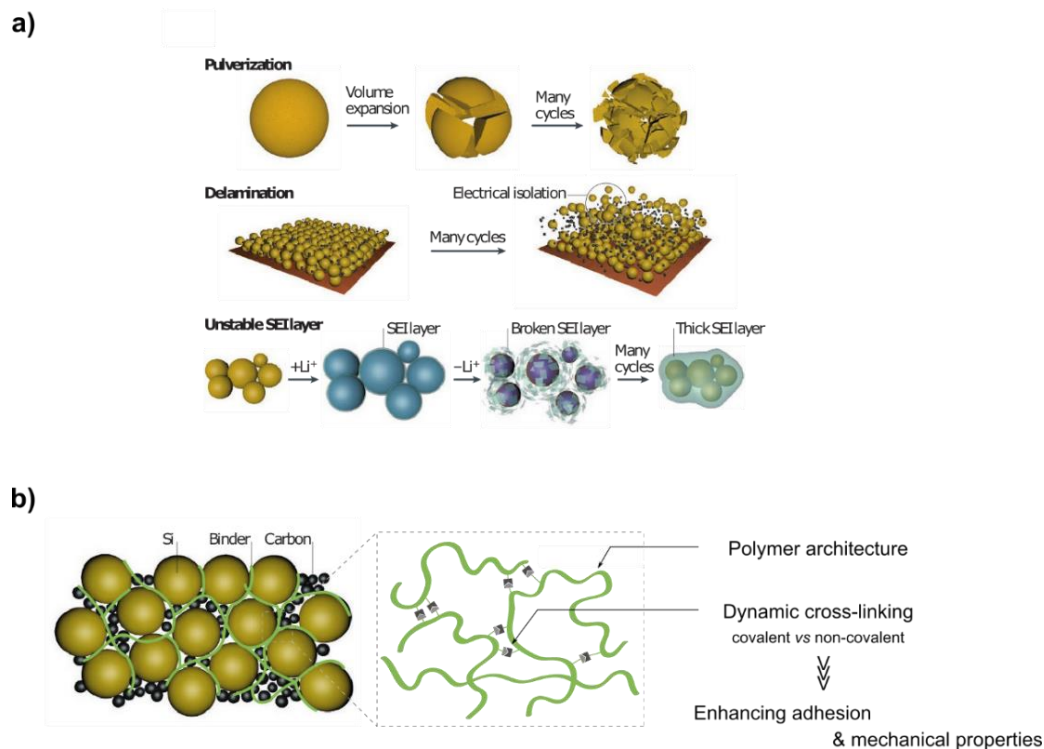
## 1. Background and motivation

As already mentioned before, this thesis fits in with the global goal of taking advantage of the dynamic nature of supramolecular chemistry in order to embed batteries components (*ie*, electrode, separator, electrolyte) with some added “*smart*” functionalities to improve their lifespan. In this part, we propose to use silicon (Si) anodes to demonstrate the benefits of  $\alpha$ -CD supramolecular *host-guest* interaction towards ethylene oxide (EO) units of poly(ethylene oxide) (PEO). Two main reasons support this choice. First, Si stands among the most promising candidate for the next-generation high-capacity electrodes in Li-ion batteries, owing to its theoretical capacity of  $3600 \text{ mAh.g}^{-1}$ , that is almost ten times higher than the commercialized graphite anodes ( $372 \text{ mAh.g}^{-1}$ )<sup>88,89</sup>. Secondly, the battery community has already witnessed the positive role played by polymers that involve supramolecular interactions, in addressing the issues caused by the massive volume changes of Si anodes<sup>94,158</sup>.

Thus, in this chapter, the focus is made on the design of new types of  $\alpha$ -CDs polymer architectures that meet the specific requirements to be used as Si anode binders. The general context of the study is depicted in this first section with a brief overview of the design principles of polymeric binders. The following sections are dedicated to the presentation of our experimental results dealing with the synthesis of mechanically interlocked architectures prepared from  $\alpha$ -CDs based polyrotaxanes (PRs), which are supramolecular assemblies on which  $\alpha$ -CDs can move freely on a threading polymer (here POE). As recently reported, polymer networks incorporating PR in their architecture exhibit outstanding mechanical properties<sup>64</sup>, hence offering the possibility to mechanically reinforce the Si electrode. Thus, we are paving the way for new routes of accommodating Si anode volume changes.

### a. Si anode volume changes being addressed through the design of binders

Due its superior high theoretical specific capacity ( $\sim 3600 \text{ mAh.g}^{-1}$ ), high abundance, low cost and low discharge voltage ( $< 0.5 \text{ V vs Li}^+/\text{Li}$ ), Si is regarded as one of the most promising anode materials for the next-generation Li-ion batteries. Nevertheless, during the electrochemical processes of lithiation (charge) and delithiation (discharge), Si experiences massive cyclic volume changes ( $\sim 300\%$ ) leading to structural collapse. This results in poor cycling performances<sup>88–91</sup>. Indeed, these colossal volume fluctuations induce some Si electrode cracking and pulverization which contribute to the delamination of the electrode and thus the electrical isolation of some Si domains. Moreover, a critical issue is the stability of the solid electrolyte interface (SEI), which constantly grows as the Si particles crack and create some fresh Si surfaces<sup>87</sup>. The illustration of these main degradation mechanisms originating from the large volume changes of Si anodes is provided in Figure III.1.a.



**Figure III.1: Si anode binder designs, adapted from ref<sup>87</sup>.** **a)** Illustration of the three main failure mechanisms of Si anodes: delamination, pulverization, and interfacial issues due to the unstable SEI layer. **b)** Concept of the design of Si anode binders.

For more than a decade, great efforts have been devoted in solving these severe issues, with partial success, either by switching to an electrolyte that improves the SEI stability or by developing Si smart nanostructures that buffer well the volume changes<sup>87,92,93</sup>. Here, we focused on another widespread strategy which consists in developing well-designed polymeric binders to maintain the electrode structure and enhance its cyclability (Figure III.1.b)<sup>94-96</sup>. Prior to move to our achievements, we first propose a brief review of the different binders engineering strategies that have been recently implemented in the literature to achieve high-capacity Si electrodes. Interestingly, they rely on the mastering of polymer science and supramolecular chemistry.

The basic role of a binder is to **maintain the cohesion** between the electrode components (*ie*, active material, conductive additive) while preserving a good adhesion to the current collector. This calls for the design of strong interactions between Si particles and the polymeric binder. With this in mind, sodium carboxymethylcellulose (CMC)<sup>99</sup>, which is a linear polymeric derivative of cellulose, and poly(acrylic acid) (PAA)<sup>97</sup> were introduced as Si anode binders allowing a considerable improvement in the Si cycling performances. They feature many interaction points with silanol groups (Si-OH) of the Si surface via both supramolecular interactions, such as ion-dipole and hydrogen bonding, and covalent ester-like bonds. Bridel *et al* used <sup>13</sup>C NMR to show for the first time the formation of these reversible ester-like bonds<sup>159</sup>. That led them to introduce the concept of self-healing that relies on the ability of these reversible bonds to act like Velcro®, by recovering in response to the external stress induced by Si anode volume changes. Subsequently, several studies addressed the influence of the density of Si-binder interaction contact points<sup>97,98</sup> as well as the nature of these chemical bonds, covalent vs non-covalent<sup>160,161</sup>, on the binder performances.

Besides, the **polymer architecture** is also underlined as a key parameter for the design of an efficient Si anode binder. 3D network polymers better accommodate the mechanical stress induced by Si volume fluctuations compared to linear polymers. Indeed, the stress can be dissipated along the branched chains, hence decreasing the force on each anchoring point<sup>102,162</sup>. The formation of a 3D network calls for cross-linking that can be made either via covalent bonding<sup>102,163,164</sup> or through non-covalent bonds with the use of supramolecular interactions such as hydrogen bonds<sup>165,166</sup>, ionic bonding<sup>167,168</sup> and even host-guest interactions<sup>100</sup>. Supramolecular interactions have been shown to be the ideal class of bonding because they can reversibly associate and dissociate in mild conditions, hence demonstrating self-healing properties.

Then, another parameter to design Si binders is to pay attention to their **mechanical properties**. The first attractive intuitive idea was to focus on elastomers<sup>169</sup> that can accommodate colossal volume changes because of their large stretchability before breaking. Several types of elastomeric binders, such as poly(vinylidene fluoride-tetrafluoroethylene-propylene) (PVDF-TFE-P)<sup>170</sup> or styrene-butadiene-rubber (SBR) mixed with CMC<sup>171</sup>, demonstrated some cycling improvements compared to the traditionally used poly(vinylidene fluoride) (PVDF). However, subsequent studies argued against this theory demonstrating that brittle polymers such as CMC<sup>99,172</sup> or PAA<sup>97</sup> were more effective than elastomeric binders. Thus, this demonstrates that not only elasticity is a relevant parameter but also other criteria are required such as the binder content, the binder-binder interactions and the Si adhesion<sup>173</sup>.

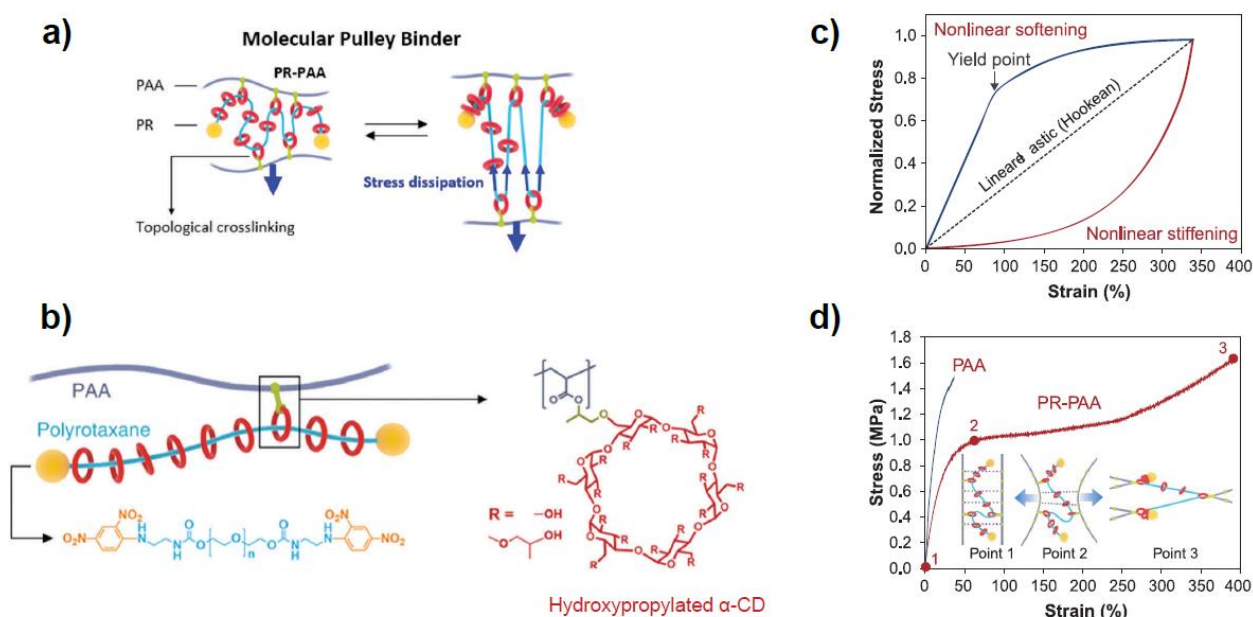
Ideally, to maintain the Si electrode integrity and buffer its volume changes, a binder must exhibit superior stiffness (ability to resist deformation as defined by both its Young's modulus  $E$  and geometry) and toughness (ability to absorb energy before fracture), high tensile strength (maximum stress at rupture), large breaking strain and particularly high elasticity combined with a good strain/stress recovery. Thus, a trade-off needs to be found via the fine tuning of the chemical bond strengths involved in the polymer network cross-linking and the Si adhesion. The cross-linking density or the flexibility of the chains must also be considered<sup>94,96</sup>.

Despite the large variety of reported binders designs and the great number of independent studies, some unanswered questions remain. The main one being the following: which property is the most useful among Si adhesion, cross-linking, self-healing, stiffness, flexibility, stretchability...? Kwon *et al*<sup>160</sup> were the first to address this question via a structure-properties relationship study of a copolymer composed of four monomer units, each one being responsible for one distinct function. It is precisely this kind of fundamental approach that we decided to adopt to understand the proper function of a new type of Si anode binders: the mechanically interlocked networks.

### b. Mechanically interlocked architectures inducing enhanced mechanical properties

As mentioned previously, supramolecular interactions have largely been used in the Si binder chemistry<sup>100,165-168</sup>. Along that line, a recent work from Choi *et al*<sup>101</sup> has attracted our attention, as described in Chapter I (see 2.b) in which they introduced a novel cross-linking concept inspired by

the working principle of moving pulleys (Figure III.2.a). This was done by cross-linking PAA with  $\alpha$ -CDs based polyrotaxanes (PR), which result from the mechanically interlocking of molecular rings (here  $\alpha$ -CDs) with a linear polymer (here PEO), hence forming a necklace architecture. The supramolecular interactions at stake are *host-guest* interactions between  $\alpha$ -CDs cavities with ethylene oxide (EO) units<sup>174</sup> (Figure III.2.b). Thus, the authors attribute the high stretchability of the PR-PAA binder to the fact that  $\alpha$ -CDs can slide on the threading polymer. Although the network is held by covalent cross-linking, this sliding motion ensures the dynamic nature of the polymer network.



**Figure III.2: Design and working principle of a molecular pulley PR-PAA binders, adapted from ref<sup>101</sup>.** **a)** Working principle of the molecular pulley binder PR-PAA, which enables the stress dissipation and high stretchability. **b)** Chemical structure of PR-PAA and its schematic representation. PR were prepared from PEO of 20 000 g.mol<sup>-1</sup> and  $\alpha$ -CDs. **c)** Representative stress-strain curves for non-linear softening, non-linear stiffening (=strain hardening) and linear elastic mechanical responses to deformation. **d)** Stress-strain curves for PAA and PR-PAA binder. The PR-PAA binder shows a non-linear stiffening behaviour at strain exceeding 200%.

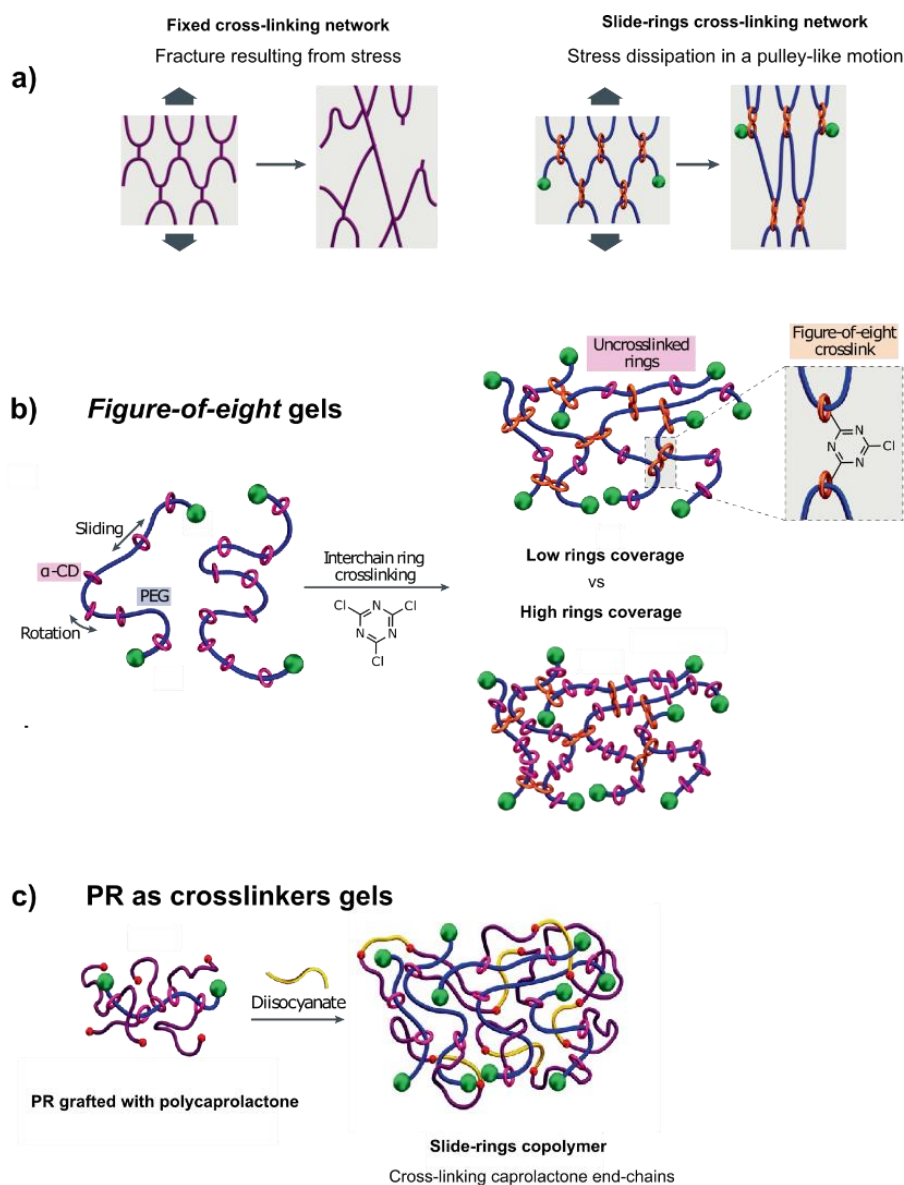
Tensile tests were carried out to examine the mechanical properties of PR-PAA networks (Figure III.2.d). They revealed that PR-PAA can sustain large strain (390%) while having good stress-strain recovery properties, as well as to resist to a high mechanical strength. Interestingly, the stress-strain curve presents a non-linear stiffening behaviour (second part of the curve) to be opposed to PAA that exhibits a non-linear strain softening (Figure III.2.c). Non-linear strain stiffening or strain hardening turns out to be advantageous for Si anodes since PR-PAA can accumulate small stress



with respect to a large increase in strain. Furthermore, to name only a few, it is noted that a similar behaviour can be found in biological systems such as artery walls or spider's webs and they are also known to display excellent resistance to damage.

Although it was the first time these topological architectures were engineered towards battery applications, polymer networks incorporating PR have already been the object of numerous studies<sup>64</sup> with many different targeted applications. To cite only a few examples, there are scratch-resistant coating, vibration-proof insulating materials<sup>71</sup> or stimuli-responsive hydrogels<sup>72,73</sup> designed for drug delivery, artificial muscles or biosensing. They are commonly called slide-rings materials<sup>175</sup> owing to their movable junctions that can slide freely along the polymer backbone. The high degrees of motion and conformational freedom result from the interlocked nature of PR.

The two different designs of slide-rings materials, prepared from  $\alpha$ -CDs based PRs, that have been reported in the literature are illustrated in Figure III.3. First, there are the *figure-of-eight gels*<sup>176,177</sup>, in which the  $\alpha$ -CDs of two different PRs are covalently cross-linked leading to "eight-shape" movable crosslinkers (Figure III.3.b). The other design consists in using *PR as cross-linkers* in a 3D polymer network by grafting  $\alpha$ -CDs threaded on the PR to the desired polymer. This second design was already used to tailor properties of poly(acrylic acid) (PAA)<sup>101</sup>, acrylates<sup>178,179</sup>, poly(lactones)<sup>180,181</sup>, poly(amides)<sup>182</sup>. Compared to materials with fixed cross-links, slide-rings materials display lower elastic modulus, superior extensibility, improved toughness, and greater swelling<sup>64</sup>. Numerous structural parameters were shown to be of paramount importance to tune the mechanical properties of slide-rings materials prepared from  $\alpha$ -CDs based PRs. Since that constitutes the corner stone of my study, I will succinctly review them.



**Figure III.3: Two main types of design for slide-rings materials prepared from  $\alpha$ -CDs based PRs, adapted from ref<sup>64</sup>.**

**a)** Illustration of the effect of stress on different nature of cross-links networks. For the fixed cross-links network, it results in the material fracture whereas the stress is dissipated thanks to the pulley-effect for the slide-rings cross-linked material.

**b)** Schematic of a figure-of-eight slide-rings material obtained from the covalent bonding between  $\alpha$ -CDs hydroxyl groups and cyanuric chloride. This example was taken from ref<sup>176</sup>. For high PR ring coverage, the proportion of uncross-linked rings is increased and the distance available for rings to slide is reduced, hence inducing different properties. **c)** Schematic of PR used as cross-linkers of a 3D polymer network. Here, the example was taken from ref<sup>183</sup>. PRs are grafted with poly(caprolactone) with the hydroxyl chain ends that can be covalently cross-linked in presence of diisocyanate.

First, the **distance available for ring sliding** appears as an intuitive key parameter to be controlled. The sliding range can be broadened by increasing the *molecular weight*<sup>184</sup> of the axis polymer or by decreasing the *PR ring coverage*, that is calculated as the percentage of the threading polymer being covered by the ring molecules. For a similar cross-linking density, several studies reported good

stress/strain recovery<sup>185</sup> and higher stress/strain at break<sup>186,187</sup> when decreasing the PR ring coverage. Additionally, a recent study<sup>188</sup> effectively demonstrated that a low coverage slide-rings materials induces higher fracture toughness but also a slower propagation of cracks. Note that for *figure-of-eight* gels, some unexpected stiffness was reported mainly due to the competition between intermolecular (between  $\alpha$ -CDs of different PR) and intramolecular (between  $\alpha$ -CD of the same PR) cross-links<sup>189</sup>.

Secondly, the **cross-linking density** also plays a significant role which is not yet fully understood. The slide-rings networks mechanical response to a rise in cross-linking density is not as predictable as conventional fixed cross-linked networks, which display higher stiffness at the expense of toughness as well as lower swelling<sup>190</sup>. Indeed, some works reported a similar trend<sup>178</sup> while other exhibited enhanced extensibility along with superior stiffness<sup>179,182,185</sup>. Thus, each slide-rings system requires a specific systematic study as the mechanical properties come from both the polymer chains and the ring sliding.

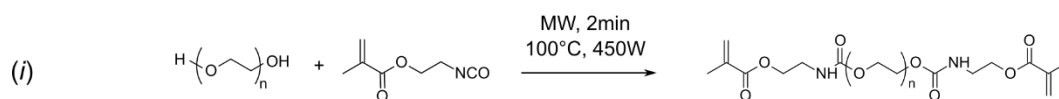
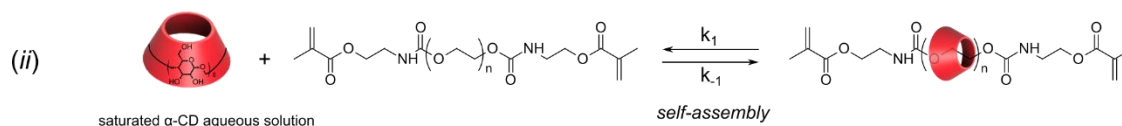
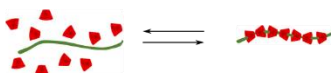
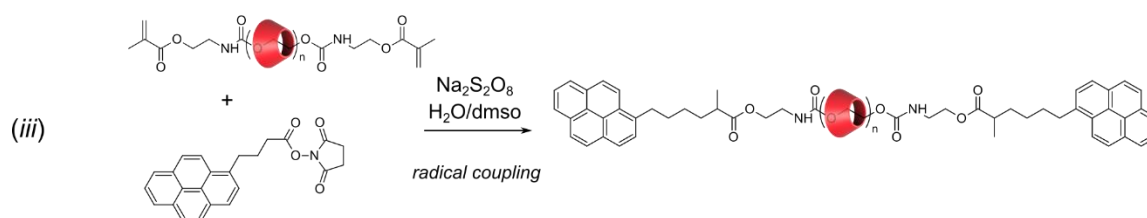
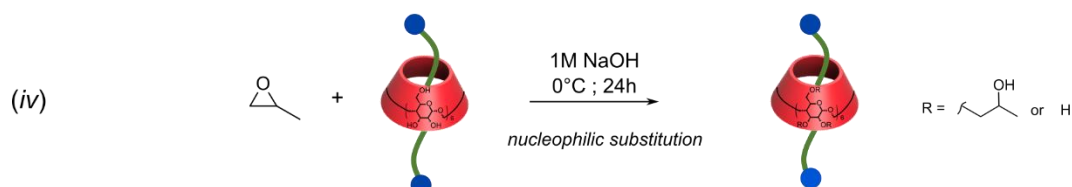
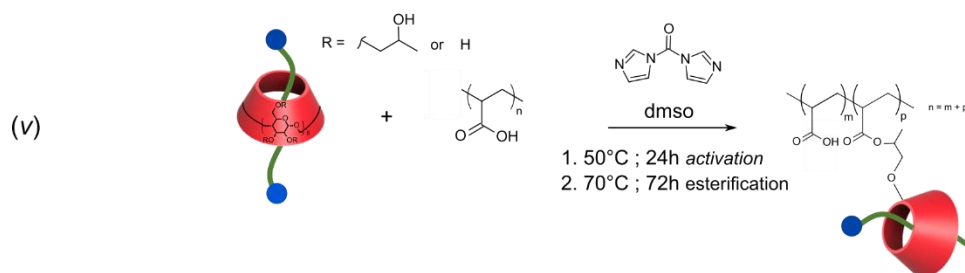
The previously mentioned work<sup>101</sup>, dealing with the impressive electrochemical capacities achieved using PR cross-linkers in the design strategy of Si anode binders, has inspired several other works as mentioned in Chapter I<sup>103–105</sup>. Nevertheless, the underlying source of performance enhancement of such topological cross-linked binders remains unclear. Which structural factors give the PR-PAA binders their unique properties? Such question drove us to conduct a structure-properties study to investigate the role of the different structural parameters on PR-PAA networks properties.

### c. Synthesis strategy of our binders

Our motivation being exposed, our experimental results will be displayed in the following sections of this Chapter. To favour the pulley effect, we synthesized high molecular weight  $\alpha$ -CDs-based PRs with different PR ring coverages that we incorporated in poly(acrylic) (PAA), as slidable cross-linkers. This Chapter is dedicated to the synthesis of PR-PAA networks and the characterization of their properties. The evaluation of the electrochemical performances of the PR-PAA architectures used as Si anode binders is the subject of Chapter IV.

Our PR-PAA synthesis route is composed of two main steps: the polyrotaxane (PR) formation and the cross-linking of poly(acrylic acid) (PAA) with PR (Figure III.4). The following sections thoroughly describe the different stages that govern the formation of such mechanically interlocked architectures: (i) the functionalization of the poly(ethylene oxide) (PEO) end-chains with methacrylate functions, (ii) the formation of the pseudopolyrotaxane (PPR) resulting from the inclusion complex between  $\alpha$ -CDs and the modified PEO, (iii) the end-capping reaction of the methacrylate functions with pyrene groups through a radical coupling reaction to form the polyrotaxane (PR), (iv) the hydroxypropylation of the  $\alpha$ -CDs born on the PR and (v) the condensation of the  $\alpha$ -CDs hydroxypropyl moieties with the carboxylic acids of PAA through an esterification.

To confirm the successful completion of the synthesis, we used different characterization techniques: Nuclear Magnetic Resonance spectroscopy (NMR), Size Exclusion Chromatography (SEC), Differential Scanning Calorimetry (DSC), mechanical testing and Fourier-transform Infrared spectroscopy (FTIR). For reasons of conciseness, we will present solely the results of these experiments, leaving the experimental details in the experimental section related to this Chapter (Supplementary Information for Chapter III).

**Step 1 :  $\alpha$ -CDs based polyrotaxane (PR) synthesis****. PEO end-chains methacrylation****. PPR formation****. PR formation****Step 2 : PR-PAA network synthesis****. Polyrotaxane hydroxypropylation****. Esterification****Figure III.4:** Illustration of the synthetic route of the formation of a PR-PAA networks.

## 2. $\alpha$ -CDs based polyrotaxanes (PRs) synthesis

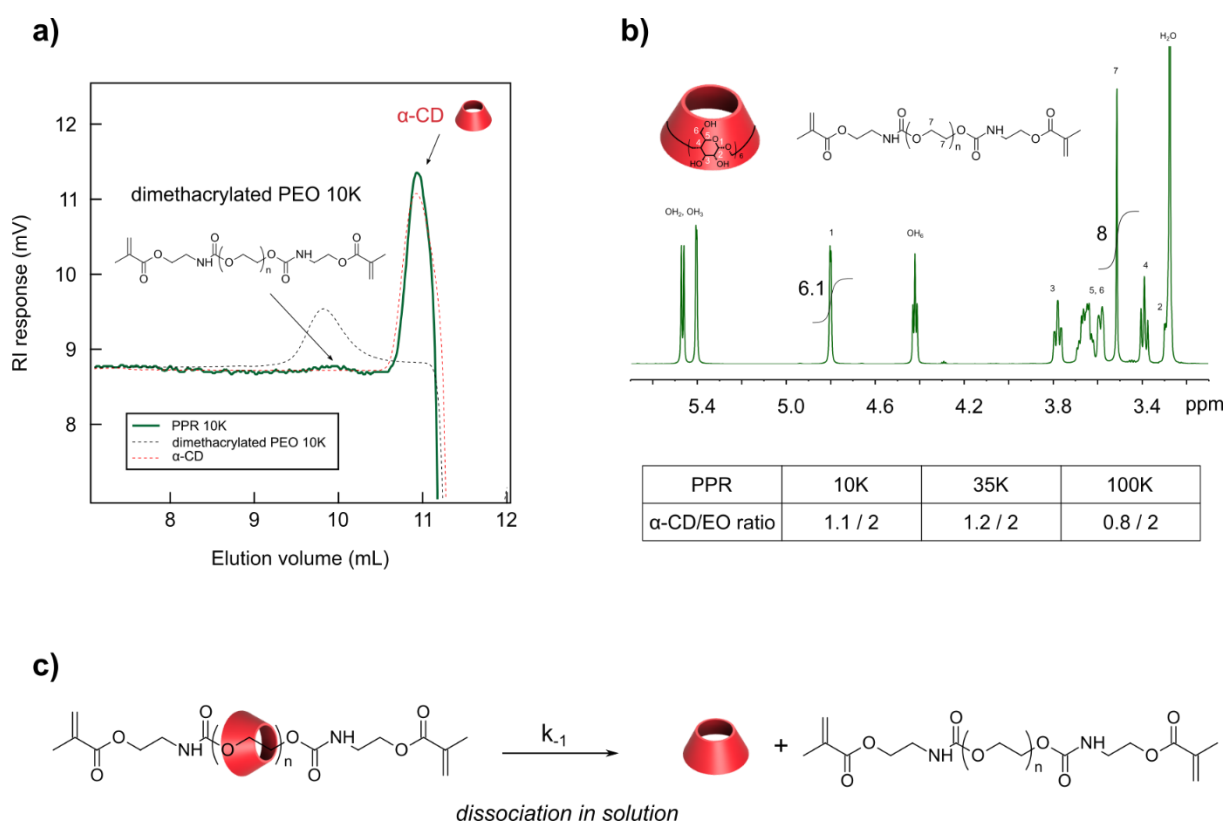
### a. PR synthesis pathway

In light of the targeted application, PRs were synthesized from commercial high number average molecular weights poly(ethylene oxide) (PEO) of 10 000, 35 000 and 100 000 g.mol<sup>-1</sup>. They are referred as PEO10K, PEO35K and PEO100K in the following of the report. The PEO end-chains were firstly functionalized with methacrylate functions through a microwave-assisted process, which has the major advantage to be a solvent-free reaction with fast kinetics<sup>191</sup> (Figure III.4, (i)). This preliminary step is essential prior pursuing our synthetic pathway because methacrylate functions are involved in the end-capping reaction of pyrene moieties to form the PR and that none of such modified PEO is commercialized. As this modification step is not the main purpose of the study, there are no further detail here, but a more detailed description can be found in Supplementary Information (Figures SI.III.2-10 & Tables SI.III.2-3).

The following step consists in the **PPR formation** that is enabled by a self-assembled process governed by the *host-guest* interaction between the ethylene oxide units (EO) of PEO and  $\alpha$ -CDs (Figure III.4, (ii)). The major driving forces for forming these tubular architectures rely on supramolecular interactions between the inner surface of the  $\alpha$ -CD ring and EO units. The head-to-head and tail-to-tail threading mode is favoured by the formation of hydrogen bonds between neighbouring  $\alpha$ -CDs<sup>43,44</sup>. The dimethacrylated POE was solubilized in a saturated aqueous solution of  $\alpha$ -CDs and the mixture was stirred for 24h to get a white precipitate that was isolated by filtration (Figure III.4, (ii)). For the three different PEO molecular weights, PEO and  $\alpha$ -CDs were introduced in stoichiometric proportions (2 EO units for 1  $\alpha$ -CD), which are known to allow the fully compact PPR<sup>174</sup>, referred as PPR10K, PPR35K and PPR100K in the following of the report.

The complex formation between  $\alpha$ -CDs and PEO was studied quantitatively by <sup>1</sup>H NMR spectroscopy and SEC measurements, by estimating the number of  $\alpha$ -CDs threaded onto the polymer chain (Figure III.5). On the SEC chromatogram of PPR10K, we can distinguish two main populations, that we attributed to PEO 10K and  $\alpha$ -CDs, with a ratio in agreement with the fully compact PPR stoichiometry (Figure III.5.a). The presence of these two populations does not come as a surprise. Indeed, the

supramolecular interactions that hold the PPR structure dissociate in solution, leading to the two constituting components (PEO and  $\alpha$ -CDs) in their native state (Figure III.5.c). We can also access the PPR10K stoichiometry, from  $^1\text{H}$  NMR spectroscopy, by integrating the signal of the  $\alpha$ -CDs anomeric protons ( $\text{H}_1$ ; 4.79 ppm) and the signal of the protons of EO units ( $\text{H}_7$ ; 3.5 ppm). For PPR10K, PPR35K and PPR100K, the stoichiometry was also verified by considering the methyl protons of the methacrylate functions (1.9 ppm). Note that, NMR characterization is consistent with the synthesis of fully compact PPRs, *ie* 1  $\alpha$ -CD for 2 EO units, for PPR35K and PPR100K as well (Figure III.5.b).



**Figure III.5: Characterization of the PPR made the different PEO.** **a)** SEC chromatograms of PPR10K, POE 10K and  $\alpha$ -CDs obtained with the RI detector ( $0.025 \text{ mg}\cdot\text{mL}^{-1}$  in DMF, Shodex KD-806M). We calculated the mass fraction of  $\alpha$ -CDs in the PPR sample ( $86\%_{\text{wt}}$ ) which corroborates quite well with the expected one ( $92\%_{\text{wt}}$ ), using the calibration (Figure SI.III.1). **b)**  $^1\text{H}$  NMR spectrum of PPR10K (DMSO- $d_6$ , 308K, 600MHz) and molarity ratios ( $\alpha$ -CD/EO) calculated by  $^1\text{H}$  NMR for PPR10K, 35K and 100K (Figures SI.III.11-13 & Table SI.III.4) **c)** Scheme of the dissociation of PPR.

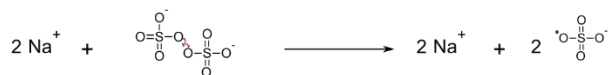
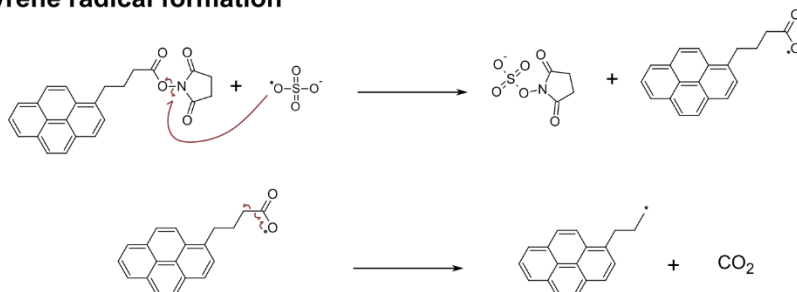
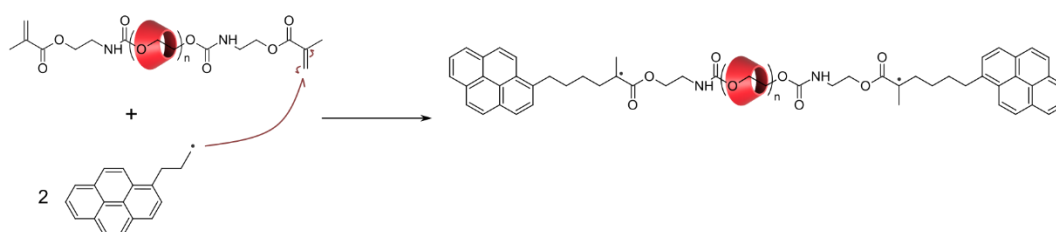
However, note that the low mass yields obtained for PPR made of PEO35K ( $30 \pm 4 \%$ ) and PEO100K ( $26 \pm 1 \%$ ) in comparison with PEO10K ( $71\%$ ), suggest that the corresponding PPRs are not fully packed. Indeed, the quantities of PEO and  $\alpha$ -CDs that were introduced should theoretically lead to a

100% mass yield. This observation is consistent with an early study showing that a threshold value for the PPR ring coverage was reached from a certain PEO molecular weight ( $> 10\,000\text{ g}\cdot\text{mol}^{-1}$ )<sup>192</sup>. But how can this finding be explained since it contradicts the NMR characterization? A possible reason could be rooted in the sluggish dissolving kinetics and the lower mobility of high molecular weight polymers that render the NMR blind towards the highest molecular weight species. Thus by NMR, we could only detect the compact PPRs resulting from the complexation of  $\alpha$ -CDs and the lowest molecular weights PEO, owing to the broadness of PEO molecular weight distributions (Figure SI.III.2 & Table SI.III.2). Note that, the obtention of non-fully compact PPRs does not represent an issue for our study, since we are targeting the synthesis of PRs with low PR ring coverage to enhance the molecular pulley mechanism.

Next, the attachment of bulky substituents at the end-chains of the threading polymer constitutes the last stage of the **PR formation** (Figure III.4 (iii)). It ensures the “molecular necklace” architecture by preventing the ring molecules from dethreading. We adopted a previously reported radical coupling reaction between the methacrylate end-chains functions of PEO and the N-hydroxysuccinimid ester group of the 1-pyrene butyric acid N-hydroxysuccinimid ester (PBS)<sup>193</sup>. The reaction was optimized under heterogeneous conditions in a mixture of water/DMSO (2/1) and sodium persulfate ( $\text{Na}_2\text{S}_2\text{O}_8$ ) is used as a free radical initiator<sup>58</sup>. The experimental conditions such as, water/DMSO ratio, addition time of  $\text{Na}_2\text{S}_2\text{O}_8$  and PBS, temperature (RT to  $80^\circ\text{C}$ ), were varied to synthesize a panel of PRs with different PR ring coverages, *ie* the percentage of the threading polymer being covered by the ring. The detailed reaction mechanism is reported in Figure III.6. The initiation step consists in the homolytic cleavage of  $\text{Na}_2\text{S}_2\text{O}_8$  in water generating two radicals that react with the succinimidic ester derivative (PBS) through an homolytic substitution followed by a decarboxylation, hence forming pyrene radicals. During the propagation step, the reaction of these radicals with the methacrylate functions of the PPR leads to the formation of the PR. The termination reaction aims in neutralising the remaining radicals.

The crude product was precipitated in diethylether and an additional purification step, involving a heating process, was conducted prior the SEC characterization. This purification method was developed during an upstream study and rely on the separation of PR and the free residuals  $\alpha$ -CDs coming from the PPR dissociation<sup>194</sup>.



**Initiation****Pyrene radical formation****Pyrene radical propagation on the methacrylate functions****Termination**

**Figure III.6: Mechanism of PBS end-capping reaction to form PR.** The proposed mechanism results in the formation of the most probable final product (steric effect). As discussed in literature<sup>193</sup>, other radicals are likely to be part of the termination step through recombination leading to different secondary products.

On top of the heterogenous conditions that prevent the spontaneous dissociation of the PPR, the main advantage of this radical coupling reaction relies on its kinetics which result in impressive yields, up to 90% reported<sup>58</sup>. Moreover, as the reaction is quasi-instantaneous, the time of addition of both PBS and  $\text{Na}_2\text{S}_2\text{O}_8$  theoretically governs the number of  $\alpha$ -CDs born by the polymer. Additionally, it is worth noticing that no undesirable secondary reaction with  $\alpha$ -CD hydroxyl group is encountered, which is a major benefit compared to the most popular synthetic pathway reported in the literature<sup>49</sup>.

The characterization of the different PRs, that will subsequently be referred as PR10K, PR35K and PR100K, is discussed in the following paragraphs. The synthesis of such high molecular weight PRs using this radical coupling chemistry had never been described before. Indeed, the conditions had

been optimized for PR made of PEO of 1 000 g.mol<sup>-1</sup><sup>58</sup>. That is why we adapted the characterization protocol combining both SEC and NMR to determine the average number of CDs threaded on the PEO chain. First, we focused on PR10K and then we extended the approach to PR35K and PR100K.

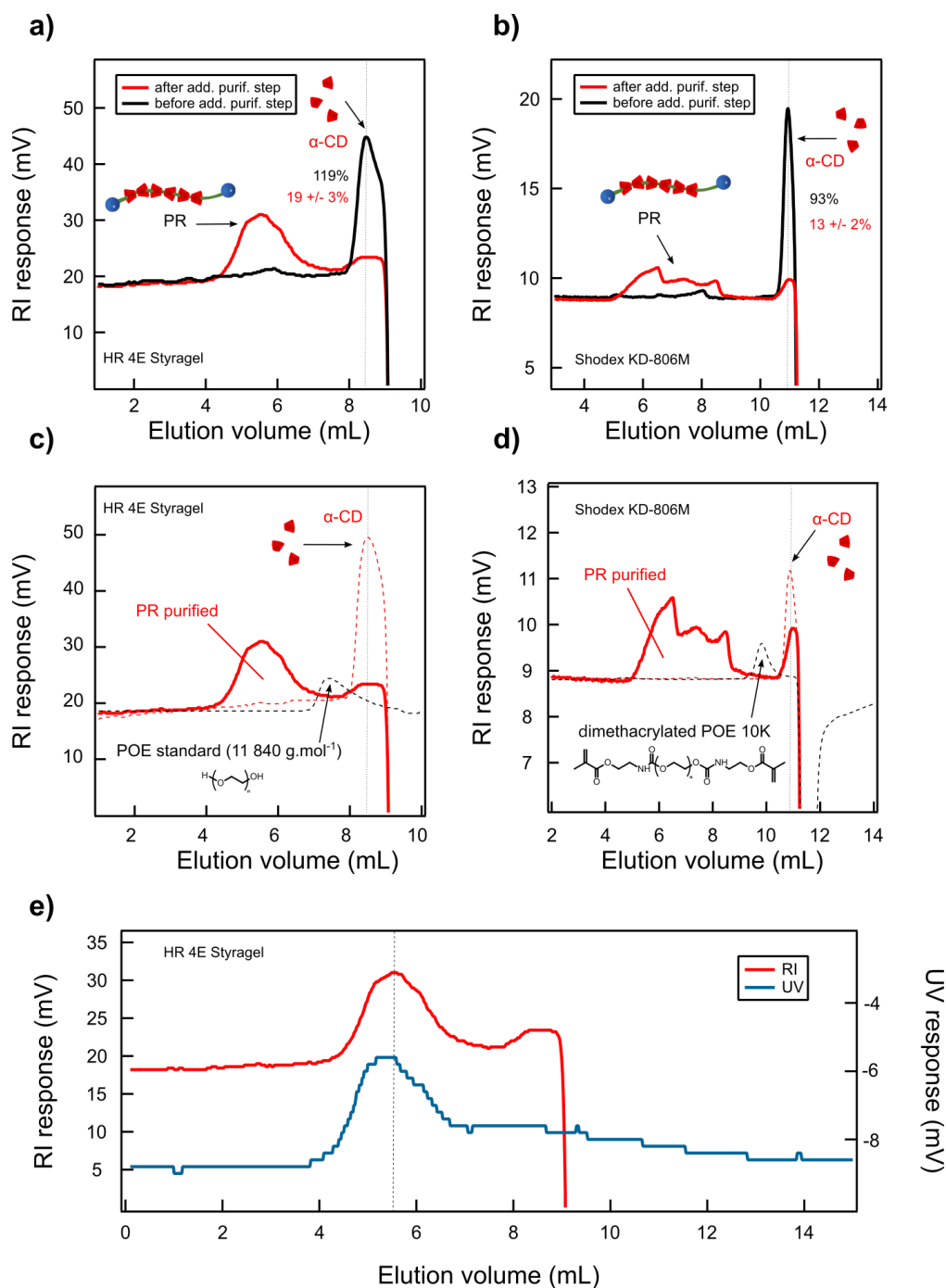
## b. Characterization of PR10K

### **Evidence of PR formation**

Prior to any SEC analysis, the calibration of the chromatography column is essential. All the calibration procedure and the sample preparation details are explained in the Materials and Methods section related to this Chapter (Supplementary Information). The calibration was carried out on the RI detection mode for the two different chromatography columns available to us (HR 4E Styragel and Shodex KD-806M) and consists in two main steps:

- the calibration of PEO monodispersed standards to determine the average molecular mass of the synthesized architecture in PEO equivalents (Table SI.III.1)
- the calibration in  $\alpha$ -CD to determine the mass fraction of free residual  $\alpha$ -CD in each PR sample (Figure SI.III.1)

For the sake of clarity, we will analyse meticulously the RI and UV chromatograms of one batch of PR10K (PR1) (Figure III.7). The same analysis was performed on the other batches (8 in total) and the results are summarized in the following section in Table III.1.



**Figure III.7: SEC characterization of a PR1 based on  $\alpha$ -CDs and PEO10K.** Overlapping of the chromatograms of PR1 before (black) and after (red) the additional purification step (0.1 mg.mL<sup>-1</sup>). These chromatograms were obtained with the **a)** HR 4E Styragel and **b)** Shodex 4D-806M columns respectively. Overlapping of the chromatograms of the purified PR1 (0.1 mg.mL<sup>-1</sup>, plain red line),  $\alpha$ -CDs (0.125 mg.mL<sup>-1</sup>, dashed red line) and standard PEO of 11 840 g.mol<sup>-1</sup> ( $\bar{M}_n = 1.04$ , 3 mg.mL<sup>-1</sup>, dashed black line) or PEO10K with methacrylate end-chains functions ( $\bar{M}_n = 1.48 \pm 0.11$ , 3 mg.mL<sup>-1</sup>, dashed black line) for the **c)** HR 4E Styragel and **d)** Shodex 4D-806M columns respectively. Only the elution volume matters, no attention is to be paid to the intensity's signals. SEC is carried out with different species natures prepared at different concentrations. Moreover, the recorded signal is a refractive index difference between the analysed sample and the eluent. **e)** Overlapping of the chromatograms of the purified PR1 obtained with the RI (red) and the UV (blue) detectors using the HR 4E Styragel chromatography column.

The RI detection provides us with a chromatogram showing two populations with a small and a larger elution volumes (5.8 & 8.55 mL for HR 4E Styragel, Figure III.7.a and 7.4 & 11 mL for Shodex KD-806M, Figure III.7.b), that are associated to high and low molecular masses ( $1.3 \cdot 10^6$  &  $1.5 \cdot 10^3$  g.mol<sup>-1</sup> for HR 4E Styragel and  $31 \cdot 10^3$  &  $1.4 \cdot 10^3$  g.mol<sup>-1</sup> for Shodex KD-806M in PEO equivalents). They are respectively attributed to the PR and the residual free  $\alpha$ -CDs. The efficiency of the additional purification step is demonstrated since the signal of the residual free  $\alpha$ -CDs drastically declines whereas the one of the PR is clearly increased (Figure III.7.a & b).

We calculated the mass fraction of free  $\alpha$ -CDs using our calibration curves (Figure SI.III.1). Furthermore, for the purified PRs, we also can estimate this mass ratio as the ratio of the peaks area, assuming that refractive indexes of free  $\alpha$ -CDs and PRs are close. Errors bars are then calculated as standard deviations. This second quantification could not be performed before the additional purification step because the PR signal is hardly distinguishable in the background noise. As expected, this quantification seems not to be column-dependent. Thereafter, we decided to estimate this free  $\alpha$ -CDs residual mass fraction using the Shodex KD-806M column since we suspected an overestimation (119% compared to 93%) of this mass fraction when calculated from the HR 4E Styragel column probably due to desorption of adsorbed  $\alpha$ -CDs.

The attribution of the two different populations of the purified PR1 RI chromatogram is supported by the overlapping of PEO10K and  $\alpha$ -CDs chromatograms (Figure III.7.c & d). As anticipated, PR1 displays a lower elution volume than PEO10K, which agrees with the fact that  $\alpha$ -CDs are born on the polymer chain, leading to a higher molecular weight. Nevertheless, no clear quantification of the average mass can be envisaged since PR and PEO, that are used as calibration standards, do not have neither the same composition, nor the same hydrodynamic volume and so behaviour in a DMF solution.

Unsurprisingly, the HR 4E Styragel and Shodex KD-806M columns do not give the same RI profile for an identical sample in terms of elution volumes, due to their stationary phase composition monitoring their steric separation power. Moreover, shapes signals are also different, as suggested by the more gaussian shape of the high molecular weight population obtained with the HR 4E Styragel column (Figure III.7.c, plain red). The RI chromatogram recorded with the Shodex KD-806M column shows a high molecular weight population that could be deconvoluted into 3 populations

(Figure III.7.d, plain red). Therefore, these 3 populations can be attributed either to the different PR populations resulting from the polydispersity of the PEO (Figure SI.III.2) that implies different numbers of threaded  $\alpha$ -CDs or to the different conformations adopted by PRs. For sure, these conformations depend on the number of threaded  $\alpha$ -CDs. They might also be induced by the tendency of these ring molecules to form some separated compact micro-domains to be opposed to some random coil parts that would be closer to the bare PEO behaviour. Thus, with PRs containing the same number of threaded  $\alpha$ -CDs, we can be in presence of different hydrodynamic sizes when dissolved in DMF and so different elution volumes measured by SEC. Further research would be needed to precisely ascribe these three different populations of PRs.

The UV detection brings additional information to the characterization of PRs (Figure III.7.e). The UV chromatograms were recorded at the pyrene maximal absorption wavelength ( $\lambda = 345$  nm). The low elution volume population signal undoubtedly exhibits the grafting of pyrene functions providing the PR formation. The absence of any high elution volume population is consistent with the fact that all the excess of pyrene was removed by purification. Note that a slight shift of the elution volume of the high molecular mass population between the RI and the UV signals can be distinguished. This is assigned to the fact that the RI and the UV detectors are placed in series.

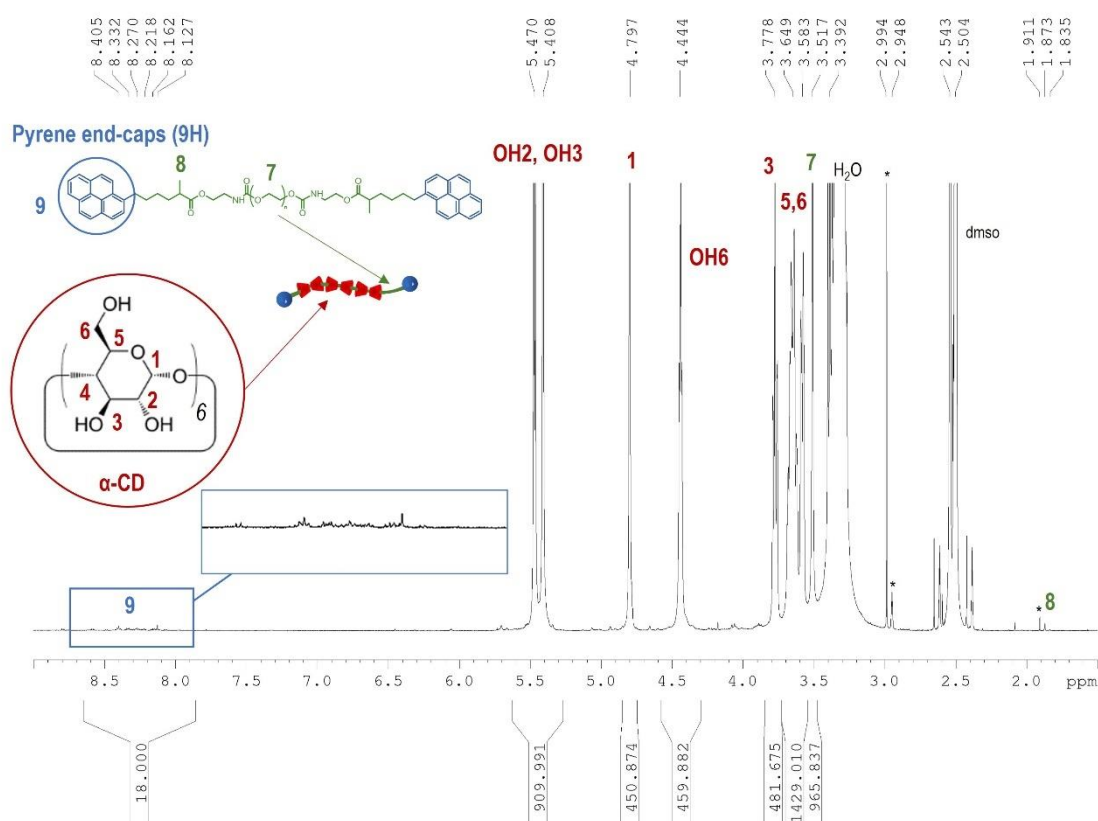
In the following of the report, the quantification of the residual  $\alpha$ -CDs mass fractions is performed with the Shodex KD-806M calibration curves (Table III.2) because as mentioned above, we suspect an overestimation due to desorption when using the HR 4E Styragel column. However, we decided to plot the RI chromatograms obtained with the HR 4E Styragel column measurements leaving aside the conformations issues (Figures III.7 & 8).

MALDI-TOF mass spectrometry (MS) was also used as a characterization method to confirm the PR synthesis route (data not shown). Unfortunately, as already disclosed, the MALDI-TOF spectra analysis cannot be interpreted as a direct quantitative analysis<sup>75</sup>. Indeed, low molecular masses polymers desorb better than higher ones resulting in the analysis of lower molecular masses PRs consisting of few  $\alpha$ -CDs and low molecular masses of the PEO. Because of this reason, we did not dwell on this characterization method further.

### Determination of the PR ring coverage

The methodology that we adopted to evaluate the average number of ring molecules born by the PR relies on the combination of both  $^1\text{H}$  NMR spectroscopy and SEC measurements. For the purpose of clear illustration, we focus on PR3 with 62 % and  $14 \pm 3$  % of residual free  $\alpha$ -CDs before and after the purification step respectively. The analysis of the other PR10K was done similarly leading to the same systematic quantifications (Table III.1).

The  $^1\text{H}$  NMR spectrum of PR3 was recorded before the additional purification step. All the peaks' attributions are reported on the spectrum (Figure III.8). The integration ratio between protons of the pyrene end-capping functions (18) and the  $\alpha$ -CD anomeric protons (451) leads to an estimated number of  $\alpha$ -CDs per PR unit. Taking into account the mass fraction of residual free  $\alpha$ -CDs quantified by SEC (62%<sub>wt</sub>), we can estimate to 38%<sub>wt</sub> the proportion of  $\alpha$ -CDs that are threaded which means that PR3 consists in an average of 29 threaded  $\alpha$ -CDs ( $0.38 \times 451/6$ ).

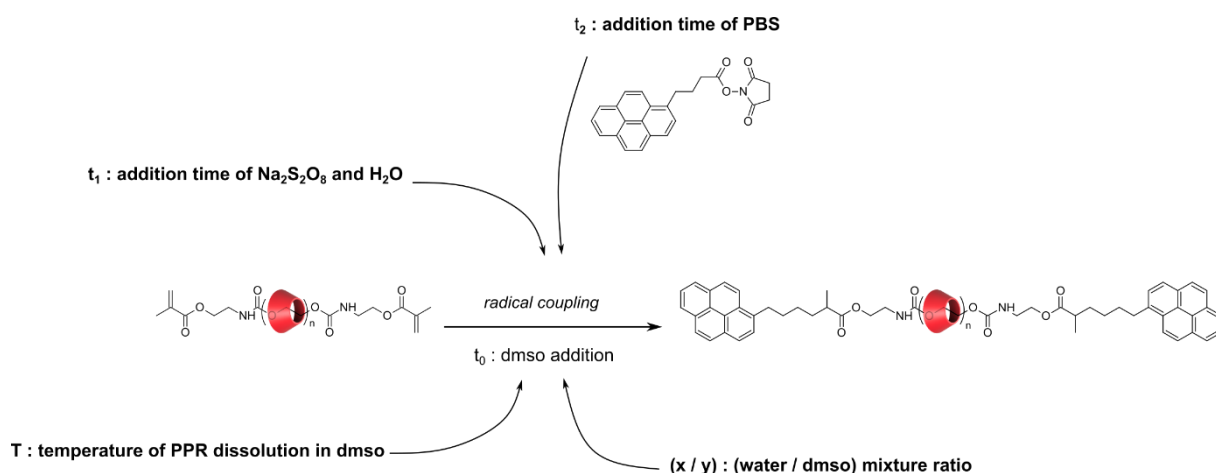


**Figure III.8:**  $^1\text{H}$  NMR spectrum in  $\text{DMSO-d}_6$  of PR3 (PR10K, 128 scans, 308K) before the additional purification step. Traces of impurities and solvents are marked with an asterisk (\*).

Note that the  $^1\text{H}$  NMR spectra used for quantification were recorded before the additional purification step. Indeed, as shown in Figure SI.III.14, the removal of the residual  $\alpha$ -CDs renders the signal fine attribution very complex. Indeed, the protons of the threaded  $\alpha$ -CDs are in different chemical environments leading to some bunch of peaks corresponding to each type of  $\alpha$ -CDs protons. We did not focus on the fine attribution of such signals since the previously described protocol was giving us the desired information.

### A large panel of PR10K

As mentioned before, different experimental conditions were explored for the PR formation, with the objective to vary the PR ring coverage. Four parameters were investigated : (i) the water/DMSO mixture ratio, (ii) the temperature of PPR dissolution in DMSO, (iii) the addition time of  $\text{H}_2\text{O}$  and  $\text{Na}_2\text{S}_2\text{O}_8$  and (iv) the addition time of PBS (Figure III.9). The stoichiometric proportions of PPR, PBS and  $\text{Na}_2\text{S}_2\text{O}_8$  and the PPR concentration remained constant as detailed in the Methods section (Supplementary Information). The experimental conditions and the resulting PR10K ring coverages are reported in Table III.1 (Figures SI.III.15-22).



**Figure III.9: Investigation of the role of the different experimental parameters during the PR formation**

PR10K	Run	(x / y)	T (°C)	t <sub>1</sub> (h)	t <sub>2</sub> (h)	Reaction time (h)	PR rings coverage (%)
PR1	1	(2 / 1)	RT	0	0	3	~ 60*
PR2	2	(2 / 1)	80	4	0	3	19
PR3	3	(2 / 1)	80	1	0	3	25
PR4	4	(2 / 1)	80	4	4	24	36
PR5	5	(2 / 1)	80	72	72	72	48
PR6	6	(2 / 1)	RT	0	0	3	48 < x < 51*
PR7	7	(1 / 2)	80	9,5	9,5	3	51
PR8	8	(1 / 2)	80	7	7	72	> 51*

**Table III.1: Overview of the experimental conditions of formation of PR10K.** DMSO was systematically added at  $t_0$  and after the addition of water the temperature was set to RT. When the signal to noise ratio was not good enough to clearly distinguish the protons signals of the pyrene extremities by  $^1\text{H}$  NMR and so to calculate exactly the number of threaded  $\alpha$ -CDs. The asterisk stands for the estimation of the PR rings coverage that was performed instead thanks to our calibration curve (Figure III.10.b).

The different experimental conditions successfully led to the obtention of PR10K with a wide panel of PR ring coverage, varying from 19% to 60%. Interestingly no highly compact PR was obtained, even using the “optimized” conditions reported in literature with the addition of all the reactants at the same time<sup>61</sup>. We could only get from 50% to 60% rings coverage (runs 1 & 6 Table III.1). The explanation may be rooted in the PEO molecular weight since the protocol was reported for a polymer of  $1\,000\text{ g}\cdot\text{mol}^{-1}$ . Switching from  $1\,000$  to  $10\,000\text{ g}\cdot\text{mol}^{-1}$  induces less mobility for the polymer chain and consequently less reactivity for the end-chain groups, leading to a more important  $\alpha$ -CDs dethreading phenomenon.

Then, from these conditions, we adapted the protocol to get some lower PR ring coverages. PPR were firstly dissolved in DMSO in presence of PBS and the mixture was stirred at  $80^\circ\text{C}$  for several hours. Water and  $\text{Na}_2\text{S}_2\text{O}_8$  were added afterwards (runs 2 & 3, Table III.1). Consequently, we obtained lower PR ring coverages, 19% and 25% for 4h and 1h of dissolution step respectively. Alternatively, PBS was added after the dissolution step at the same time as water and  $\text{Na}_2\text{S}_2\text{O}_8$  (runs 4 & 5, Table III.1) and we got PR ring coverages of 48% and 36% after a dissolution step of 72h and 4h respectively. Thus, not surprisingly, the temperature favours the dissociation of supramolecular interactions, here enhancing the  $\alpha$ -CDs dethreading phenomenon. Such finding was already reported in an early work<sup>195</sup>. These results also highlight the role of the duration of the PPR



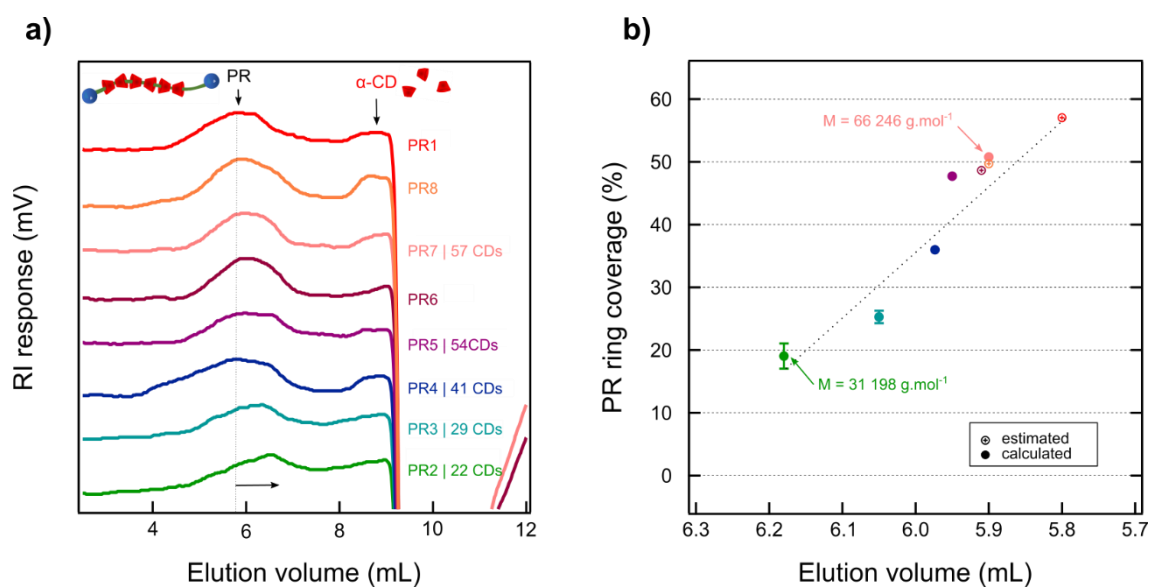
dissolution step, even if run 5 does not comply with this finding probably due to a failure in the temperature control. Finally, the lower PR ring coverages obtained for runs 2 & 3 might come from the formation of inclusion complexes between PBS and  $\alpha$ -CDs originating from the dissociation of PPR, thus decreasing the reactivity of PBS during the radical coupling reaction<sup>196</sup>.

Eventually, we enriched the medium with DMSO by switching to a water/DMSO mixture ratio of (1/2) (runs 7 & 8, Table III.1) and notably we obtained some high PR ring coverages up to 51%. We should mention that this finding was not consistent with the work that motivated our approach according to which such proportions would exacerbate the  $\alpha$ -CDs dethreading phenomenon<sup>58</sup>. Nevertheless, this work had dealt with the formation of PR from a lower molecular PEO weight (1 000 g.mol<sup>-1</sup>), inducing a faster dissociation rate of the resulting PPR than what we observed for PPR10K.

To conclude, we succeeded in achieving the synthesis of PR10K with different PR ring coverages thanks to our knowledge of PR chemistry. Table III.2 provides the characterization details for the different PR10K and Figure III.10 gathers the RI chromatograms of the different PR10K recorded after the additional purification step.

PR 10K sample	%wt of residual free $\alpha$ -CD		PR peak elution volume (mL)	Nb of threaded $\alpha$ -CD per PR	Filling ratio of PR (%)
	BEFORE add. purif. step	AFTER add. purif. step			
PR1	93 %	13 $\pm$ 2 %	5.8		~ 60
PR2	62 %	14 $\pm$ 5 %	6.18	22	19
PR3	62 %	14 $\pm$ 3 %	6.05	29	25
PR4	101 %	19 $\pm$ 4 %	5.97	41	36
PR5	80 %	11 $\pm$ 1 %	5.95	54	48
PR6	73 %	9 $\pm$ 0 %	5.91		48 < x < 51
PR7	80 %	15 $\pm$ 0 %	5.90	57	51
PR8	89 %	16 $\pm$ 6 %	5.90		> 51

**Table III.2: Characterization of the different PR10K.** PR ring coverages and mass fractions of free residual  $\alpha$ -CDs were calculated as detailed previously (Shodex KD-806M, Figure SI.III.23). The PR peak elution volume was estimated as the maximum of the almost gaussian peak (HR 4E Styragel, Figure III.10). The shaded boxes correspond to an estimation and not a real calculation.



**Figure III.10: Determination of the PR10K ring coverages.** **a)** Overlapping of the RI chromatograms of the different PR10K (HR 4E Styragel column). The evolution of the elution volumes is unscored by the vertical dashed line. **b)** Representation of the PR ring coverage as a function of the elution volume of the PR10K. The corresponding molecular masses of the extreme PR are reported. The dashed line serves as an eye guideline.

First, Table III.2 highlights the efficiency of the additional purification step involving the heat treatment process with a decrease by a factor of around 5 of the  $\alpha$ -CDs mass fraction. This step is crucial for the detection of the PR peak.

Interestingly, a nice correlation was drawn between the PR peak elution volume and the PR ring coverage: the higher the  $\alpha$ -CDs density is, the lower the elution volume of the PR population is (Figure III.10). From an analytical point of view, our quantification of the number of  $\alpha$ -CDs born by the polymer chain turns out to perfectly suit with the SEC partitioning principle. Indeed, the largest molecules elute first followed by components of progressively smaller sizes. Moreover, a linear trend that was not anticipated emerges from the plot representing the PR ring coverage as a function of the elution volume. This trend suggests that the combination of the HR 4E Styragel column, its thermostated temperature ( $60^{\circ}\text{C}$ ) and the eluent (DMF) is appropriate to separate PR10K with different PR ring coverages, *ie* different molecular masses that we approximated from  $\sim 30\,000$  to  $\sim 70\,000\text{ g.mol}^{-1}$  (Figure III.10.b). Thus, we consider the column to be in the linear separation range and we could envisage this curve as a molecular mass distribution calibration curve for such PRs. This represents a new result, namely enabling SEC quantification for such topological macromolecular architectures which differ from conventional polymers.

Additionally, this trend allowed us to provide an estimation of the PR ring coverage for PR1, PR6 and PR8 (Table III.2, shaded boxes). Indeed, the signal to noise ratio on their  $^1\text{H}$  NMR spectra was not good enough to clearly distinguish the protons signals of the pyrene end-capping functions and thus to calculate the average number of  $\alpha$ -CDs born per PR (Figures SI.III.16, SI.III.20, SI.III.22). Interestingly, this concerns the most fully packed PRs and this is not surprising. Because of the high affinity between pyrene and the  $\alpha$ -CD cavity, the probability of the pyrene end-capping function to be inside an  $\alpha$ -CD cavity is increased<sup>196</sup>. This results in the restriction of mobility of the pyrene protons and so a lower intensity for their signals.

### c. Characterization of PR35K and PR100K

On the basis of the above results, we carried out the same crossed-characterization methodology for PR35K and PR100K. As well as for PR10K, we explored different experimental conditions with the aim to tune the PR ring coverage (Figure III.9). These experimental conditions are summarized in Table III.3. The conditions that led to the highest rings coverages for PR10K (runs 1 & 6, Table III.1) were reproduced for PR9 and PR10 (runs 9 & 10, Table III.3). A dissolution step for the PPR in DMSO at 80°C during 4h was also conducted for PR100K (run 11, Table III.3). Table III.4 gathers the characterization details of PR35K and PR100K and Figure III.11 displays their RI chromatograms.

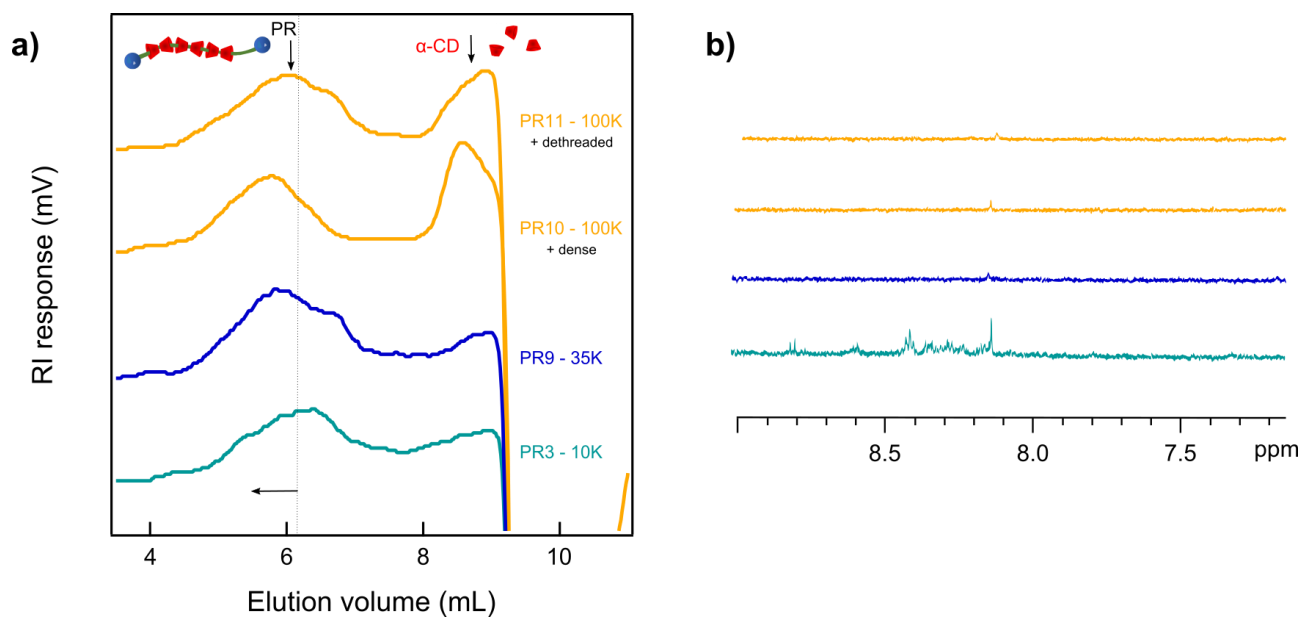
Sample	Run	PEO molecular weight (g.mol <sup>-1</sup> )	T (°C)	t <sub>1</sub> (h)	t <sub>2</sub> (h)	Reaction time (h)
PR9	9	35 000	RT	0	0	16
PR10	10	100 000	RT	0	0	16
PR11	11	100 000	80	0	4	12

**Table III.3: Overview of the experimental conditions of PR35K and PR100K.** The ratio of the water/DMSO mixture were kept constant to (2/1). DMSO was systematically added at t<sub>0</sub> and after the addition of water the temperature was set to RT. The PPR concentration was of 45 and 100 mg.mL<sup>-1</sup> for PPR35K and PPR100K respectively and the stoichiometric proportions of PPR, PBS and Na<sub>2</sub>S<sub>2</sub>O<sub>8</sub> also remained constant.

Sample	PEO molecular weight (g.mol <sup>-1</sup> )	% <sub>wt</sub> of residual free α-CD		PR peak elution volume (mL)
		BEFORE add. purif. step	AFTER add. purif. step	
PR9	35 000	87 %	16 ± 0 %	5.92
PR10	100 000	85 %	49 ± 6 %	5.78
PR11	100 000	76 %	32 ± 3 %	6.03

**Table III.4: Characterization of the different PR35K and PR100K.** Mass fractions of free residual α-CDs were calculated from the RI chromatograms as detailed previously (Shodex KD-806M, Figure SI.III.27). The PR peak elution volume was estimated as the maximum of the almost gaussian peak (HR 4E Styragel, Figure III.11).

First, we witness a poorer efficiency of the additional purification step, although the same conditions used for PR10K were adopted (200°C during 15 min). This is particularly marked for PR100K which shows three times more residuals free α-CDs than PR10K (Table III.4). Therefore, an optimization of the conditions could be envisioned later, such as modifying the temperature and/or the time.



**Figure III.11: Characterization of PR35K and PR100K.** **a)** The RI chromatograms of two PR10K (PR1 & PR3) were added to PR35 and PR100K chromatograms for comparison (HR 4E Styragel column). The evolution of the elution volumes is unscored by the vertical dashed line. **b)** Overlapped <sup>1</sup>H NMR spectra of the different PRs in DMSO (16 scans, 308K). A zoom was made on the pyrene chemical shift area.

Further analysing the RI chromatograms of PR100K, PR10 shows a lower elution volume than PR11 (5.78 vs 6.03 mL) (Figure III.11.a). The observed signals shift corroborates with the logic observed for PR10K, the 4h of dissolution process inducing more dethreading, hence a lower PR ring coverage. Unfortunately, this assumption cannot be confirmed easily since we failed in implementing our crossed-characterization protocol to precisely calculate the PR ring coverages. Indeed, we can hardly distinguish pyrene signals on the different  $^1\text{H}$  NMR spectra (Figure III.11.b). Despite our trials to use a higher magnetic field spectrometer (800 MHz) or to increase the number of scans (128 scans), no real improvement in the signal to noise ratio was observed. The full  $^1\text{H}$  NMR spectra of these three higher molecular weight PRs can be found in Supplementary Information (Figures SI.III.24-26).

In conclusion, we successfully manage to provide a detailed characterization of the synthesized PR10K, especially in terms of PR ring coverage. Nevertheless, quite a tough challenge has been pointed out for the highest molecular weight PRs. By extending our findings on PR10K, we assume that the shift in terms of elution volume can still be assign to a PR ring coverage change meaning that PR10 is more packed than PR11. This assumption is of importance since we are expecting more sliding motion of  $\alpha$ -CDs on PR11 than on PR10. When it comes to comparing PRs obtained from different molecular weight PEO, we cannot transpose the PR ring coverage from the PR10K study. Indeed, PPR 35K and PPR100K differ from PPR10K because they are less fully packed with  $\alpha$ -CDs. Additionally, the dethreading rate is likely to be slower increasing the PEO molecular weight. Thus, the only assumption we can make is that increasing the PEO molecular weight implies more sliding motion of the ring molecules.

These hypotheses are investigated in the following section dealing with the properties of PR-PAA slide-rings networks in which PAA is cross-linked with the  $\alpha$ -CDs based PRs.

### 3. PR-PAA network synthesis

In this part, PRs were covalently integrated to PAA in order to form a three-dimensional PR-PAA network. The influence of the PR structural parameters exposed above (PEO molecular weight and PR ring coverages), the proportion of PR cross-linkers compared to PAA and the cross-linking density was evaluated using Differential Scanning Calorimetry (DSC) and mechanical testing to provide information about the PR-PAA mechanical properties such as deformability and elasticity.

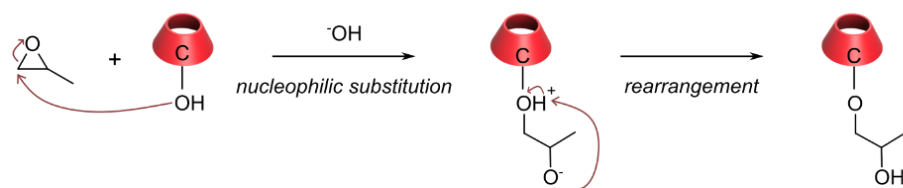
#### a. PR-PAA synthesis pathway

The PR-PAA synthesis route was adapted from Choi's early work<sup>101</sup>. It consists in the two following stages: the hydroxypropylation of the  $\alpha$ -CDs born by the polymer chain (Figure III.4 (iv)) and the condensation of PAA carboxylic acid groups with the hydroxyl groups of  $\alpha$ -CDs hydroxypropylated moieties through an esterification (Figure III.4 (v)). First, to confirm the synthesis pathway, we synthesized  $\alpha$ -CD-PAA networks. The mechanism description is reported in Figure III.12.

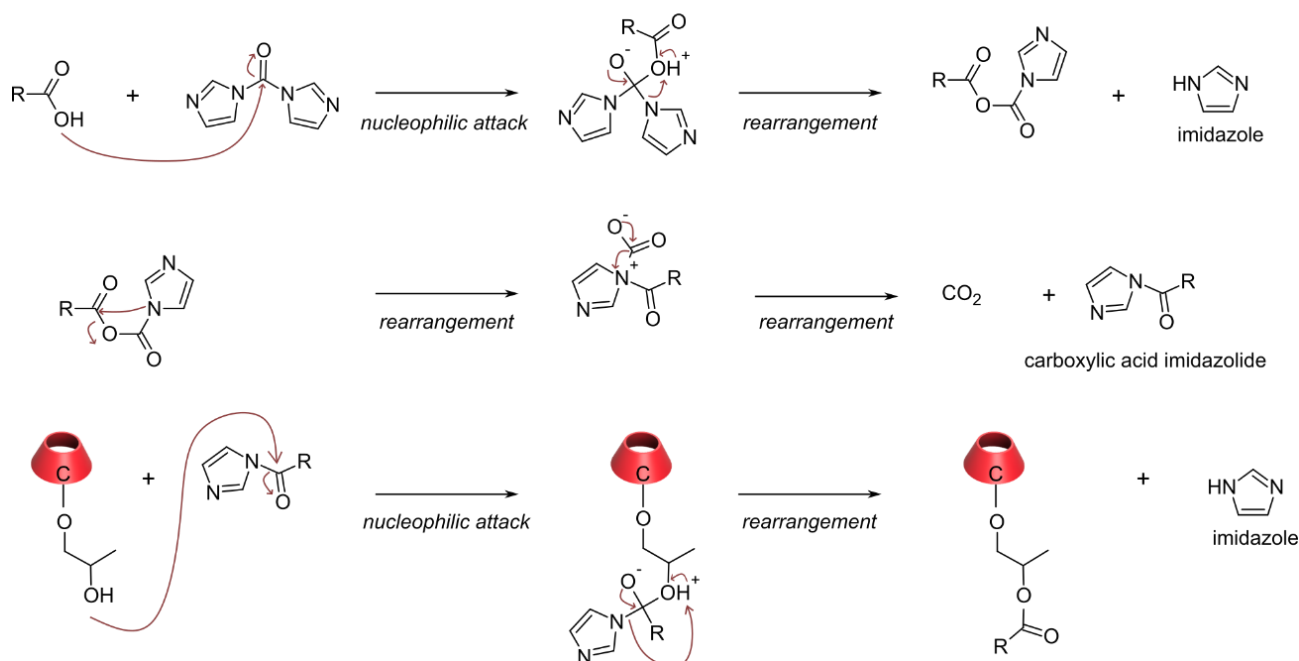
The protocol involves the nucleophilic substitution of  $\alpha$ -CD hydroxyl groups at the unsubstituted carbon of propylene oxide in 1M NaOH aqueous medium at low temperature (0°C)<sup>197,198</sup>. The purification consists in the precipitation of the crude product in DMSO followed by a freeze-drying step (-80°C; 12  $\mu$ bar). The hydroxypropylated  $\alpha$ -CD (Hydroxy- $\alpha$ -CD) was characterized by <sup>1</sup>H NMR and we showed that approximately 53% the hydroxyl groups are substituted by 2-hydroxypropyl groups (Figure SI.III.28 & A.III.29).

The esterification synthesis route is based on a N,N'-carbonyl diimidazole (CDI) mediated method developed for cellulose<sup>199</sup>. CDI was first dissolved in anhydrous DMSO and mixed with PAA for 24h at 50°C. An argon gas flow was used to remove evolved CO<sub>2</sub>. Indeed, during the carboxylic acid imidazolide formation, CO<sub>2</sub> is part of the only two by-products with imidazole, the latter being removed by several precipitations in THF afterwards. Once the carboxylic acids are efficiently activated, the hydroxypropylated  $\alpha$ -CDs are added to the mixture and the reaction proceed for 72h additional hours at 70°C to get the desired esters. The purification consists in two precipitations in THF and a final freeze-drying step (-80°C; 12  $\mu$ bar).

### Hydroxypropylation



### CDI-mediated esterification



**Figure III.12:** Scheme of the proposed mechanism of CDI-promoted esterification of carboxylic acids with  $\alpha$ -CDs.

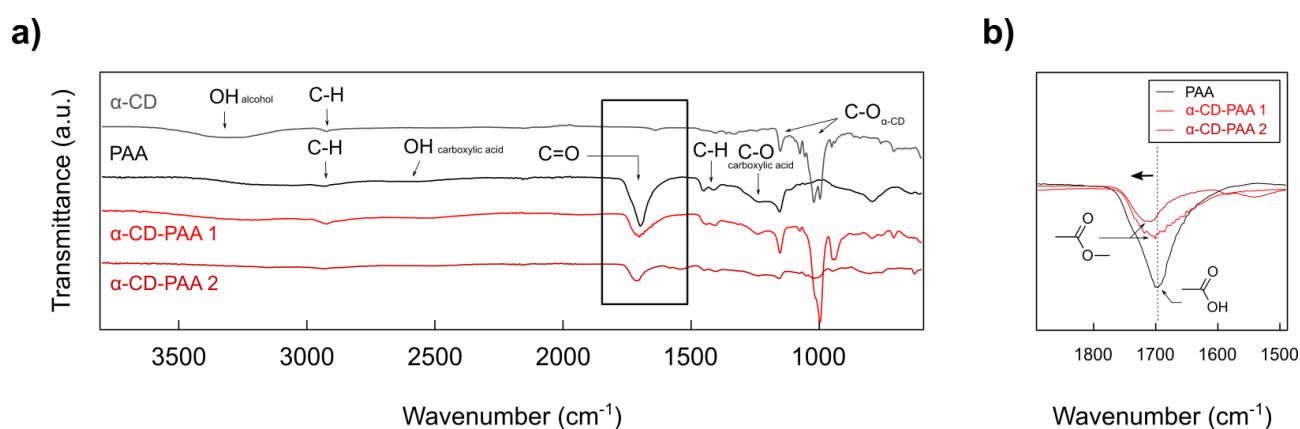
This CDI-promoted esterification presents the advantages of mild reaction conditions, limited number of by-products and pretty high yields (80%)<sup>199</sup>. Note that any trace of water must be avoided because of its high reactivity with CDI, as displayed in the  $^1\text{H}$  NMR spectrum of CDI in  $\text{DMSO-d}_6$  which is already partially hydrolysed (28%) (Figure SI.III.30).

$\alpha$ -CD-PAA sample	Cross-linking density (%)	$\alpha$ -CD/PAA mass ratio (%wt)	Network illustration
$\alpha$ -CD-PAA 1	0.4	6	
$\alpha$ -CD-PAA 2	8.1	69	

**Table III.5:** Experimental conditions of  $\alpha$ -CD-PAA networks preparation. The cross-linking corresponds to the proportion of CDI-activated COOH units. The illustration is purely explicative.

Table III.5 provides the reaction conditions used for the synthesis of  $\alpha$ -CD-PAA networks. The cross-linking density is directly correlated to the mass of CDI introduced.  $\alpha$ -CD-PAA networks were characterized by means of FTIR spectroscopy (Figure III.13). The characteristic peaks of  $\alpha$ -CD can be observed: C-O stretching at 910 & 1030  $\text{cm}^{-1}$ , C-H/C-H<sub>2</sub> vibration at 2900  $\text{cm}^{-1}$  and O-H stretching vibration 3500  $\text{cm}^{-1}$ . Concerning the carboxylic acid groups of PAA, the enlargement of the band at 1700  $\text{cm}^{-1}$  and the appearance of an ester stretching band at around 1730  $\text{cm}^{-1}$  clearly indicates the successful cross-linking of the carboxylic acid units of PAA with the hydroxyl moieties of  $\alpha$ -CD. As expected, this shifting phenomenon is magnified for  $\alpha$ -CD-PAA 2 that corresponds to a larger amount of activated carboxylic acids leading to more ester bond formation. It is worth noticing that the set temperature of 70°C cannot lead to the formation of anhydride functions even if the IR band shift would be similar. Indeed, a much higher temperature is needed ( $\sim 150^\circ\text{C}$ )<sup>200</sup>.

An attempt to characterize such  $\alpha$ -CD-PAA networks by NMR spectroscopy was also made to support the ester bond formation (<sup>1</sup>H NMR, <sup>13</sup>C NMR and HMBC, Figure SI.III.31). Although some shifts clearly exhibit a reaction occurring, this was not fully conclusive.



**Figure III.13: Validation of the esterification synthesis route: ATR-FTIR characterization of the two different  $\alpha$ -CD-PAA networks.** a) Overlapped ATR-FTIR spectra of PAA,  $\alpha$ -CD-PAA 1 and  $\alpha$ -CD-PAA 2 b) Zoom-in of the carbonyl groups stretching bands showing the formation of the ester bonds. The vertical dashed line underscores the band shift resulting from the appearance of this new band of higher wavenumber.



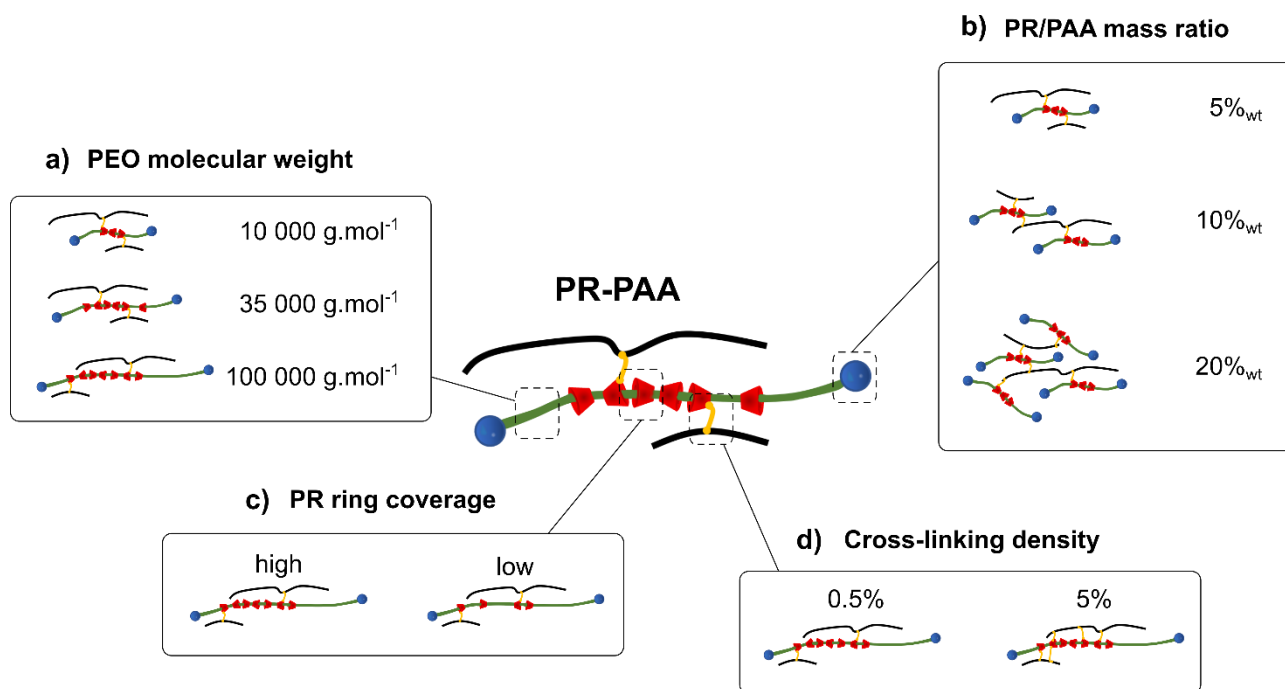
The previously synthesized PRs were then used to prepare different types of PR-PAA networks (PR3, PR6, PR9, PR10 & PR11, Tables III.1 & III.3). First, the hydroxypropylation reaction was carried out and the conversion of  $\alpha$ -CD hydroxyl groups into 2-hydroxypropyl groups was quantified by  $^1\text{H}$  NMR. The results are reported in Table III.6 and the  $^1\text{H}$  NMR spectra can be found in the Supporting Information (Figures SI.III.32-36).

Hydroxypropylated sample	Starting PEO molecular weight ( $\text{g}\cdot\text{mol}^{-1}$ )	Residual free $\alpha$ -CDs in PR sample (% <sub>wt</sub> )	Hydroxypropylation proportion (%)
Hydroxy- $\alpha$ -CD	/	100	53
Hydroxy-PR3	10 000	62	34
Hydroxy-PR6	10 000	76	$47 \pm 4$
Hydroxy-PR9	35 000	87	36
Hydroxy-PR10	100 000	85	44
Hydroxy-PR11	100 000	76	58

**Table III.6: PR hydroxypropylation characterization.** The hydroxypropylation proportion corresponds to the yield of conversion of the  $\alpha$ -CD hydroxyl groups into 2-hydroxypropyl groups. It was evaluated by  $^1\text{H}$  NMR (Figures SI.III.32-36). The residual free  $\alpha$ -CD proportion was calculated by SEC (Tables III.1 & III.4).

As expected, the hydroxypropylation yield is 10% lower for PRs than for  $\alpha$ -CD itself. This is consistent with the mobility restriction originating from the interlocked architecture of PR that implies less reactivity for threaded  $\alpha$ -CD than for free  $\alpha$ -CD.


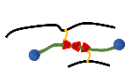
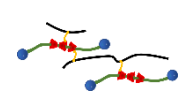
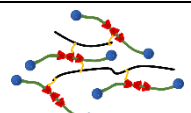
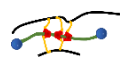
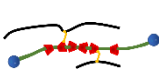

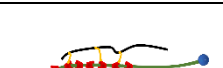

The following step concerns the cross-linking reaction between PR and PAA. Different parameters were investigated to impart enhanced mechanical properties to the different PR-PAA networks synthesized. Besides to the PR structural parameters already evoked in the previous section, *ie* PEO molecular weight (**x**) and PR ring coverage (**rc**), we examined the PR/PAA mass ratio (**y**) and the cross-linking density (**z**), which corresponds to the proportion of CDI-activated COOH units per PAA. To make the discussion clearer, some illustrations of the expected PR-PAA architectures are provided in Figure III.14. Similarly to  $\alpha$ -CD-PAA networks, FTIR spectra support the ester bond formation for PR-PAA networks. They are included in Supplementary Information for sake of clarity (Figure SI.III.37).



**Figure III.14: Illustration of the four different parameters investigated in the PR-PAA networks synthesis. a)** Influence of the PEO molecular weight ( $x$ ) and **b)** PR/PAA mass ratio ( $y$ ), keeping the crosslinking density ( $z$ ) constant. **c)** Influence of the PR ring coverage ( $rc$ ). **d)** Influence of the cross-linking density ( $z$ ).

The reaction conditions of PR-PAA networks formation are summarized in Table III.7. We took for reference the conditions published in Choi's work<sup>101</sup>, that is to say activating 0.5% of the COOH units of PAA (ie 33/6250 COOH) and doping PAA with 5%<sub>wt</sub> of PR. PR was prepared from PEO20K and its ring coverage was evaluated to 29%. Subsequently, the nine types of PR-PAA networks are identified using the following notation: PR $\mathbf{X}$ -PAA  $\mathbf{y}$  % ( $\mathbf{z}$  %) with  $\mathbf{X}$  corresponding to the label of the PR sample implying the PEO molecular weight ( $\mathbf{x}$ ) and the PR ring coverage ( $\mathbf{rc}$ ).  $\mathbf{y}$  and  $\mathbf{z}$  stand as the PR/PAA mass ratio and the crosslinking density respectively. For reason of conciseness, we numbered PR-PAA specimens (Table III.7).

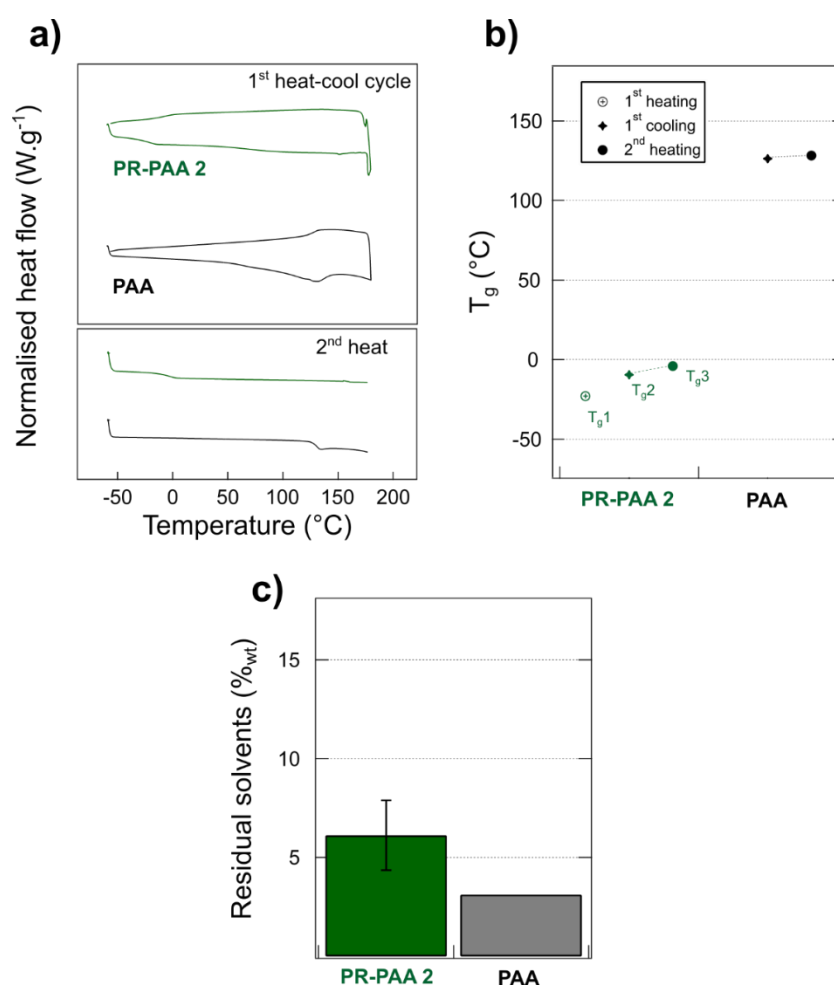
To highlight the value of such PR-PAA architectures as being efficient Si binders, we first evaluated their thermal properties by DSC. Then we set up a collaboration with SIMM lab at ESPCI to perform some mechanical strength tests to investigate their mechanical properties such as stiffness (Young's modulus) or tensile strength/strain (maximum stress/strain at rupture). The ultimate goal is to draw a structure-properties correlation and exhibit the best PR-PAA network configuration that best meets the standards of being a good Si binder.

PR-PAA sample	PEO molecular weight (x) (g.mol <sup>-1</sup> )	PR ring coverage (rc) (%)	Cross-linking density (z) (%)	Mass ratio PR/PAA (y) (%wt)	Network illustration
<b>PR-PAA 1</b> PR3-PAA 5 % (0.5 %)	10 000	25	0.5	5	
<b>PR-PAA 2</b> PR6-PAA 5 % (0.5 %)	10 000	50	0.5	5	
<b>PR-PAA 3</b> PR6-PAA 10 % (0.5 %)	10 000	50	0.5	10	
<b>PR-PAA 4</b> PR6-PAA 20 % (0.5 %)	10 000	50	0.5	20	
<b>PR-PAA 5</b> PR6-PAA 5 % (5 %)	10 000	50	5	5	
<b>PR-PAA 6</b> PR9-PAA 5 % (0.5 %)	35 000	high*	0.5	5	
<b>PR-PAA 7</b> PR10-PAA 5 % (0.5 %)	100 000	high*	0.5	5	
<b>PR-PAA 8</b> PR10-PAA 5 % (5 %)	100 000	high*	5	5	
<b>PR-PAA 9</b> PR11-PAA 5 % (0.5 %)	100 000	low*	0.5	5	

**Table III.7: Experimental conditions of PR-PAA synthesis.** The illustrations are purely explicative. The asterisk (\*) refer to the PR ring coverages that we could not precisely determined. An indication of their estimate value is reported (high or low).

## b. Thermal properties investigation

The glass-transition temperature ( $T_g$ ) of the different PR-PAA networks was measured using DSC via a heat-cool-heat procedure between  $-60^\circ\text{C}$  and  $180^\circ\text{C}$  at a rate of  $15^\circ\text{C}\cdot\text{min}^{-1}$ . Figure III.15.a shows the thermograms of both PR-PAA 2 and PAA. The resulting  $T_g$  values,  $T_{g1}$ ,  $T_{g2}$ ,  $T_{g3}$  collected for the first, second and third heating ramps are summarized in Figure III.15.b. For reason of conciseness, we solely report the detailed characterization of PR-PAA 2, the thermograms of the other PR-PAA networks can be found in Supplementary Information (Figure SI.III.38 & Table SI.III.5).

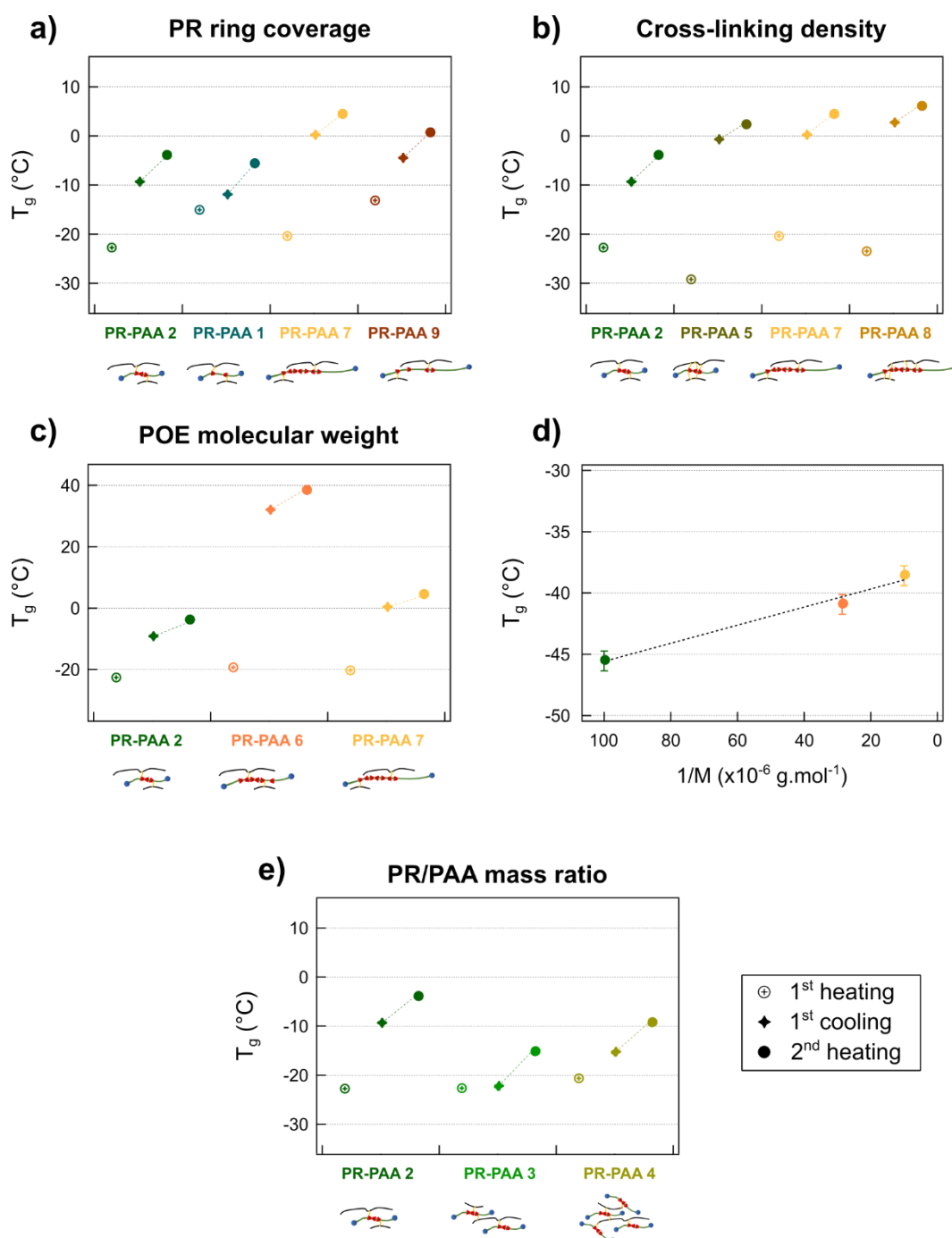


**Figure III.15: DSC analysis of PAA and PR-PAA 2.** **a)** Overlapped DSC thermograms for PAA (black) and PR-PAA 2 (green) during the heat-cool-heat procedure carried out between  $-60^\circ\text{C}$  and  $180^\circ\text{C}$  at a rate of  $15\cdot\text{min}^{-1}$ . The measurements were carried out after the freeze-drying process for PR-PAA 2 and with no further purification for PAA. **b)**  $T_g$  values obtained by data treatment with the TRIOS software, the error bar on the temperature determination is estimated to  $\pm 0.6^\circ\text{C}$ . The overlapping of an endothermic peak and the glass transition temperature ( $T_g$ ) signal does not allow measuring  $T_{g1}$  for PAA. **c)** Mass fractions of remaining solvents. Errors bars were obtained by performing three independent experiments.

Interestingly, PR-PAA networks are amorphous and show a typical elastomer behaviour, with their  $T_g$  well below room temperature (25 °C) and almost 10 times lower than the  $T_g$  of PAA (Table SI.III.5). The  $T_g$  values of PAA ( $T_{g2} = 126.3^\circ\text{C}$  &  $T_{g3} = 128.2^\circ\text{C}$ ) confirm its brittleness at room temperature (Figure III.15.b). On the contrary, the  $T_g$  values of PR-PAA are below room temperature which ensures the propagation of movements along the polymer chains ( $T_{g1} = -22.9^\circ\text{C}$ ;  $T_{g2} = -9.6^\circ\text{C}$  &  $T_{g3} = -4.1^\circ\text{C}$ ). It may also indicate the presence of  $\alpha$ -CD sliding motion. Moreover, the absence of any phase transitions of pure PAA, PEO, or  $\alpha$ -CDs on the DSC thermograms suggests we are in presence of a homogeneous network structure.

It is worth noticing the significant difference between  $T_{g1}$  and  $T_{g2}$  for PR-PAA. It partially originates from traces of solvents used during the synthesis, that may be trapped in the PR tubular architecture (water or DMSO). These residuals act as plasticizers and the first heating ramp was made to remove them (here for PR-PAA 2:  $T_{g1} = -22.9^\circ\text{C} < T_{g2} = -9.6^\circ\text{C}$ ). This preliminary heating process was also relevant for commercial PAA which contain adsorbed water (endotherm at 100°C). The solvent residuals were estimated to approximately 10%<sub>w</sub> for PR-PAA and PAA by simply weighting the DSC non-hermetic aluminium capsule at the end of the DSC experiments (Figure III.15.c & Figure SI.III.39). Thus, to compare PR-PAA networks, the attention will be solely paid on  $T_{g3}$  in the following of the report.

Next, we investigated the effects of the PR ring coverage (**rc**), the crosslinking density (**z**), the PEO molecular weight (**x**) and the PR/PAA mass ratio (**y**) on the thermal properties of the different PR-PAA networks (Figure III.16).



**Figure III.16: Influence of the structural parameters of PR-PAA networks on their glass transition temperature  $T_g$ .** PR-PAA networks were called using their corresponding label (Table III.7).  $T_{g1}$ ,  $T_{g2}$  and  $T_{g3}$  are reported for each sample. **a)** Influence of the PR ring coverage ( $rc$ ) for PR10K (runs 1 & 2) and PR100K (runs 7 & 9). **b)** Influence of the crosslinking density ( $z$ ) for PR10K (runs 2 & 5) and PR100K (runs 7 & 8). **c)** Influence of the PEO molecular weight ( $x$ ): PEO10K (run 2, green), PEO35K (run 6, orange) and PEO100K (run 7, yellow). **d)**  $T_g$  of the dimethacrylated PEO10K, PEO35K and PEO100K. Verification of the Fox and Fleury law<sup>70</sup>. **e)** Influence of the PR/PAA mass ratio ( $y$ ) for PR-PAA network prepared from PR6 (PR10K, 50% ring coverage).

### Effect of the PR ring coverage (Figure III.16.a)

First, we investigated the influence of the PR ring coverage for PR-PAA networks prepared from PR10K (PR-PAA 1 and PR-PAA 2) and PR100K (PR-PAA 7 and PR-PAA 9). Both the cross-linking density ( $z = 0.5\%$ ) and the PR/PAA mass ratio ( $y = 5\%_{\text{wt}}$ ) were kept constant. Clearly, PR-PAA 1 ( $T_g = -5.8^\circ\text{C}$ ) exhibits a lower  $T_g$  than PR-PAA 2 ( $T_g = -4.1^\circ\text{C}$ ). Their corresponding PR ring coverages are 25% and 50% respectively. Therefore, the  $T_g$  difference demonstrates the influence of a low PR ring coverage on the mobility of the polymer chains. A similar trend was observed when comparing PR-PAA 9 ( $T_g = 0.5^\circ\text{C}$ ) with PR-PAA 7 ( $T_g = 4.3^\circ\text{C}$ ). Such observation validated our hypothesis of having successfully synthesized two PR100K only differing by their PR rings coverages, PR10 being denser than PR11.

As a conclusion, the  $T_g$  value is slightly reduced as the PR ring coverage decreases, owing to a better mobility of the  $\alpha$ -CDs on the threading polymer chain. Note that the decrease in  $T_g$  values is two times greater for PR100K than for PR10K:  $\Delta T_{g3} [\text{PR100K}] = -3.8^\circ\text{C}$  compared to  $\Delta T_{g3} [\text{PR10K}] = -1.7^\circ\text{C}$ . As expected, this sliding phenomenon is enhanced with PR100K as a result of a greater distance for sliding. Lastly, the decline in the average  $T_g$  values for PR-PAA networks prepared with PR10K compared to PR100K can be attributed to the restriction of mobility implied by incorporating a higher molecular mass PRs in the system. This assumption is supported by the Fox and Flory's law<sup>70</sup> which reports an increase of  $T_g$  as raising the molecular mass of a polymer. (Figure III.16.d & Figure SI.III.40).

### Effect of cross-linking density (Figure III.16.b)

Then, we increased the cross-linking density by a factor of 10, from 0.5% to 5%, *ie* activating 32 and 320 COOH units per PAA (6250 units in total). PR-PAA 5 and PR-PAA 8 correspond to a 5% cross-linking density while PR-PAA 2 and PR-PAA 7 stand for a 0.5% cross-linking density. Considering PR10K, PR-PAA 5 exhibits higher  $T_g$  values than PR-PAA 2 ( $T_g = 2.2^\circ\text{C}$  vs  $-4.1^\circ\text{C}$ ). The same trend is seen for PR100K, when comparing PR-PAA 8 to PR-PAA 7 ( $T_g = 5.9^\circ\text{C}$  vs  $4.3^\circ\text{C}$ ). Therefore, in our PR-PAA systems,  $T_g$  increases with raising the cross-linking density. Such finding suggests an equivalent behaviour between conventional cross-linked polymers and PR-PAA networks<sup>190</sup>.

The rise in  $T_g$  values is two times higher for PR10K than for PR100K:  $\Delta T_{g3} [\text{PR10K}] = +6.3^\circ\text{C}$  compared to  $\Delta T_{g3} [\text{PR100K}] = +1.6^\circ\text{C}$ . Thus, despite the greater reticulation, we assume PR-PAA networks made of

PR100K still offer nice possibilities for  $\alpha$ -CDs sliding motion compared to PR-PAA networks made of PR10K.

### **Effect of PEO molecular weight (Figures III.16. c & d)**

Moreover, we examined the influence of the molecular weight of the PEO used to synthesize the PRs. We compared PR-PAA networks that exhibit a similar PR ring coverage : PR-PAA 2 (PR10K), PR-PAA 6 (PR35K) and PR-PAA 7 (PR100K). Notably, the  $T_g$  values are very dependent on the PEO molecular weight. PR-PAA 6 exhibiting a lot higher  $T_g$  ( $T_{g3} = 38.2^\circ\text{C}$ ) than both PR-PAA 2 ( $T_{g3} = -4.1^\circ\text{C}$ ) and PR-PAA 7 ( $T_{g3} = 4.3^\circ\text{C}$ ). Some hints for interpretation of the upside down U-trend can be found in the following paragraph.

We would have expected<sup>201</sup> an increasing trend for  $T_g$  while incorporating higher molecular weight PRs in PR-PAA networks. Indeed, such observation is true for dimethacrylated PEO10K, PEO35K and PEO100K (Figure III.16.d & Figure SI.III.40). Therefore, the rupture reported for PR100K may be attributed to the enhanced  $\alpha$ -CD sliding motion counterbalancing the expected increase in  $T_g$ . Moreover, the proportion of non-slidable  $\alpha$ -CDs crosslinks cannot explain this huge difference, since the PR-PAA networks were synthesized from PRs having identical proportions of residual free  $\alpha$ -CDs.

### **Effect of PR/PAA mass ratio (Figure III.16.e)**

Finally, we evaluated the role played by the PR/PAA mass ratio in the PR-PAA networks prepared from PR6 (PR10K). Keeping the cross-linking density constant, we compared PR-PAA 2, PR-PAA 3 and PR-PAA 4 corresponding to 5%<sub>wt</sub>, 10%<sub>wt</sub> and 20%<sub>wt</sub> respectively. First, we observed a decline in  $T_g$  when increasing the PR doping from 5%<sub>wt</sub> to 10%<sub>wt</sub>, whereas no more decline is seen, even a slight increase is seen for 20%<sub>wt</sub>. At this stage, it is difficult to give a clear explanation for these findings. If the first decline observed between 5%<sub>wt</sub> and 10%<sub>wt</sub> of doping ratio could be attributed to the amplification of the sliding motion phenomenon, the absence of further decreased in  $T_g$  might originate from the presence of too few cross-linkers.

In conclusion, due to their  $T_g$  lower than room temperature, the PR-PAA networks are elastomers. That ensures the conditions for the presence of spontaneous mobility of the polymer chain, in particular the  $\alpha$ -CD sliding motion. Moreover, this thermal analysis allowed us to bring to light the role played by the PEO molecular weight, the PR ring coverage and the cross-linking density on



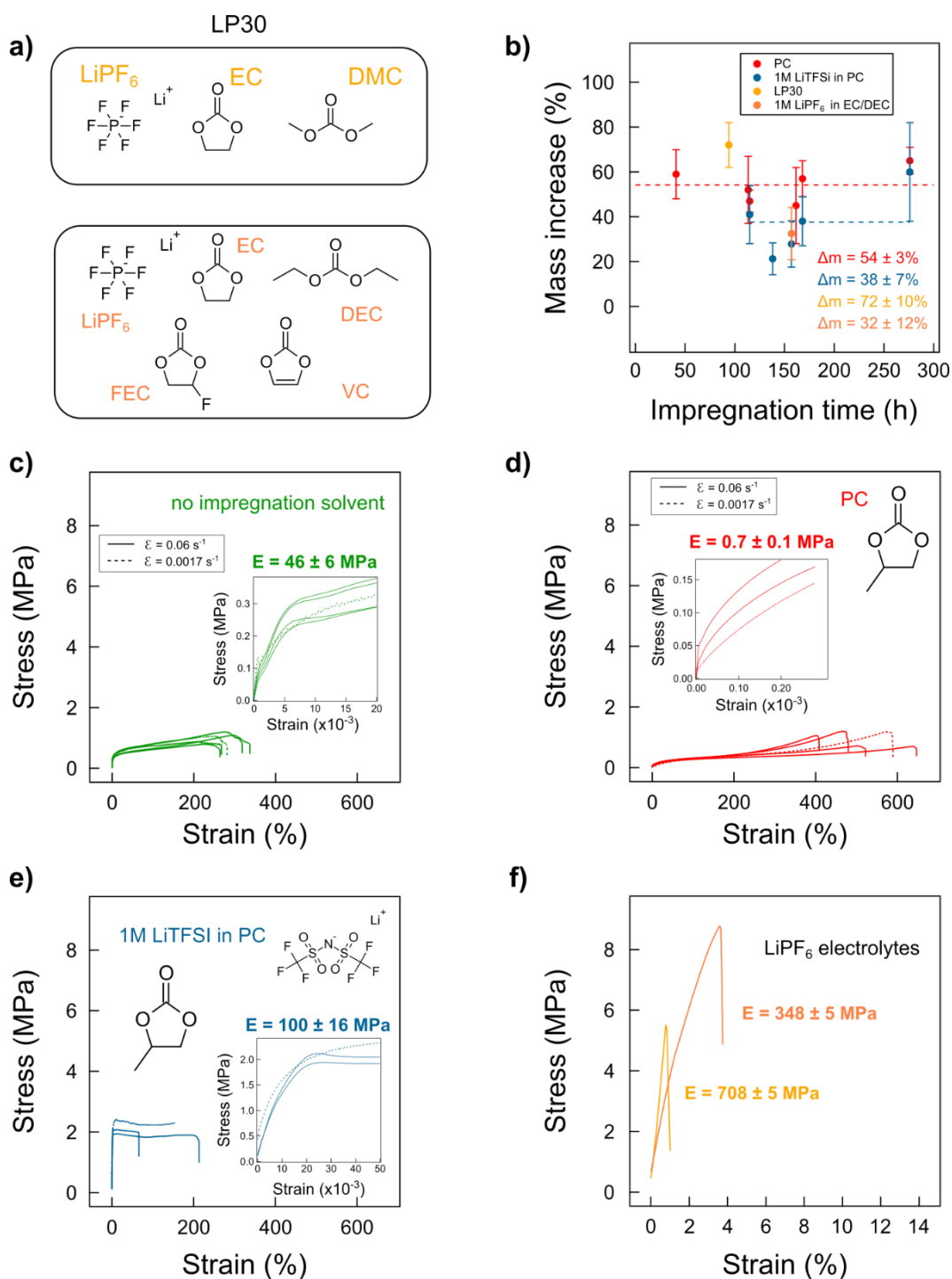
enhancing the mobility of  $\alpha$ -CDs along the threading polymer. The effect of PR/PAA mass ratio was also considered, but the complete understanding of this parameter would require a deeper study. In view of the targeted application, we then investigated the mechanical properties of these slidable PR-PAA networks.

### c. Mechanical properties evaluation

As both PAA and PR-PAA networks are sticky powders, we prepared some standardized membranes on which to perform the mechanical strength tests. PAA and PR-PAA networks were dissolved in DMSO to form a transparent slurry that was casted in a rectangular mould and then cured 24h at 80°C followed by an additional 24h at 80°C under vacuum. Transparent rectangular specimens (37 mm x 14 mm x 100  $\mu$ m) were obtained. We assume the good holding of the membranes is ensured through the reticulation of PAA chains (anhydride)<sup>200</sup>. Therefore, the membranes are composed of both sliding and fixed cross-linked points and the correlation between mechanical properties and thermal analyses is not always relevant.

Preliminary tensile tests were performed on PAA membranes that were previously soaked in four different types of electrolytes : propylene carbonate (PC), 1M LiTFSI in PC, LP30 which is composed of 1M LiPF<sub>6</sub> in ethylene carbonate/dimethyl carbonate (EC/DMC) and 1M LiPF<sub>6</sub> in ethylene carbonate/diethyl carbonate (EC/DEC) with fluoroethylene carbonate (FEC, 7.5%<sub>w</sub>t) and vinylene carbonate (VC, 5%<sub>w</sub>t) as additives. The two electrolytes composed of a mixture of carbonates are common for Si anodes cycling, the latter being used by Choi<sup>101</sup> (Figure III.17.a).

The mass increases ( $\Delta m$ ) were calculated for the different impregnation electrolytes according to the following equation:  $\Delta m = 100 \times (m_{swollen} - m_{dried})/m_{dried}$ . PAA membranes soaked in PC display a mass increase of  $54 \pm 3\%$  whereas the  $\Delta m$  value is lowered to  $38 \pm 7\%$  for 1M LiTFSI in PC (Figure III.17.a & b) A similar swelling was obtained for 1M LiPF<sub>6</sub> in EC/DEC ( $32 \pm 12\%$ ). Note that we do not expect the mass increase measured for LP30 to be that high ( $72 \pm 10\%$ ). It can be explained by the fact that there might be some extra solvent at the membrane surface that we could not easily remove because of DMC evaporation and EC solidification during the impregnation.



**Figure III.17: Mechanical testing of PAA membranes soaked in different electrolytes.** **a)** Composition of the LiPF<sub>6</sub> containing electrolytes. **b)** Equilibrium swelling ratio of the PAA membranes soaked in the different electrolytes. Errors bars were calculated as the standard deviations. For the tensile experiments, two different strain rates were investigated  $\dot{\epsilon} = 0.06 \text{ s}^{-1}$  (plain line) and  $\dot{\epsilon} = 0.0017 \text{ s}^{-1}$  (dashed line). The Young's moduli were calculated with the fitting of the 3% of the first deformation. Stress-strain curves obtained with the 10 N load cell for PAA membranes **c)** not impregnated in any electrolyte, **d)** in propylene carbonate (PC), **e)** in 1M LiTFSI in PC, **f)** in LP30 and 1M LiPF<sub>6</sub> in ethylene carbonate/diethylene carbonate (EC/DEC) (1/1 v/v) with 7.5%<sub>wt</sub> of fluoroethylene carbonate (FEC) and 0.5%<sub>wt</sub> of vinylene carbonate (VC) (100N load cell).

The tensile tests were performed for the different impregnation electrolytes at two different strain rates ( $\dot{\epsilon} = 0.0017 \text{ s}^{-1}$  compared to  $\dot{\epsilon} = 0.06 \text{ s}^{-1}$ ) under ambient atmosphere. The dry PAA displays a conventional elasto-plastic stress-strain curve with an elastic modulus  $E = 46 \pm 6 \text{ MPa}$  (Figure III.17.c). When PAA membranes are soaked in PC, they show a rubbery behaviour: high strains are produced at very low stress levels. The Young's modulus is lower than 1 MPa ( $E = 0.7 \pm 0.1 \text{ MPa}$ ) (Figure III.17.d). PC acts as a plasticizer and its interactions with PAA importantly affect its mechanical properties. On the opposite, for  $\text{LiPF}_6$  containing electrolytes, the PAA membranes become brittle. They have higher Young's moduli ( $E = 348 \pm 5 \text{ MPa}$  and  $E = 708 \pm 5 \text{ MPa}$  for the EC/DEC and EC/DMC mixtures respectively) and fracture while deforming elastically (Figure III.17.f) The Young's moduli difference is explained by the solvents nature and the probable DMC evaporation resulting in EC solidification. For 1M LiTFSI in PC, there is a high resistance to deformation ( $E = 100 \pm 16 \text{ MPa}$ ) but a plastic domain can be seen afterwards (Figure III.17.e).

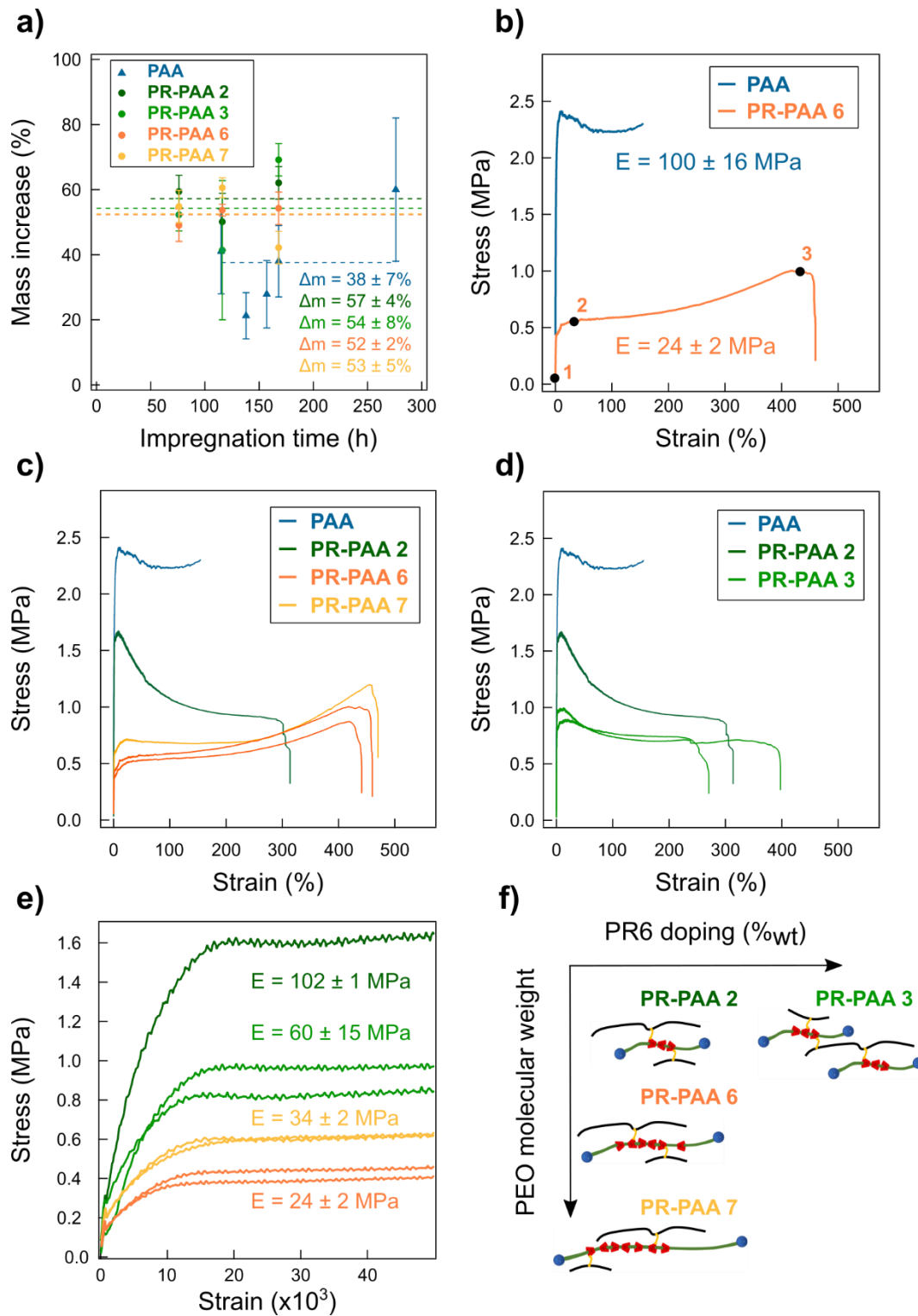
In conclusion, the PAA membranes behaviour is highly dependent on the impregnation electrolytes whereas the strain rate does not seem to have any influence (dashed vs plain lines). When PAA membranes are soaked in electrolytes composed of Li salts, the stress-strain curves are characterized by their stiffness, even their brittleness and they show similarities with the ones reported by Choi *et al*<sup>32</sup> (see 1.b). Based on these results, we determined the experimental conditions to evaluate the mechanical properties of PR-PAA networks. With the objective to be close to the batteries operating conditions, we opted for 1M LiTFSI in PC because  $\text{LiPF}_6$  is known to decompose when exposed to moisture<sup>202</sup>.

Membranes were prepared from the previously synthesized PR-PAA networks: PR-PAA 2, PR-PAA 3, PR-PAA 6 and PR-PAA 8 (Table III.7). They were swelled into the 1M LiTFSI in PC electrolyte and their equilibrium mass increases are reported in Figure III.18.a. The PR-PAA membranes showed a larger swelling ratio as compared with PAA membranes (+10%). The slidable cross-linkers play a dominant role in these swelling properties since they are assumed to relax the stress concentration in the increase in swelling pressure inside the material<sup>64</sup>. On the opposite, the fixed cross-linking points in the PAA network (anhydride bond) cause a small swelling property. These results, which exhibit the movability of the threaded  $\alpha$ -CDs cross-linkers, are in adequation with the thermal analysis above, *ie*  $T_g \text{ PR-PAA} < T_g \text{ PAA}$ .

Then, tensile tests were conducted at a low strain rate ( $\dot{\epsilon} = 0.0017 \text{ s}^{-1}$ ) because the intention was to let enough time to the PR-PAA network to rearrange itself, and to observe the expected  $\alpha$ -CDs sliding motion influence. On Figure III.18.b, the stress-strain curves of a PAA and a PR-PAA 6, manufactured from PR35K are overlapped. As shown, two drastically different profiles are obtained. The stiffness and the brittleness of PAA ( $E = 100 \pm 16 \text{ MPa}$ ) differ from the PR-PAA 6 membrane which Young's modulus is lower ( $E = 24 \pm 2 \text{ MPa}$ ). Indeed, from points 1 to 2, PR-PAA 6 exhibits a linear profile similar to the one of PAA except that the stress is lower. This corroborates with the fact that PR-PAA networks are softer as underlined with their  $T_g$ . Then, another kind of regime providing high elasticity is observed between point 2 et 3. It is assimilated to a non-linear stiffening strain profile: while increasing strain, a smaller stress is accumulated (=strain hardening). The fracture takes place at a very high strain ( $\sim 450\%$ ). It is assumed that  $\alpha$ -CD sliding motion is responsible for the strain hardening and improvement in toughness that extend the end of the curve.

Note that quite a significant difference in terms of tensile strength could be discussed when comparing our results with the PR-PAA mechanical behaviour exposed in Choi's work (Figure III.2.c). Thus, for a comparable PR-PAA network made from PR20K with a 29% ring coverage, they report similar tensile strengths for PR-PAA and PAA itself (1.6 vs 1.5 MPa), which does not seem to be the case in our study (0.9 vs 2.4 MPa). The nature of the swelling electrolyte or the type of clamps that could induce a premature damage might contribute to this value difference. To conclude, fracture experiments on notched specimens should be run to quantify fracture resistance through a statistical analysis and overcome materials defect distribution or clamping effects.

Next, we studied the influence of PEO molecular weight (Figure III.18.c) and the PR doping ratio of PR (%<sub>w</sub>) (Figure III.18.d) on PR-PAA mechanical properties.



**Figure III.18: Mechanical testing of PR-PAA membranes in soaked in the 1M LiTFSI in PC electrolyte.** The stress-strain curves are obtained with the 10 N load cell under ambient atmospheric conditions with a strain rate of  $\dot{\epsilon} = 0.0017$  Hz. **a)** Equilibrium swelling ratios. Errors bars were calculated as the standard deviations. **b)** Overlapping of the stress-strain curves for PAA and PR-PAA 6 (Table III.7). **c)** Influence of the PEO molecular weight. **d)** Influence of the PR doping ratio (%wt) for PR-PAA network prepared from PR6 (PR10K, 50% rings coverage). **e)** Young's moduli calculated with the fitting of the first 1% of deformation. **f)** Illustration of the tested PR-PAA networks.

**Effect of PEO molecular weight (Figures III.18.c)**

The PR-PAA 7 prepared with PR100K also shows a non-linear stiffening strain behaviour coupled with an impressive toughness. A higher tensile strength is obtained compared to PR-PAA 6 made of PR35K. The strain at rupture ( $\sim 450\%$ ) along with the Young's modulus ( $E = 34 \pm 2$  MPa) are of the same order of magnitude than the PR-PAA 6 ( $E = 24 \pm 2$  MPa). Switching to PR10K induces a clear modification of the stress-strain curve profiles. For PR-PAA 2, the non-linear stiffening profile has disappeared to give way to plastic deformation accompanied with a large increase in stiffness ( $E = 102 \pm 1$  MPa). Thus, we expect the  $\alpha$ -CD sliding motion being progressively attenuated while decreasing PEO molecular weight, hence the distance for sliding. Quite surprisingly, the Young's moduli difference does not corroborate with the DSC results ( $T_g$  run 8  $<$   $T_g$  run 6) which is still not perfectly understood at the moment of writing.

**Effect of PR doping ratio (Figure III.18.d)**

Keeping the cross-linking density constant, we increased the PR mass fraction in the PR-PAA networks prepared from PR6 (PR10K with a 50% ring coverage) from 5%<sub>wt</sub> to 10%<sub>wt</sub>. A decrease in the Young's modulus value is observed ( $E = 60 \pm 15$  MPa). The stress-strain curves do not show any non-linear stiffening behaviour though indicating the absence of  $\alpha$ -CDs sliding motion. The decline in Young's modulus is in agreement with the  $T_g$  decrease (section above). Increasing the PR doping ratio is supposed to reduce the number of cross-linking points on the same PR, hence leading to a softer material. The mechanical testing has not been carried out on the 20%<sub>wt</sub> yet, so it would be too ambitious to draw a clear conclusion about the PR doping ratio trend.

However, given the reported results so far, this study would have been more relevant on PR35K or PR100K because they display the desired elastic behaviour. Indeed, in term of mechanical properties, no real interest lies in PR-PAA made of PR10K. Moreover, at the time of writing, the investigation of the PR ring coverage and the cross-linking density is missing to our study.

## 4. Conclusions and discussions

Inspired from a recent original work, we have adopted a systematic synthesis strategy to prepare a large panel of PR-PAA networks resulting from the cross-linking of PAA with  $\alpha$ -CDs based PRs made of high molecular weight PEO. As shown through SEC,  $^1\text{H}$  NMR and thermal analysis, different structural parameters were successfully varied. Among them, one can find the PEO molecular weight (x), the PR ring coverage (rc), the PR/PAA mass ratio (y) and the cross-linking density (z).

The main goal of this project was to better understand the underlying mechanisms responsible for the better cyclability of Si anodes in which Choi *et al* incorporated PR-PAA binders. As we believe that the  $\alpha$ -CD sliding motion is at stake, we have designed PR-PAA architectures with theoretical enhanced sliding ability by increasing the PEO molecular weight, lowering the PR ring coverage and the PR/PAA mass ratio. Of course, the best way to know which PR-PAA architecture has the best ability to accommodate Si volume changes is to investigate the cycling performances of the Si anodes which incorporate PR-PAA as binders. Thus, this synthesis work is to be intimately linked with the following Chapter dealing with the evaluation of the performances of Si anodes that incorporate PR-PAA as binders.

In our scientific approach, we aim to correlate the cycling performances of PR-PAA binders with their mechanical properties. Unfortunately, at the time of writing, the mechanical tests have not been carried out on all the PR-PAA, but some trends have already emerged from our thermal and mechanical analyses. For a 5%<sub>wt</sub> PR/PAA mass ratio, we expect a better ability to accommodate Si volume changes for PR-PAA made of PR35K and PR100K rather than PR10K, since they exhibit a non-linear strain stiffening profile that we attribute to the  $\alpha$ -CDs sliding motion. To go further in the understanding, some dynamic cycling experiments are also envisioned to evaluate the stretch recovery of our systems and especially the rearrangement of the network relying on the  $\alpha$ -CDs sliding motion.

Finally, we hope this systematic study to be useful in the more general design of Si anode binders. Indeed, the interconnection of the requirements that should be met for a polymer to sustain the Si volume changes is currently the main issue to be addressed (interaction, cross-linking nature and

density...). Moreover, the specifications in term of mechanical properties remain vague as underlined by the debate among brittle or elastomers polymer mentioned in the Chapter introduction. Therefore, providing such a broad range of model PR-PAA with the willingness to establish a structure/properties relationship makes our approach very original and unique. We hope this will pave the way towards a better understanding of the design principles of Si anodes binders.





# Chapter IV: Understanding the electrochemical performances of Si anodes incorporating mechanically interlocked binders prepared from $\alpha$ -cyclodextrins based polyrotaxanes

## 1. Background and motivation

Successful binders for Si anode must meet a variety of requirements to produce stable Si electrodes<sup>96</sup>. They should strongly adhere to the electrode components and sustain sufficient elastic deformation during charge and discharge to maintain connectivity. Moreover, they should be electrochemically stable, and show a reasonable electrolyte uptake to provide Li ions mobility. Among these criteria, the electrolyte uptake and the mechanical properties of PR-PAA networks, which synthesis has been thoroughly reported in Chapter III, have already been evaluated.

This chapter concerns the electrochemical measurements that were carried out to verify the electrochemical stability of PR-PAA and to investigate the cycling performances of Si anodes in which these mechanically interlocked binders are incorporated. The main goal is to provide an understanding of PR-PAA structure-properties relationships to correlate the cycling performances with the specific structural parameters of the different binders, through a systematic study.

Given the complexities of Si anode processing and their impact on the electrode stability, the first section deals with the development of reference Si composite electrodes using a commercial polymer, poly(acrylic acid) (PAA), as a binder. The second section tackles the incorporation of PR-PAA in the Si electrode formulation and aims to elucidate the design criteria guiding the optimization of PR-PAA Si anode binders.

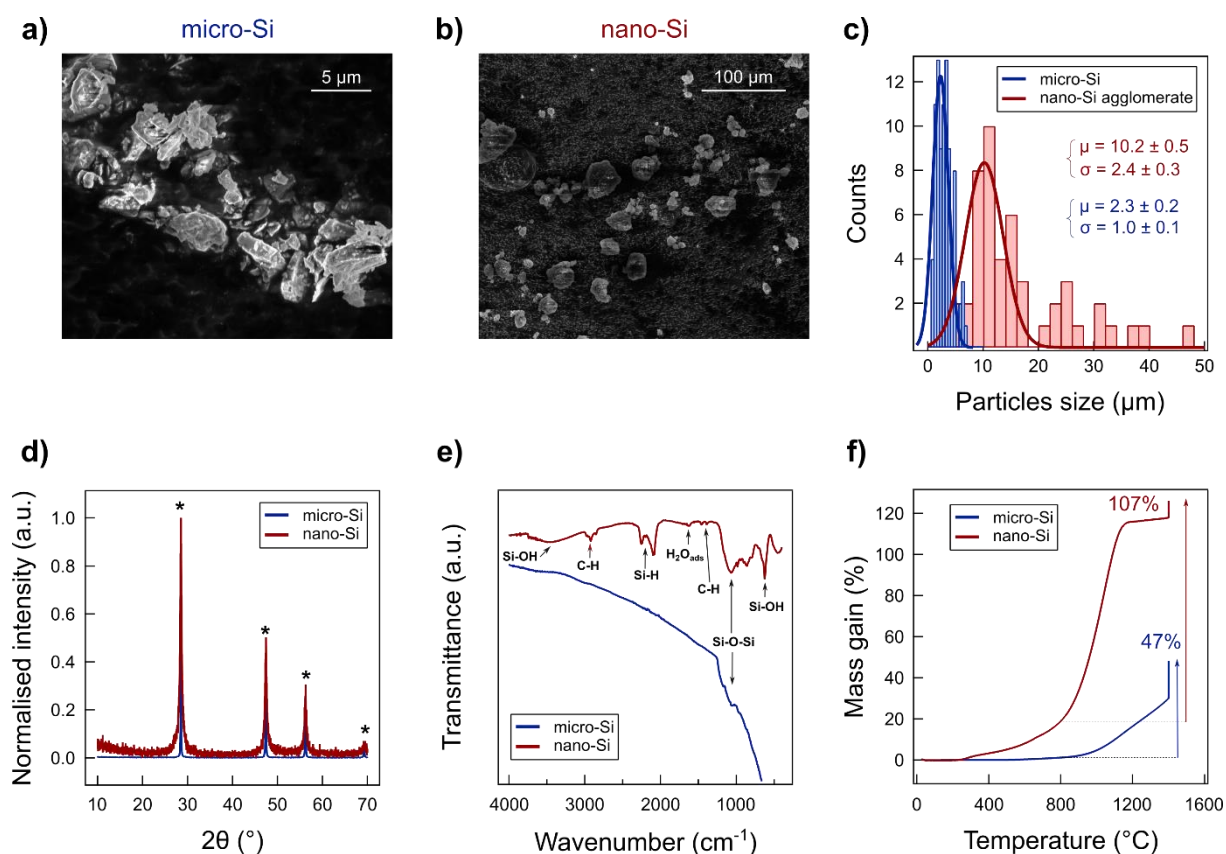
## 2. Development of reference Si composite electrodes

Unlike graphite, where lithium ions are intercalated between the individual layers of graphene, silicon (Si) reacts with lithium ions via an alloying process<sup>203</sup>. Owing to the significant volume changes of such reaction (lithiation, delithiation), Si cannot be cycled otherwise than being processed as casted films. We got inspired from the formulation recipes developed by Beattie *et al* and Bridel *et al*<sup>159,204</sup> and we prepared Si electrodes with a relatively low Si content (50%) and high binder content (25%) to specifically observe the binder influence. PAA was used as the reference binder, to be compared with PR-PAA.

### a. Si particles choice

Bearing in mind that the lithium alloying process depends on Si particle size<sup>205</sup> (see 2.c), we have prepared Si electrodes from commercial Si nanoparticles (nano-Si, 40 nm) and microparticles (micro-Si, 1-5  $\mu\text{m}$ ). Preliminary characterizations of the Si particles were performed by scanning electron microscopy (SEM), X-ray diffraction (XRD), infrared spectroscopy (FTIR) and thermal gravimetric analysis (TGA) (Figure IV.1).

On the SEM pictures, only micro-Si particles can be seen at the particle level. They appear as sharp-edged particles with a non-smooth surface, and they have a narrow particles size range distribution ( $\mu = 2.3 \mu\text{m}$  &  $\sigma = 1.0 \mu\text{m}$ ) (Figure IV.1.a & c). Nano-Si particles form micro-sized agglomerates which are five times larger than the micro-Si and wider size-distributed ( $\mu = 10 \mu\text{m}$  &  $\sigma = 2.5 \mu\text{m}$ ) (Figure IV.1.b & c). The XRD patterns of nano-Si and micro-Si only show sharp reflexions at  $28^\circ$ ,  $47^\circ$ ,  $58^\circ$  and  $69^\circ$  which are ascribed to the cubic structure of pure crystalline Si. Unsurprisingly, micro-Si get more defined peaks than nano-Si, owing to their dimensions (Figure IV.1.d).



**Figure IV.1: Characterization of micro-Si and nano-Si particles.** Scanning electron microscopy (SEM) micrographs for **a)** micro-Si (blue) and **b)** nano-Si (red) particles (5 kV, 50 pA) and **c)** their size distributions with the corresponding gaussian fits.  $\mu$  and  $\sigma$  stand as the means and the standard deviations respectively. **d)** XRD patterns, **e)** ATR-FTIR spectra and **f)** thermograms obtained by TGA (heating ramp  $5^{\circ}\text{C}\cdot\text{min}^{-1}$  followed by a 2 hours isotherm at  $1400^{\circ}\text{C}$ ) for micro and nano-Si.

While XRD is relatively blind to amorphous phase such as  $\text{SiO}_2$ , the FTIR spectrum of nano-Si exhibit the characteristic peaks of Si-O-Si and Si-OH stretching at around  $1100\text{ cm}^{-1}$  and  $900\text{ cm}^{-1}$  respectively<sup>206–208</sup>. Such observation is consistent with the supplier information indicating the presence of  $\text{SiO}_2$  (3%wt). The signals at around  $2200\text{ cm}^{-1}$  are assigned to Si-H stretching and the broad signal at around  $3500\text{ cm}^{-1}$  corresponds either to the stretching of H-bonded silanols (Si-OH) and/or stands for residual adsorbed water, which could correlate with the small peaks at  $1625\text{ cm}^{-1}$  (bending mode of adsorbed water)<sup>209</sup>. Additionally, the peaks at  $1400$  and  $2900\text{ cm}^{-1}$  may be attributed to C-H stretching, hypothesizing about the presence of a carbon layer. Notably, the presence of any oxidized form of Si is less straightforward for micro-Si, resulting from the lower surface reactivity of micro-sized particles (Figure IV.1.e)

Subsequently, TGA was carried out under an air flux, to estimate the proportion of  $\text{SiO}_2$  (Figure IV.1.f). A heating ramp of  $5^{\circ}\text{C}\cdot\text{min}^{-1}$  until  $1400^{\circ}\text{C}$  followed by a 2 hours isotherm was applied. Theoretically,

oxidation should occur at around  $800^{\circ}\text{C}$ <sup>210</sup> and a 114% mass increase is expected for pure Si. For nano-Si, the mass starts to increase before  $400^{\circ}\text{C}$ , supporting the hypothesis of the existence of a carbon layer. Starting from  $800^{\circ}\text{C}$ , the mass gain was estimated to 107%, which corresponds to 6%<sub>wt</sub> of  $\text{SiO}_2$  and corroborates quite well with the supplier information (3%<sub>wt</sub>). Note that for micro-Si, the oxidation was not complete (mass increase of 47%) and it would be worth to extend the isotherm duration to estimate the  $\text{SiO}_2$  proportion. Notwithstanding, based on the FTIR spectrum, we expect a small  $\text{SiO}_2/\text{Si}$  ratio.

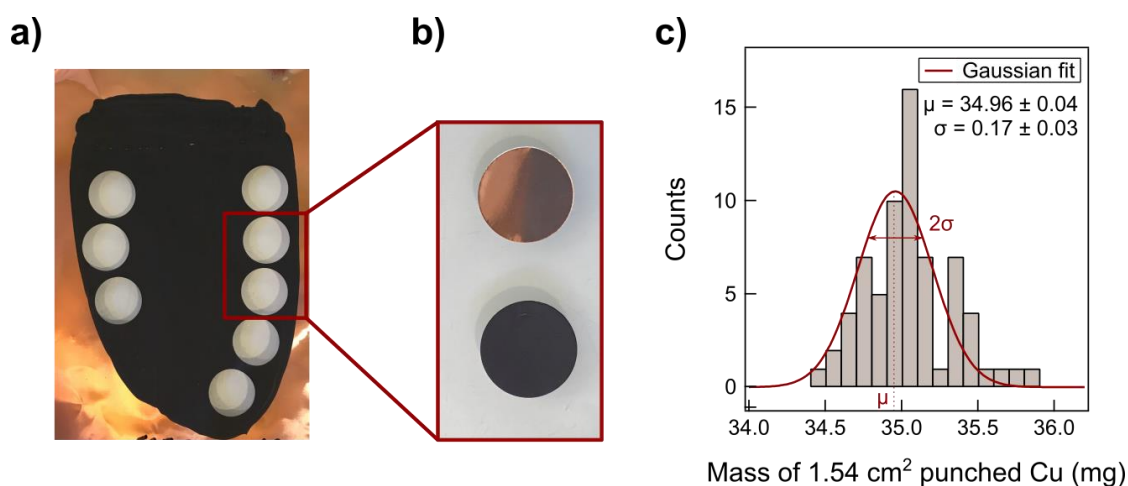
Interestingly, these preliminary characterizations allowed us to exclude Alfa Aesar Si nanoparticles (nano-Si AA, < 100 nm) from our study (Figure SI.IV.1). Indeed, TGA revealed the significant presence of  $\text{SiO}_2$  (64%<sub>wt</sub>), which was also confirmed by XRD with the broad and weak peak at around  $2\theta=23^{\circ}$  (amorphous  $\text{SiO}_2$ ). Hence, the existence of a thick layer of inactive  $\text{SiO}_2$  may cause the poor capacity of the corresponding Si electrodes<sup>207</sup>.

Following these characterizations, we proceeded to the preparation of Si electrodes from micro-Si and nano-Si.

## b. Si composite electrodes preparation

### **Formulation process**

In typical Si composite electrodes, three components are present, the active material (here Si), the conductive additive, which enhances the electrical conductivity of the electrode and the binder that holds the electrode components together. Here, we use Si particles, conductive carbon Csp and PAA in a weight ratio of (2:1:1) respectively. The three powders were first hand milled prior to the addition of solvent (water, ethanol or DMSO), keeping the dry mass ratio between 15-25%. The obtained slurry was gently mixed for 24h to favour the intimate mixture and homogenisation. The resulting ink was then casted on a  $26\ \mu\text{m}$  thick copper foil using a doctor blade with a  $200\ \mu\text{m}$  slit and the film was later dried for at least 24 hours in a vacuum oven at  $80^{\circ}\text{C}$  (Figure IV.2.a).



**Figure IV.2: Preparation of Si electrodes** **a)** Photograph of a Si electrode film (nano-Si/Csp/PAA in EtOH) coated onto a Cu foil. **b)** Recto and verso of the corresponding 1.54 cm<sup>2</sup> punched electrodes. **c)** Mass distribution of 1.54 cm<sup>2</sup> Cu disks (68 in total) and the corresponding gaussian fit.  $\mu$  and  $\sigma$  stand as the mean and the standard deviation respectively.

Since this formulation process was developed to study the synthesized PR-PAA binders, several rational choices were made for the slurry preparation. No vigorous mixing conditions were investigated, to avoid any deterioration of the binder structure as already reported for high molecular weight PAA under high energy ball-milling step<sup>211</sup>. Moreover, different solvents were considered to anticipate any solubility difference between PAA and PR-PAA. Therefore, besides water and ethanol which are commonly used, we also worked with DMSO. It might be more exotic but note that it was the solvent chosen by Choi *et al*<sup>101</sup> to incorporate PR-PAA binders in Si electrodes.

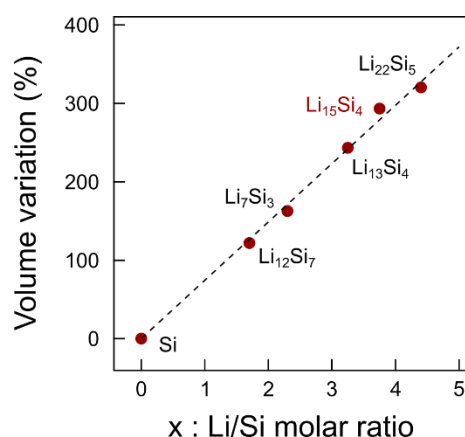
### Characteristics of Si electrodes

For battery assembly, Si electrodes were punched as 1.54 cm<sup>2</sup> disks (Figure IV.2.b). Each electrode was weighted to evaluate its Si loading (mg<sub>Si</sub>.cm<sup>-2</sup>), knowing the Cu disk mass and the mass ratios of the electrode components. Figure IV.2.c shows the mass distribution of 68 Cu disks that was fitted according to a Gaussian law centered in  $34.96 \pm 0.04$  mg ( $\mu$ ) with a standard deviation of  $0.17 \pm 0.03$  mg ( $\sigma$ ). In average, the total mass of the electrode components represents  $\sim 2$  mg, *ie* 6% of the total weight of Si electrode (electrode components + Cu disk). Therefore, Si loadings are estimated at  $\sim 0.6$  mg<sub>Si</sub>.cm<sup>-2</sup>, which is consistent with the literature. However, we should be aware that such evaluation might induce a meaningful error coming from the relatively close values of Si mass per electrode ( $\sim 1$  mg) and the standard deviation of the Cu disk mass distribution ( $\sigma \sim 0.2$  mg). Note that, in the following of the Chapter, Si loading refers to the mass of active material (50%<sub>wt</sub>), regardless the SiO<sub>2</sub>/Si ratio.

Besides from the Si loading, other physical characteristics of the different Si reference electrodes were evaluated (Table SI.1). Their thickness was determined with a palmer and their porosity was estimated from the true density of each electrode component that was measured on a Helium pycnometer. The porosity turns out to be a fundamental aspect to prepare good Si anodes. Nevertheless, we need to strike the right balance between a too high porosity which penalises electronic contact or a too compact electrode with no buffer volume to successfully accommodate the Si volumes variations<sup>212</sup>. Actually, we have shown the detrimental effect of calendaring the cycling performances of our Si electrodes (Figure SI.IV.2).

### c. Battery assembling and cycling performances

During the alloying process of Si with lithium, various stable intermediates can be formed under heat treatment  $\text{Li}_{12}\text{Si}_7$  ( $\text{Li}_{1.7}\text{Si}$ ),  $\text{Li}_7\text{Si}_3$  ( $\text{Li}_{2.3}\text{Si}$ ),  $\text{Li}_{13}\text{Si}_4$  ( $\text{Li}_{3.25}\text{Si}$ ) and  $\text{Li}_{22}\text{Si}_5$  ( $\text{Li}_{4.4}\text{Si}$ )<sup>213</sup>. Note that at ambient temperature, a new phase,  $\text{Li}_{15}\text{Si}_4$  ( $\text{Li}_{3.75}\text{Si}$ ), is the highest lithiated phase achievable by electrochemical reaction of Si with lithium, with a specific capacity of 3579 mAh/g<sub>Si</sub><sup>88</sup>. This attractive theoretical value goes hand in hand with the linear volume expansion of the above-mentioned  $\text{Li}_x\text{Si}$  phases (Figure IV.3). As reported in the introduction of Chapter III, these colossal volume changes are responsible for : delamination, cracking and pulverization, and the SEI layer instability<sup>87</sup>, hence hindering the cycling performances of Si electrodes.

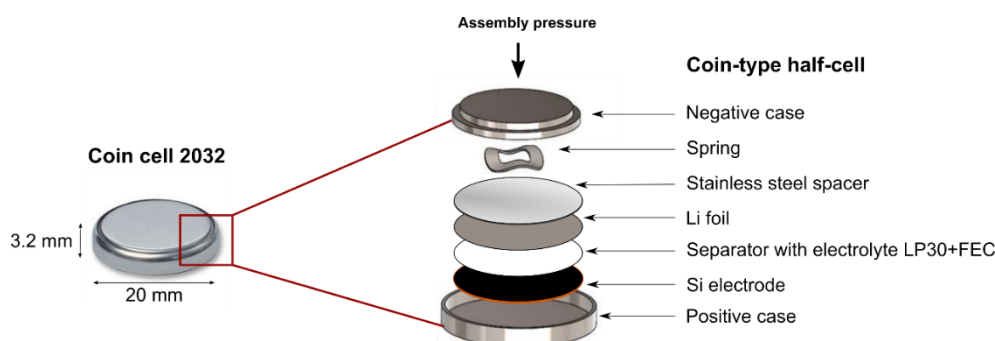


**Figure IV.3: Volume variation of  $\text{Li}_x\text{Si}$** , calculated from the reported lattice parameters of the  $\text{Li}_x\text{Si}$  phases<sup>214</sup>

In the following section, we report our cycling protocol to study the influence of the formulation parameters (Si particle sizes and solvent of the slurry preparation) on both the lithiation/delithiation mechanisms and the cycling performances of our Si electrodes.

### Half-cell assembly and cycling protocol

To investigate the cycling performances of the prepared Si electrodes, coin cells were assembled in an argon-filled glovebox (Figure IV.4). Such cell configuration was preferred to Swagelock® cells because good airtightness and reproducible applied pressure can be achieved. Indeed, coin cells are sealed by an automatic crimping machine. Lithium (Li) half-cells were assembled using Li metal as the counter electrode and our homemade LP30+FEC electrolyte prepared by adding 5%<sub>w</sub>t of 4-fluoro-1,3-dioxolan-2-one (FEC) to a commercial LP30 electrolyte. FEC is an often-used electrolyte additive that promotes the formation of a protective and flexible SEI able to accommodate Si volume changes upon cycling<sup>215,216</sup>.



**Figure IV.4: Photograph and schematic representation of a 2032 coin cell.**

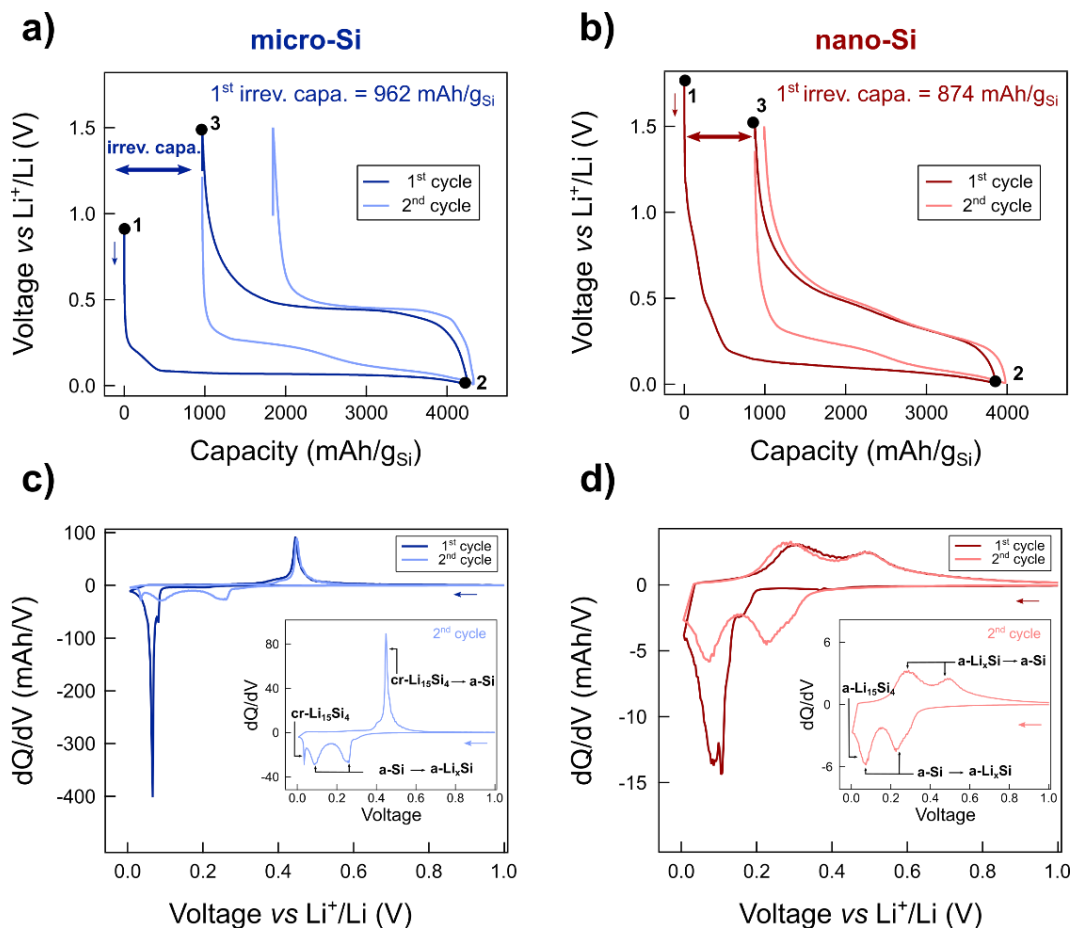
The electrochemical performances of the cells were studied by galvanostatic discharge-charge cycling at constant current in the voltage range of 0.005 – 1.5 V vs. Li<sup>+</sup>/Li. The cells were cycled at C/10 (~360 mA/g<sub>Si</sub>) for at least 50 cycles. All specific capacities and current densities in this study are based on the mass of Si, that we estimated for each electrode (see 1.b).

### Influence of the particles size

First, the influence of the Si particles size was studied by cycling coin-type half cells assembled with micro-Si and nano-Si electrodes prepared from the aqueous slurry process. Figure IV.5 reports the corresponding galvanostatic discharge-charge profiles of the two first cycles, with the voltage vs specific capacity plots (Figure IV.5.a & b) and the differential capacity (dQ/dV) curves (Figure IV.5.c & d) for micro-Si (blue) and nano-Si (red).



Each cycle of the voltage vs capacity plots can be divided into two regimes : the discharge (points 1 to 2, 1<sup>st</sup> cycle), which corresponds to the electrochemically-driven alloying process of Si to form the  $\text{Li}_{15}\text{Si}_4$  phase and the following charge (points 2 to 3, 1<sup>st</sup> cycle) associated to the delithiation of Si (Figure IV.5.a & b). During the first discharge, micro-Si and nano-Si produce high capacities of 4243 and 3845 mAh/g<sub>Si</sub> respectively. After the subsequent charge, they display irreversible capacity losses of 962 and 874 mAh/g<sub>Si</sub> respectively, which correspond to approximately 23% of their respective initial discharge capacity. Such a large irreversibility loss for Si composite electrodes is commonly attributed either to the electrolyte decomposition at so low potential to form the SEI, or to consequences of Si volume changes that leads to the electrical isolation of disconnected Si particles<sup>91</sup>. During the second cycle, lower capacities are reached. Interestingly, a significant irreversible capacity loss is still observed for micro-Si whereas for nano-Si almost the full discharge capacity is recovered.



**Figure IV.5: Galvanostatic discharge-charge profiles for micro-Si and nano-Si.** Coin-type half-cells were assembled with micro-Si and nano-Si electrodes (Si/Csp/PAA in water). They were cycled at C/10 between 0.005 V and 1.5 V. Only the two first cycles are represented (1<sup>st</sup> cycle in dark, 2<sup>nd</sup> cycle in light). **a) and b)** Voltage vs specific capacities curves for a) micro-Si and b) nano-Si. **c) and d)** Differential capacity vs voltage curves for c) micro-Si and d) nano-Si. The 2<sup>nd</sup> cycles are enlarged in the inset panels.

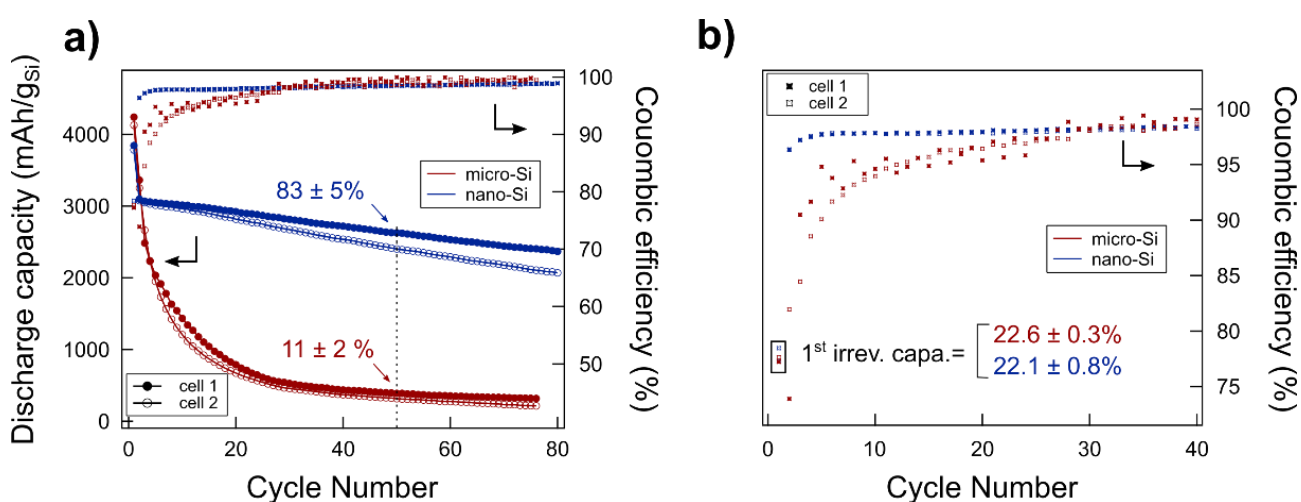
The electrochemical reaction of lithium with Si at room temperature differs from micro-Si and nano-Si electrodes, as underlined by the differential capacity ( $dQ/dV$ ) vs potential curves which amplify the voltage vs capacity profiles (Figure IV.5.c & d).

For micro-Si, during the first discharge, the lithiation process is observed through the plateau at around 0.07 V where amorphous  $\text{Li}_x\text{Si}$  is formed (Figure IV.5.a). When the lithium concentration reaches the critical value of  $x=3.75$ , the transformation of amorphous  $\text{a-Li}_{15}\text{Si}_4$  into the crystalline  $\text{cr-Li}_{15}\text{Si}_4$  induces a slope change<sup>89</sup>. During the following charge, the  $dQ/dV$  curve exhibits a sharp delithiation peak (flat plateau on the voltage curve), which indicates a two-phase region (Figure IV.5.c). Si does not transform back into the original crystalline Si (cr-Si) but remains in its amorphous state (a-Si). During the 2<sup>nd</sup> cycle discharge, two lithiation peaks are noted due to the amorphous phase changes ( $\text{a-Li}_x\text{Si}$ ). The crystallisation of  $\text{Li}_{15}\text{Si}_4$  is manifested by the well-documented small sharp peak at 0.05 V<sup>89</sup>. The 2<sup>nd</sup> cycle charge profile is similar to the 1<sup>st</sup> cycle charge.

For nano-Si, the voltage profile slightly differs from micro-Si during the first lithiation (gently sloping plateau) (Figure IV.5.b). The absence of any sharp delithitation peak in the  $dQ/dV$  plots indicates that nano-Si did not transition to the  $\text{cr-Li}_{15}\text{Si}_4$  (Figure IV.5.d). The resulting two delithitation peaks stand for the amorphous phase changes  $\text{a-Li}_x\text{Si} \rightarrow \text{a-Si}$ . In theory,  $\text{cr-Li}_{15}\text{Si}_4$  should occur independently from the particles size, notwithstanding several studies have also enlightened the absence of crystallisation of  $\text{Li}_{15}\text{Si}_4$  at 0.05 V for Si nanoparticles<sup>203</sup>. We highlighted that polarization issues may shift the crystallisation under 0 V (data not shown), but we could also consider the reaction between nano- $\text{cr-Li}_{15}\text{Si}_4$  and FEC, as observed by Gao *et al* working under similar conditions<sup>217</sup>.

Once the lithiation and delithitation mechanisms were elucidated for micro-Si and nano-Si electrodes, we evaluated their cycling performances through the analysis of the variation of the discharge capacity and coulombic efficiency upon cycling (Figure IV.6). The coulombic efficiency, defined here as the delithitation capacity divided by the lithiation capacity, indicates the good reversibility of the Si alloying process.

Notably, Si electrodes are losing capacity every cycle. However, despite their similar first irreversible capacities (micro-Si,  $22.6 \pm 0.3\%$  and nano-Si,  $22.1 \pm 0.8\%$ ), nano-Si obviously show better cycling performances than micro-Si. The capacity of the latter dramatically decreases from the outset as witnessed by its poorer initial coulombic efficiencies ( $< 95\%$  during the first 30 cycles, Figure IV.6.b). In order to rationalize this observation, we calculated the corresponding capacity retentions after 50 cycles (=the ratio of delithitation capacity of the 50<sup>th</sup> cycle and the 1<sup>st</sup> cycle, hence not considering the first irreversible capacity loss). While micro-Si only retained  $11 \pm 0.8\%$  of its initial capacity after 50 cycles,  $83 \pm 5\%$  of the capacity was retained for nano-Si with a coulombic efficiency of  $98.52 \pm 0.03\%$ .



**Figure IV.6: Cycling performances of the micro-Si and nano-Si electrodes.** Coin-type half-cells were assembled with micro-Si and nano-Si electrodes (Si/Csp/PAA in water). They were cycled at C/10 between 0.005 V and 1.5 V. **a)** Discharge capacity vs cycle number for micro-Si (red) and nano-Si (blue), with the indication of their respective capacity retention at the 50<sup>th</sup> cycle. **b)** Coulombic efficiencies variation upon the first 40 cycles. Capacities retentions and first irreversible capacities are calculated as the mean of the two duplicate cells.

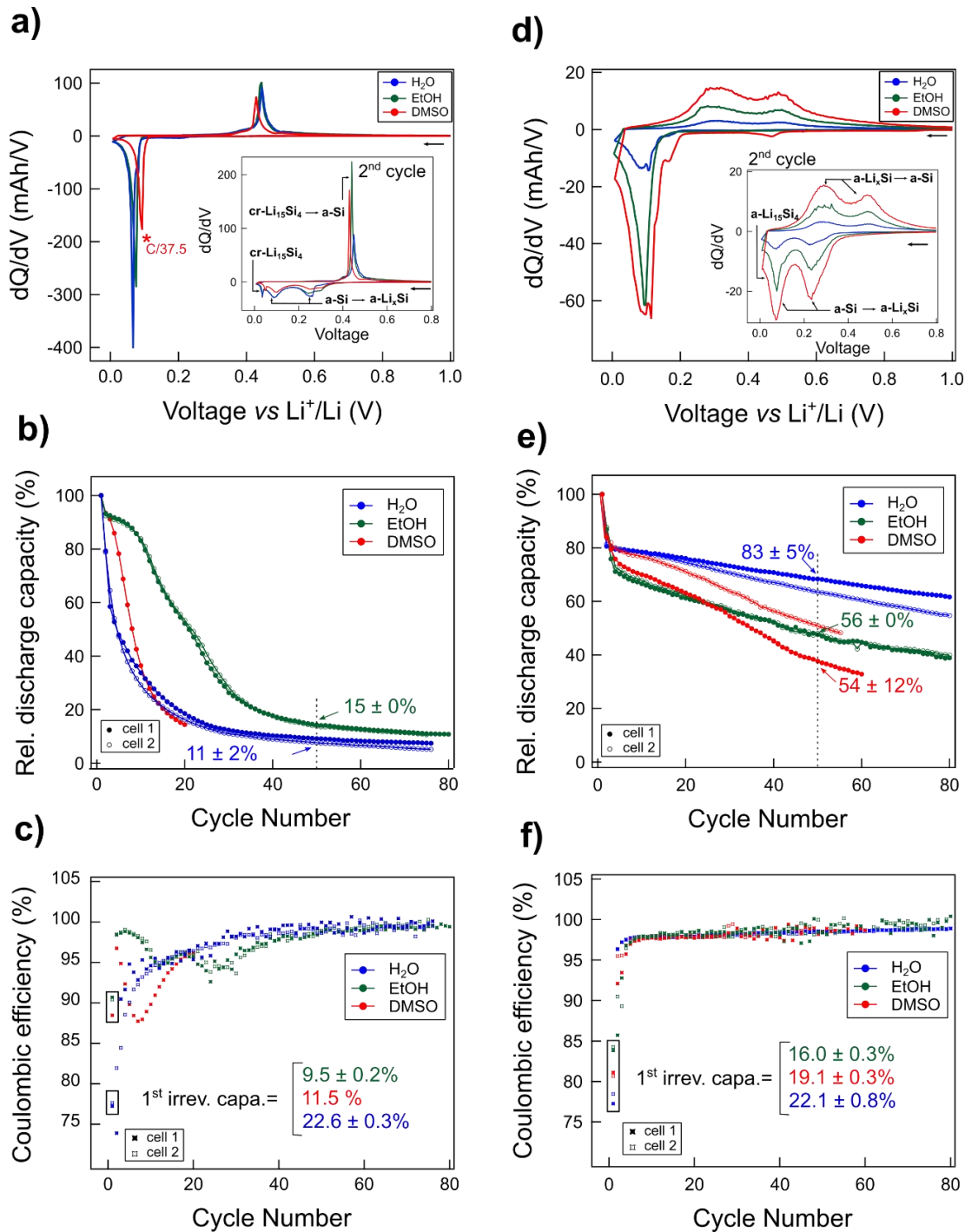
The better cyclability of nano-Si was expected, as downsizing Si particles significantly enhances the fracture tolerance of electrodes as well as mitigate the physical stress<sup>205</sup>. This hypothesis was verified in our lab by placing non-invasive optical sensors on the top of our micro and nano-Si electrodes to measure their stress evolution upon cycling (L. Albero Blanquer *et al.* under review). Interestingly it was found that during the first lithiation, the stress response of micro-Si is drastic passing through a maximum (63 MPa), that we linked to cracking and the onset of pulverization mechanisms. For nano-Si, the stress increases more smoothly and regularly to reach a maximum value around three times lower than for micro-Si (26 MPa).

Finally, we explored the critical role of the Si particles size and morphology on the cycling performances via SEM. At pristine states, the cross-sections of both electrodes (Figure SI.IV.3) show relatively similar thickness (16.4 vs 7.2  $\mu\text{m}$  for micro and nano-Si respectively). Nevertheless, after cycling, micro-Si electrode delaminated (111  $\mu\text{m}$ ), while the electrode cohesion was maintained for nano-Si (11  $\mu\text{m}$ ). Additionally, both the size and depth of cracks are greater for micro-Si than for nano-Si. Altogether, these experiments rationalized the poorer cycling performances of micro-Si.

### **Influence of the solvent of the slurry preparation**

We next investigated the role played by the solvent used in the slurry process on the cycling performances of the reference Si electrodes. The results are reported in Figure IV.7, left and right for micro-Si and nano-Si respectively. According to the  $dQ/dV$  plots (Figure IV.7.a & d), both the lithiation and delithiation mechanisms are not affected and the red-ox processes occur at the same potentials for these three solvents of slurry. On the one hand, micro-Si lithiation still ends up with the formation of  $\text{cr-Li}_{15}\text{Si}_4$  (small sharp peak at 0.05 V, Figure IV.7.a). Note that the slight shift of the lithiation and delithiation peaks of DMSO-based micro-Si only results from the change in C-rate (C/37.5 vs C/10, marked with an asterisk). On the other hand, no crystallisation was observed for nano-Si. The difference in amplitude in  $dQ/dV$  plots (Figure IV.7.a & d) should not be considered since it is a consequence of the different Si loadings of the electrodes (Table SI.IV.1).

When it comes to comparing cycling performances, we intentionally plotted the relative discharge capacity - normalisation against the 1<sup>st</sup> discharge capacity - vs the cycle number. Both micro-Si and nano-Si show similar capacity retention trends independently of the solvent used for the slurry preparation (Figure IV.7.b & e). A severe decline of capacity is observed for micro-Si, while nano-Si exhibit flatter capacity retentions. Interestingly, the drastic loss in capacity for micro-Si seems to be slightly mitigated for ethanol-based slurries during the first 20 cycles, as underlined by the higher coulombic efficiency (Figure IV.7.c). On the contrary, the capacity retention of nano-Si is not favoured by switching from water to ethanol since it is estimated to  $83 \pm 5\%$  and  $56 \pm 1\%$  after 50 cycles respectively. DMSO-based nano-Si electrodes show the lowest capacity retention ( $54 \pm 12\%$ ) despite the reproducibility issues that arise. The reasons of the difference in capacity retention remain yet unclear. It could be nested in the affinity between the solvent and the electrode components that affects the slurry homogeneity and the resulting cohesion of the electrode or the porosity.



**Figure IV.7: Influence of the solvent used for the slurry process on the cycling performances of the micro-Si and nano-Si electrodes.** Micro-Si and nano-Si electrodes (Si/Csp/PAA) were prepared in water (blue), ethanol (green) and DMSO (red). Coin-type half-cells were assembled in duplicate and cycled between 0.005 V and 1.5 V at C/10, except the DMSO-based micro-Si electrode labelled with an asterisk (C/37.5). **a) and d)** Differential capacity vs voltage curves of the two first cycles for a) micro-Si and d) nano-Si. **b) and e)** Relative discharge capacity vs cycle number plots for b) micro-Si and e) nano-Si with the indication of the respective capacity retention at the 50<sup>th</sup> cycle. **c) and f)** Coulombic efficiency variations of c) micro-Si and f) nano-Si upon the first 80 cycles with the indication of the first irreversible capacity. Capacity retentions and 1<sup>st</sup> irreversible capacities are calculated as the mean value of the two duplicate cells.

Furthermore, the first irreversible capacity loss strongly depends on the solvent used for the slurry preparation, especially for micro-Si electrodes ( $22.6 \pm 0.3\%$  for water,  $9.5 \pm 0.2\%$  for ethanol and  $11.5\%$  for DMSO). The nano-Si electrodes show the same trend ( $22.1 \pm 0.8\%$  for water,  $16.0 \pm 0.3\%$  for ethanol and  $19.1 \pm 0.3\%$  for DMSO) but they exhibit higher irreversible capacity values, owing to their greater surface area which induces more parasitic reactions at the electrode/electrolyte interface (SEI). Such trend between solvents might originate from an imperfect drying of the electrodes leading to solvent residuals. Note that we cannot fully rule out the porosity effect.

This study clearly highlights how formulation can drastically affect the cycling performances of Si particles and therefore justifies that this step was mandatory prior to explore the performances of PR-PAA binders. Moreover, to strengthen the quality of our investigation, we felt it was needed to benchmark our binders' performances against the performances of "credible" reference Si electrodes, which is unfortunately often not the case in many studies dealing with the design of new binders<sup>98,100,102,166</sup>. Whatever, the influence of PR-PAA binders on the performances of Si anodes are next described.

### 3. Evaluation of the cycling performances of PR-PAA binders

PR-PAA binders are referred according to the nomenclature adopted in Chapter III and their cycling performances are discussed next. In the interests of clarity, Table IV.1 summarizes the structural parameters of the different mechanically interlocked architectures which have been prepared. We also added the PR-PAA network that was used in the work of Choi<sup>101</sup> (data in red).

Sample	PR <b>X</b> = ( <b>x</b> K, <b>rc</b> )		<b>y</b> PR/PAA mass ratio (% <sub>wt</sub> )	<b>z</b> Cross-linking degree (% <sub>COOH</sub> )
	<b>x</b> POE molecular weight ( $\times 10^3$ g.mol <sup>-1</sup> )	<b>rc</b> PR ring coverage (%)		
<b>PR-PAA 1</b>	10	25	5	0.5
<b>PR-PAA 2</b>	10	50	5	0.5
<b>PR-PAA 3</b>	10	50	10	0.5
<b>PR-PAA 4</b>	10	50	20	0.5
<b>PR-PAA 5</b>	10	50	5	5
<b>PR-PAA 6</b>	35	high	5	0.5
<b>PR-PAA 7</b>	100	high	5	0.5
<b>PR-PAA 8</b>	100	high	5	5
<b>PR-PAA 9</b>	100	low	5	0.5
<b>PR-PAA</b>	<b>20</b>	<b>29</b>	<b>5</b>	<b>0.5</b>

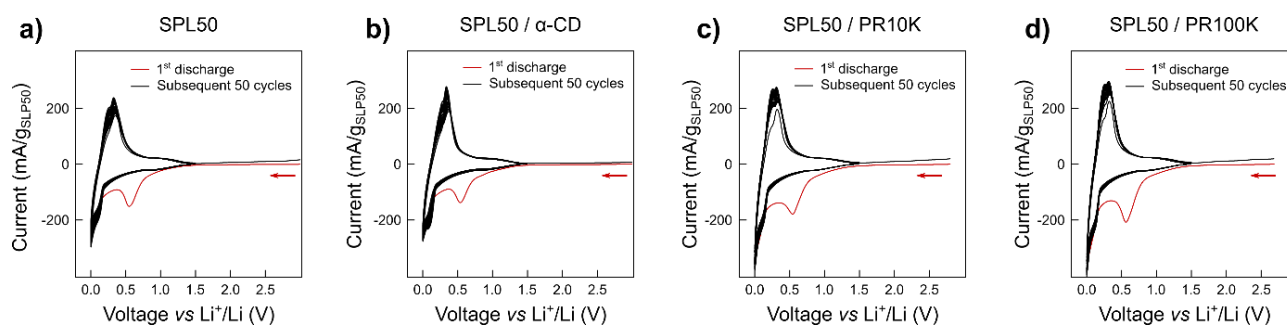
**Table IV.1: Structural parameters of the PR-PAA binders.**

#### a. Electrochemical stability

Prior to examine the performances of PR-PAA binders, we ensured that they were electrochemically stable at low potentials. Using graphite (SLP50) as a model material ( $372 \text{ mAh.g}^{-1}$ ), we conducted cyclic voltammetry studies and galvanostatic cycling. This choice is justified by the fact that graphite operates in the same voltage window as Si [0.005-1.5 V] and it is more processable.

#### Cyclic voltammetry

Cyclic voltammetry was carried out to evaluate the electrochemical stability of  $\alpha$ -CD architectures composing the PR-PAA binders (Figure IV.8). Native  $\alpha$ -CD and two  $\alpha$ -CDs-based PR differing by the molecular weight of their threading polymer (PEO 10K and PEO 100K) were hand-milled together with a powder mixture based on SLP50/Csp (80:20%<sub>wt</sub>). Li half-cells were assembled using LP30 electrolyte in a Swagelock® configuration and cyclic voltammograms (CVs) were recorded in the voltage range of 0.005-1.5 V at a scan rate of  $0.2 \text{ mV.s}^{-1}$ .



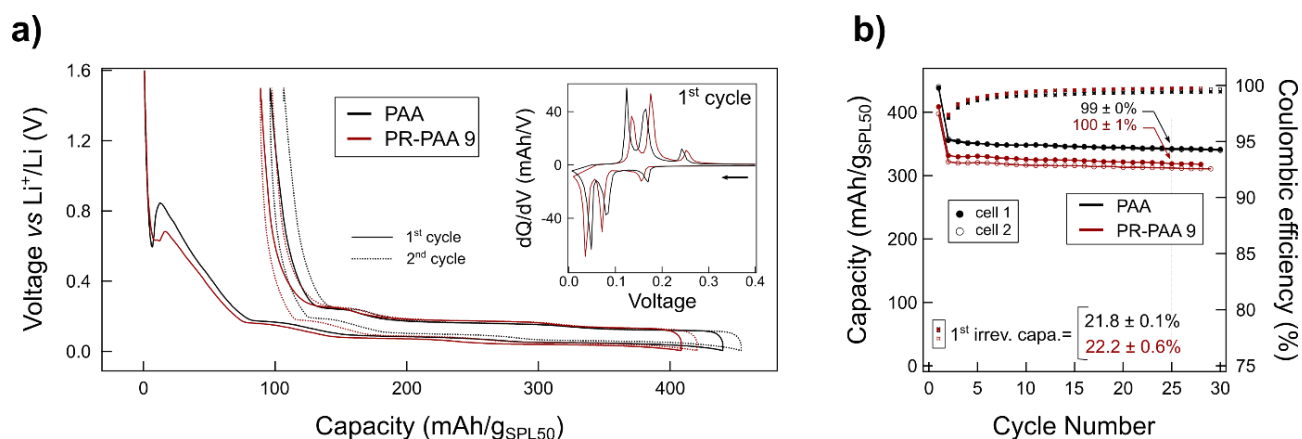
**Figure IV.8: Cyclic voltammograms of  $\alpha$ -CD architecture/graphite/Csp mixtures in LP30 vs Li metal.** CV starts from open circuit voltage (OCV). Current is normalised with the mass of graphite (SLP50). SLP50/Csp ratio was maintained to (80:20 %wt) and  $\alpha$ -CD architectures were added in 25%wt of the total mass. 50 cycles at a scan rate of  $0.2 \text{ mV}\cdot\text{s}^{-1}$  were recorded for **a)** the reference SLP50/Csp (7.85 mg), **b)** SLP50/Csp/ $\alpha$ -CD (6.32 mg), **c)** SLP50/Csp/PR10K (3.93 mg) and **d)** SLP50/Csp/PR100K (3.81 mg).

It must be observed that the four CV profiles are identical, showing an irreversible anodic peak at 0.6 V which is ascribed to the formation of SEI. A pair of broad cathodic (0.4 V) and anodic (0.1 V) reversible peaks reflect the delithitation and lithium insertion respectively in graphite. No additional peaks can be seen on the CVs of  $\alpha$ -CD architectures, hence confirming their electrochemical stability at low potentials.

#### PR-PAA as graphite anode binders

Then, graphite electrodes were prepared to verify the use of PR-PAA as binders focusing on the slurry preparation and the adhesion on the copper substrate. For this study, SLP50, Csp, PR-PAA 9 or PAA were mixed in 92:4:4 weight ratio and solubilized in water for 24h (37% dry mass ratio for PAA and 33% for PR-PAA) and the resulting slurry was casted as described earlier (see 2.b). SLP50 loadings were estimated to  $4.3 \pm 0.2 \text{ mg}\cdot\text{cm}^{-2}$  and  $4.8 \pm 0.2 \text{ mg}\cdot\text{cm}^{-2}$  for PAA and PR-PAA respectively. Half-type coin cells were assembled using LP30+FEC electrolyte and Li metal as the counter electrode and each experiment was duplicated. Galvanostatic cycling was carried out at C/10 between 0.005 and 1.5 V (Figure IV.9).





**Figure IV.9: Galvanostatic cycling of graphite electrodes with PAA and PR-PAA as binders in LP30+FEC vs Li metal.**

**a)** Voltage vs Capacity curves of the two first cycles of PAA (black) and PR-PAA 9 (red). The corresponding differential capacity curves ( $dQ/dV$ ) for the 1<sup>st</sup> cycles are overlapped in the inset. **b)** Discharge capacity vs cycle number plots and coulombic efficiencies variation upon the first 30 cycles with the indication of the capacity retention at the 25<sup>th</sup> cycle and the first irreversible capacity. Capacities retentions and 1<sup>st</sup> irreversible capacities are calculated as the mean value of the two duplicate cells.

Voltage vs capacity curves for PAA and PR-PAA almost perfectly overlap for the two first cycles (Figure IV.9.a). Lithium insertion in graphite occurs through the well-known multi-step process as shown by the three plateaux in discharge (0.18 V, 0.09 V and 0.02 V), that can be better distinguished as three anodic peaks on the differential capacity curves ( $dQ/dV$ ). Three cathodic peaks (0.12 V, 0.18 V, 0.25 V) are associated to the delithitation stages of graphite. These peaks were not detected on the CV performed on graphite in powder, most likely owing to the too fast scan rate (Figure IV.8.a). Moreover, we assume that the small shifts in the graphite intercalation/desintercalation peaks that can be observed between PAA and PR-PAA only result from the small polarization differences between the cells.

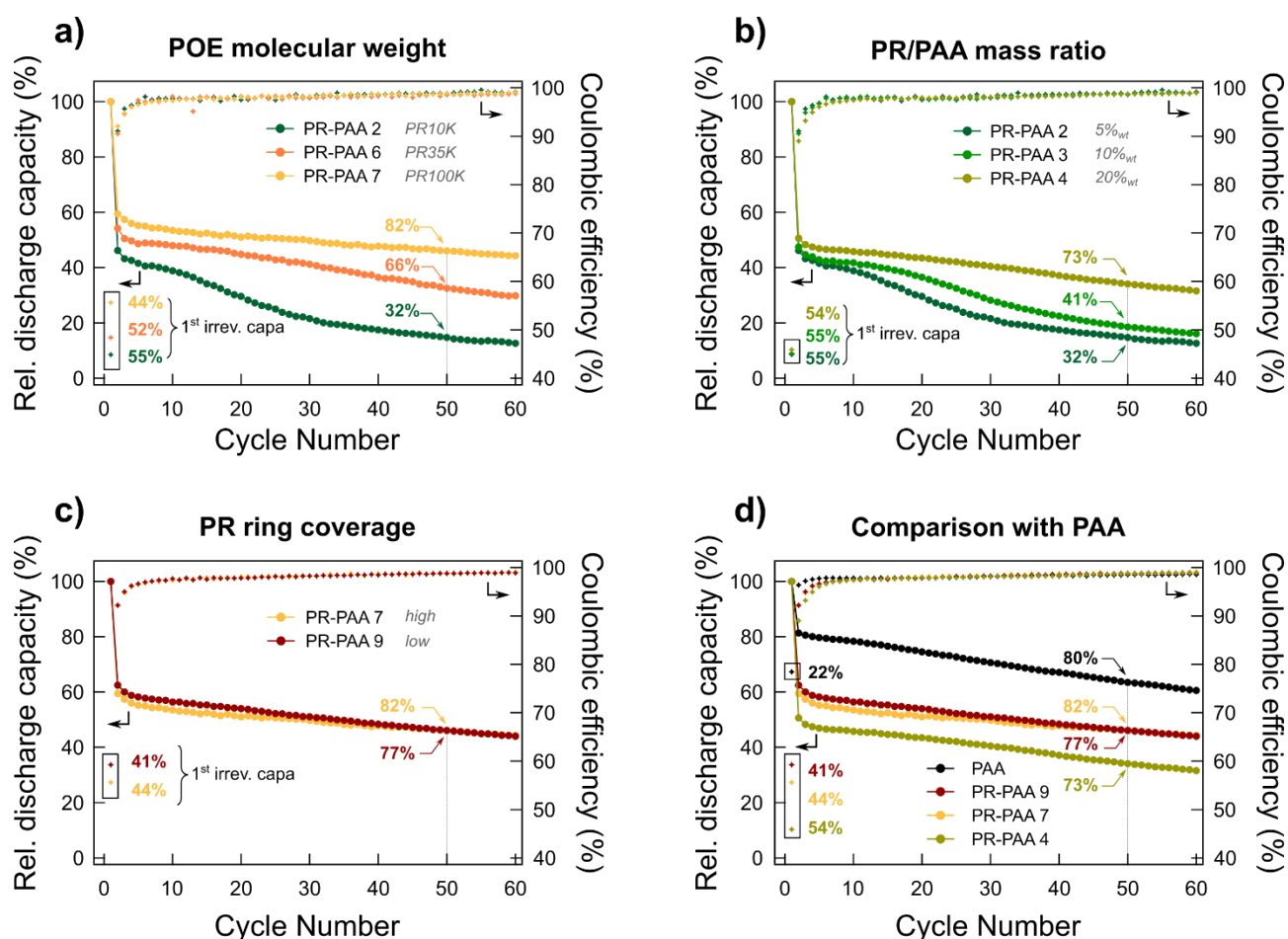
During the first discharge, PAA and PR-PAA graphite electrodes produce high capacities of 440 and 409 mAh/g<sub>SPL50</sub> respectively (Figure IV.9.a), with identical irreversible capacity losses corresponding to approximately 22% of their respective initial discharge capacity. These irreversibility losses are mainly associated to the SEI formation. After 25 cycles, the capacity retentions – calculated as the 25<sup>th</sup> charge capacity divided by the 1<sup>st</sup> charge capacity – are impressive both for PAA and PR-PAA (~100%) (Figure IV.9.b). Equally, high coulombic efficiencies (99.74% for PR-PAA vs 99.51% for PAA after 25 cycles) can be obtained.

Having checked that PR-PAA binders do not show any detrimental effect at low potentials, the series of PR-PAA binders was analysed through their electrochemical performances in Si composite anodes in half-cell batteries. Our first idea was to tackle the short cycle-life of micro-Si (Figure IV.7.b), which are more susceptible to pulverization during the severe volume variations of Si as compared with their nano-Si counterparts. In reality, it turns out that the capacity fading induced by these volume expansions is excessively drastic, and our expectations for PR-PAA binders to strikingly mitigate this loss for micro-Si were too high (Figure SI.IV.4). Nevertheless, we succeeded in enhancing both the capacity retention and coulombic efficiency of such micro-sized particles during the 5 first cycles, attributing these improvements to the better stress dissipation of PR-PAA binders as compared with PAA.

In spite of such improvements, the capacity decay was remaining too severe. Thus, we decided to conduct our study on nano-Si rather than micro-Si particles, that were already shown to display a better capacity retention. So from on, we solely focus on nano-Si electrodes.

#### b. Aqueous formulation

According to the formulation protocol established in water (see 2.b), Si anodes were produced using PR-PAA binders. Their cycling performances are reported in Figure IV.10. The influence of the different PR-PAA structural parameters (Table IV.1) was examined: the PEO molecular weight ( $x$ , Figure IV.10.a), the PR/PAA mass ratio ( $y$ , Figure IV.10.b) and the PR ring coverage ( $r_c$ , Figure IV.10.c). Note that for lack of time, we have not included the role played by the crosslinking density ( $z$ ) since the cells are still cycling at the moment of writing.



**Figure IV.10: Cycling performances of aqueous nano-Si electrodes incorporating PR-PAA binders.** Galvanostatic cycling was performed at C/10 in LP30+FEC vs Li metal between 0.005 V and 1.5 V. Nano-Si electrodes were made through the aqueous slurry process and consist of nano-Si/Csp/PR-PAA in weight ratio of (2:1:1). Their Si loadings are lower than  $0.7 \text{ mg}_{\text{Si}}\cdot\text{cm}^{-2}$ . The relative discharge capacities were calculated by normalising the discharge capacity of each cycle by the initial discharge capacity. The capacity retentions after 50 cycles – 50<sup>th</sup> charge capacity divided by the 1<sup>st</sup> charge capacity – are reported on the plots as well as the first irreversible capacity losses. **a)** Influence of the PEO molecular weight: PR-PAA 2 (dark green,  $0.5 \pm 0.1 \text{ mg}_{\text{Si}}\cdot\text{cm}^{-2}$ ), PR-PAA 6 (orange,  $0.2 \pm 0.1 \text{ mg}_{\text{Si}}\cdot\text{cm}^{-2}$ ) and PR-PAA 7 (yellow,  $0.3 \pm 0.1 \text{ mg}_{\text{Si}}\cdot\text{cm}^{-2}$ ). **b)** Influence of the PR/PAA mass ratio: PR-PAA 3 (light green,  $0.6 \pm 0.2 \text{ mg}_{\text{Si}}\cdot\text{cm}^{-2}$ ), PR-PAA 4 (khaki green,  $0.2 \pm 0.1 \text{ mg}_{\text{Si}}\cdot\text{cm}^{-2}$ ). **c)** Influence of the PR ring coverage: PR-PAA 9 (red,  $0.6 \pm 0.1 \text{ mg}_{\text{Si}}\cdot\text{cm}^{-2}$ ). **d)** Comparison with the cycling performances of the reference Si electrode (nano-Si/Csp/PAA 2:1:1 in water,  $0.5 \pm 0.1 \text{ mg}_{\text{Si}}\cdot\text{cm}^{-2}$ ).

### Cycling performances

First, the influence of the **PEO molecular weight** was examined (Figure IV.10.a), comparing PR-PAA 2 (PR10K), PR-PAA 6 (PR35K) and PR-PAA 7 (PR100K). During the initial cycles, the three capacity retentions are relatively steady, but PR-PAA 2 and PR-PAA 6 undergo an accelerated decline in capacity at the 10<sup>th</sup> and 20<sup>th</sup> cycle respectively. This results in the poor capacity retentions of 32% for

PR-PAA 2 and 56% for PR-PAA 6 after 50 cycles. Notably PR-PAA 7 exhibits the best performances since it retains 82% of its initial capacity after 50 cycles.

Thereafter, we looked at the **PR/PAA mass ratio** (Figure IV.10.b). We also notice a point of significant capacity fading for PR-PAA 3 (10%<sub>wt</sub>), but this onset of capacity fade is delayed compared to PR-PAA 2 (5%<sub>wt</sub>), since it occurs at the 18<sup>th</sup> cycle. Interestingly, increasing the PR/PAA mass ratio to 20%<sub>wt</sub> (PR-PAA 4) leads to a flatter capacity retention profile. As a comparison, PR-PAA 4 exhibits a 73% capacity retention after 50 cycles, whereas PR-PAA 2 and PR-PAA 3 only reach 32% and 41% respectively.

Then, we compared PR-PAA 7 with PR-PAA 9 to investigate the influence of the **PR ring coverage** working with PR100K (Figure IV.10.c). After 50 cycles, almost identical capacity retentions are achieved whether the PR ring coverage is high (PR-PAA 7, 82%) or low (PR-PAA 9, 77%). However, we note that a better cyclability is observed for PR-PAA 9 during the first 20 cycles, which is in accordance with our expectations. Indeed, a more pronounced  $\alpha$ -CD sliding motion should improve the electrochemistry performances (Figure IV.10.c).

Lastly, we confronted the cycling performances of PAA and the best PR-PAA binders (Figure IV.10.d). Some promising findings are underscored, since after 50 cycles, the capacity retention of PR-PAA 7 exceeds the one of PAA (82% vs 80% for PAA). This trend is even more stressed after 25 more cycles (75% vs 70% for PAA) (Figure SI.IV.5). Nevertheless, the most apparent aspect is the significant first irreversible capacity losses of PR-PAA. They vary between 41% and 55% depending on the binder, while we only report a 22% irreversible initial capacity for PAA. This severe issue prevented us to push further the understanding of the relation between structure and electrochemical properties of PR-PAA binders. Instead, we tried to unveil the origin of this major first irreversible capacity loss, occurring in the aqueous Si anodes incorporating PR-PAA binders.

### **Understanding the first irreversible capacity loss**

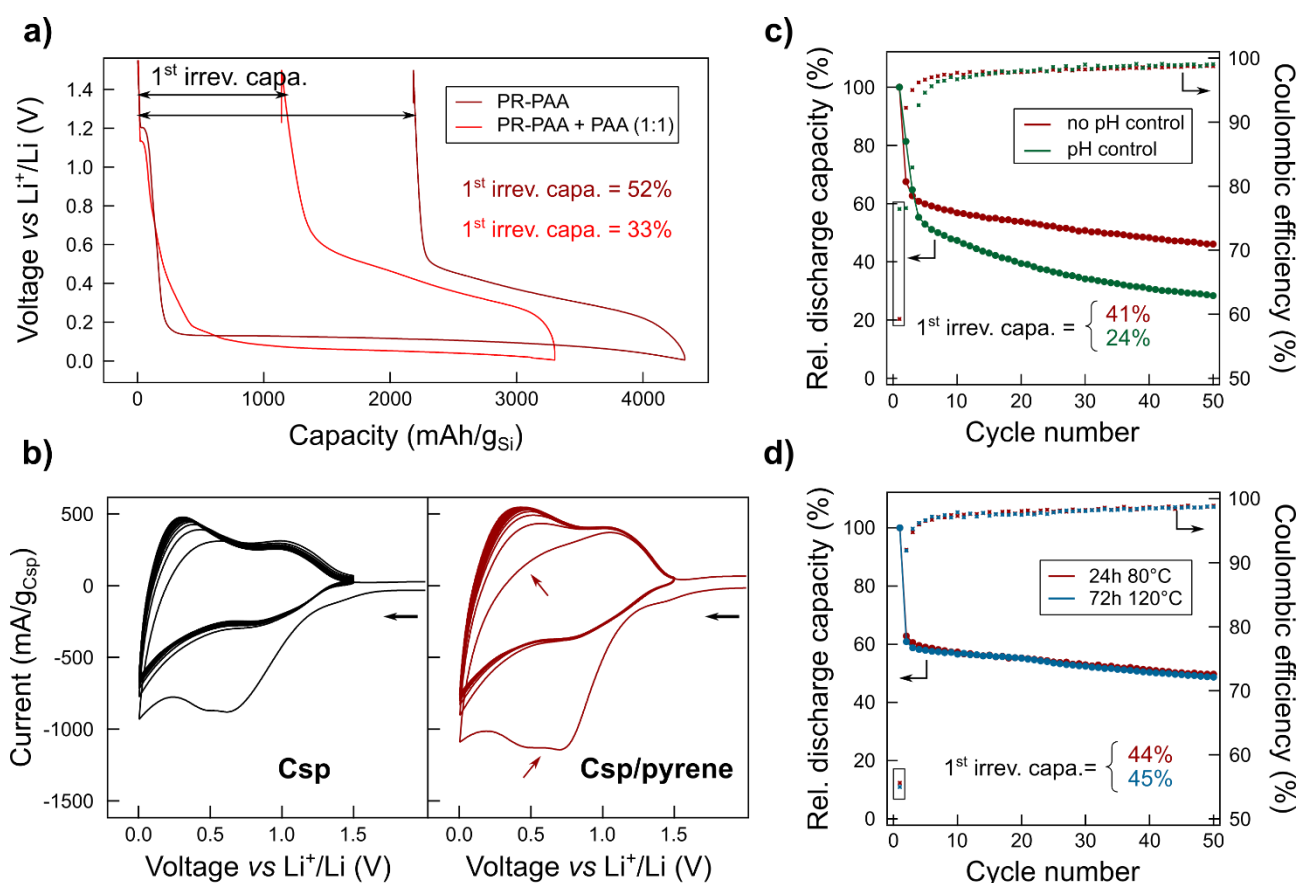
The large irreversibility that we have brought to light above cannot be attributed neither to the electrolyte decomposition, nor to the consequences of Si volume changes since exactly the same experimental conditions were used to cycle our reference Si electrodes (see 2.c). Therefore, it can only be induced by our PR-PAA binders. Several sets of experiments were conducted to elucidate

the origin of this initial capacity loss by looking again at (i) the electrochemical stability of PR-PAA, or (ii) investigating the stability of PR-PAA during the water-based slurry process. Key experiments are reported in Figure IV.11 while the others can be found in Supplementary Information (Table SI.IV.2 & Figures SI.IV.6-8).

We found that **electrochemical degradation of PR-PAA** (i) upon cycling might lead to the formation of a thick SEI layer which blocks the Li transport to the Si particles. This assumption is supported by the higher ohmic resistances measured after the 1<sup>st</sup> delithiation for PR-PAA electrodes (Table SI.2) and the intense sharp signal at 110 mV which emerges in the differential capacity curves (dQ/dV) for PR-PAA electrodes (Figure SI.IV.6). Next, we prepared a nano-Si electrode in which a mixture of PAA and PR-PAA (1:1) was incorporated as the binder (Figure IV.11.a). The lower irreversible capacity loss observed during the first cycle (33% vs 52% for PR-PAA alone), reinforces the causal relationship between PR-PAA and the first irreversibility.

Later, considering the chemical composition of PR-PAA, we questioned the pyrene extremities of our PRs which are the only difference lying between our binders and the one synthesized by Choi et al, equipped with dinitrobenzene<sup>101</sup>. Despite the successful implementation of pyrene in low potential binders<sup>104</sup>, we performed cyclic voltammetry (CV) on Csp alone and on a Csp/pyrene mixture to compare their electrochemical signatures (Figure IV.11.b). The first anodic peak of the Csp/pyrene mixture is broader than Csp, indicating an additional reduction, and the reduced intensity of the following cathodic peak could confirm the formation of a passivating layer that might hinder the reversible red-ox process. We also considered (Na<sub>2</sub>S<sub>2</sub>O<sub>8</sub>), a synthesis precursor which might exist as residuals in the binder, but the CV of Csp/(Na<sub>2</sub>S<sub>2</sub>O<sub>8</sub>) was strictly identical to the Csp one (Figure SI.IV.7). Consequently, the contribution of PR-PAA to the irreversible capacity loss seems to be verified.

Nevertheless, as no such drastic irreversible capacity loss was observed neither for micro-Si (Figure SI.IV.4) and nor for graphite (Figure IV.8) electrodes, we believe the binder electrochemical stability is not the only feature behind the high irreversibility. Thus, we investigated as a last option the role of the water-based slurry process (ii) and namely possible pH changes.



**Figure IV.11: Investigation of the irreversible capacity loss of aqueous Si anode in which PR-PAA are incorporated as binders. a)** Voltage vs Capacity curves of PR-PAA 6 (dark red) and PAA+PR-PAA 6 (light red). **b)** Cyclic voltammograms of Csp and Csp/pyrene (95:5) mixtures. CV starts from open circuit voltage (OCV) and 10 cycles at a scan rate of 1 mV.s<sup>-1</sup> were recorded. The current is normalised with the mass of Csp. **c)** Influence of the pH on the cycling performances of PR-PAA 9 binder. The slurry pH was controlled at pH ~ 6 through the addition of droplets of NaOH (1 M). **d)** Influence of the drying process on PR-PAA 7 binder. The drying process for the blue curve is 72h at 120°C in a vacuum oven (Büchi). Galvanostatic cycling was performed on aqueous nano-Si electrodes (nano-Si/Csp/binder) at C/10 in LP30+FEC vs Li metal. The dark red curves correspond to the electrodes made through the reference protocol, *ie* 24h of slurry mixing and 24h of drying at 80°C in a vacuum oven (see 2.b)

The possible importance of pH arises bearing the fact that ester bonds that are holding PR-PAA structures through the PEO/pyrene linkage and the PR/PAA cross-links might be broken. To check this point, we prepared a new nano-Si slurry controlling the pH to 6 as compared to nearly 3 in our original electrode preparation (Figure IV.11.c). Although the resulting irreversible capacity loss slightly improved, the capacity retentions immediately got worse after the second cycle, so this pH-controlled procedure cannot be used to solve the initial capacity loss. We also tried to reduce the slurry mixing time from 24h to 4h with no success (Figure SI.IV.8). Finally, we envisioned that the

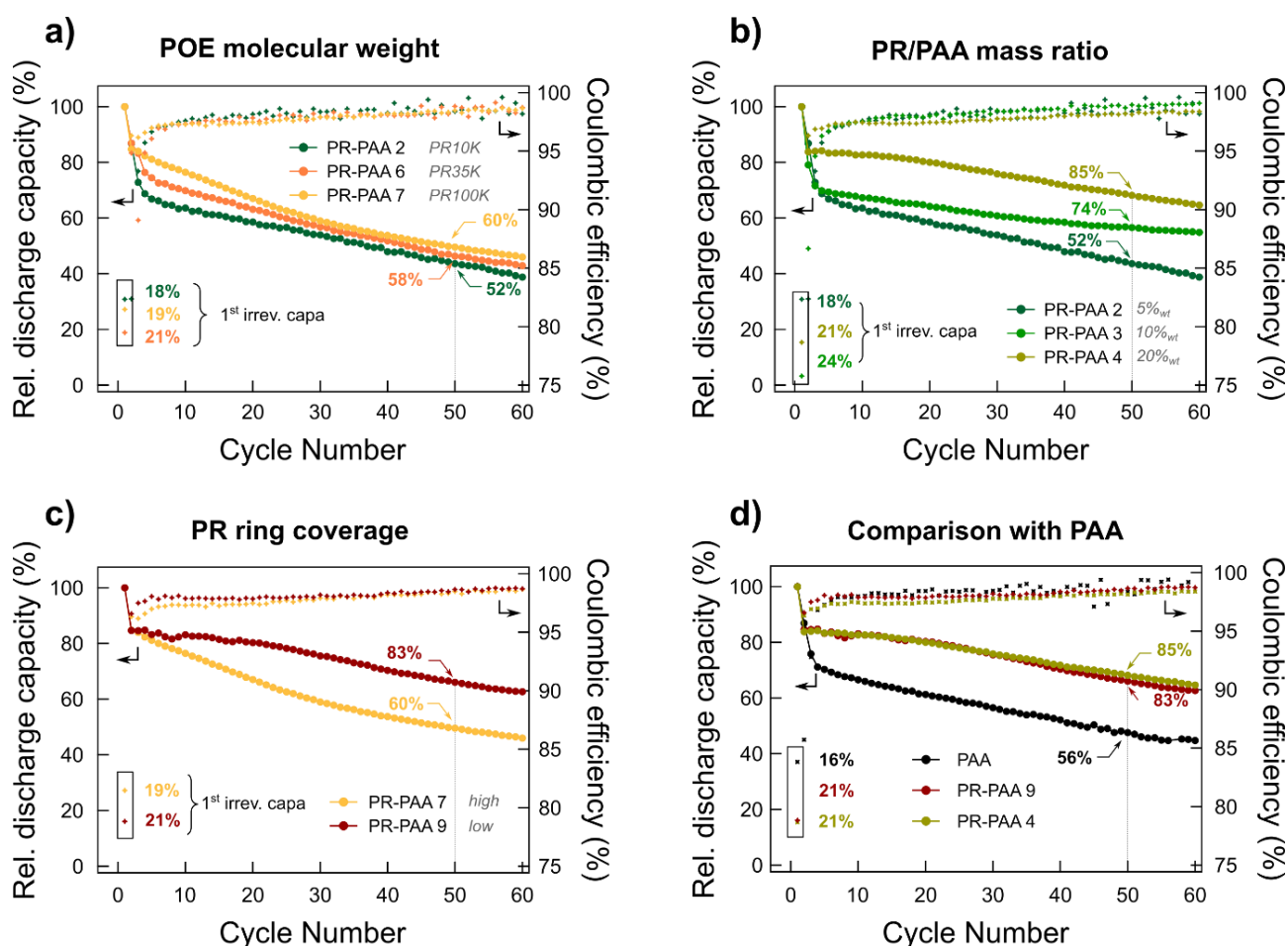
drying process of the Si electrodes was not efficient enough, hence the feasibility of having minute amounts of water traces trapped in the PR tubular architectures. Despite our trials to better dry the PR-PAA electrodes, no improvement of both the irreversible capacity and the capacity retention profiles was detected (Figure IV.11.d).

In conclusion, by conducting a survey of several parameters and colossal amount of experiments, we concluded that such the large initial irreversible capacity was mainly nested in a specific detrimental chemical interaction between PR-PAA, nano-Si and water. Indeed, no comparable capacity loss was noted neither for graphite (Figure IV.9), nor for micro-Si electrodes (Figure SI.IV.4) prepared through the aqueous slurry process and incorporating PR-PAA, hence implying that this synergy is surface dependent. However, we could not find any chemical-physical ways to cure it. Therefore, we decided to modify the slurry process and switch from water to ethanol or DMSO.

### c. Ethanol-based formulation

Accordingly, nano-Si anodes were prepared using PR-PAA binders through either an ethanol-based or a DMSO-based slurry process. Their cycling performances were evaluated similarly as before (Figure IV.12 & Figure SI.IV.9 respectively). The overall trend is an enhanced cyclability for PR-PAA than for PAA. This time, the initial capacity losses are broadly acceptable comparing to the reference electrodes:  $\sim 21 \pm 2\%$  for all PR-PAA vs 16% for PAA when the Si electrodes are prepared in ethanol (Figure IV.12), and  $25 \pm 1\%$  for PR-PAA 9 vs  $19 \pm 0\%$  for PAA for DMSO-based electrodes (Figure SI.IV.9). However, due to better initial coulombic efficiencies and a more environmentally friendly solvent, we focused on ethanol-based electrodes to investigate the relation between structure and electrochemical properties of PR-PAA binders.

Subsequently, Figure IV.12 was built similarly to Figure IV.10 with the study of the influence of the PEO molecular weight (x, Figure IV.12.a), the PR/PAA mass ratio (y, Figure IV.12.b) and the PR ring coverage ( $r_c$ , Figure IV.12.c) on the Si electrodes cyclability.



**Figure IV.12: Cycling performances of ethanol-based nano-Si electrodes incorporating PR-PAA binders.** Galvanostatic cycling was performed at C/10 in LP30+FEC vs Li metal between 0.005 V and 1.5 V. Nano-Si electrodes were made through a slurry process in ethanol and consist of nano-Si/Csp/PR-PAA in weight ratio of (2:1:1). Their Si loadings are lower than  $1 \text{ mg}_{\text{Si}} \cdot \text{cm}^{-2}$ . The relative discharge capacities were calculated by normalising the discharge capacity of each cycle by the initial discharge capacity. The capacity retentions after 50 cycles – 50<sup>th</sup> charge capacity divided by the 1<sup>st</sup> charge capacity – are reported on the plots as well as the first irreversible capacity losses. **a)** Influence of the PEO molecular weight: PR-PAA 2 (dark green,  $0.9 \pm 0.1 \text{ mg}_{\text{Si}} \cdot \text{cm}^{-2}$ ), PR-PAA 6 (orange,  $0.5 \pm 0.0 \text{ mg}_{\text{Si}} \cdot \text{cm}^{-2}$ ) and PR-PAA 7 (yellow,  $0.08 \pm 0.04 \text{ mg}_{\text{Si}} \cdot \text{cm}^{-2}$ ). **b)** Influence of the PR/PAA mass ratio: PR-PAA 3 (light green,  $0.2 \pm 0.1 \text{ mg}_{\text{Si}} \cdot \text{cm}^{-2}$ ), PR-PAA 4 (khaki green,  $0.3 \pm 0.0 \text{ mg}_{\text{Si}} \cdot \text{cm}^{-2}$ ). **c)** Influence of the PR ring coverage: PR-PAA 9 (red,  $0.5 \pm 0.1 \text{ mg}_{\text{Si}} \cdot \text{cm}^{-2}$ ). **d)** Comparison with the cycling performances of the reference Si electrode (nano-Si/Csp/PAA 2:1:1 in ethanol,  $0.4 \text{ mg}_{\text{Si}} \cdot \text{cm}^{-2}$ ).

### Cycling performances

Interestingly, the capacities retentions trends of ethanol-based electrodes are very similar than the ones observed for aqueous electrodes. Notably, a high **PEO molecular weight** seems to improve the cycling performances (Figure IV.12.a). As a result, PR-PAA 7 (PR100K) preserves 60% of its initial capacity after 50 cycles and therefore outperforms both PR-PAA 6 (58%) and PR-PAA 2 (52%).



Although the trend is less pronounced than for aqueous electrodes, this agrees with our expectations according to which a better sliding distance is possible for longer PR.

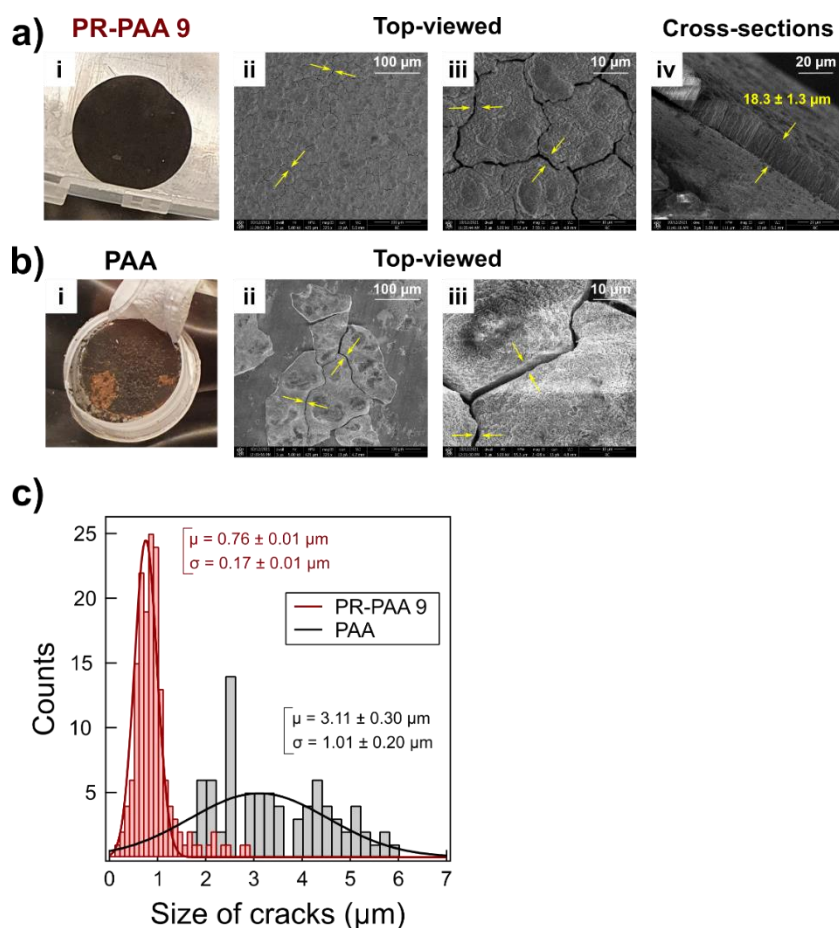
Looking at the **PR/PAA mass ratio**, the red-ox processes of the Si electrode doped with 20%<sub>wt</sub> of PR (PR-PAA 4) are highly reversible during the first five cycles, as shown by a quite high coulombic efficiency for the 5<sup>th</sup> cycle : 96.32% to be compared with 82.36% and 86.67% for PR-PAA 2 (5%<sub>wt</sub>) and PR-PAA 3 (10%<sub>wt</sub>) respectively (Figure IV.12.b). It induces an impressive capacity retention of 85% after 50 cycles, which largely exceeds both PR-PAA 3 and PR-PAA 2 only reaching 74% and 52% respectively.

When it comes to the influence of the **PR ring coverage**, a real improvement arises for PR-PAA 9 which retains 83% of its initial capacity after 50 cycles, compared to PR-PAA 7 which has a higher PR ring coverage resulting in a smaller capacity retention (60%) (Figure IV.12.c). The rationale according to which a low PR ring coverage favour the  $\alpha$ -CD sliding motion is reflected. The main enhancement of the capacity retention is occurring during the first 20 cycles, as it is the case for aqueous electrodes even if it is less pronounced (Figure IV.10.c).

Finally, we compared the cycling performances of PAA and the best PR-PAA binders namely PR-PAA 4 and PR-PAA 9 (Figure IV.12.d). Undeniably, these PR-PAA binders show better cyclability than that of PAA preserving almost one third more capacity than PAA after 50 cycles (56%), and this trend is even more emphasized after 80 cycles (Figure SI.IV.10).

#### **Ex-situ analysis of cycled Si composite electrodes**

The high capacity retentions of PR-PAA 4 and 9 prompted us to study their critical role on the electrochemical performances through the analysis of ethanol-based electrodes morphology by SEM (Figure IV.13). After approximately a hundred of cycles for PAA (107<sup>th</sup> delithitation) and PR-PAA 9 (150<sup>th</sup> delithitation), we dismantled the cells. Visually, the electrode cohesion is preserved with PR-PAA as proven by the smooth surface and no visible degradation, whereas the surface of the reference PAA electrode is highly damaged as the electrode is peeling off (Figure IV.13.i). This striking macroscopic observation reveals the superior role of PR-PAA through the more robust adhesion of the electrode onto the copper foil.



**Figure IV.13: Ex situ SEM characterization of ethanol-based nano-Si electrodes after cycling.** Nano-Si/Csp/binder (2:1:1) electrodes were cycled vs Li metal in LP30+5FEC electrolyte at C/10 between 0.005 V and 1.5 V. Coin cells were dismantled, and the Si electrodes were washed with DMC prior SEM analysis. All images in this figure are obtained under secondary electron mode. The thicknesses and the sizes of the cracks are measured using ImageJ software. The electrodes morphologies were imaged for **a)** PR-PAA 9 and **b)** PAA after the 150<sup>th</sup> and 107<sup>th</sup> delithitation respectively. **i)** Photographs of the cycled electrodes. Top-viewed SEM images **ii)** x 650 and **iii)** x 5000. **iv)** Cross-sectional SEM image (x 2500). **c)** Size distributions of the cracks observed by SEM for PAA (black) and PR-PAA (dark red) with the corresponding gaussian fits.  $\mu$  and  $\sigma$  stand as the means and the standard deviations respectively.

We then performed microscopic imaging on the cycled electrodes to evaluate the electrodes cohesion. Unfortunately, the delamination of PAA electrodes made them too fragile under vacuum and only top-viewed images of some remaining areas were obtained (Figure IV.13.b.ii & iii). On Figure IV.13.b.ii the copper foil is apparent as an indication of the poor adhesion of the electrode. By contrast, the good adherence of the PR-PAA electrode on the copper foil is shown on the cross-section image (Figure IV.13.a.iv). Its thickness increased from 12.2  $\mu\text{m}$  (measured with a palmer) to 18.1  $\mu\text{m}$ , hence reflecting that the cohesion of the electrode is maintained. Moreover, the PR-PAA electrode shows a better surface homogeneity as compared with PAA (Figure IV.13.ii & iii). This

implies the better stability of the SEI layer under cycling and underlines the efficiency of PR-PAA to accommodate volume changes of the Si electrodes. The poorer ability of PAA to adapt to the volume expansions also translates into the size of the electrode cracks which are three times bigger than PR-PAA electrode (3.11  $\mu\text{m}$  vs 0.76  $\mu\text{m}$  for PR-PAA) (Figure IV.13.c).

Although these preliminary SEM analyses are succinct, they are very convincing about the beneficial aspects of such binders in buffering volume changes and cracking of Si composite electrodes. They are also consistent with Choi *et al*'s work and highlight that PR-PAA binders can resolve issues originating from the volume expansion of Si electrodes in a better way than commercial traditional binders such as PAA. We attribute such performances to the sliding motion of  $\alpha$ -CDs which induces an enhanced stretchability and recovery.

#### 4. Conclusions and discussions

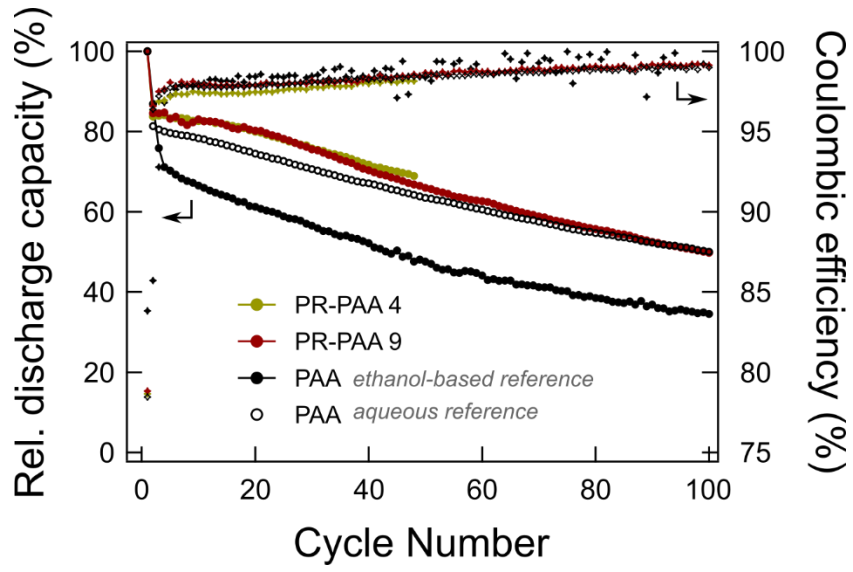
In summary, an essential preliminary study led us to the development of stable model Si composite electrodes using PAA as the binder. Such an optimized electrode formulation was taken as a reference to investigate the cycling performances of Si electrodes in which PR-PAA were incorporated as binders. We have thus demonstrated some cyclability improvements resulting from the use of such mechanically interlocked architectures as Si anode binders, hence confirming the previous work of Choi *et al*<sup>101</sup>. The better performances of PR-PAA result from its ability to accommodate the Si volume changes better than PAA, owing to the sliding motion of  $\alpha$ -CDs along the treading polymer. Therefore, the cohesion of Si electrode is more maintained upon cycling preventing any delamination or uncontrolled growth of the SEI.

What makes our study unique is the investigation of the influence of the design of PR-PAA architectures on the cycling performances of Si anodes which incorporate them as binders. The systematic cycling experiments highlighted the most relevant structural parameters leading to the improvement of the cycling performances of Si anodes. As expected, enhancing the  $\alpha$ -CD sliding motion seems to be the key to design efficient PR-PAA binders. In this sense, **working with high molecular weight POE (x) results in better cycling performances**, as it favours the  $\alpha$ -CD sliding motion. Moreover, **tuning the PR ring coverage (rc) to low values has a positive impact** on the

cycling performances as illustrated by the impressive capacity retention of PR-PAA 9 ( $x=100K$ ,  $rc=low$ ,  $y=5\%_{wt}$ ). Finally, **increasing the PR/PAA mass ratio (y) drastically improves** the cyclability of Si electrodes as shown by the cycling performances of PR-PAA 4 ( $x=10K$ ,  $rc=50\%$ ,  $y=20\%_{wt}$ ) which displays a similar profile than PR-PAA 9. Accordingly, some new PR-PAA networks are being synthesized to enhance the pulley effect, such as ( $x=100K$ ,  $rc=low$ ,  $y=20\%_{wt}$ ). Moreover, the influence of the cross-linking density is currently being investigated with the evaluation of the cycling performances of Si electrodes in which PR-PAA 5 and PR-PAA 8 were incorporated as binders.

Obviously, improvements can still be made. The rationalization of the cycling performances of the different PR-PAA binders is imminent, involving a more systematic post-mortem study of the cycled electrodes by SEM and the correlation between electrochemical performances and mechanical properties of the different binders. The latter is very challenging since the mechanical tests are not carried out exactly in battery operating conditions (polymer only, different electrolyte, speed) and some practical reproducibility issues have been encountered (see Chapter III).

One of the crucial aspects this study has pointed out is that the production of stable Si anode is very sensitive to the formulation process and that the change of binder dramatically affects the electrode preparation. As an illustration, we compared the performances of our best nano-Si/PR-PAA electrodes prepared through the ethanol-based process, with the reference aqueous nano-Si/PAA electrode (Figure IV.14). Despite the greater performances of PR-PAA during the first 30 cycles, over a long-term cycling, ethanol-based PR-PAA and aqueous PAA display an identical capacity retention. Thus, this study underlines the somewhat wobbly nature of the development of new viable Si anode binders, and we must admit that we are still far from defeating the commercial ones such as PAA. It seems necessary to find the right balance between the elegance of supramolecular chemistry and the more realistic practical application.



**Figure IV.14: Comparison of the long-term cycling performances of nano-Si electrodes equipped with PAA or PR-PAA independently from the slurry process.** Nano-Si/Csp/binder (2:1:1) electrodes were cycled vs Li metal in LP30+5FEC electrolyte at C/10 between 0.005 V and 1.5 V.

## General conclusion and perspectives

This PhD work is the result of the recent collaboration between LAMBE (Laboratory of Analysis and Modelling for Biology and Environment, University of Evry Val d'Essonne) and CSE (Solid-state Chemistry and Energy Lab, Collège de France). Therefore, we have explored a fairly new research direction dealing with the role that supramolecular chemistry can play in extending batteries lifespan, hence targeting sustainability. To this end, we selected cyclodextrin (CD) as a versatile supramolecular tool, which main property lies in the *host-guest* interaction, and identified some of the various benefits this biocompatible cage-molecule can provide to address inherent batteries issues. In this general conclusion, we summarize the main achievements of this PhD work, further bearing in mind that much remains to be done. Then, guided by both the pending questions and the discussions initiated as a result of each chapter, we will propose some future research directions that would deserve to be investigated.

As the implementation of the CD *host-guest* supramolecular chemistry in battery is still in its infancy, I have intentionally written **Chapter I** from the CD point of view. This organisation actually reflects the scientific approach that I have adopted to show the benefits that CD can bring to batteries. First, we depicted the design of CDs-based systems equipped with some *smart* properties lying on the dynamic *host-guest* interaction. Thereafter, we enlisted all the battery technologies in which this *host-guest* interaction had already been implemented. After having acquired a global view of the different persistent batteries' failures, we have finally identified the two most promising playgrounds for CD, *ie* the electrode swelling, illustrated by Si anode, and the uncontrolled dissolution of electrode as exemplified by the parasitic polysulfides dissolution occurring in Li-S batteries.

**Chapter II** first deals with the characterization of the *host-guest* complexation equilibrium between CDs and polysulfides, while providing an insight on the thermo-responsiveness of this process. Such a clear rationalization of the trapping properties of CD towards polysulfides was missing in the literature and we have closed this gap. We have unveiled the influence of the CD cavity size or the polysulfide chain lengths on the interaction strength. We have viewed the deep exploration of this *host-guest* interaction as an attractive way to a new sulfur confinement strategy with the development of CDs-based binders.

Then, using the CD/polysulfide complexation, we have shown that the nanopore single-molecule detection can be envisioned to elucidate the unwanted polysulfide red-ox shuttle. Indeed, it has enabled a reliable identification of the aqueous polysulfide intermediates with a single sulfur atom resolution. Provided that an easy implementation into practical cells is possible, there is a considerable scope for this characterization tool borrowed from biology, to be widely adopted by the battery community as a powerful electrolyte probe. Among the main obstacles, we report the extension of our aqueous *proof-of-concept* to organic media, that is currently undertaken through the post-Doctoral project of Erika Trindade. Retrospectively, I also think that, from the battery point of view, further insight would be gained by implementing such sensitive tool in the context of electrolytes design by identifying the nature of the electrolyte degradation products leading to the formation of the SEI.

Note that the image of the selective protein channel inserted into a lipidic membrane has gotten us inspired and we have come up with the idea of the design of a regenerable CDs-based separator for Li-S batteries. While trying to develop this disruptive concept, some discussions rapidly drove me to the conclusion that this project needed to be aborted for practical reasons. Not only the orientated release would require a sophisticated grafting chemistry, but the significant concentrations of polysulfides in the electrolyte as well as the thermal stimulus also make our approach somehow unrealistic.

Facing our concerns about the viability of the design of CDs-based separators for Li-S batteries, I reoriented my PhD project towards the design of Si anode binders. This time, we extended the exploitation of the CD *host-guest* interaction to the macromolecular scale. We synthesized a large panel of PR-PAA, which are mechanically interlocked architectures prepared through the cross-linking of  $\alpha$ -CDs based PRs with PAA, a commercial Si anode binder. The sliding motion of  $\alpha$ -CDs provides these prototypes with new routes of accommodating Si anodes volume changes, hence improving their cycling performances. Throughout **Chapter III** and **Chapter IV**, we have shown that an optimized design for PR-PAA binders could be reached by controlling their structural parameters. Working with high molecular weight PEO, tuning the PR ring coverage to low values and increasing the PR/PAA mass ratio have drastically improved the cyclability of Si anodes. The benefits of such binders in buffering volume changes and maintaining the integrity of Si composite electrodes have been demonstrated through SEM *post-mortem* analyses of cycled electrodes. Unfortunately, I remain

frustrated at this stage because of the difficulty to correlate the electrochemical performances of these advanced binders with their mechanical properties, owing to the lack of characterization tools for monitoring the mechanical properties of electrodes under operating conditions.

As a perspective, the design of chelating membranes may be more appropriate to tackle the dissolution of transition metal cations from the Li-ion batteries cathodes (LNO, LMO, LCO) than for trapping polysulfides. Although not reported in the manuscript, we have shown that CD was not a suitable candidate to trap these parasitic cations, whereas great hope is expected for amine or pyridine functions which exhibit stronger supramolecular interactions. Since October 2021, a new PhD student, Dorian Crevel, has been dedicated to this research direction. The nature of the chelating molecules<sup>218</sup>, their doping proportions and the incorporation or grafting strategies are one of the parameters that could be investigated to further optimize the design of chelating membranes.

However, our results have undeniably revealed how supramolecular chemistry can enable the battery community to move forward by bringing some revolutionary concepts to enhance batteries lifespan. This burgeoning dynamic has been made possible by building my PhD through the prism of different research fields such as, supramolecular chemistry, batteries, and biophysics, with both fundamental and practical aspects. This demanding scientific environment was my driving fuel for these 3 years, through which I have learned that working at the interfaces of various disciplines is essential for innovation. The most considerable challenge has been to acquire an in-depth knowledge from the different fields and particularly the requirements specifications of each battery technology not to pursue in a too exotic dead-end project, as we could have done by pushing further to the regenerable separator for Li-S batteries. Moreover, I have learned that designing a collaborative project, equally appealing for all the scientific communities involved, is challenging. For example, the discrimination of polysulfides with a single sulfur atom resolution represents a breakthrough for the nanopore community but it is still seen as a more elegant than practical concept for the battery counterpart, which research is driven by the "be practical" motto.

Finally, the study of the molecular pulley Si anode binders allows me to uncover the beauty of research: providing some novel seducing concepts while achieving great fundamental knowledge. Indeed, the elegance of the scientific approach has prevailed over realism and viability in order to highlight the added-value that CD supramolecular chemistry can provide to the battery community.





## Bibliography

1. Summary for policymakers. in *Climate Change 2021: The Physical Science Basis. Contribution of Working Group I to the Sixth Assessment Report of the Intergovernmental Panel on Climate Change* (eds. Masson-Delmotte, V. et al.) (Cambridge University Press, 2021).
2. Paris Agreement, Accord de Paris, 21ème Conférence des Parties. Climate Action - European Commission [https://ec.europa.eu/clima/policies/international/negotiations/paris\\_en](https://ec.europa.eu/clima/policies/international/negotiations/paris_en) (2015).
3. Callonnec, G., Landa, G., Maillet, P. & Reynes, F. L'évaluation macroéconomique des visions énergétiques 2030-2050 de l'ADEME. 36.
4. Tarascon, J.-M. & Armand, M. Issues and challenges facing rechargeable lithium batteries. *Nature* **414**, 359–367 (2001).
5. Batteries and hydrogen technology: keys for a clean energy future – Analysis - IEA. <https://www.iea.org/articles/batteries-and-hydrogen-technology-keys-for-a-clean-energy-future>.
6. Start - Battery 2030. <https://battery2030.eu/>.
7. Vegge, T., Tarascon, J.-M. & Edström, K. Toward Better and Smarter Batteries by Combining AI with Multisensory and Self-Healing Approaches. *Adv. Energy Mater.* **11**, 2100362 (2021).
8. Rekharsky, M. V. & Inoue, Y. Complexation Thermodynamics of Cyclodextrins. *Chem. Rev.* **98**, 1875–1918 (1998).
9. Szejtli, J. Introduction and General Overview of Cyclodextrin Chemistry. *Chem. Rev.* **98**, 1743–1754 (1998).
10. Crini, G. et al. Cyclodextrins, from molecules to applications. *Environ. Chem. Lett.* **16**, 1361–1375 (2018).
11. Kfoury, M., Landy, D. & Fourmentin, S. Characterization of Cyclodextrin/Volatile Inclusion Complexes: A Review. *Molecules* **23**, 1204 (2018).
12. Mura, P. Analytical techniques for characterization of cyclodextrin complexes in aqueous solution: A review. *J. Pharm. Biomed. Anal.* **101**, 238–250 (2014).
13. Connors, K. A. The Stability of Cyclodextrin Complexes in Solution. *Chem. Rev.* **97**, 1325–1358 (1997).
14. Harada, A., Takashima, Y. & Nakahata, M. Supramolecular Polymeric Materials via Cyclodextrin–Guest Interactions. *Acc. Chem. Res.* **47**, 2128–2140 (2014).
15. Fouquey, C., Lehn, J.-M. & Levelut, A.-M. Molecular recognition directed self-assembly of supramolecular liquid crystalline polymers from complementary chiral components. *Adv. Mater.* **2**, 254–257 (1990).
16. Dong, S., Zheng, B., Wang, F. & Huang, F. Supramolecular Polymers Constructed from Macrocyclic-Based Host–Guest Molecular Recognition Motifs. *Acc. Chem. Res.* **47**, 1982–1994 (2014).
17. Wei, P., Yan, X. & Huang, F. Supramolecular polymers constructed by orthogonal self-assembly based on host–guest and metal–ligand interactions. *Chem. Soc. Rev.* **44**, 815–832 (2015).
18. Harada, A., Takashima, Y. & Yamaguchi, H. Cyclodextrin -based supramolecular polymers. *Chem. Soc. Rev.* **38**, 875–882 (2009).
19. Yao, X., Huang, P. & Nie, Z. Cyclodextrin-based polymer materials: From controlled synthesis to applications. *Prog. Polym. Sci.* **93**, 1–35 (2019).
20. Zheng, Y., Hashidzume, A., Takashima, Y., Yamaguchi, H. & Harada, A. Macroscopic Observations of Molecular Recognition: Discrimination of the Substituted Position on the Naphthyl Group by Polyacrylamide Gel Modified with  $\beta$ -Cyclodextrin. *Langmuir* **27**, 13790–13795 (2011).

21. Hashidzume, A., Zheng, Y., Takashima, Y., Yamaguchi, H. & Harada, A. Macroscopic Self-Assembly Based on Molecular Recognition: Effect of Linkage between Aromatics and the Polyacrylamide Gel Scaffold, Amide versus Ester. *Macromolecules* **46**, 1939–1947 (2013).
22. Zheng, Y., Hashidzume, A., Takashima, Y., Yamaguchi, H. & Harada, A. Switching of macroscopic molecular recognition selectivity using a mixed solvent system. *Nat. Commun.* **3**, 831 (2012).
23. Yamaguchi, H. et al. Photoswitchable gel assembly based on molecular recognition. *Nat. Commun.* **3**, 603 (2012).
24. Yuan, S., Chen, J., Sheng, J., Hu, Y. & Jiang, Z. Paclitaxel-Loaded  $\beta$ -Cyclodextrin-Modified Poly(Acrylic Acid) Nanoparticles through Multivalent Inclusion for Anticancer Therapy. *Macromol. Biosci.* **16**, 341–349 (2016).
25. Nakahata, M., Takashima, Y., Hashidzume, A. & Harada, A. Redox-Generated Mechanical Motion of a Supramolecular Polymeric Actuator Based on Host–Guest Interactions. *Angew. Chem. Int. Ed.* **52**, 5731–5735 (2013).
26. Xiao, Y.-Y. et al. Light-, pH- and thermal-responsive hydrogels with the triple-shape memory effect. *Chem. Commun.* **52**, 10609–10612 (2016).
27. Redondo, J. A. et al. Polymeric Gene Carriers Bearing Pendant  $\beta$ -Cyclodextrin: The Relevance of Glycoside Permethylation on the “In Vitro” Cell Response. *Macromol. Rapid Commun.* **37**, 575–583 (2016).
28. Guo, X. et al. Tailoring Polymeric Hydrogels through Cyclodextrin Host–Guest Complexation. *Macromol. Rapid Commun.* **31**, 300–304 (2010).
29. Li, L. et al. Polymer Networks Assembled by Host–Guest Inclusion between Adamantyl and  $\beta$ -Cyclodextrin Substituents on Poly(acrylic acid) in Aqueous Solution. *Macromolecules* **41**, 8677–8681 (2008).
30. Wang, J. et al. Polymeric Networks Assembled by Adamantyl and  $\beta$ -Cyclodextrin Substituted Poly(acrylate)s: Host–Guest Interactions, and the Effects of Ionic Strength and Extent of Substitution. *Ind. Eng. Chem. Res.* **49**, 609–612 (2010).
31. Hashidzume, A., Ito, F., Tomatsu, I. & Harada, A. Macromolecular Recognition by Polymer-Carrying Cyclodextrins: Interaction of a Polymer Bearing Cyclodextrin Moieties with Poly(acrylamide)s Bearing Aromatic Side Chains. *Macromol. Rapid Commun.* **26**, 1151–1154 (2005).
32. Ohashi, H., Abe, T., Tamaki, T. & Yamaguchi, T. Influence of Spacer Length between Actuator and Sensor on Their Mutual Communications in Poly(N-Isopropylacrylamide-co- $\beta$ -Cyclodextrin), an Autonomous Coordinative Shrinking/Swelling Polymer. *Macromolecules* **45**, 9742–9750 (2012).
33. Bertrand, A., Stenzel, M., Fleury, E. & Bernard, J. Host–guest driven supramolecular assembly of reversible comb-shaped polymers in aqueous solution. *Polym. Chem.* **3**, 377–383 (2012).
34. Jazkewitsch, O., Mondrzyk, A., Staffel, R. & Ritter, H. Cyclodextrin-Modified Polyesters from Lactones and from Bacteria: An Approach to New Drug Carrier Systems. *Macromolecules* **44**, 1365–1371 (2011).
35. Moers, C. et al. Supramolecular Linear-g-Hyperbranched Graft Polymers: Topology and Binding Strength of Hyperbranched Side Chains. *Macromolecules* **46**, 9544–9553 (2013).
36. Koopmans, C. & Ritter, H. Formation of Physical Hydrogels via Host–Guest Interactions of  $\beta$ -Cyclodextrin Polymers and Copolymers Bearing Adamantyl Groups. *Macromolecules* **41**, 7418–7422 (2008).
37. Pouliquen, G., Amiel, C. & Tribet, C. Photoresponsive Viscosity and Host–Guest Association in Aqueous Mixtures of Poly-Cyclodextrin with Azobenzene-Modified Poly(acrylic)acid. *J. Phys. Chem. B* **111**, 5587–5595 (2007).

38. Harada, A., Kobayashi, R., Takashima, Y., Hashidzume, A. & Yamaguchi, H. Macroscopic self-assembly through molecular recognition. *Nat. Chem.* **3**, 34–37 (2011).
39. Takashima, Y. et al. Complex Formation and Gelation between Copolymers Containing Pendant Azobenzene Groups and Cyclodextrin Polymers. *Chem. Lett.* **33**, 890–891 (2004).
40. Tan, S. et al. Photocontrolled Cargo Release from Dual Cross-Linked Polymer Particles. *ACS Appl. Mater. Interfaces* **8**, 6219–6228 (2016).
41. Tamesue, S., Takashima, Y., Yamaguchi, H., Shinkai, S. & Harada, A. Photoswitchable Supramolecular Hydrogels Formed by Cyclodextrins and Azobenzene Polymers. *Angew. Chem. Int. Ed.* **49**, 7461–7464 (2010).
42. Harada, A. & Kamachi, M. Complex formation between poly(ethylene glycol) and  $\alpha$ -cyclodextrin. *Macromolecules* **23**, 2821–2823 (1990).
43. Harada, A., Li, J., Kamachi, M., Kitagawa, Y. & Katsube, Y. Structures of polyrotaxane models. *Carbohydr. Res.* **305**, 127–129 (1997).
44. Harada, A., Li, J. & Kamachi, M. Preparation and Characterization of a Polyrotaxane Consisting of Monodisperse Poly(ethylene glycol) and  $\alpha$ -Cyclodextrins. *J. Am. Chem. Soc.* **116**, 3192–3196 (1994).
45. Wenz, G., Han, B.-H. & Müller, A. Cyclodextrin Rotaxanes and Polyrotaxanes. *Chem. Rev.* **106**, 782–817 (2006).
46. Harada, A., Okada, M., Li, J. & Kamachi, M. Preparation and Characterization of Inclusion Complexes of Poly(propylene glycol) with Cyclodextrins. *Macromolecules* **28**, 8406–8411 (1995).
47. Harada, A., Li, J. & Kamachi, M. Complex Formation between Poly(methyl vinyl ether) and  $\gamma$ -Cyclodextrin. *Chem. Lett.* **22**, 237–240 (1993).
48. Harada, A., Li, J. & Kamachi, M. Double-stranded inclusion complexes of cyclodextrin threaded on poly(ethylene glycol). *Nature* **370**, 126–128 (1994).
49. Harada, A., Li, J. & Kamachi, M. The molecular necklace: a rotaxane containing many threaded  $\alpha$ -cyclodextrins. **356**, 3 (1992).
50. Ooya, T., Mori, H., Terano, M. & Yui, N. Synthesis of a biodegradable polymeric supramolecular assembly for drug delivery. *Macromol. Rapid Commun.* **16**, 259–263 (1995).
51. Ooya, T., Eguchi, M. & Yui, N. Enhanced Accessibility of Peptide Substrate toward Membrane-Bound Metalloexopeptidase by Supramolecular Structure of Polyrotaxane. *Biomacromolecules* **2**, 200–203 (2001).
52. Ooya, T. & Yui, N. Multivalent interactions between biotin–polyrotaxane conjugates and streptavidin as a model of new targeting for transporters. *J. Controlled Release* **80**, 219–228 (2002).
53. Fujita, H., Ooya, T. & Yui, N. Thermally Induced Localization of Cyclodextrins in a Polyrotaxane Consisting of  $\beta$ -Cyclodextrins and Poly(ethylene glycol)–Poly(propylene glycol) Triblock Copolymer. *Macromolecules* **32**, 2534–2541 (1999).
54. Fujita, H., Ooya, T. & Yui, N. Thermally-Responsive Properties of a Polyrotaxane Consisting of  $\beta$ -Cyclodextrins and a Poly(ethylene glycol)–Poly(propylene glycol) Triblock-Copolymer. *Polym. J.* **31**, 1099–1104 (1999).
55. Tamura Makio & Ueno Akihiko. Energy Transfer and Guest Responsive Fluorescence Spectra of Polyrotaxane Consisting of  $\alpha$ -Cyclodextrins Bearing Naphthyl Moieties. *Bull. Chem. Soc. Jpn.* (2001) doi:10.1246/bcsj.73.147.
56. Araki, J., Zhao, C. & Ito, K. Efficient Production of Polyrotaxanes from  $\alpha$ -Cyclodextrin and Poly(ethylene glycol). *Macromolecules* **38**, 7524–7527 (2005).
57. Zhao, T. & Beckham, H. W. Direct Synthesis of Cyclodextrin-Rotaxanated Poly(ethylene glycol)s and Their Self-Diffusion Behavior in Dilute Solution. *Macromolecules* **36**, 9859–9865 (2003).

58. Jarroux, N., Guégan, P., Cheradame, H. & Auvray, L. High Conversion Synthesis of Pyrene End Functionalized Polyrotaxane Based on Poly(ethylene oxide) and  $\alpha$ -Cyclodextrins. *J. Phys. Chem. B* **109**, 23816–23822 (2005).
59. Kihara, N., Hinoue, K. & Takata, T. Solid-State End-Capping of Pseudopolyrotaxane Possessing Hydroxy-Terminated Axle to Polyrotaxane and Its Application to the Synthesis of a Functionalized Polyrotaxane Capable of Yielding a Polyrotaxane Network. *Macromolecules* **38**, 223–226 (2005).
60. Arai, T. & Takata, T. One-pot Synthesis of Main Chain-type Polyrotaxane Containing Cyclodextrin Wheels. *Chem. Lett.* **36**, 418–419 (2007).
61. Araki, J. & Ito, K. Recent advances in the preparation of cyclodextrin-based polyrotaxanes and their applications to soft materials. *Soft Matter* **3**, 1456–1473 (2007).
62. Kakuta, T. et al. Preorganized Hydrogel: Self-Healing Properties of Supramolecular Hydrogels Formed by Polymerization of Host–Guest-Monomers that Contain Cyclodextrins and Hydrophobic Guest Groups. *Adv. Mater.* **25**, 2849–2853 (2013).
63. Nakahata, M., Takashima, Y., Yamaguchi, H. & Harada, A. Redox-responsive self-healing materials formed from host–guest polymers. *Nat. Commun.* **2**, 511 (2011).
64. Hart, L. F. et al. Material properties and applications of mechanically interlocked polymers. *Nat. Rev. Mater.* **6**, 508–530 (2021).
65. Mohamadhoseini, M. & Mohamadnia, Z. Supramolecular self-healing materials via host-guest strategy between cyclodextrin and specific types of guest molecules. *Coord. Chem. Rev.* **432**, 213711 (2021).
66. Kobayashi, Y., Zheng, Y., Takashima, Y., Yamaguchi, H. & Harada, A. Physical and Adhesion Properties of Supramolecular Hydrogels Cross-linked by Movable Cross-linking Molecule and Host-guest Interactions. *Chem. Lett.* **47**, 1387–1390 (2018).
67. Tomatsu, I., Hashidzume, A. & Harada, A. Contrast Viscosity Changes upon Photoirradiation for Mixtures of Poly(acrylic acid)-Based  $\alpha$ -Cyclodextrin and Azobenzene Polymers. *J. Am. Chem. Soc.* **128**, 2226–2227 (2006).
68. Takashima, Y. et al. Expansion–contraction of photoresponsive artificial muscle regulated by host–guest interactions. *Nat. Commun.* **3**, 1270 (2012).
69. Takashima, Y. et al. Multifunctional Stimuli-Responsive Supramolecular Materials with Stretching, Coloring, and Self-Healing Properties Functionalized via Host–Guest Interactions. *Macromolecules* **50**, 4144–4150 (2017).
70. Zheng, Y., Hashidzume, A., Takashima, Y., Yamaguchi, H. & Harada, A. Temperature-Sensitive Macroscopic Assembly Based on Molecular Recognition. *ACS Macro Lett.* **1**, 1083–1085 (2012).
71. Noda, Y., Hayashi, Y. & Ito, K. From topological gels to slide-ring materials. *J. Appl. Polym. Sci.* **131**, (2014).
72. Imran, A. B., Seki, T. & Takeoka, Y. Recent advances in hydrogels in terms of fast stimuli responsiveness and superior mechanical performance. *Polym. J.* **42**, 839–851 (2010).
73. Sood, N., Bhardwaj, A., Mehta, S. & Mehta, A. Stimuli-responsive hydrogels in drug delivery and tissue engineering. *Drug Deliv.* **23**, 748–770 (2016).
74. Harada, A., Li, J. & Kamachi, M. Synthesis of a tubular polymer from threaded cyclodextrins. *Nature* **364**, 516–518 (1993).
75. Mamad-Hemouch, H. et al. Biomimetic Nanotubes Based on Cyclodextrins for Ion-Channel Applications. *Nano Lett.* **15**, 7748–7754 (2015).
76. Shimomura, T., Funaki, T., Ito, K., Choi, B.-K. & Hashizume, T. Circular Dichroism Study of the Inclusion-Dissociation Behavior of Complexes between a Molecular Nanotube and Azobenzene Substituted Linear Polymers. *J. Incl. Phenom. Macrocycl. Chem.* **44**, 275–278 (2002).

77. Ooya, T., Eguchi, M. & Yui, N. Supramolecular Design for Multivalent Interaction: Maltose Mobility along Polyrotaxane Enhanced Binding with Concanavalin A. *J. Am. Chem. Soc.* **125**, 13016–13017 (2003).
78. Seo, J.-H. et al. Inducing Rapid Cellular Response on RGD-Binding Threaded Macromolecular Surfaces. *J. Am. Chem. Soc.* **135**, 5513–5516 (2013).
79. Lopez, J., Mackanic, D. G., Cui, Y. & Bao, Z. Designing polymers for advanced battery chemistries. *Nat. Rev. Mater.* **4**, 312–330 (2019).
80. Xu, K. Nonaqueous Liquid Electrolytes for Lithium-Based Rechargeable Batteries. *Chem. Rev.* **104**, 4303–4418 (2004).
81. Aziz, S. B., Woo, T. J., Kadir, M. F. Z. & Ahmed, H. M. A conceptual review on polymer electrolytes and ion transport models. *J. Sci. Adv. Mater. Devices* **3**, 1–17 (2018).
82. Jeschke, S., Jankowski, P., Best, A. S. & Johansson, P. Catching TFSI: A Computational–Experimental Approach to  $\beta$ -Cyclodextrin-Based Host–Guest Systems as electrolytes for Li-Ion Batteries. *ChemSusChem* **11**, 1942–1949 (2018).
83. Imholt, L. et al. Supramolecular Self-Assembly of Methylated Rotaxanes for Solid Polymer Electrolyte Application. *ACS Macro Lett.* **7**, 881–885 (2018).
84. Imholt, L. et al. Grafted polyrotaxanes as highly conductive electrolytes for lithium metal batteries. *J. Power Sources* **409**, 148–158 (2019).
85. Kato, K., Inoue, K., Kudo, M. & Ito, K. Synthesis of graft polyrotaxane by simultaneous capping of backbone and grafting from rings of pseudo-polyrotaxane. *Beilstein J. Org. Chem.* **10**, 2573–2579 (2014).
86. Yang, L.-Y., Wei, D.-X., Xu, M., Yao, Y.-F. & Chen, Q. Transferring Lithium Ions in Nanochannels: A PEO/Li<sup>+</sup> Solid Polymer Electrolyte Design. *Angew. Chem.* **126**, 3705–3709 (2014).
87. Choi, J. W. & Aurbach, D. Promise and reality of post-lithium-ion batteries with high energy densities. *Nat. Rev. Mater.* **1**, 1–16 (2016).
88. Obrovac, M. N. & Christensen, L. Structural Changes in Silicon Anodes during Lithium Insertion/Extraction. *Electrochem. Solid-State Lett.* **7**, A93 (2004).
89. Obrovac, M. N. & Krause, L. J. Reversible Cycling of Crystalline Silicon Powder. *J. Electrochem. Soc.* **154**, A103 (2006).
90. Beaulieu, L. Y., Eberman, K. W., Turner, R. L., Krause, L. J. & Dahn, J. R. Colossal Reversible Volume Changes in Lithium Alloys. *Electrochem. Solid-State Lett.* **4**, A137 (2001).
91. Li, J. & Dahn, J. R. An In Situ X-Ray Diffraction Study of the Reaction of Li with Crystalline Si. *J. Electrochem. Soc.* **154**, A156 (2007).
92. Guo, J. et al. Silicon-Based Lithium Ion Battery Systems: State-of-the-Art from Half and Full Cell Viewpoint. *Adv. Funct. Mater.* **31**, 2102546 (2021).
93. Chan, C. K. et al. High-performance lithium battery anodes using silicon nanowires. *Nat. Nanotechnol.* **3**, 31–35 (2008).
94. Kwon, T., Choi, J. W. & Coskun, A. The emerging era of supramolecular polymeric binders in silicon anodes. *Chem. Soc. Rev.* **47**, 2145–2164 (2018).
95. Shi, Y., Zhou, X. & Yu, G. Material and Structural Design of Novel Binder Systems for High-Energy, High-Power Lithium-Ion Batteries. *Acc. Chem. Res.* **50**, 2642–2652 (2017).
96. Miranda, A. et al. Molecular design principles for polymeric binders in silicon anodes. *Mol. Syst. Des. Eng.* **5**, 709–724 (2020).
97. Magasinski, A. et al. Toward Efficient Binders for Li-Ion Battery Si-Based Anodes: Polyacrylic Acid. *ACS Appl. Mater. Interfaces* **2**, 3004–3010 (2010).
98. Kovalenko, I. et al. A major constituent of brown algae for use in high-capacity Li-ion batteries. *Science* **334**, 75–79 (2011).

99. Li, J., Lewis, R. B. & Dahn, J. R. Sodium Carboxymethyl Cellulose: A Potential Binder for Si Negative Electrodes for Li-Ion Batteries. *Electrochem. Solid-State Lett.* **10**, A17 (2006).
100. Kwon, T. et al. Dynamic Cross-Linking of Polymeric Binders Based on Host–Guest Interactions for Silicon Anodes in Lithium Ion Batteries. *ACS Nano* **9**, 11317–11324 (2015).
101. Choi, S., Kwon, T., Coskun, A. & Choi, J. W. Highly elastic binders integrating polyrotaxanes for silicon microparticle anodes in lithium ion batteries. *Science* **357**, 279–283 (2017).
102. Jeong, Y. K. et al. Hyperbranched  $\beta$ -Cyclodextrin Polymer as an Effective Multidimensional Binder for Silicon Anodes in Lithium Rechargeable Batteries. *Nano Lett.* **14**, 864–870 (2014).
103. Xie, Z. H., Rong, M. Z. & Zhang, M. Q. Dynamically Cross-Linked Polymeric Binder-Made Durable Silicon Anode of a Wide Operating Temperature Li-Ion Battery. *ACS Appl. Mater. Interfaces* **13**, 28737–28748 (2021).
104. Cho, Y. et al. A Pyrene–Poly(acrylic acid)–Polyrotaxane Supramolecular Binder Network for High-Performance Silicon Negative Electrodes. *Adv. Mater.* **31**, 1905048 (2019).
105. Yoo, D.-J. et al. Highly Elastic Polyrotaxane Binders for Mechanically Stable Lithium Hosts in Lithium-Metal Batteries. *Adv. Mater.* **31**, 1901645 (2019).
106. Bruce, P. G., Freunberger, S. A., Hardwick, L. J. & Tarascon, J.-M. Li–O<sub>2</sub> and Li–S batteries with high energy storage. *Nat. Mater.* **11**, 19–29 (2012).
107. Manthiram, A., Chung, S.-H. & Zu, C. Lithium–Sulfur Batteries: Progress and Prospects. *Adv. Mater.* **27**, 1980–2006 (2015).
108. Xiong, S., Xie, K., Diao, Y. & Hong, X. Characterization of the solid electrolyte interphase on lithium anode for preventing the shuttle mechanism in lithium–sulfur batteries. *J. Power Sources* **246**, 840–845 (2014).
109. Manthiram, A., Fu, Y. & Su, Y.-S. Challenges and Prospects of Lithium–Sulfur Batteries. *Acc. Chem. Res.* **46**, 1125–1134 (2013).
110. WU, Y.-L., YANG, J., WANG, J.-L., YIN, L.-C. & NULI, Y.-N. Composite Cathode Structure and Binder for High Performance Lithium-Sulfur Battery. *Acta Phys.-Chim. Sin.* **26**, 283–290 (2010).
111. Wang, J., Yao, Z., Monroe, C. W., Yang, J. & Nuli, Y. Carbonyl- $\beta$ -Cyclodextrin as a Novel Binder for Sulfur Composite Cathodes in Rechargeable Lithium Batteries. *Adv. Funct. Mater.* **23**, 1194–1201 (2013).
112. Zeng, F. et al. Multidimensional Polycation  $\beta$ -Cyclodextrin Polymer as an Effective Aqueous Binder for High Sulfur Loading Cathode in Lithium–Sulfur Batteries. *ACS Appl. Mater. Interfaces* **7**, 26257–26265 (2015).
113. Tegman, R. The crystal structure of sodium tetrasulphide, Na<sub>2</sub>S<sub>4</sub>. *Acta Crystallogr. B* **29**, 1463–1469 (1973).
114. Ni, L. et al. Supramolecular complexation of polysulfides by  $\beta$ -cyclodextrin polymer functionalized graphene hybrid cathode for high-performance lithium-sulfur batteries. *Energy Storage Mater.* **21**, 378–389 (2019).
115. Ren, X. et al. Unveiling the Role of Hydroxyl Architecture on Polysulfide Trapping for High-Performance Lithium–Sulfur Batteries. *ACS Appl. Energy Mater.* **3**, 4023–4032 (2020).
116. Dominko, R., Demir-Cakan, R., Morcrette, M. & Tarascon, J.-M. Analytical detection of soluble polysulphides in a modified Swagelok cell. *Electrochem. Commun.* **13**, 117–120 (2011).
117. Tan, J., Liu, D., Xu, X. & Mai, L. In situ/operando characterization techniques for rechargeable lithium–sulfur batteries: a review. *Nanoscale* **9**, 19001–19016 (2017).
118. Ying, Y.-L., Cao, C. & Long, Y.-T. Single molecule analysis by biological nanopore sensors. *Analyst* **139**, 3826–3835 (2014).
119. Schwiening, C. J. A brief historical perspective: Hodgkin and Huxley. *J. Physiol.* **590**, 2571–2575 (2012).

120. Cressiot, B. et al. Aerolysin, a Powerful Protein Sensor for Fundamental Studies and Development of Upcoming Applications. *ACS Sens.* **4**, 530–548 (2019).
121. Restrepo-Pérez, L., Joo, C. & Dekker, C. Paving the way to single-molecule protein sequencing. *Nat. Nanotechnol.* **13**, 786–796 (2018).
122. Lepoitevin, M., Ma, T., Bechelany, M., Janot, J.-M. & Balme, S. Functionalization of single solid state nanopores to mimic biological ion channels: A review. *Adv. Colloid Interface Sci.* **250**, 195–213 (2017).
123. Cressiot, B., Greive, S. J., Mojtabavi, M., Antson, A. A. & Wanunu, M. Thermostable virus portal proteins as reprogrammable adapters for solid-state nanopore sensors. *Nat. Commun.* **9**, 4652 (2018).
124. Branton, D. et al. The potential and challenges of nanopore sequencing. *Nat. Biotechnol.* **26**, 1146–1153 (2008).
125. Cao, C. et al. Discrimination of oligonucleotides of different lengths with a wild-type aerolysin nanopore. *Nat. Nanotechnol.* **11**, 713–718 (2016).
126. Piguet, F. et al. Identification of single amino acid differences in uniformly charged homopolymeric peptides with aerolysin nanopore. *Nat. Commun.* **9**, 966 (2018).
127. Huang, G., Voet, A. & Maglia, G. FraC nanopores with adjustable diameter identify the mass of opposite-charge peptides with 44 dalton resolution. *Nat. Commun.* **10**, 835 (2019).
128. Wang, Y., Zheng, D., Tan, Q., Wang, M. X. & Gu, L.-Q. Nanopore-based detection of circulating microRNAs in lung cancer patients. *Nat. Nanotechnol.* **6**, 668–674 (2011).
129. Quick, J. et al. Real-time, portable genome sequencing for Ebola surveillance. *Nature* **530**, 228–232 (2016).
130. Restrepo-Pérez, L. et al. Resolving Chemical Modifications to a Single Amino Acid within a Peptide Using a Biological Nanopore. *ACS Nano* **13**, 13668–13676 (2019).
131. Ouldali, H. et al. Electrical recognition of the twenty proteinogenic amino acids using an aerolysin nanopore. *Nat. Biotechnol.* **38**, 176–181 (2020).
132. Wanunu, M. Nanopores: A journey towards DNA sequencing. *Phys. Life Rev.* **9**, 125–158 (2012).
133. Merstorf, C. et al. Wild Type, Mutant Protein Unfolding and Phase Transition Detected by Single-Nanopore Recording. *ACS Chem. Biol.* **7**, 652–658 (2012).
134. Galenkamp, N. S., Biesemans, A. & Maglia, G. Directional conformer exchange in dihydrofolate reductase revealed by single-molecule nanopore recordings. *Nat. Chem.* **12**, 481–488 (2020).
135. Yu, J., Cao, C. & Long, Y.-T. Selective and Sensitive Detection of Methylcytosine by Aerolysin Nanopore under Serum Condition. *Anal. Chem.* **89**, 11685–11689 (2017).
136. Simpson, J. T. et al. Detecting DNA cytosine methylation using nanopore sequencing. *Nat. Methods* **14**, 407–410 (2017).
137. Tekin, B., Sevinc, S., Morcrette, M. & Demir-Cakan, R. A New Sodium-Based Aqueous Rechargeable Battery System: The Special Case of Na<sub>0.44</sub>MnO<sub>2</sub>/Dissolved Sodium Polysulfide. *Energy Technol.* **5**, 2182–2188 (2017).
138. Gross, M. M. & Manthiram, A. Development of low-cost sodium-aqueous polysulfide hybrid batteries. *Energy Storage Mater.* **19**, 346–351 (2019).
139. Sevinc, S. et al. In-situ tracking of NaFePO<sub>4</sub> formation in aqueous electrolytes and its electrochemical performances in Na-ion/polysulfide batteries. *J. Power Sources* **412**, 55–62 (2019).
140. Song, L. et al. Structure of Staphylococcal  $\alpha$ -Hemolysin, a Heptameric Transmembrane Pore. *Science* **274**, 1859–1865 (1996).



141. Steudel, R. & Chivers, T. The role of polysulfide dianions and radical anions in the chemical, physical and biological sciences, including sulfur-based batteries. *Chem. Soc. Rev.* **48**, 3279–3319 (2019).
142. Piguet, F. et al. Electroosmosis through  $\alpha$ -Hemolysin That Depends on Alkali Cation Type. *J. Phys. Chem. Lett.* **5**, 4362–4367 (2014).
143. Gu, L.-Q. & Bayley, H. Interaction of the Noncovalent Molecular Adapter,  $\beta$ -Cyclodextrin, with the Staphylococcal  $\alpha$ -Hemolysin Pore. *Biophys. J.* **79**, 1967–1975 (2000).
144. Gu, L.-Q., Braha, O., Conlan, S., Cheley, S. & Bayley, H. Stochastic sensing of organic analytes by a pore-forming protein containing a molecular adapter. *Nature* **398**, 686–690 (1999).
145. Pringle, D. L. The nature of the polysulfide anion. (1967).
146. Thordarson, P. Determining association constants from titration experiments in supramolecular chemistry. *Chem. Soc. Rev.* **40**, 1305–1323 (2011).
147. Berman, H. M. et al. The Protein Data Bank. *Acta Crystallogr. D Biol. Crystallogr.* **58**, 899–907 (2002).
148. Ni, L. et al. Supramolecular complexation of polysulfides by  $\beta$ -cyclodextrin polymer functionalized graphene hybrid cathode for high-performance lithium-sulfur batteries. *Energy Storage Mater.* **21**, 378–389 (2019).
149. Bétermier, F. et al. Single-sulfur atom discrimination of polysulfides with a protein nanopore for improved batteries. *Commun. Mater.* **1**, 59 (2020).
150. Astier, Y., Braha, O. & Bayley, H. Toward Single Molecule DNA Sequencing: Direct Identification of Ribonucleoside and Deoxyribonucleoside 5'-Monophosphates by Using an Engineered Protein Nanopore Equipped with a Molecular Adapter. *J. Am. Chem. Soc.* **128**, 1705–1710 (2006).
151. Bhamidimarri, S. P., Prajapati, J. D., Berg, B. van den, Winterhalter, M. & Kleinekathöfer, U. Role of Electroosmosis in the Permeation of Neutral Molecules: CymA and Cyclodextrin as an Example. *Biophys. J.* **110**, 600–611 (2016).
152. Gu, L.-Q., Cheley, S. & Bayley, H. Prolonged Residence Time of a Noncovalent Molecular Adapter,  $\beta$ -Cyclodextrin, within the Lumen of Mutant  $\alpha$ -Hemolysin Pores. *J. Gen. Physiol.* **118**, 481–494 (2001).
153. Di Muccio, G., Rossini, A. E., Di Marino, D., Zollo, G. & Chinappi, M. Insights into protein sequencing with an  $\alpha$ -Hemolysin nanopore by atomistic simulations. *Sci. Rep.* **9**, 6440 (2019).
154. Tarascon, J.-M., Gozdz, A. S., Schmutz, C., Shokoohi, F. & Warren, P. C. Performance of Bellcore's plastic rechargeable Li-ion batteries. *Solid State Ion.* **86–88**, 49–54 (1996).
155. Yan, G. et al. Assessment of the Electrochemical Stability of Carbonate-Based Electrolytes in Na-Ion Batteries. *J. Electrochem. Soc.* **165**, A1222 (2018).
156. Huang, J. et al. Operando decoding of chemical and thermal events in commercial Na(Li)-ion cells via optical sensors. *Nat. Energy* **5**, 674–683 (2020).
157. Huang, J., Blanquer, L. A., Gervillié, C. & Tarascon, J.-M. Distributed Fiber Optic Sensing to Assess In-Live Temperature Imaging Inside Batteries: Rayleigh and FBGs. *J. Electrochem. Soc.* **168**, 060520 (2021).
158. Kwon, T., Choi, J. W. & Coskun, A. Prospect for Supramolecular Chemistry in High-Energy-Density Rechargeable Batteries. *Joule* **3**, 662–682 (2019).
159. Bridel, J.-S., Azais, T., Morcrette, M., Tarascon, J.-M. & Larcher, D. Key Parameters Governing the Reversibility of Si/Carbon/CMC Electrodes for Li-Ion Batteries. *Chem. Mater.* **22**, 1229–1241 (2010).

160. Kwon, T. et al. Systematic molecular-level design of binders incorporating Meldrum's acid for silicon anodes in lithium rechargeable batteries. *Adv. Mater. Deerfield Beach Fla* **26**, 7979–7985 (2014).
161. Ryou, M.-H. et al. Mussel-Inspired Adhesive Binders for High-Performance Silicon Nanoparticle Anodes in Lithium-Ion Batteries. *Adv. Mater.* **25**, 1571–1576 (2013).
162. Murase, M. et al. Crop-Derived Polysaccharides as Binders for High-Capacity Silicon/Graphite-Based Electrodes in Lithium-Ion Batteries. *ChemSusChem* **5**, 2307–2311 (2012).
163. Jeena, M. T. et al. Multifunctional Molecular Design as an Efficient Polymeric Binder for Silicon Anodes in Lithium-Ion Batteries. *ACS Appl. Mater. Interfaces* **6**, 18001–18007 (2014).
164. Koo, B. et al. A Highly Cross-Linked Polymeric Binder for High-Performance Silicon Negative Electrodes in Lithium Ion Batteries. *Angew. Chem. Int. Ed.* **51**, 8762–8767 (2012).
165. Chen, Z. et al. High-Areal-Capacity Silicon Electrodes with Low-Cost Silicon Particles Based on Spatial Control of Self-Healing Binder. *Adv. Energy Mater.* **5**, 1401826 (2015).
166. Wang, C. et al. Self-healing chemistry enables the stable operation of silicon microparticle anodes for high-energy lithium-ion batteries. *Nat. Chem.* **5**, 1042–1048 (2013).
167. Kang, S., Yang, K., White, S. R. & Sottos, N. R. Silicon Composite Electrodes with Dynamic Ionic Bonding. *Adv. Energy Mater.* **7**, 1700045 (2017).
168. Yoon, J., Oh, D. X., Jo, C., Lee, J. & Hwang, D. S. Improvement of desolvation and resilience of alginate binders for Si-based anodes in a lithium ion battery by calcium-mediated cross-linking. *Phys. Chem. Chem. Phys.* **16**, 25628–25635 (2014).
169. Chen, Z., Christensen, L. & Dahn, J. R. Large-volume-change electrodes for Li-ion batteries of amorphous alloy particles held by elastomeric tethers. *Electrochem. Commun.* **5**, 919–923 (2003).
170. Chen, Z., Christensen, L. & Dahn, J. R. Comparison of PVDF and PVDF-TFE-P as Binders for Electrode Materials Showing Large Volume Changes in Lithium-Ion Batteries. *J. Electrochem. Soc.* **150**, A1073 (2003).
171. Liu, W.-R., Yang, M.-H., Wu, H.-C., Chiao, S. M. & Wu, N.-L. Enhanced Cycle Life of Si Anode for Li-Ion Batteries by Using Modified Elastomeric Binder. *Electrochem. Solid-State Lett.* **8**, A100 (2004).
172. Lestriez, B., Bahri, S., Sandu, I., Roué, L. & Guyomard, D. On the binding mechanism of CMC in Si negative electrodes for Li-ion batteries. *Electrochem. Commun.* **9**, 2801–2806 (2007).
173. Buqa, H., Holzapfel, M., Krumeich, F., Veit, C. & Novák, P. Study of styrene butadiene rubber and sodium methyl cellulose as binder for negative electrodes in lithium-ion batteries. *J. Power Sources* **161**, 617–622 (2006).
174. Harada, A. & Kamachi, M. Complex formation between poly(ethylene glycol) and  $\alpha$ -cyclodextrin. **3**.
175. de Gennes, P.-G. Sliding gels. *Phys. Stat. Mech. Its Appl.* **271**, 231–237 (1999).
176. Okumura, Y. & Ito, K. The Polyrotaxane Gel: A Topological Gel by Figure-of-Eight Cross-links. *Adv. Mater.* **13**, 485–487 (2001).
177. Ito, K. Novel Cross-Linking Concept of Polymer Network: Synthesis, Structure, and Properties of Slide-Ring Gels with Freely Movable Junctions. *Polym. J.* **39**, 489–499 (2007).
178. Koyanagi, K., Takashima, Y., Yamaguchi, H. & Harada, A. Movable Cross-Linked Polymeric Materials from Bulk Polymerization of Reactive Polyrotaxane Cross-Linker with Acrylate Monomers. *Macromolecules* **50**, 5695–5700 (2017).
179. Gotoh, H. et al. Optically transparent, high-toughness elastomer using a polyrotaxane cross-linker as a molecular pulley. *Sci. Adv.* **4**, eaat7629 (2018).
180. Minato, K. et al. Mechanical properties of supramolecular elastomers prepared from polymer-grafted polyrotaxane. *Polymer* **128**, 386–391 (2017).

181. Kato, K., Hori, A. & Ito, K. An efficient synthesis of low-covered polyrotaxanes grafted with poly( $\epsilon$ -caprolactone) and the mechanical properties of its cross-linked elastomers. *Polymer* **147**, 67–73 (2018).
182. Bin Imran, A. et al. Extremely stretchable thermosensitive hydrogels by introducing slide-ring polyrotaxane cross-linkers and ionic groups into the polymer network. *Nat. Commun.* **5**, 5124 (2014).
183. Araki, J., Kataoka, T. & Ito, K. Preparation of a “sliding graft copolymer”, an organic solvent-soluble polyrotaxane containing mobile side chains, and its application for a crosslinked elastomeric supramolecular film. *Soft Matter* **4**, 245–249 (2008).
184. Fleury, G., Schlatter, G., Brochon, C. & Hadziioannou, G. From high molecular weight precursor polyrotaxanes to supramolecular sliding networks. The ‘sliding gels’. *Polymer* **46**, 8494–8501 (2005).
185. Jiang, L. et al. Highly Stretchable and Instantly Recoverable Slide-Ring Gels Consisting of Enzymatically Synthesized Polyrotaxane with Low Host Coverage. *Chem. Mater.* **30**, 5013–5019 (2018).
186. Kato, K., Okabe, Y., Okazumi, Y. & Ito, K. A significant impact of host–guest stoichiometry on the extensibility of polyrotaxane gels. *Chem. Commun.* **51**, 16180–16183 (2015).
187. Lee, D. H., Tamura, A., Arisaka, Y., Seo, J.-H. & Yui, N. Mechanically Reinforced Gelatin Hydrogels by Introducing Slidable Supramolecular Cross-Linkers. *Polymers* **11**, 1787 (2019).
188. Liu, C. et al. Direct Observation of Large Deformation and Fracture Behavior at the Crack Tip of Slide-Ring Gel. *J. Electrochem. Soc.* **166**, B3143–B3147 (2019).
189. Fleury, G. et al. Topological Polymer Networks with Sliding Cross-Link Points: The “Sliding Gels”. Relationship between Their Molecular Structure and the Viscoelastic as Well as the Swelling Properties. *Macromolecules* **40**, 535–543 (2007).
190. Gent, A. N. & Tobias, R. H. Threshold tear strength of elastomers. *J. Polym. Sci. Polym. Phys. Ed.* **20**, 2051–2058 (1982).
191. Lin-Gibson, S. et al. Synthesis and Characterization of PEG Dimethacrylates and Their Hydrogels. *Biomacromolecules* **5**, 1280–1287 (2004).
192. Ooya, T., Utsunomiya, H., Eguchi, M. & Yui, N. Rapid Binding of Concanavalin A and Maltose–Polyrotaxane Conjugates Due to Mobile Motion of  $\alpha$ -Cyclodextrins Threaded onto a Poly(ethylene glycol). *Bioconjug. Chem.* **16**, 62–69 (2005).
193. Jarroux, N., Guégan, P., Buchmann, W., Tortajada, J. & Cheradame, H. A New Versatile Radical Addition on  $\alpha$ ,  $\omega$ -Dimethacrylate Poly(ethylene oxide). *Macromol. Chem. Phys.* **205**, 1206–1217 (2004).
194. Abad, M., Ramoul, H. & Jarroux Blachere, N. Methode De Purification Des Polyrotaxanes a Base De Cyclodextrines. (2017).
195. Fleury, G. et al. Synthesis and characterization of high molecular weight polyrotaxanes: towards the control over a wide range of threaded  $\alpha$ -cyclodextrins. *Soft Matter* **1**, 378–385 (2005).
196. Rekharsky, M. V. & Inoue, Y. Complexation Thermodynamics of Cyclodextrins. *Chem. Rev.* **98**, 1875–1918 (1998).
197. Araki, J. & Ito, K. Polyrotaxane derivatives. I. Preparation of modified polyrotaxanes with nonionic functional groups and their solubility in organic solvents. *J. Polym. Sci. Part Polym. Chem.* **44**, 6312–6323 (2006).
198. Chitwood, H. C. & Freure, B. T. The Reaction of Propylene Oxide with Alcohols. *J. Am. Chem. Soc.* **68**, 680–683 (1946).
199. Hussain, M. A., Liebert, T. & Heinze, T. Acylation of Cellulose with N,N'-Carbonyldiimidazole-Activated Acids in the Novel Solvent Dimethyl Sulfoxide/Tetrabutylammonium Fluoride. *Macromol. Rapid Commun.* **25**, 916–920 (2004).

200. McGaugh, M. C. & Kottle, S. The thermal degradation of poly(acrylic acid). *J. Polym. Sci. [B]* **5**, 817–820 (1967).
201. Fox, T. G. & Flory, P. J. Second-Order Transition Temperatures and Related Properties of Polystyrene. I. Influence of Molecular Weight. *J. Appl. Phys.* **21**, 581–591 (1950).
202. Kawamura, T., Okada, S. & Yamaki, J. Decomposition reaction of LiPF<sub>6</sub>-based electrolytes for lithium ion cells. *J. Power Sources* **156**, 547–554 (2006).
203. Kim, M., Yang, Z. & Bloom, I. Review—The Lithiation/Delithiation Behavior of Si-Based Electrodes: A Connection between Electrochemistry and Mechanics. *J. Electrochem. Soc. Online* **168**, (2021).
204. Beattie, S. D., Larcher, D., Morcrette, M., Simon, B. & Tarascon, J.-M. Si Electrodes for Li-Ion Batteries—A New Way to Look at an Old Problem. *J. Electrochem. Soc.* **155**, A158 (2007).
205. Zhao, X. & Lehto, V.-P. Challenges and prospects of nanosized silicon anodes in lithium-ion batteries. *Nanotechnology* **32**, 042002 (2020).
206. Panwar, K., Jassal, M. & Agrawal, A. K. In situ synthesis of Ag–SiO<sub>2</sub> Janus particles with epoxy functionality for textile applications. *Particuology* **19**, 107–112 (2015).
207. Xun, S. et al. The Effects of Native Oxide Surface Layer on the Electrochemical Performance of Si Nanoparticle-Based Electrodes. *J. Electrochem. Soc.* **158**, A1260 (2011).
208. Shen, D. et al. Rational Design of Si@SiO<sub>2</sub>/C Composites Using Sustainable Cellulose as a Carbon Resource for Anodes in Lithium-Ion Batteries. *ACS Appl. Mater. Interfaces* **10**, 7946–7954 (2018).
209. Feng, L., He, L., Ma, Y. & Wang, Y. Grafting poly(methyl methacrylate) onto silica nanoparticle surfaces via a facile esterification reaction. *Mater. Chem. Phys.* **116**, 158–163 (2009).
210. Massoud, H. Z. The onset of the thermal oxidation of silicon from room temperature to 1000°C. *Microelectron. Eng.* **28**, 109–116 (1995).
211. Chartrel, T. et al. Revisiting and improving the preparation of silicon-based electrodes for lithium-ion batteries: ball milling impact on poly(acrylic acid) polymer binders. *Mater. Chem. Front.* **3**, 881–891 (2019).
212. Karkar, Z. et al. How silicon electrodes can be calendered without altering their mechanical strength and cycle life. *J. Power Sources* **371**, 136–147 (2017).
213. van der Marel, C., Vinke, G. J. B. & van der Lugt, W. The phase diagram of the system lithium-silicon. *Solid State Commun.* **54**, 917–919 (1985).
214. Robert, D. Etude multi-échelle des mécanismes de (dé)lithiation et de dégradation d'électrodes à base de LiFePO<sub>4</sub> et de Silicium pour accumulateurs Li-ion. 221.
215. Etacheri, V. et al. Effect of Fluoroethylene Carbonate (FEC) on the Performance and Surface Chemistry of Si-Nanowire Li-Ion Battery Anodes. *Langmuir* **28**, 965–976 (2012).
216. Chen, X. et al. Reduction Mechanism of Fluoroethylene Carbonate for Stable Solid Electrolyte Interphase Film on Silicon Anode. *ECS Meet. Abstr.* **MA2014-01**, 294 (2014).
217. Gao, H. et al. Parasitic Reactions in Nanosized Silicon Anodes for Lithium-Ion Batteries. *Nano Lett.* **17**, 1512–1519 (2017).
218. Luski, S. et al. Lithium ion battery. (2018).
219. Trott, O. & Olson, A. J. AutoDock Vina: Improving the speed and accuracy of docking with a new scoring function, efficient optimization, and multithreading. *J. Comput. Chem.* **31**, 455–461 (2010).
220. Gutschmann, T., Heimburg, T., Keyser, U., Mahendran, K. R. & Winterhalter, M. Protein reconstitution into freestanding planar lipid membranes for electrophysiological characterization. *Nat. Protoc.* **10**, 188–198 (2015).

221. Montal, M. & Mueller, P. Formation of Bimolecular Membranes from Lipid Monolayers and a Study of Their Electrical Properties. *Proc. Natl. Acad. Sci.* **69**, 3561–3566 (1972).
222. Elgrishi, N. et al. A Practical Beginner's Guide to Cyclic Voltammetry. *J. Chem. Educ.* **95**, 197–206 (2018).
223. Gross, M. M. & Manthiram, A. Rechargeable Zinc-Aqueous Polysulfide Battery with a Mediator-Ion Solid Electrolyte. *ACS Appl. Mater. Interfaces* (2018) doi:10.1021/acsami.8b00981.

# Supporting Information for Chapter II

## 1. Materials & Methods

**Materials:** All materials were used as received without further purification step. Sodium sulfide anhydrous ( $\text{Na}_2\text{S}$ ), lithium sulfide (99.9%) and sulfur (S) were purchased from Sigma Aldrich. Sodium salts NaOH,  $\text{NaHCO}_3$  (99%) and NaCl were obtained from Sigma Aldrich. To prepare the planar lipid bilayer membrane, diphytanoyl-phosphatidylcholine-lecithin purchased from Avanti was solubilized in anhydrous decane (Sigma Aldrich). The monomeric  $\alpha$ -HL was obtained from Sigma Aldrich.  $\alpha$ -cyclodextrin ( $\alpha$ -CD, >99%),  $\beta$ -cyclodextrin ( $\beta$ -CD 98%) and  $\gamma$ -cyclodextrin ( $\gamma$ -CD) were produced by Wacker and purchased from Sigma Aldrich. Randomly methylated  $\beta$ -cyclodextrin (RM $\beta$ -CD) was kindly supplied by collaborators. Poly(tetrafluoroethylene) dispersion 60%<sub>w</sub>t (PTFE) was obtained from Sigma, PVDF-HFP (2801) was supplied by Solvay. Conductive carbon black acetylene was received from Alfa Aesar. Whatman borosilicate glass microfibre membranes were purchased from GE Healthcare Life Sciences. Lithium bis(trifluoromethane sulfonyl)imide (LiTFSI, 99.9%, extra dry) and LP30 were obtained from Solvionic and stored in an argon glovebox. Lithium nitrate ( $\text{LiNO}_3$ , 99.99% trace metal basis), lithium metal (99%), 1,3-dioxolane anhydrous (DOL, >99.5% stabilized) and dimethoxyethane anhydrous (DME, 99.5%) were purchased from Sigma Aldrich before being stored in an argon glovebox.

**Preparation of polysulfides solutions:** Sodium polysulfides solutions ( $\text{Na}_2\text{S}_x$ , 100 mM) were prepared according to a previously described method<sup>145</sup>.  $\text{Na}_2\text{S}$  and S are added in stoichiometric ratios to a degassed aqueous buffer solution set (25 mM  $\text{NaHCO}_3$ , pH 10) and the solution is continuously stirred for a week. All the preparations are done in under argon atmosphere. The characterization of the different polysulfides solutions was performed by UV-*vis* absorbance spectroscopy through the calculation of the different molar extinction coefficients ( $\epsilon$ ). Absorbance spectral profiles were measured over 200–1100 nm in a 1 cm airtight quartz cuvette for different diluted polysulfides solutions (0.3 mM to 1 mM) with a UV5 Bio Mettler Toledo spectrophotometer. Lithium polysulfides solutions ( $\text{Li}_2\text{S}_x$ ) were prepared similarly by mixing  $\text{Li}_2\text{S}$  and S for 24h in an organic electrolyte (DOL/DME, DME, PC, THF). An additional heating process could be carried out (80°C).

**Aqueous CD/polysulfide complex characterization by NMR:** Both continuous variation method and titration experiments were performed as previously described using a 600 MHz NMR spectrometer from Brüker<sup>146</sup>. The stoichiometry of the different CD/polysulfide complexes was determined using continuous variation method, also known as Job's plot. The mole fraction of polysulfide,  $\text{Na}_2\text{S}_x$ , was varied while keeping the total concentration of CD and polysulfide constant, to 50 mM, 16 mM, and 50 mM for  $\alpha$ -,  $\beta$ -, and  $\gamma$ -CDs respectively. Approximately 8 different *host-guest* concentration ratios were investigated for each complex and a  $^1\text{H}$  NMR spectrum was recorded for each condition (298K, 16 scans). The chemical shifts  $\Delta$  of the selected *host* protons ( $\text{H}_3$  essentially) were measured with Top Spin 3.6. The resulting chemical shift multiplied with the CD concentration (quantity proportional to the population of CD that is complexed) was plotted as a function of the stoichiometric ratio  $\Sigma$ , with  $\Sigma = [\text{Na}_2\text{S}_5]/[\text{Na}_2\text{S}_5] + [\text{CD}]$ . According to the Job's plot approach, the stoichiometry of the studied complex was obtained from the  $x$ -coordinate corresponding to the maximum of the curve that was fitted with a second order polynomial. The resulting association constants  $K_a(T)$  were determined from the binding isotherm equation corresponding to the (1:1) stoichiometry, approximating the activity coefficients to unity, as mainly performed in cyclodextrins experimental studies<sup>8</sup>.

$$\frac{2 \times [\text{CD}] \times \Delta}{\Delta_{max}} = [\text{CD}] + [\text{Na}_2\text{S}_x] + \frac{1}{K_a} - \sqrt{\left([\text{CD}] + [\text{Na}_2\text{S}_x] + \frac{1}{K_a}\right)^2 - (4 \times [\text{CD}] \times [\text{Na}_2\text{S}_x])}$$

Different diluted solutions of polysulfides (from 10 mM to 100 mM) were prepared in a deuterated buffer (25 mM  $\text{NaHCO}_3$  in  $\text{D}_2\text{O}$ ) and mixed with *pre*-weighted cyclodextrin ( $\pm 1$  mg) under argon atmosphere. Mixtures were vortexed for 1 min before the NMR acquisition. The CD protons chemical shifts were measured and compared to the chemical shifts of the native CD (10 mM) in the same deuterated buffer. The resulting variations of chemical shifts were plotted against the concentration of polysulfides introduced to obtain the experimental binding isotherm. An iterative least-squares fitting procedure was performed with Igor software (Wavemetrics) to calculate  $K_a(T)$  and  $\Delta_{max}$  which corresponds to the maximum chemical shift recorded if 100% of CDs are complexed. Therefore, the fraction of CD molecules that are complexed  $f_b$  is easily accessed by  $f_b = \Delta/\Delta_{max}$ . The statistic error relative to the chemical shift measurement, estimated to 9%, was calculated as the standard deviation of 10 similar and independent experiments. The plotted error bars were calculated considering the

uncertainties propagation assuming the experimental errors (dilution  $\pm 10 \mu\text{L}$ , and weighting  $\pm 0.1 \text{ mg}$ ) for each condition.

**Molecular docking of polysulfides with CDs:** To provide molecular information on the CD/polysulfide inclusion complexes, we performed a series of Molecular Docking calculations. In a first set of calculations we used as receptors all the CD crystallographic structures extracted from the Protein Data Bank (PDB)<sup>147</sup>. In a second set, we used as receptors the structures generated by Molecular Dynamics simulations. The structures of the polysulfides ligands  $S_3$ ,  $S_4$ ,  $S_5$  were extracted from crystallized proteins extracted from PDB (ID PS5, S4P and S3H respectively). All the calculations were performed using Autodock Vina<sup>219</sup>. The center of the box was aligned with the center of CD glycosidic oxygens while the search space is  $20 \times 20 \times 20 \text{ \AA}^3$ . The results for each calculation are the affinity score ( $\text{kcal mol}^{-1}$ ) values for each ligand conformation in its respective complex.

**Electrical detection, data acquisition and analysis:** Membrane lipid bilayers were made according to previously described methods<sup>220,221</sup>. In brief, a film of a 1% solution of diphytanoylphosphatidylcholine-lecithin in anhydrous decane was spread across a  $150 \mu\text{m}$  diameter hole drilled in a polysulfone wall separating the two compartments of a chamber. Each compartment contained  $900 \mu\text{L}$  of  $1 \text{ M NaCl}$ ,  $25 \text{ mM NaHCO}_3$ , pH 10 in an argon filled glovebox. After thinning of the decane film and formation of a planar lipid bilayer, a single  $\alpha$ -hemolysin ( $\alpha$ -HL) pore is inserted by adding monomeric  $\alpha$ -HL (Sigma) from a stock solution into the *cis* compartment. Insertion and orientation of the  $\alpha$ -HL pore was systematically checked to ensure transport of  $\beta$ -CD or  $\beta$ -CD/ $\text{Na}_2\text{S}_x$  complex into the stem part of the pore.  $100 \mu\text{L}$  of  $10 \text{ mM } \beta$ -CD or  $10 \text{ mM } \beta$ -CD/ $\text{Na}_2\text{S}_x$  complex was added to the *trans* compartment. Each data set was collected using independent experiments and different pores. Data were collected using Chimera Instruments VC100 at a sampling rate of  $4.17 \text{ MHz}$  and low-pass filtered at  $10 \text{ kHz}$ . Data were analyzed with a homemade macro using Igor software (Wavemetrics). The event measurements were based on a statistical analysis of the current traces: 425, 3904, 1254, and 1178 events analyzed for  $\beta$ -CD,  $\beta$ -CD/ $\text{Na}_2\text{S}_3$ ,  $\beta$ -CD/ $\text{Na}_2\text{S}_4$  and  $\beta$ -CD/ $\text{Na}_2\text{S}_5$ , respectively. The statistical analysis of the current traces has been previously described<sup>120</sup>. As the blockades shorter than  $100 \mu\text{s}$  are attributed to bumpings of  $\beta$ -CD or complexes at the entrance of the channel, we removed them from the scatter plot to obtain Figure II.10.c. Nevertheless, in this figure, blockades could be attributed both to  $\beta$ -CD or complexes. In order to discriminate both blockade types, we took the blockade ratio into account (Figure II.10.d), which depends on the nature,

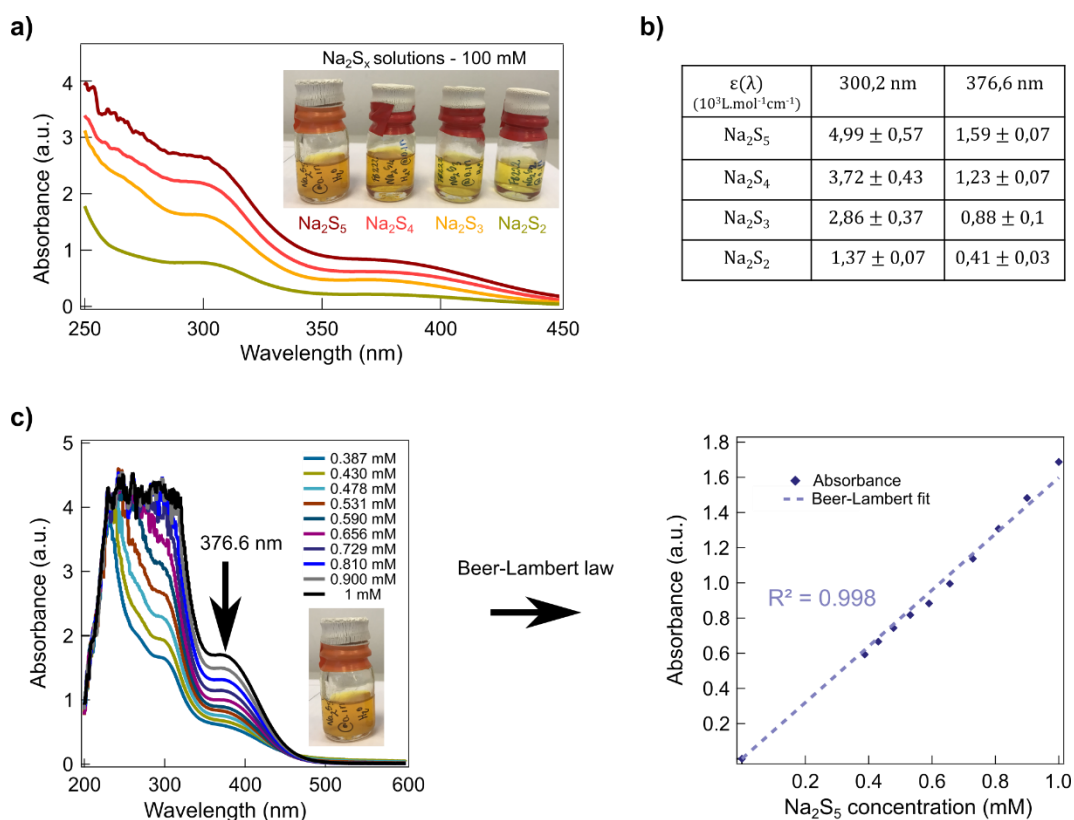


shape of the analyte. From the blockade ratio distribution, we removed the part attributed to the  $\beta$ -CD, which was previously characterized in Figure II.10.b, left (blue). Finally, we obtained the blockade ratio distribution attributed to the complexes (Figure II.11.d). The center of each blockade ratio distribution was calculated from the average of results obtained from 5 different positions of the interval fits.

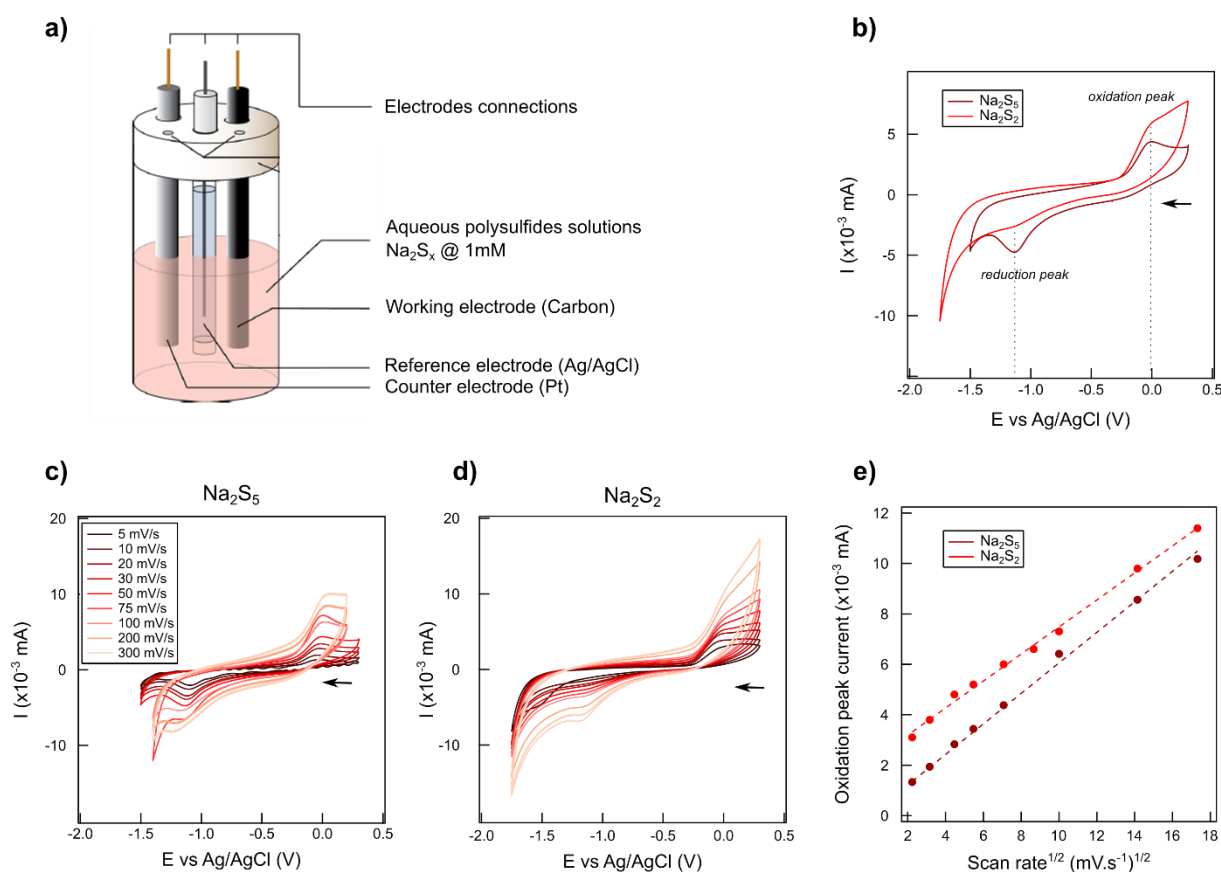
**Atomistic simulation of the  $\alpha$ -HL nanopore and nanopore hindrance estimator** : see ref<sup>149</sup>.

**Li-S battery assembly and testing** : Sulfur composite electrodes were prepared through a self-standing method by thoroughly hand-grinding a sulfur impregnated carbon (60/40 wt%), obtained by heat-treatment under air (160°C during 7h), and PTFE (5%<sub>w</sub>) as an aqueous binder. Sulfur electrodes were punched into circular disks of  $\sim 0.785 \text{ cm}^2$  from the self-standing film and were dried under vacuum at 70°C for 10h. Swagelock® cells were assembled in an argon-filled glovebox using Li metal foil as the negative electrode and the above mentioned sulfur composite electrode as the positive electrode. The tested PVDF-HFP separator, prepared according to the well-known Bellcore process<sup>154</sup>, was sandwiched between two layers of a Whatman borosilicate glass microfibre membranes soaked with electrolyte. The electrolyte used was 1 M LiTFSI and 0.25 M LiNO<sub>3</sub> in 1,3-dioxolane (DOL) : dimethoxyethane (DME) in a 1:1 volume ratio. The cells were cycled with a VMP2 potentiostat (BioLogic, France) at ambient temperature. The electrochemical performances of the cells were studied by galvanostatic discharge-charge cycling in the voltage range of 1.7 – 2.8 V vs Li/Li<sup>+</sup> at a constant current (C/10).

## 2. Supporting Figures: Polysulfides characterization



**Figure SI.II.1: Characterization of aqueous sodium polysulfides solutions by UV-vis spectroscopy.** **a)** UV-vis spectra of aqueous polysulfides solutions ( $\text{Na}_2\text{S}_5$ ,  $\text{Na}_2\text{S}_4$ ,  $\text{Na}_2\text{S}_3$  and  $\text{Na}_2\text{S}_2$ ) at 0.5 mM in a 1 cm quartz UV-vis. Inset showing the typical colour of sodium polysulfides at 100 mM (25 mM  $\text{NaHCO}_3$ , pH 10). **b)** Summary table of the different molar extinction coefficients ( $\epsilon$ ) of the different sodium polysulfide solutions for two defined wavelengths ( $\lambda = 300.2$  nm and 376.6 nm). Errors bars were estimated as the standard deviations of 13, 17, 14, and 18 of independent UV-vis spectra acquisitions for different concentrations of respectively  $\text{Na}_2\text{S}_5$ ,  $\text{Na}_2\text{S}_4$ ,  $\text{Na}_2\text{S}_3$  and  $\text{Na}_2\text{S}_2$ . **c)** Evidence of Beer Lambert law shown for  $\text{Na}_2\text{S}_5$ . The dashed line represents the linear fit.

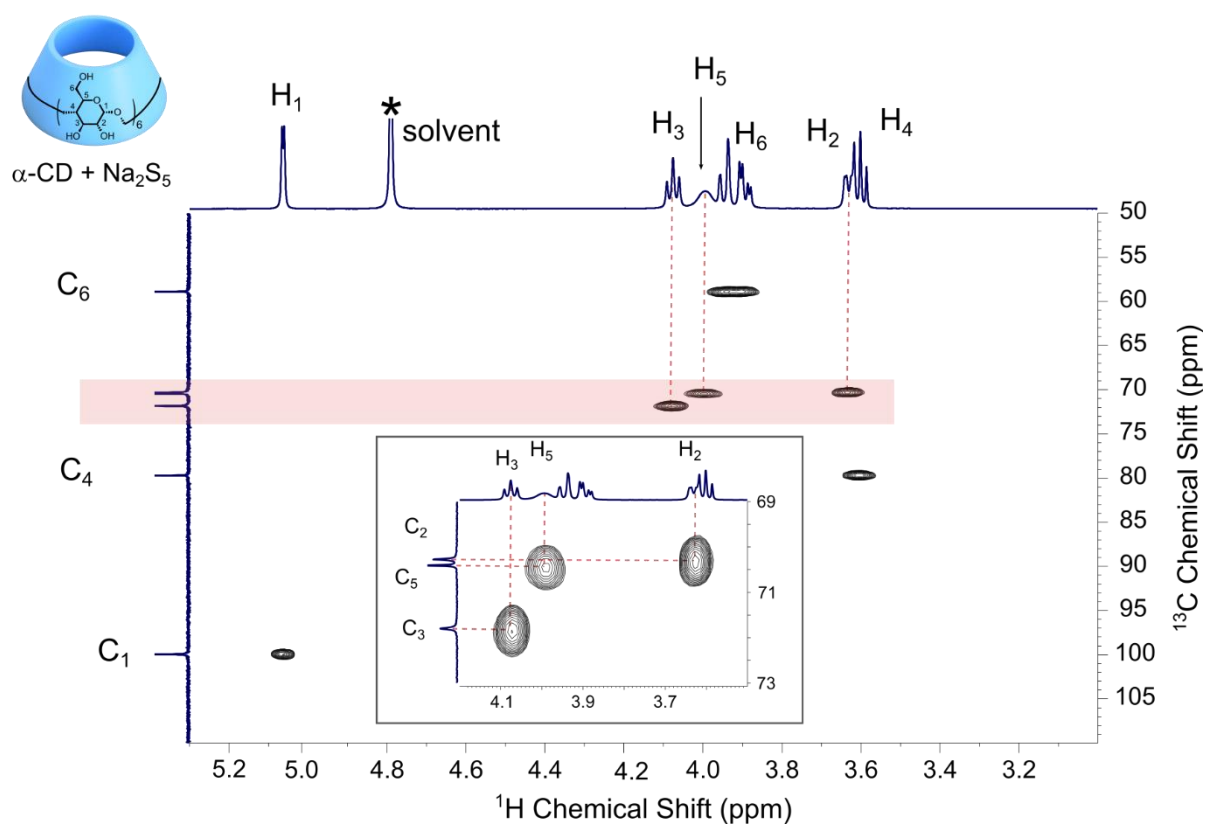


**Figure SI.II.2: Characterization of aqueous sodium polysulfides by cyclic voltammetry. a)**

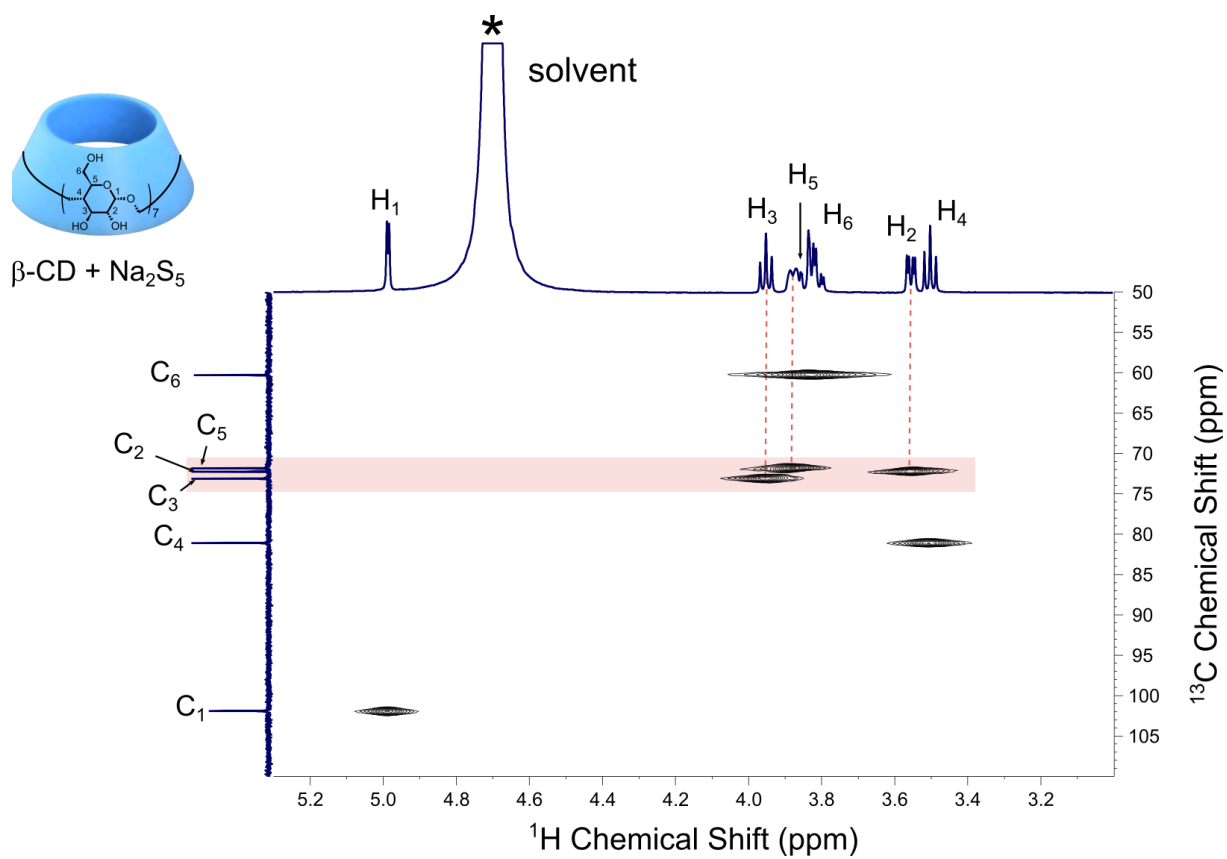
Scheme of the tight 3-electrodes electrochemical cell that was used involving glassy carbon as the working, Pt as the counter and Ag/AgCl as the reference electrodes, adapted from ref<sup>222</sup>. **b)**

Overlapping of the cyclic voltammograms obtained for aqueous polysulfides solutions at 1 mM, Na<sub>2</sub>S<sub>2</sub> and Na<sub>2</sub>S<sub>5</sub>, with a 50 mV.s<sup>-1</sup> scan rate. Na<sub>2</sub>S<sub>5</sub> and Na<sub>2</sub>S<sub>2</sub> are electrochemically active as shown by the oxidation and reduction peaks, but the low differences values of these potentials do not allow the distinction of the different species. Cyclic voltammetry curves obtained for **c)** Na<sub>2</sub>S<sub>5</sub> and **d)** Na<sub>2</sub>S<sub>2</sub> solutions at 1 mM (25 mM NaHCO<sub>3</sub> pH 10) over a wide range of scan rates, from 5 to 300 mV.s<sup>-1</sup>. **e)**

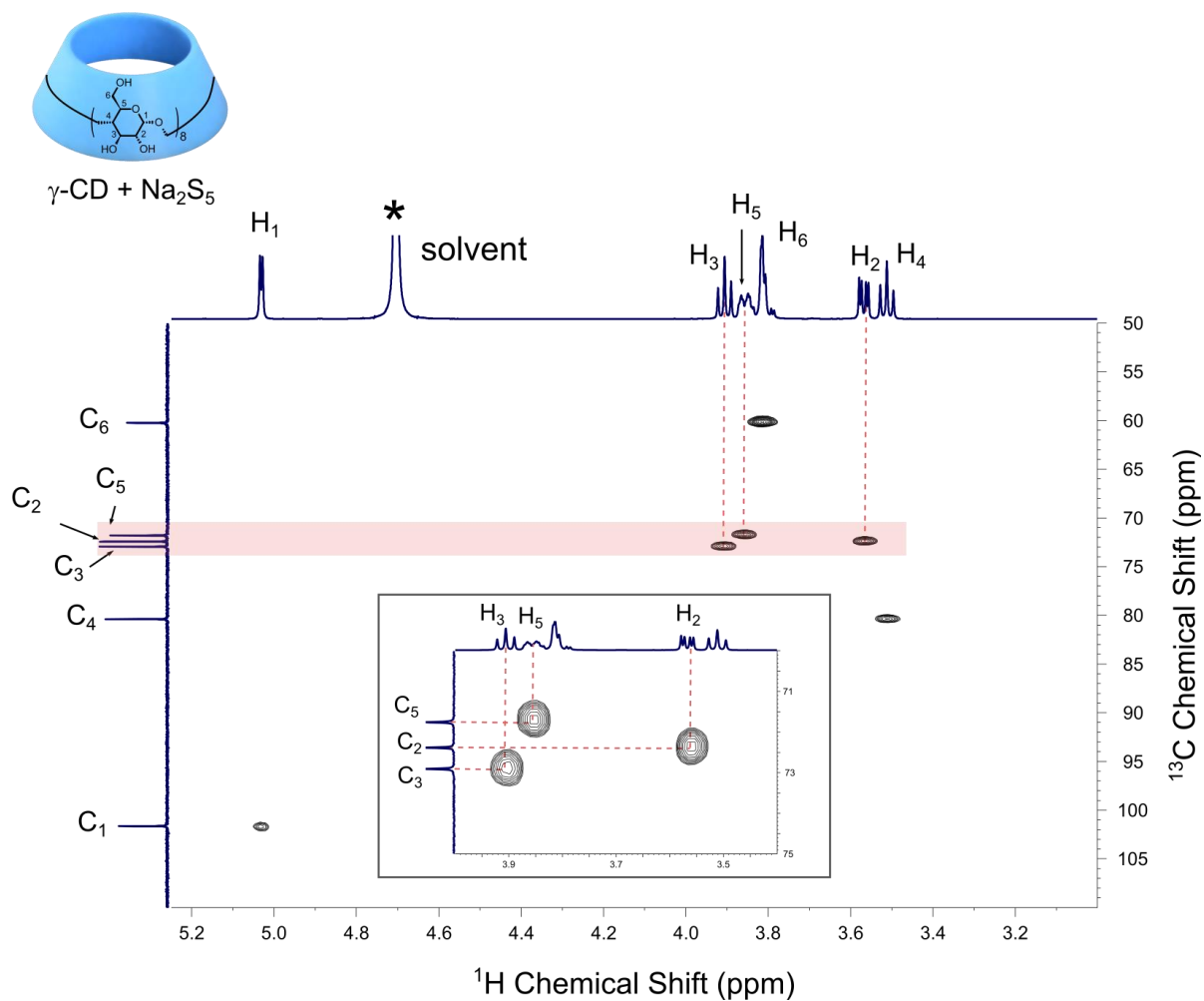
Evidence of the linear dependence of the oxidation peak current with the square root of the scan rate. Verification of the Randle-Sevcik equation,  $i_p = 0.446nFAC^0 \left( \frac{nFvD_0}{RT} \right)^{1/2}$  with  $i_p$  the current maximum peak,  $n$  the number of transferred electrons in the red-ox process,  $F$  the Faraday Constant,  $A$  the electrode surface,  $C^0$  the species concentration,  $D_0$  the diffusion coefficient,  $v$  the scan rate,  $R$  the Gas constant,  $T$  the temperature, enlightening the free diffusion a diffusion process for the polysulfides species in such experiment.

3. Supporting Figures: CD/polysulfide interaction by  $^1\text{H}$  NMR

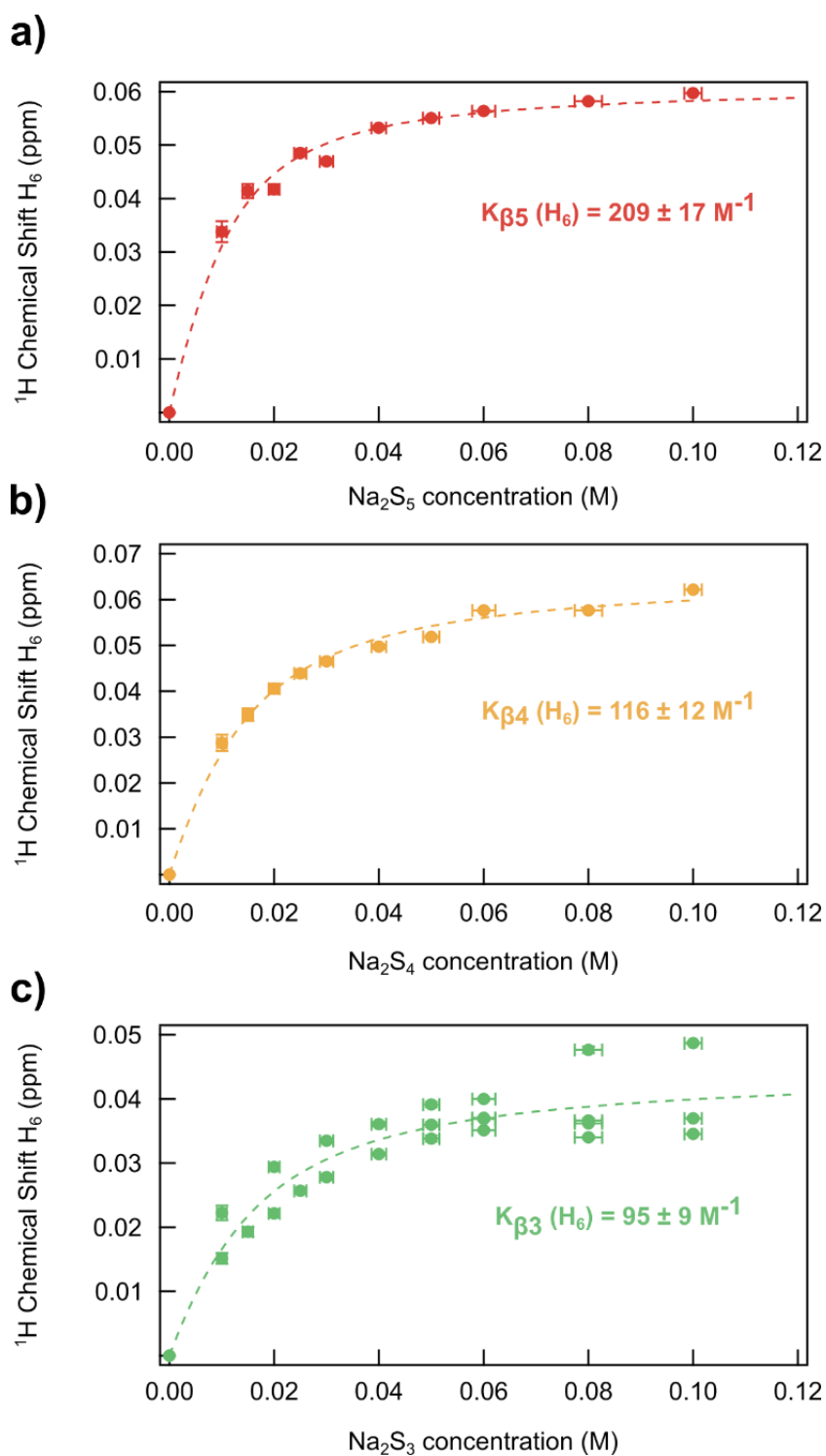
**Figure SI.II.3:** 2D  $^1\text{H}$ - $^{13}\text{C}$  HSQC NMR (600 MHz,  $\text{D}_2\text{O}$ , 25 mM  $\text{NaHCO}_3$ , 298K) spectra of  $\alpha$ -CD with  $\text{Na}_2\text{S}_5$ . The pink-boxed cross peaks are a zoomed-in (insert) to perform the signals attribution.



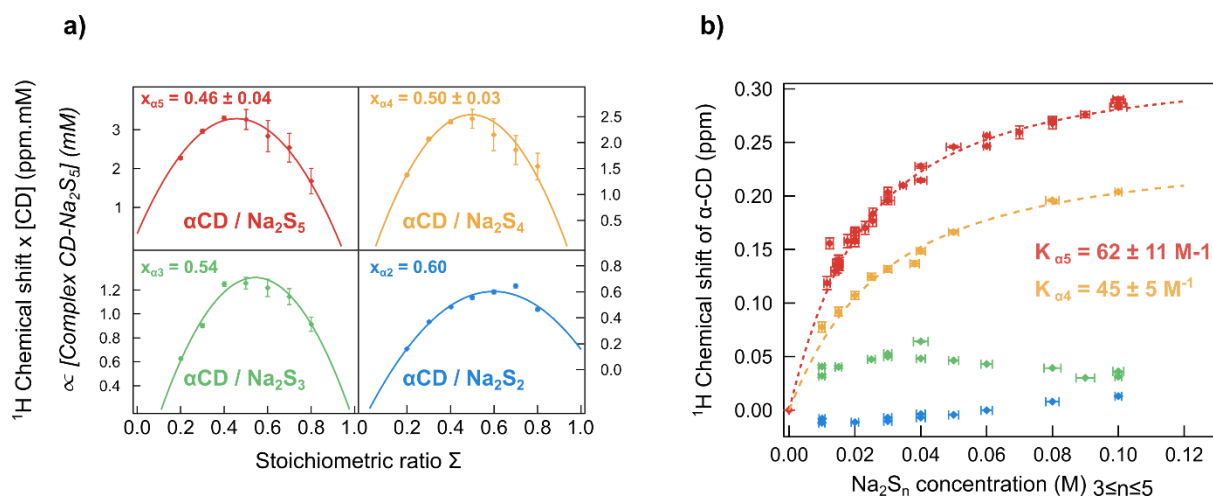
**Figure SI.II.4:** 2D  $^1\text{H}$ - $^{13}\text{C}$  HSQC NMR (600 MHz,  $\text{D}_2\text{O}$ , 25 mM  $\text{NaHCO}_3$ , 298K) spectra of  $\beta$ -CD with  $\text{Na}_2\text{S}_5$ . The pink-boxed cross peaks are a zoomed-in (insert) to perform the signals attribution.



**Figure SI.II.5:** 2D  $^1\text{H}$ - $^{13}\text{C}$  HSQC NMR (600 MHz,  $\text{D}_2\text{O}$ , 25 mM  $\text{NaHCO}_3$ , 298K) spectra of  $\gamma$ -CD with  $\text{Na}_2\text{S}_5$ . The pink-boxed cross peaks are a zoomed-in (insert) to perform the signals attribution.



**Figure SI.II.6:** Binding isotherms and resulting association constants for  $\beta$ -CD complexes considering  $H_6$  chemical shifts instead of  $H_3$  (Figure II.6). Errors bars were estimated similarly to Figure II.6. **a)**  $\beta$ -CD/ $\text{Na}_2\text{S}_5$  **b)**  $\beta$ -CD/ $\text{Na}_2\text{S}_4$  and **c)**  $\beta$ -CD/ $\text{Na}_2\text{S}_3$ . The correlation between the length of the sulfur chain of polysulfides is validated.

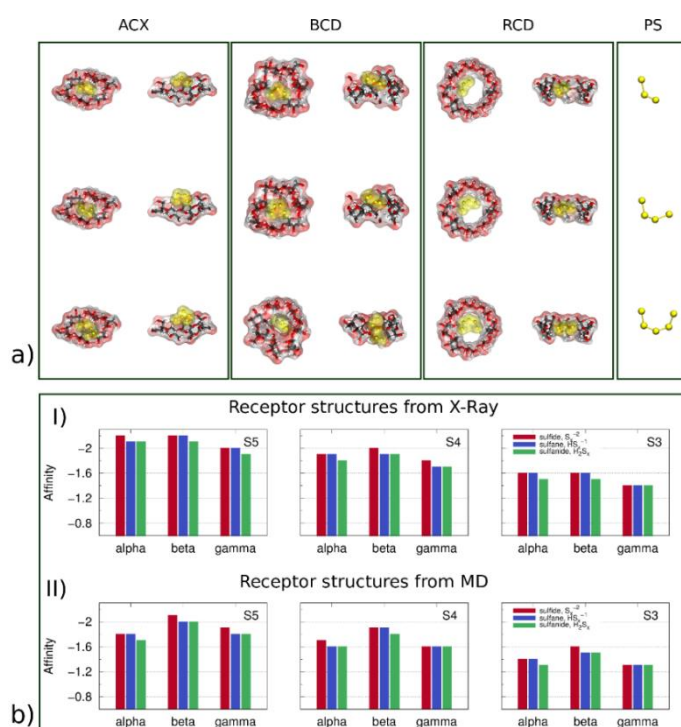


**Figure SI.II.7:** Job's plot and binding isotherm for  $\alpha$ -CD/polysulfide complexes. **a)** Job's plot for  $\alpha$ -CD/ $\text{Na}_2\text{S}_5$  (red),  $\alpha$ -CD/ $\text{Na}_2\text{S}_4$  (yellow),  $\alpha$ -CD/ $\text{Na}_2\text{S}_3$  (green) and  $\alpha$ -CD/ $\text{Na}_2\text{S}_2$  (blue). **b)**  $^1\text{H}$  NMR titration plots for the corresponding inclusion complexes and fitted binding isotherms with indication of the association constants that could be determined.

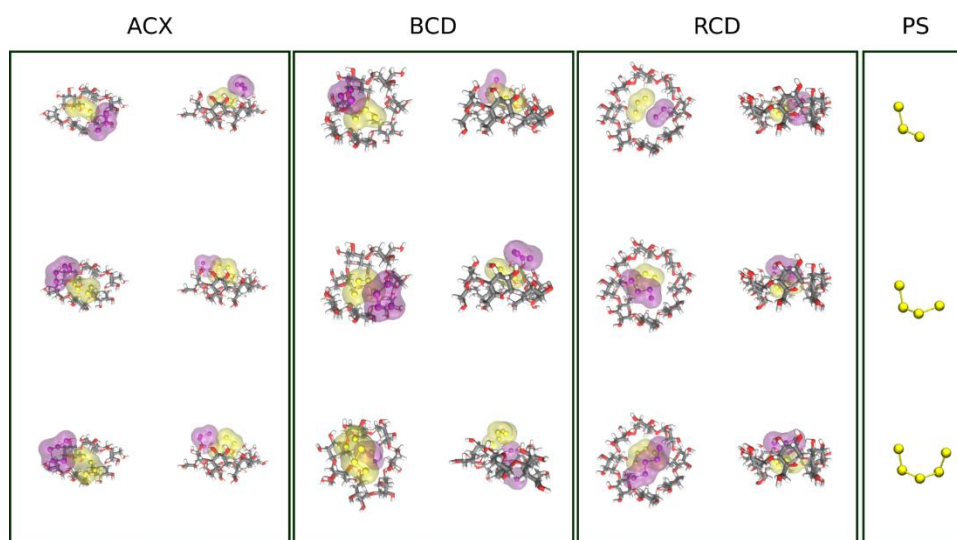


#### 4. Supporting Figures: CD/polysulfide interaction by Molecular Docking calculations

For the Molecular docking experiments, two sets of calculations were carried out depending on the CDs structures used as receptors. On the one hand, the calculations were performed from CD crystallographic structures extracted from the Protein Data Bank, denominated as “X-ray”. On the other hand, CDs structures were generated from Molecular Dynamics Simulations which are supposed to represent better the CDs behaviour in solution. The exhaustive details of calculations are provided in the Materials & Methods part of ref<sup>149</sup>.



**Figure SI.II.8: Molecular Docking calculations. a)** Best Docking Poses. Receptors structures, ACX ( $\alpha$ -CD), BCD ( $\beta$ -CD) and RCD ( $\gamma$ -CD), are those obtained from MD simulations, as described in the Methods part of ref<sup>149</sup>. Polysulfides are represented in yellow. Non-polar hydrogens are not shown for sake of clarity. **b)** Best Docking Affinities (kcal.mol<sup>-1</sup>) over all the calculated CD/polysulfide inclusion complexes. Red, blue and green bars are related to the affinity of sulfide (S<sub>x</sub><sup>2-</sup>), sulfanide (HS<sub>x</sub><sup>-</sup>) and sulfane (H<sub>2</sub>S<sub>x</sub>) respectively. Indeed, dissolved polysulfides are known to form such species in aqueous media<sup>223</sup>. Two sets of calculations (I & II) were carried out depending on the CDs structures used as receptors.

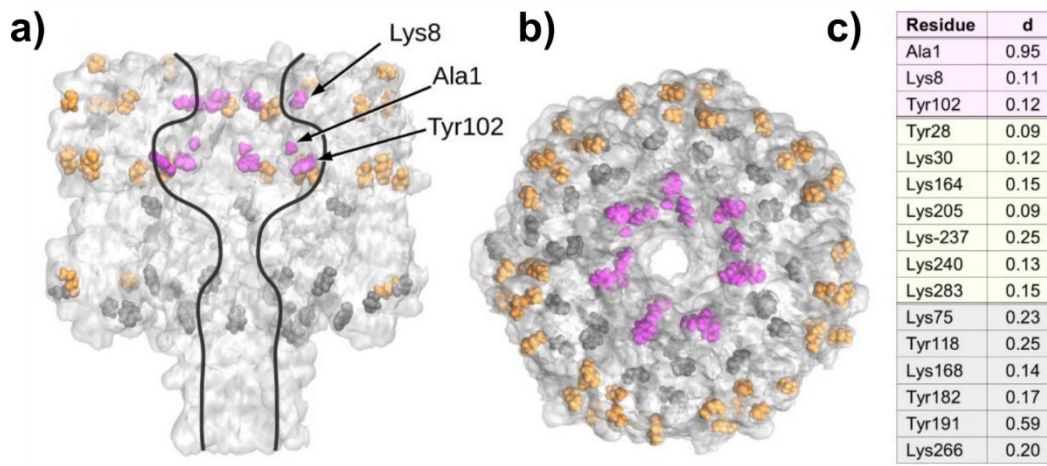


**Figure SI.II.9: Second polysulfide docking.** Best docked conformations of the second sulfide (purple) docked on the *pre*-formed complex shown in Figure SI.II.8. Columns from left to right represent  $\alpha$ - (ACX),  $\beta$ - (BCD) and  $\gamma$ -CD (RCD) receptors, while from top to bottom rows are the representative of  $S_3^{2-}$ ,  $S_4^{2-}$ ,  $S_5^{2-}$ , respectively. For most cases there is no room to accommodate a second sulfide in the CD cavity, except for  $S_3^{2-}$  in  $\gamma$ -CD (RCD). At best the second sulfide resides on top of the cavity, with very little contact with CD and in general with a lower affinity score with respect to the first docked sulfide. Affinities are reported in Table SI.II.1.

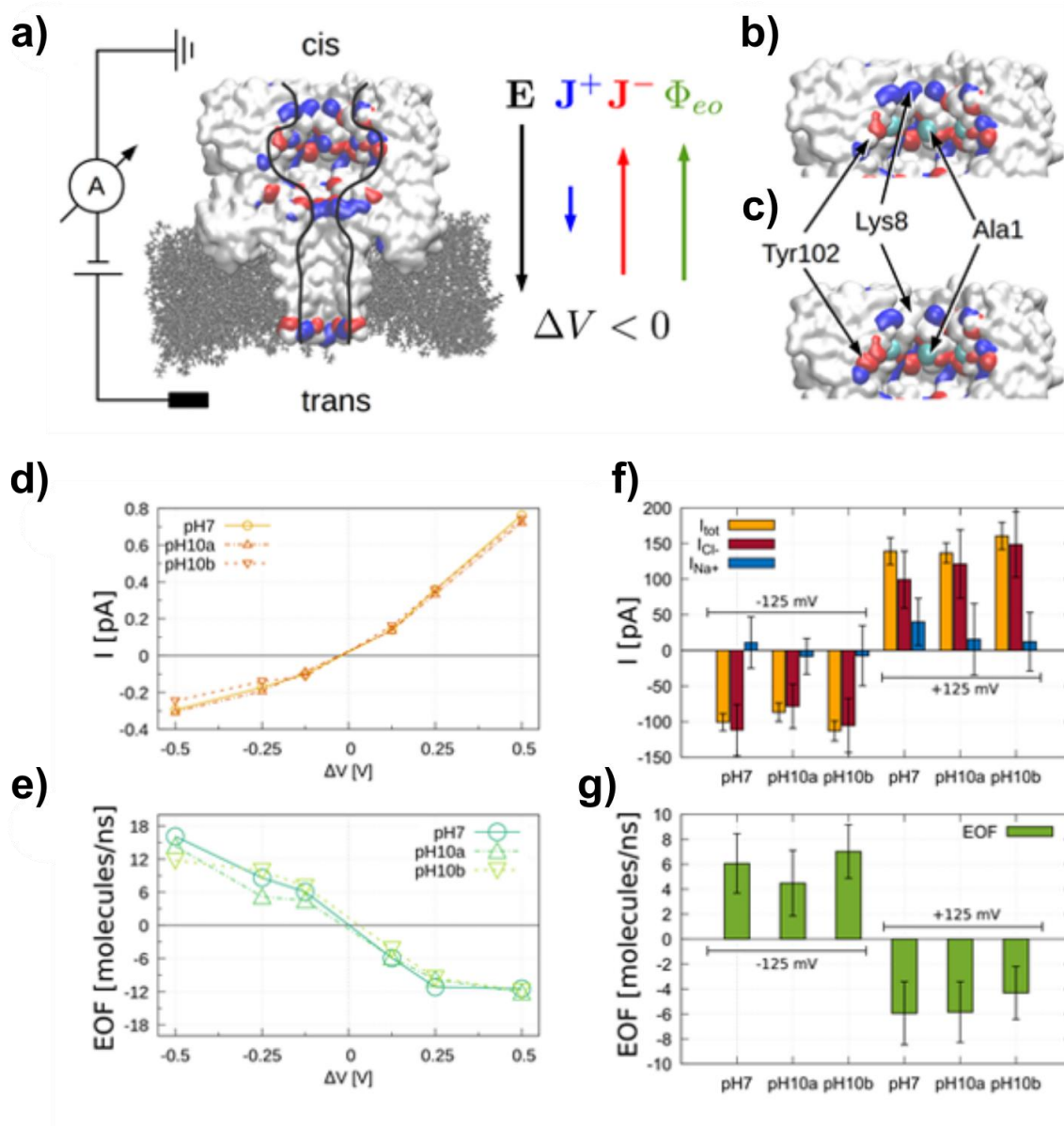
kcal.mol <sup>-1</sup>	$S_5^{2-}$	$S_4^{2-}$	$S_3^{2-}$
$\alpha$ -CD	-1.1	-1.0	-0.9
$\beta$ -CD	-1.4	-1.1	-1.0
$\gamma$ -CD	-1.6	-1.4	-1.4

**Table SI.II.1:** Docking affinities of the second sulfide docked on the *pre*-formed complex, see Figure SI.II.9.

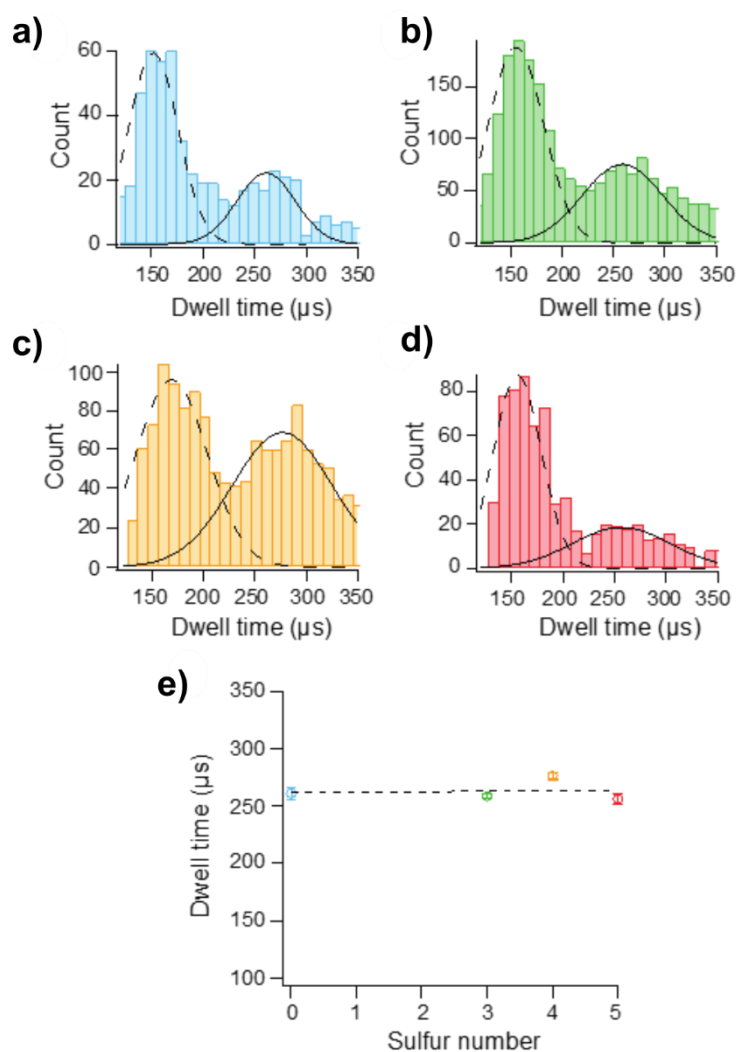
## 5. Supporting Figures: Nanopore detection



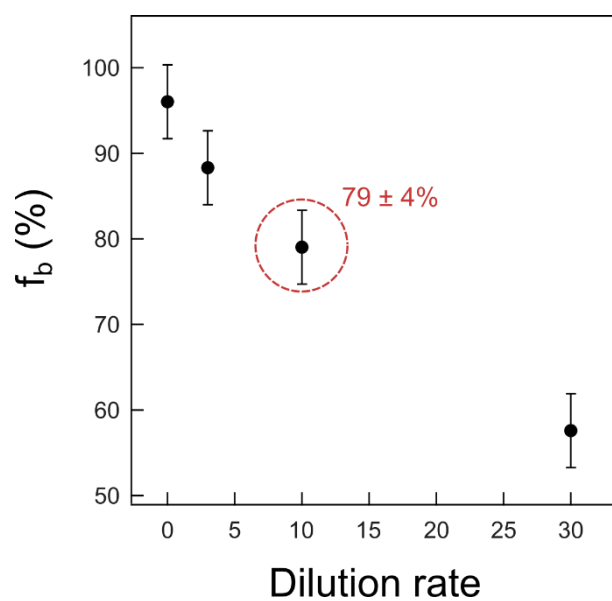
**Figure SI.II.10:  $\alpha$ -HL titratable amino acid residues with  $8 < pK_a < 11$ .** **a)** Side and **b)** top view of the  $\alpha$ -HL pore with the identification of the amino acids that might be deprotonated at pH 10 (lysine, alanine and tyrosine). They are colored in magenta, yellow and grey when exposed to the interior, to the exterior of the pore or buried respectively. **c)** Deprotonation fraction of each titratable amino acid (see ref<sup>149</sup> for detail of calculations). Two different protonation cases, pH10a and pH10b, are considered taking into account only the amino acids orientated to the interior of the pore. For pH10a, the only exposed residues that change protonation state is Ala1 (the N-terminal,  $d = 0.95$ ) while for pH10b we also deprotonated one, out of seven, Lys8 ( $d = 0.11$ ) and one, out of seven, Tyr102 ( $d = 0.12$ ).



**Figure SI.II.11: Ionic current and electro-osmotic flux (EOF) from MD simulations for  $\alpha$ -HL in the three different protonated systems pH7, pH10a and pH10b.** **a)**  $\alpha$ -HL nanopore Molecular Dynamics (MD) set-up at pH7. Highlight of the residues that change protonation state in the **b)** pH10a and **c)** pH10b titration cases. **d)** I-V curves, **e)** EOF vs applied voltage, **f)** total anion and cation currents and **g)** EOF at +125 mV and -125 mV. Error bars in panels d) and e) are smaller than the size of the symbols. The substantial equivalence among the pH7, pH10a, pH10b systems indicates that the change in the protonation due to the increase of the pH from 7 to 10 does not significantly affect the rectification of the total current. The  $\alpha$ -HL remains anion selective and EOF has, in essence, the same intensity in the three analysed conditions.



**Figure SI.II.12: Dwell time histograms of  $\beta$ -CD (blue),  $\beta$ -CD/ $\text{Na}_2\text{S}_3$  (green),  $\beta$ -CD/ $\text{Na}_2\text{S}_4$  (orange) and  $\beta$ -CD/ $\text{Na}_2\text{S}_5$  (red). a-d) Short dwell times events attributed to bumping events are fitted by a gaussian (dashed line). The corresponding short dwell times events are  $151.6 \pm 3.0 \mu\text{s}$ ,  $155.1 \pm 1.9 \mu\text{s}$ ,  $169.0 \pm 1.6 \mu\text{s}$  and  $155.7 \pm 3.0 \mu\text{s}$  for  $\beta$ -CD,  $\text{Na}_2\text{S}_3/ \beta$ -CD,  $\text{Na}_2\text{S}_4/ \beta$ -CD and  $\text{Na}_2\text{S}_5/ \beta$ -CD respectively. Long dwell times events attributed to interactions with  $\alpha$ -HL are fitted by a gaussian (solid line). The corresponding long dwell times events are  $261.0 \pm 5.0 \mu\text{s}$ ,  $258.7 \pm 1.6 \mu\text{s}$ ,  $276.5 \pm 3.0 \mu\text{s}$  and  $256.4 \pm 4.0 \mu\text{s}$  for  $\beta$ -CD,  $\text{Na}_2\text{S}_3/ \beta$ -CD,  $\text{Na}_2\text{S}_4/ \beta$ -CD and  $\text{Na}_2\text{S}_5/ \beta$ -CD respectively. e) Dwell times as a function of sulfur number. The dashed line represents a linear fit with an average dwell time of  $262.9 \pm 1.1 \mu\text{s}$ .**



**Figure SI.II.13: NMR quantification of  $f_b$  in the nanopore experiment conditions.** The  $\beta$ -CD/ $\text{Na}_2\text{S}_5$  complex solution was initially prepared mixing 1 mM  $\beta$ -CD with 10mM  $\text{Na}_2\text{S}_5$ . The nanopore experiment conditions correspond to this solution being diluted 10 times.



# Supporting Information for Chapter III

## 1. Materials & Methods

**Materials:** All materials were used as received without further purification step and the solvents used for synthesis were purchased “pure for analysis” from VWR (dichloromethane  $\text{CH}_2\text{Cl}_2$ , diethyl ether, dimethyl sulfoxide DMSO, tetrahydrofuran THF).  $\alpha$ -cyclodextrin ( $\alpha$ -CD, > 99%) was produced by Wacker and purchased from Sigma Aldrich. 2-isocyanatoethyl methacrylate (IEM, 98%), poly(acrylic acid) (PAA,  $M_w \approx 450\,000 \text{ g}\cdot\text{mol}^{-1}$ ), 1,1-carbonyldiimidaole (CDI, for synthesis), poly(ethylene oxide) (PEO10K,  $M_w \sim 10\,000 \text{ g}\cdot\text{mol}^{-1}$  and PEO35K,  $M_w \sim 35\,000 \text{ g}\cdot\text{mol}^{-1}$ ), sodium persulfate ( $\text{Na}_2\text{S}_2\text{O}_8$ ), sodium hydroxide pellets (NaOH, 98%) and propylene oxide (for synthesis) were obtained from Sigma Aldrich. 1-pyrene butyric acid N- hydroxysuccinimid ester (PBS) was purchased from ChemCruz. Poly(ethylene oxide) (PEO100K,  $M_w \sim 100\,000 \text{ g}\cdot\text{mol}^{-1}$ ) was obtained from Polysciences Inc. Lithium bis(trifluoromethane sulfonyl)imide (LiTFSI, 99.9%, extra dry), LP30 electrolyte (99.9%) and were purchased from Solvionic. 4-fluoro-1,3-dioxolan-2-one (FEC, 98%) was purchased from Alfa Aesar, vinylene carbonate (VC, 99.5%) was obtained from Sigma Aldrich. Lithium hexafluorophosphate ( $\text{LiPF}_6$ ), propylene carbonate (PC) and ethylene carbonate (EC) were supplied from DodoChem and diethyl carbonate (DEC, 99+%) was purchased from Alfa Aesar.

**PEO microwave-assisted dimethacrylation synthesis**<sup>191</sup>: The synthesis is conducted in a microwave synthesis reactor (Anton Paar Monowave 300). PEO (1 eq.) and IEM (10 eq.) are introduced in a microwave vessel that is irradiated at  $100^\circ\text{C}$  (by modulation of power < 450 W) for 2 min. The solution is cooled rapidly in an ice bath. The crude product is dissolved in  $\text{CH}_2\text{Cl}_2$  and filtrated under vacuum. Once the solvent is evaporated, the dimethacrylated PEO is precipitated in diethylether and dried under vacuum to obtain a stringy white powder.

**PR synthesis:** PR is synthesized according to a modified procedure from literature<sup>61,64</sup>. Dimethacrylated PEO is added to a saturated solution of  $\alpha$ -CDs ( $145 \text{ g}\cdot\text{L}^{-1}$ ) in  $\text{H}_2\text{O}$  at room temperature for 24h. As described in literature<sup>33</sup>, precursors are introduced in stoichiometric proportions: 1 eq. of  $\alpha$ -CD for 2 eq. of ethylene oxide (EO) units. The corresponding inclusion complex, called PPR, precipitates as a white paste. After the PPR (1 eq.) is gathered by filtration by



suction and dried under vacuum (yield > 25%), PBS (10 eq.) and sodium persulfate (5%<sub>w</sub>) are added and stirred at room temperature in a H<sub>2</sub>O/DMSO mixture (2/1) (v/v) for 12h at ~60 mg.mL<sup>-1</sup>. When the two solvents are added at the same time, a high number of  $\alpha$ -CDs born by the PEO chain is ensured. To get a PR with fewer threaded  $\alpha$ -CDs, PPR was firstly dissolved in DMSO at 80°C and H<sub>2</sub>O is added secondly after several hours with PBS and sodium persulfate as a free-radical initiator. Once the solvent is removed by evaporation, the crude product is solubilized in small amount of DMSO and purified by 3 successive precipitations in diethyl ether. The PR is finally lyophilized and stored as a yellowish powder. To isolate the PR from the remaining free  $\alpha$ -CDs, an additional purification step is performed<sup>72</sup>. Hand-milled PRs are heated to 200°C for 15 min and the calcinated product is dissolved in milliQ water for 1 week. After filtration or sonication to remove the insoluble part, the purified PR is obtained by lyophilization of the aqueous filtrate and stored as a brownish powder.

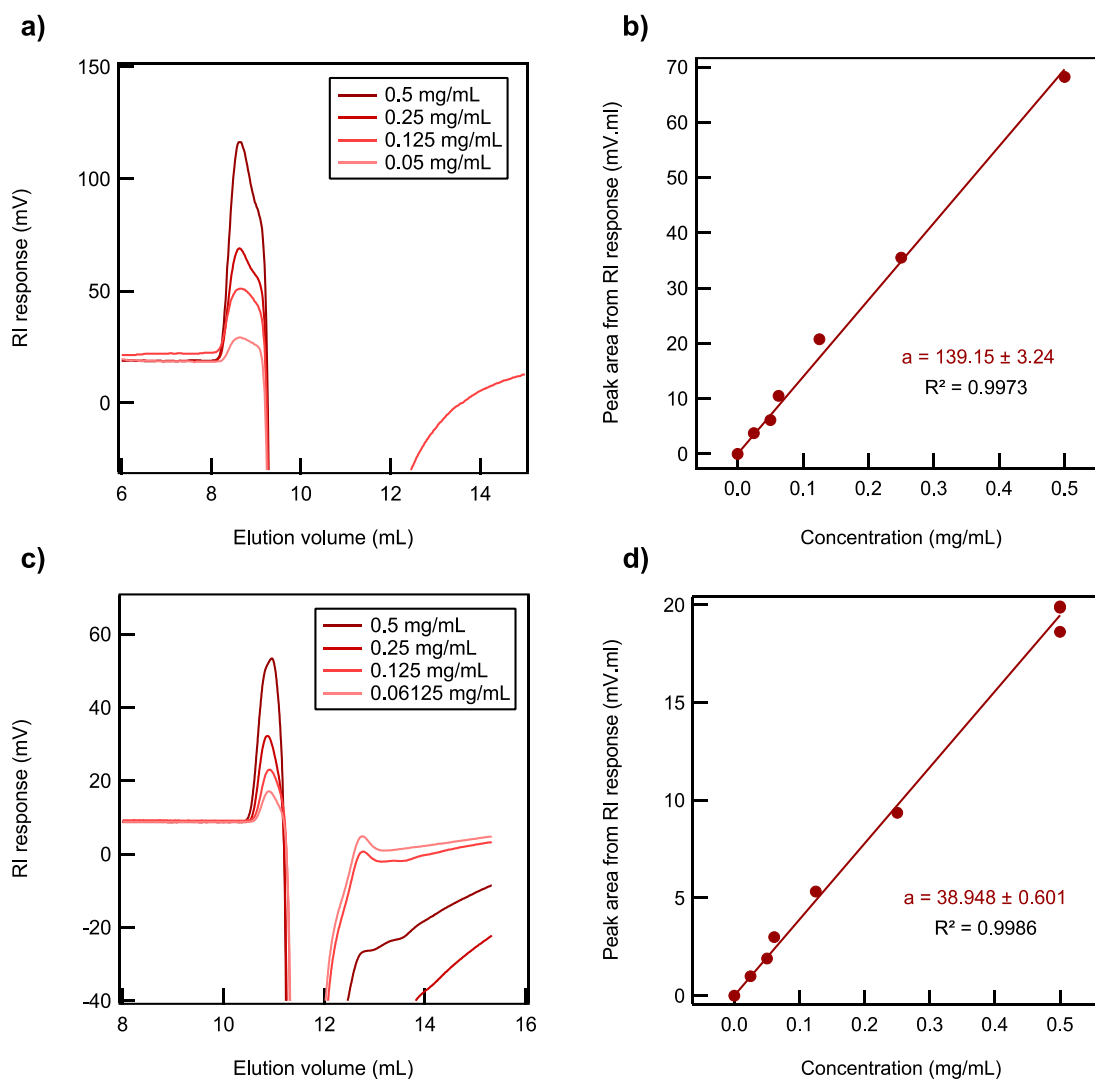
**PR-PAA synthesis:** PRs are hydroxypropylated according to an already published protocol<sup>67</sup>. PR (10 mg.mL<sup>-1</sup>) is dissolved in 1M NaOH aqueous solution at 0°C. Propylene oxide (11 eq. per OH) is added dropwise, the mixture is then stirred for 12h from 0°C to RT while the ice bath is melting. After the neutralisation of the medium, salts are removed by two precipitations in DMSO. The soluble hydroxypropylated PR is finally freeze-dried. The grafting of PR on PAA is carried out according to a reported protocol<sup>32</sup>. The reaction is conducted in a three-necked round-bottomed flask equipped with a condenser under magnetic stirring. A solution of both PAA (50 mg.mL<sup>-1</sup>) and CDI is prepared in anhydrous DMSO and stirred at 50°C for 24h under argon atmosphere. This solution is cooled down and a solution of PR (100 mg.mL<sup>-1</sup>) prepared in anhydrous DMSO is added. The mixture is stirred at 70°C for additional 72h under argon atmosphere. CDI proportions are varied from 0.5% to 5% equivalents of PAA COOH units and the PR/PAA mass ratio is also varied from 5%<sub>w</sub> to 20%<sub>w</sub>. The resulting PR-PAA polymer is precipitated from THF and filtered three times. It is then lyophilized to yield a white powder.

**Synthesis characterization:** <sup>1</sup>H Nuclear Magnetic Resonance (NMR) spectra were recorded on a Brüker spectrometer (600 MHz) at 308K for samples prepared in DMSO-d<sub>6</sub> and 298K in other deuterated solvents. Spectra were analysed with TopSpin 3.6. Size exclusion chromatography (SEC) was performed in DMF, as the eluent, with both UV ( $\lambda=345$  nm) and refractive index (RI) detectors (T = 35°C ; sensibility = 256). Two different types of columns from Waters were used: HR 4E Styragel column thermostated at 60°C and Shodex KD-806M. The eluent flow rate was 1 mL.min<sup>-1</sup> and the

samples were injected at low concentrations: 3 mg.mL<sup>-1</sup> for PEO and 0.1 mg.mL<sup>-1</sup> for  $\alpha$ -CD, PPR and PR samples in order to prevent parasitic phenomena such as CDs adsorption or diffusion in the columns. The reported molecular weights are expressed in PEO equivalents as the calibration was performed with PEO standards (Table SI.III.1) using a conventional calibration method for homopolymers (OmniSEC™). As the peaks area is proportional to the mass concentration injected, both columns were calibrated with  $\alpha$ -CD solutions to titrate the weight proportion of free  $\alpha$ -CDs in each sample (Figure SI.III.1). FTIR spectra were acquired in ATR mode on a Nicolet™ iS™ 5 FTIR spectrometer (Thermo Fisher Scientific) in the range of ~500 to 4000 cm<sup>-1</sup>.

PEO standard $M_p$ (g.mol <sup>-1</sup> )	PEO standard $\bar{D}$
1 470	1.03
4 120	1.02
7 100	1.02
11 840	1.04
20 000	1.05
31 380	1.04
58 700	1.06
71 700	1.06
106 500	1.04

**Table SI.III.1 PEO standards used for SEC calibration**

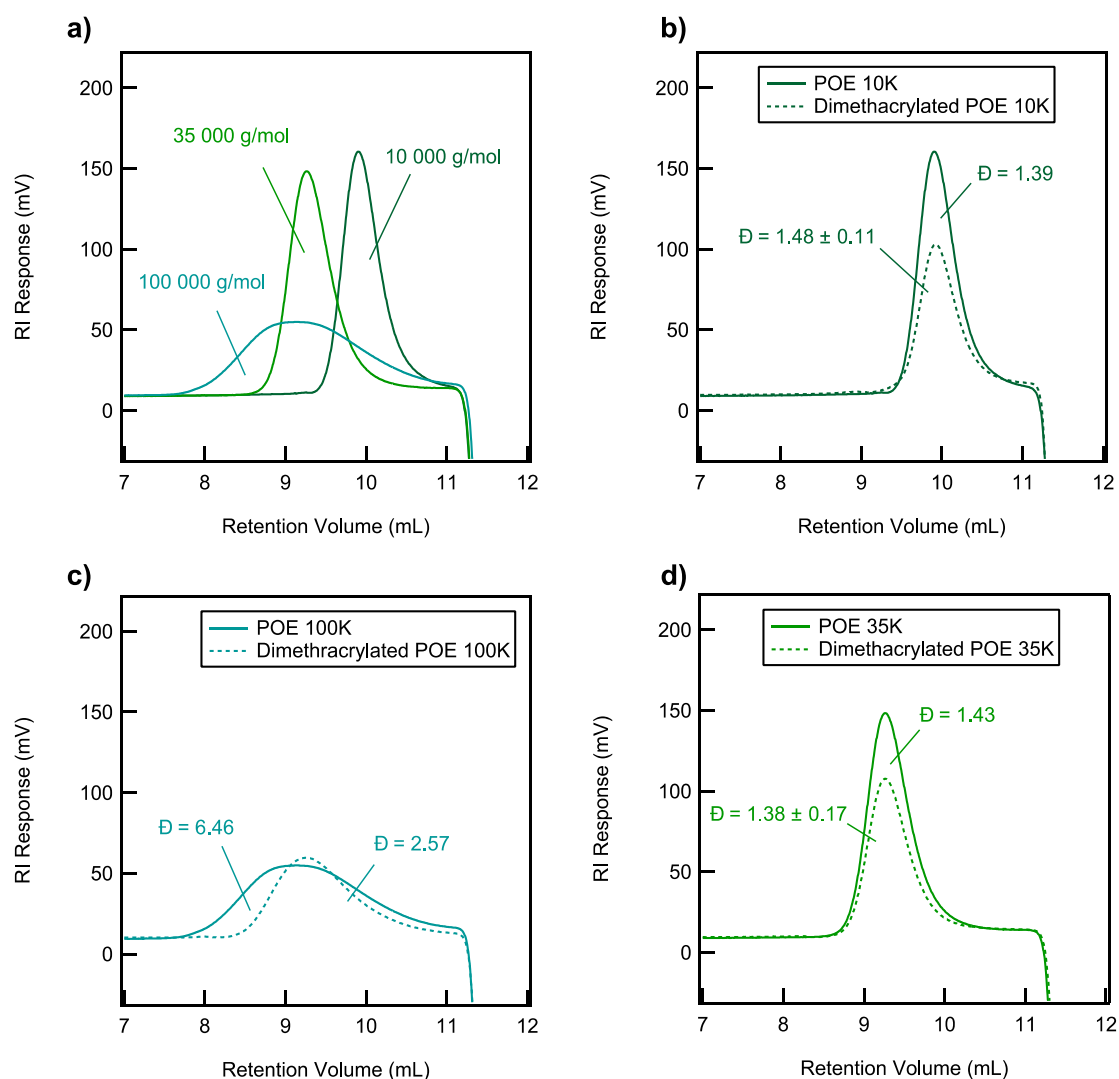


**Figure SI.III.1 SEC calibration in  $\alpha$ -CD with the two different chromatography columns.** Samples were solubilized in DMF. **a)** Overlapped SEC chromatograms obtained with the HR 4E Styragel column by RI detection for different concentrations of  $\alpha$ -CD solutions and **b)** linear fitting between peak areas and  $\alpha$ -CD concentration. **c)** Overlapped SEC chromatograms obtained with the Shodex KD-806M column by RI detection for different concentrations of  $\alpha$ -CD solutions and **d)** linear fitting between peak areas and  $\alpha$ -CD concentration.

**Thermal characterization:** DSC measurements were carried out with a DSC Discovery 25 (TA Instruments) in non-hermetic aluminium capsules. From  $-60^{\circ}\text{C}$ , specimens were heated to  $180^{\circ}\text{C}$  at a rate of  $15^{\circ}\text{C}\cdot\text{min}^{-1}$ , then cooled to  $-70^{\circ}\text{C}$  at a rate of  $-15^{\circ}\text{C}\cdot\text{min}^{-1}$  and heated back to  $180^{\circ}\text{C}$  at the rate of  $15^{\circ}\text{C}\cdot\text{min}^{-1}$ . The DSC thermograms were recorded in the third steps. Residual solvent traces (DMSO and water) were removed during the first heating and their quantities were estimated by weighing the capsules after de DSC experiments.

**Mechanical characterization of polymers:** For tensile experiments, PR-PAA and PAA membranes were prepared according to already reported protocol<sup>32</sup>. Polymers were dissolved in DMSO ( $50\text{ mg}\cdot\text{mL}^{-1}$ ) to make a transparent slurry that was casted in a Teflon rectangular mould ( $37\text{ mm} \times 14\text{ mm}$ ). They are then dried 24h at  $80^{\circ}\text{C}$  in a convection oven and additional 24h at  $80^{\circ}\text{C}$  under vacuum. The dimensions of the polymer membranes are approximatively  $37\text{ mm} \times 14\text{ mm}$  and their thickness is approximately  $100\text{ }\mu\text{m}$ . The samples were soaked in an electrolyte until the equilibrium state was reached either in a argon glovebox or under ambient atmospheric conditions depending on the electrolyte nature. Several electrolytes were investigated: PC ; 1M LiTFSI in PC ; LP30 ; LP30 with 5%<sub>wt</sub> of FEC ; 1M LiPF<sub>6</sub> in EC/DEC (1/1 v/v) with 7.5%<sub>wt</sub> of FEC and 0.5%<sub>wt</sub> of VC. Mechanical tests were performed under ambient atmospheric conditions with an Instron tensile machine (model 5965) equipped with Bluehill software and a load cell (10 N of 100 N). Tensile tests were performed on soaked polymer membranes (the electrolyte on the surface was removed using tissue paper) at room temperature using home-made clamps covered by Velcro®-like grips to avoid any slippage (12 cN.m). The deformation was followed using a video extensometer (relative uncertainty of 0.11% at full scale), by drawing 2 separate white dots on the sample. The strain rates used are either  $0.06\text{ s}^{-1}$  or  $0.0017\text{ s}^{-1}$ . The Young's modulus of the polymer membranes was calculated by a linear fit within the first 10% deformation of the stress-strain curves.

## 2. Supporting Figures: PEO end-chains methacrylation



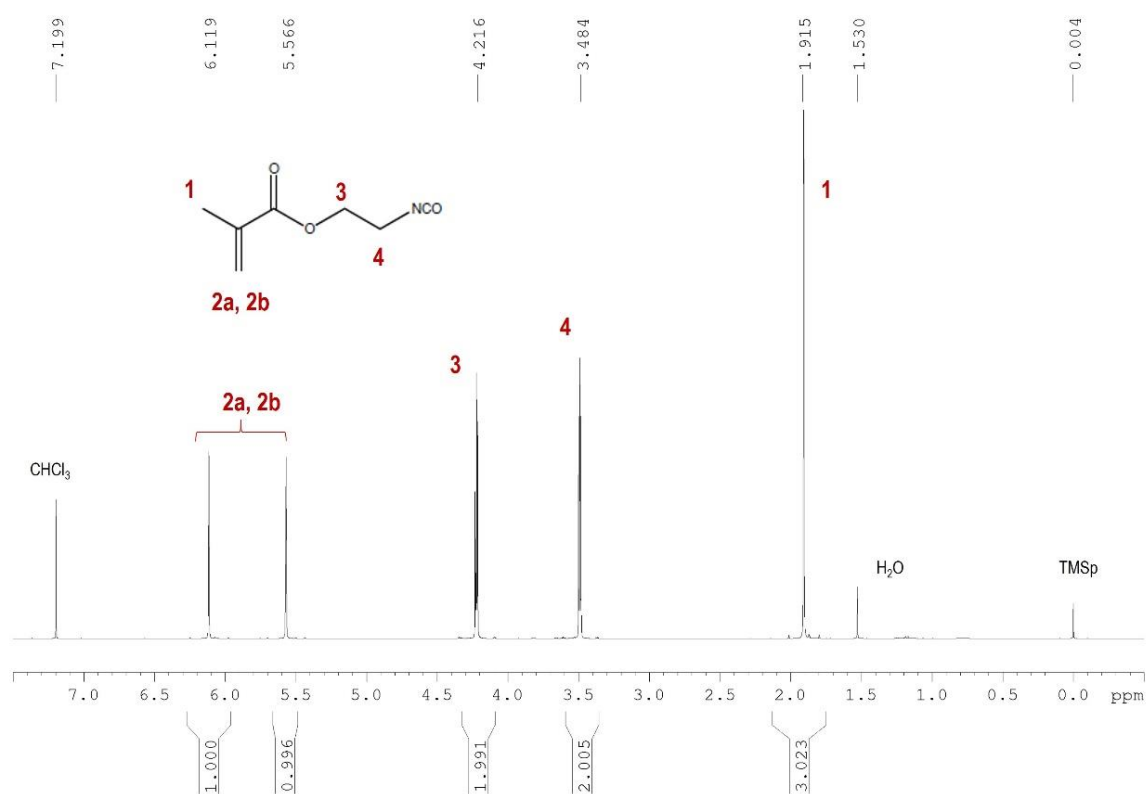
**Figure SI.III.2 Dimethacrylated PEO SEC characterization.** Samples were solubilized at  $3 \text{ mg} \cdot \text{mL}^{-1}$  in DMF. **a)** Overlapped RI chromatograms of commercial PEO10K, PEO35K and PEO100K (Shodex KD-806M column). Overlapped RI chromatograms of the commercial vs the end-chains modified PEO **b)** 10K **c)** 100K and **d)** 35K. The end-chains methacrylation reaction does not affect the polydispersity index  $\bar{D}$  except for PEO100K whose distribution has been considerably narrowed and centered on a lower average molecular mass. After the synthesis, modified PEO are recovered by solubilization in  $\text{CH}_2\text{Cl}_2$ , the solubility issues observed for high molecular weight polymer chains may explain the selection of lower masses. Errors bars were calculated as the standard deviation of the measured  $\bar{D}$  for different synthesis batches.

<b>Polymer</b>	<b>M<sub>w</sub> th</b> (g.mol <sup>-1</sup> )	<b>M<sub>w</sub> exp</b> (g.mol <sup>-1</sup> )	<b>M<sub>n</sub> exp</b> (g.mol <sup>-1</sup> )	<b>M<sub>p</sub> exp</b> (g.mol <sup>-1</sup> )	<b>Đ = M<sub>w</sub> / M<sub>n</sub></b>
<b>PEO 10K</b>	10 000	10 900	7 800	11 800	1.39
<b>Dimethacrylated PEO 10K</b>	10 310	10 000	6800	10300	1.48 ± 0.11
<b>PEO 35K</b>	35 000	35 500	24 800	36 200	1.43
<b>Dimethacrylated PEO 35K</b>	35 310	32 600	22 800	33 900	1.38 ± 0.17
<b>PEO 100K</b>	100 000	109 600	17 000	47 100	6.46
<b>Dimethacrylated PEO 100K</b>	100 310	107 200	13 700	35 600	2.57

**Table SI.III.2 PEO and dimethacrylated PEO SEC characterization.** Samples were solublized in DMF at 3 mg.mL<sup>-1</sup>. All the average masses were determined by SEC using the RI detector coupled with the SHODEX column that was previously calibrated with PEO standards according to the protocol described in Methods (Table SI.III.1). Errors bars on polydispersity index Đ were calculated as the standard deviations of the measured Đ for different synthesis batches when several batches were synthesized. Note that no correction was made on the measured Đ which might explain a possible overestimation by the column.

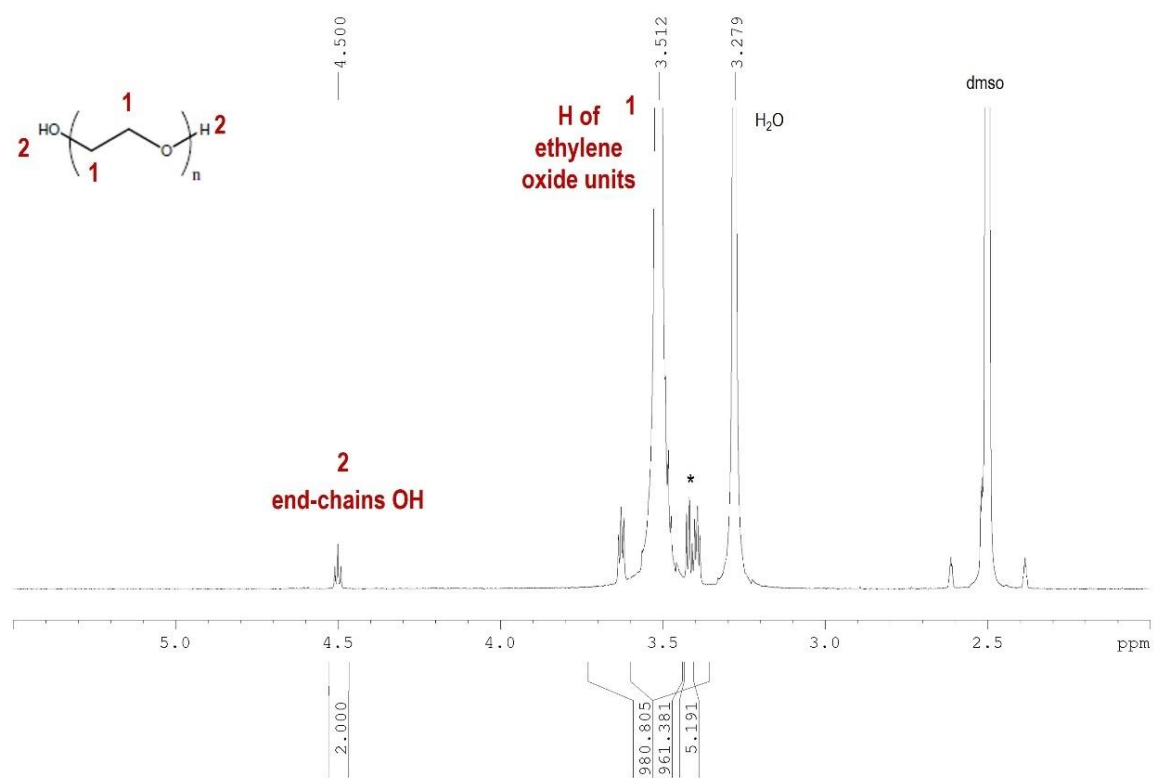
Polymer	Theoretical number of ethylene oxide units	Estimated number of ethylene oxide units by $^1\text{H}$ NMR
PEO 10K	227	245
Dimethacrylated PEO 10K		232
PEO 35K	795	819
Dimethacrylated PEO 35K		913
PEO 100K	2272	525
Dimethacrylated PEO 100K		1147

**Table SI.III.3 PEO and dimethacrylated PEO  $^1\text{H}$  NMR characterization.** Theoretical number of EO units was calculated from the number average molecular weight of the different PEO and the molecular mass of a EO unit ( $44 \text{ g.mol}^{-1}$ ) taking into account the end-chains hydroxyl groups.  $^1\text{H}$  NMR spectra were acquired in  $\text{DMSO-d}_6$  and  $\text{CDCl}_3$  for commercial and dimethacrylated PEO respectively. The protons signals attribution is performed in detail in each following spectrum (Figures SI.III.5-9). The integration ratio between protons of EO units and protons of the end-chains (hydroxyl groups and methacrylate functions respectively) for commercial and modified PEO leads to the estimated number of EO units per PEO chain. Interestingly, the estimated number of EO units correlates quite well with the theoretical one except for PEO100K. Such difference may be explained by both the broad molecular weight distribution and the sluggish dissolving time of the highest molecular weight chains, thus distorting the estimation to lower values. It is worth noticing that for the analysis of dimethacrylated PEO,  $\text{CDCl}_3$  was used for solubility consideration. However, the  $^1\text{H}$  NMR spectra of these synthesized products in  $\text{DMSO-d}_6$  showed the disappearance of the triplet at 4.5 ppm attributed to the end-chains hydroxyl groups evidencing the dimethacrylation reaction (Figure SI.III.10).

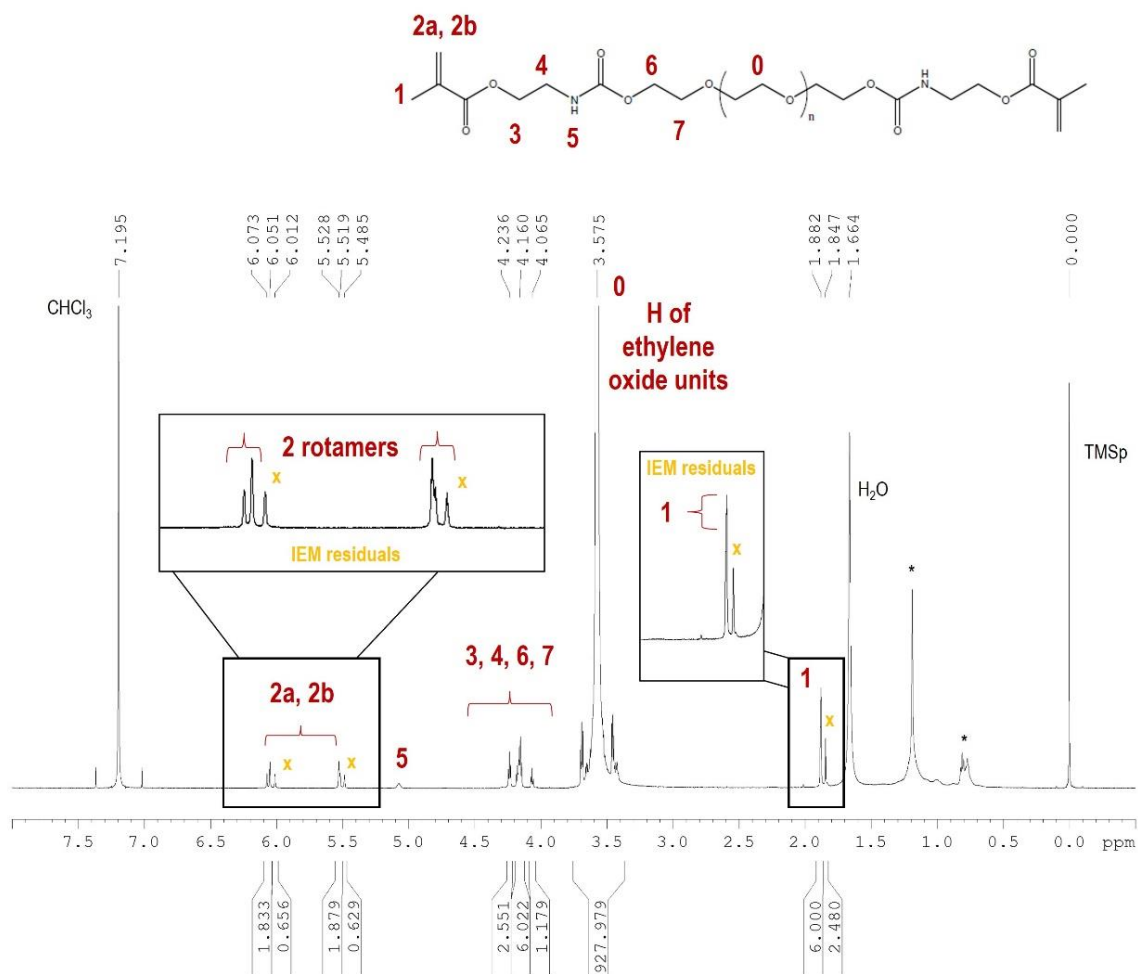


**Figure SI.III.3  $^1\text{H}$  NMR spectrum in  $\text{CDCl}_3$  of 2-isocyanatoethyl methacrylate (IEM) (16 scans, 298K)**



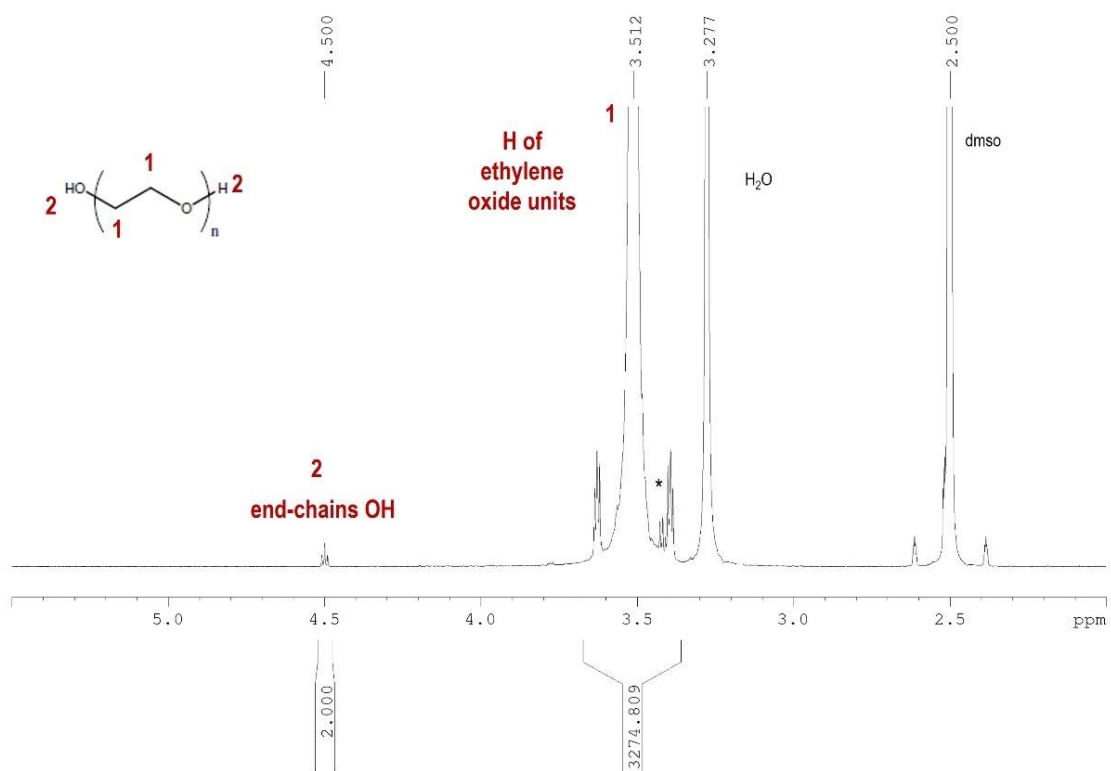


**Figure SI.III.4**  $^1\text{H}$  NMR spectrum in  $\text{DMSO-d}_6$  of PEO10K (16 scans, 308K). Identified impurities are marked with an asterisk (\*).



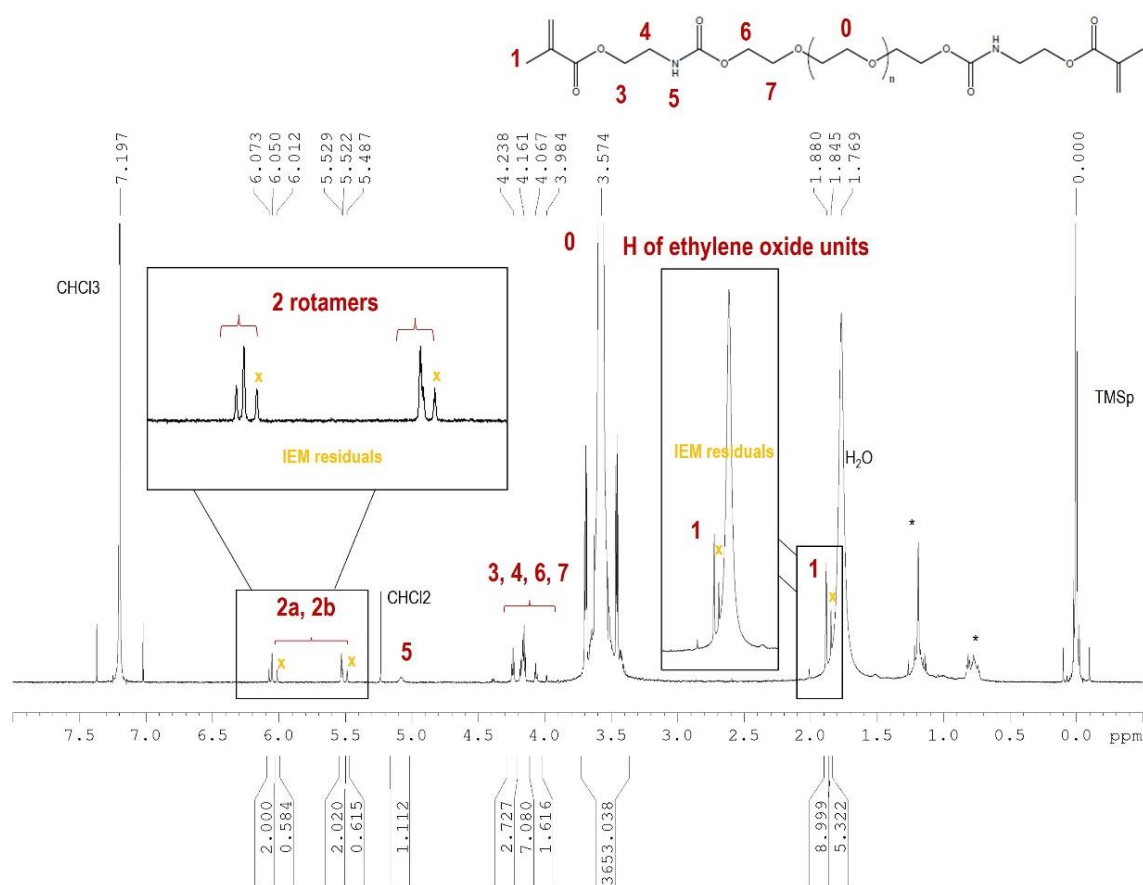
**Figure SI.III.5  $^1\text{H}$  NMR spectrum in  $\text{CDCl}_3$  of end-chains modified PEO10K (16 scans, 298K).**

Impurities marked with an asterisk (\*) results from the degradation of the plastic vial by  $\text{CDCl}_3$ . IEM residuals were identified and quantified (0.6%<sub>wt</sub>). No further purification step was performed.

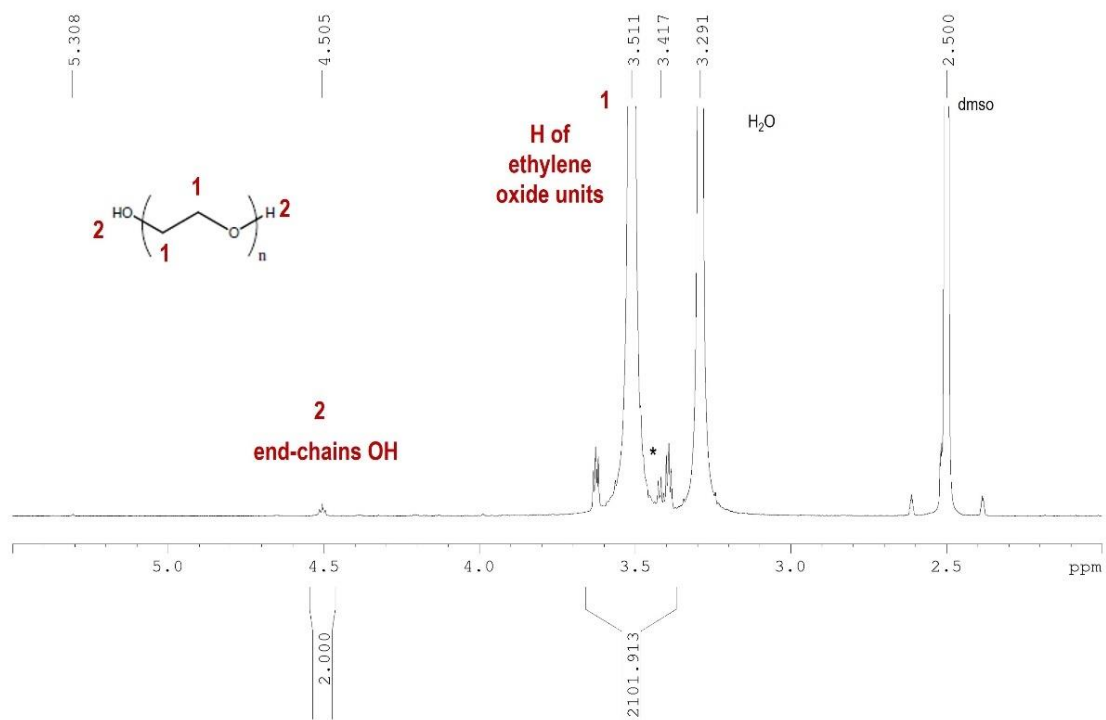


72

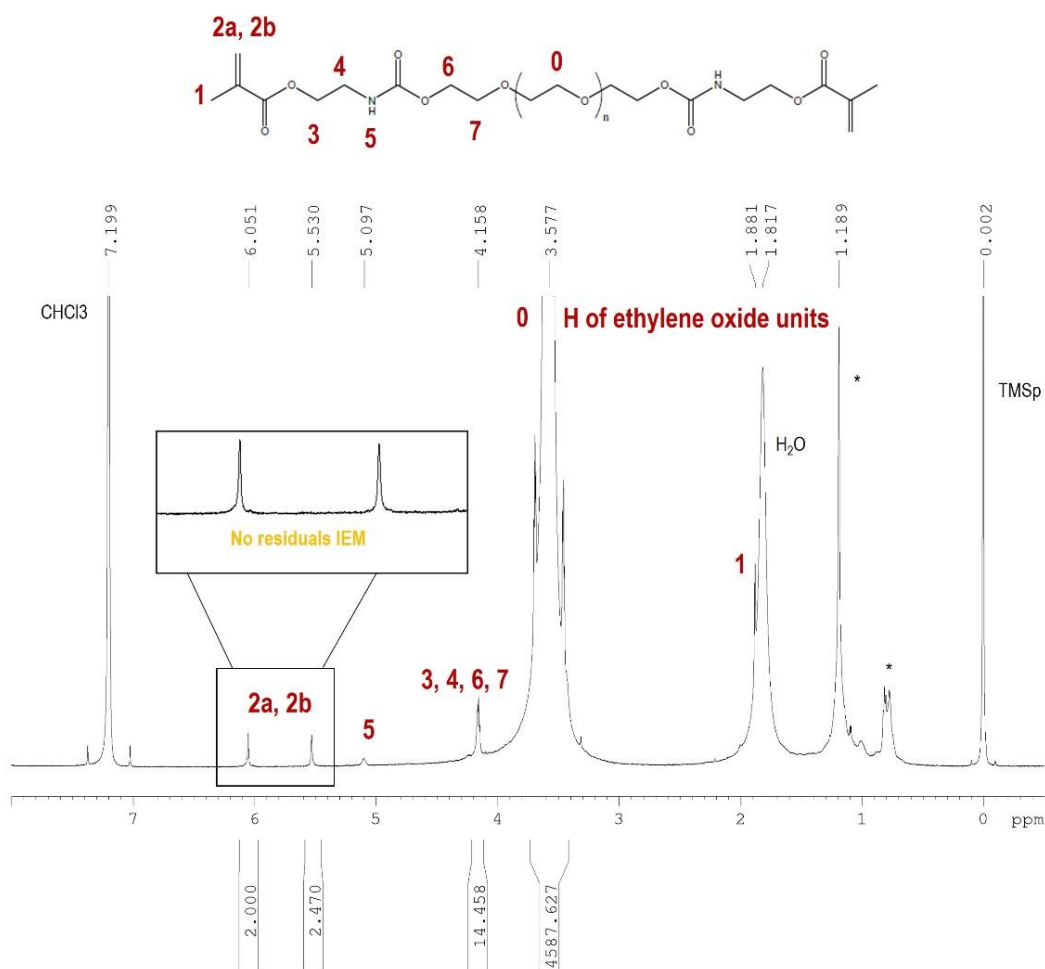
**Figure SI.III.6** <sup>1</sup>H NMR spectrum in DMSO-d<sub>6</sub> of PEO35K (16 scans, 308K). Identified impurities are marked with an asterisk (\*).



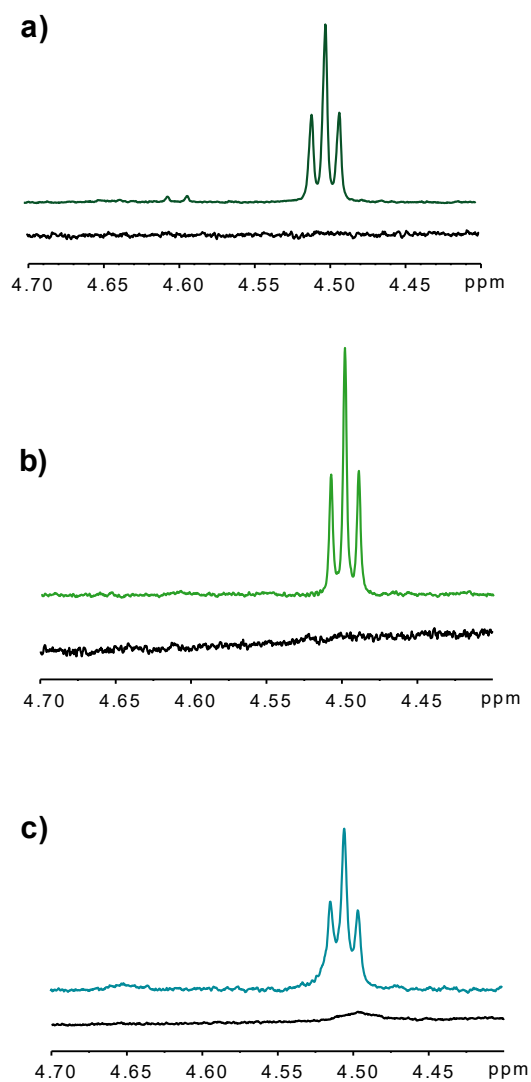
**Figure SI.III.7**  $^1\text{H}$  NMR spectrum in  $\text{CDCl}_3$  of end-chains modified PEO35K (16 scans, 298K). Impurities resulting from plastic vial degradation by  $\text{CDCl}_3$  are marked with an asterisk (\*). IEM residuals were identified and quantified (0.1%<sub>wt</sub>). No further purification step was performed.



**Figure SI.III.8**  $^1\text{H}$  NMR spectrum in  $\text{DMSO-d}_6$  of PEO100K (16 scans, 308K). Identified impurities are marked with an asterisk (\*).



**Figure SI.III.9**  $^1\text{H}$  NMR spectrum in  $\text{CDCl}_3$  of end-chains modified PEO100K (16 scans, 298K). Impurities resulting from plastic vial degradation by  $\text{CDCl}_3$  are marked with an asterisk (\*). No IEM residuals were identified.



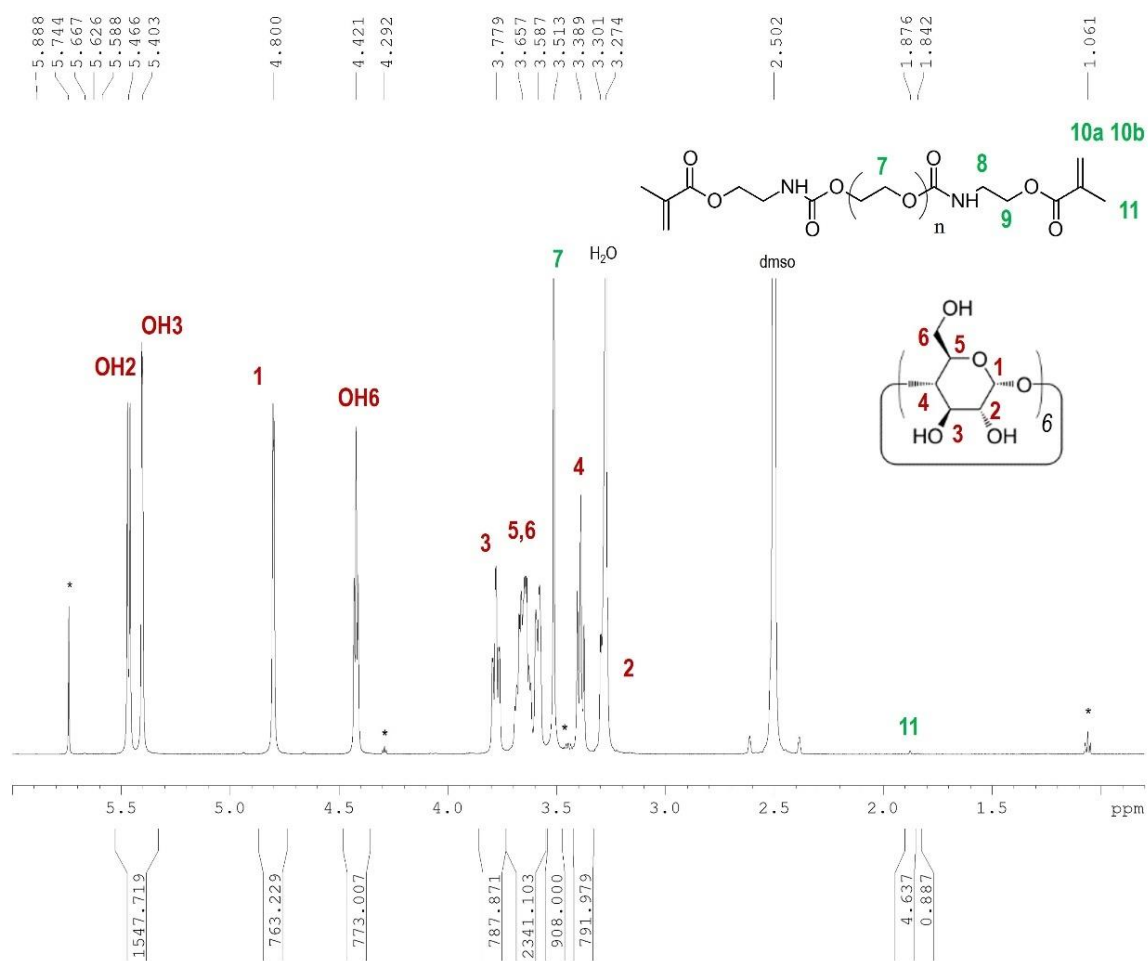
**Figure SI.III.10 Evidence of the PEO dimethacrylation reaction.** Overlapped  $^1\text{H}$  NMR spectra in  $\text{DMSO-d}_6$  of the commercial (colored line) and dimethacrylated (black line) **a)** PEO10K **b)** PEO35K and **c)** PEO100K. The focus is made on the region [4 ; 5 ppm] to observe the disappearance of the terminal hydroxyl groups (t; ~4.5 ppm) of PEO when methacrylate functions are added.

### 3. Supporting Figures: PPRs characterization

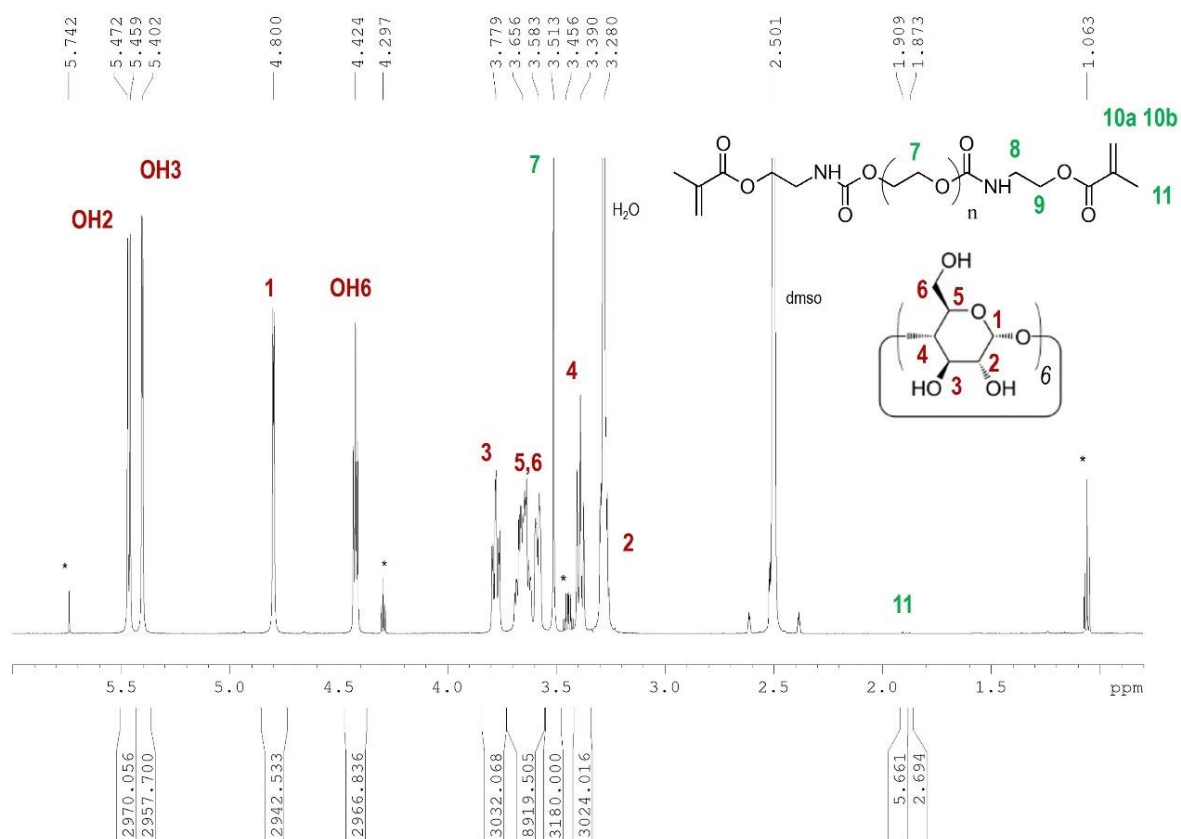
Sample	OE units number per polymer chain	Integration of OE units signal (3.5 ppm)	Integration of the anomeric proton signal of $\alpha$ -CD (4.8 ppm)	$\alpha$ -CD number	Molarity ratio ( $\alpha$ -CD / OE )
PPR10K	227	908	763	127	1.1 / 2
PPR35K	795	3180	2943	490	1.2 / 2
PPR100K	2272	9088	5449	908	0.8 / 2

**Table SI.III.4  $^1\text{H}$  NMR characterization of PPRs based on  $\alpha$ -CDs and PEO.** Samples were solubilized in DMSO- $d_6$  a day before the NMR spectrum acquisition in order to analyse PPRs in a completely dissociated state. The protons signals attribution is performed in detail in each following spectrum (Figure SI.III.11-13). Molarity ratio  $\alpha$ -CD / OE was calculated with the integration and can be compared to the expected stoichiometry is  $(1 / 2)^{42}$ . Interestingly, the estimated molarity ratio correlates quite well with the theoretical one. For the PPRs based on PEO35K and PEO100K the difference may be explained by the slower dissociation kinetics for highest molecular weight chains. Indeed, the  $\alpha$ -CD hydroxyl protons signals are broadened for PEO100K, which suggests the non-complete dissociation of the architecture and the remaining existence of H-bonds between  $\alpha$ -CDs threaded on PEO chains. One could also mention the mobility restriction of the protons born by a macromolecule as a threaded  $\alpha$ -CD. The dissociation was tried to be forced by heating up to 80°C the NMR tube, but this approach was not successful. Dilution may have also been considered. Nevertheless, a balance would have to be found since dilution would have decrease the protons signal intensities.

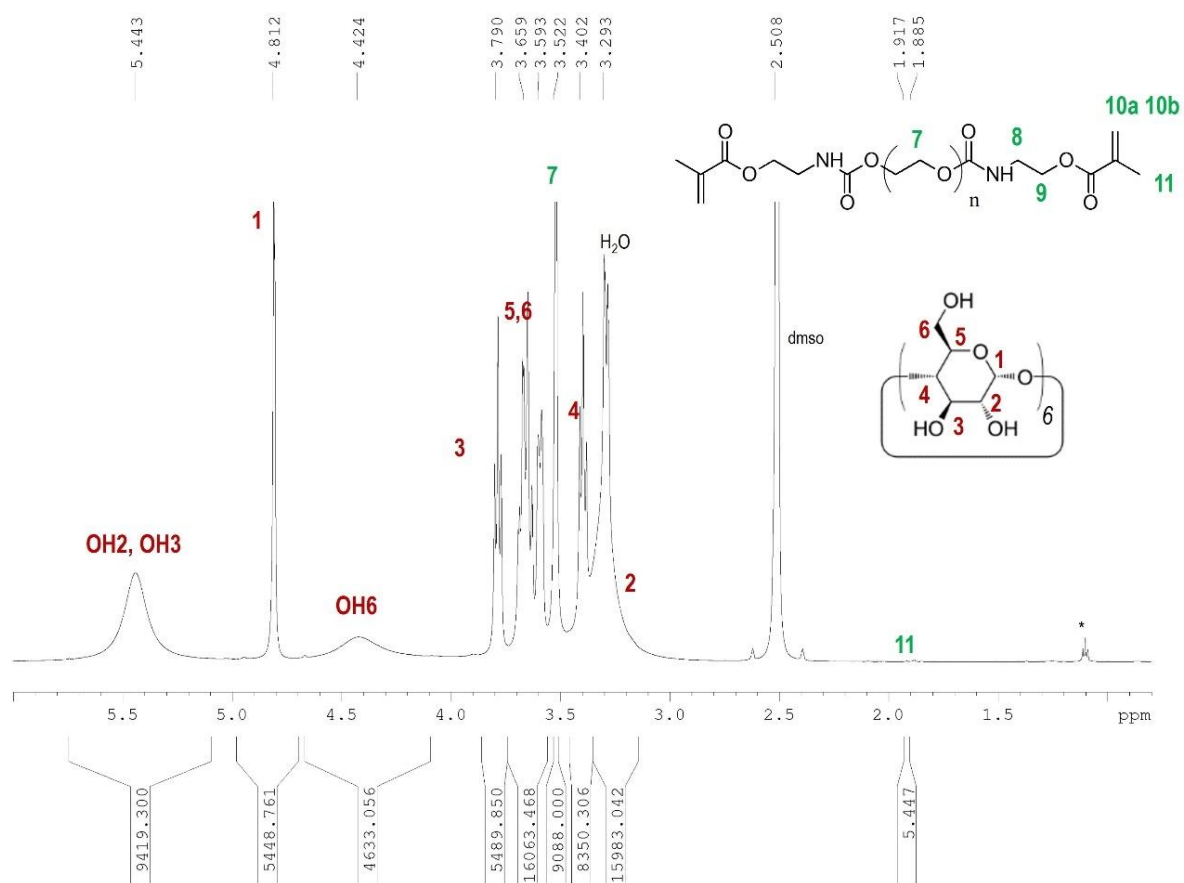




**Figure SI.III.11**  $^1\text{H}$  NMR spectrum in  $\text{DMSO-d}_6$  of PPR10K (16 scans, 308K). Traces of dichloromethane (s, 5.89 ppm) and diethylether (t, 1.06 ; q, 3.39 ppm ; t, 4.29 ppm) are marked with an asterisk (\*).

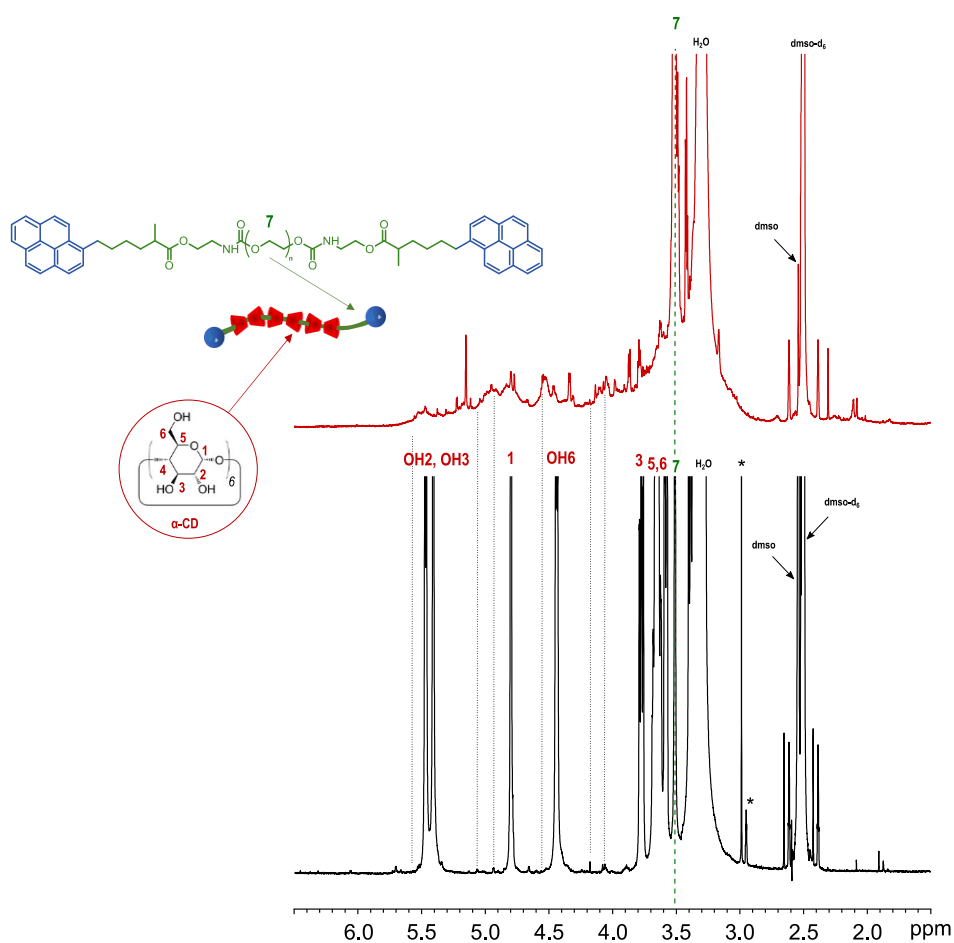


**Figure SI.III.12**  $^1\text{H}$  NMR spectrum in  $\text{DMSO-d}_6$  of PPR35K (16 scans, 308K). Traces of dichloromethane (s, 5.74 ppm) and diethylether (t, 1.06 ; q, 3.46 ppm ; t, 4.30 ppm) are marked with an asterisk (\*).

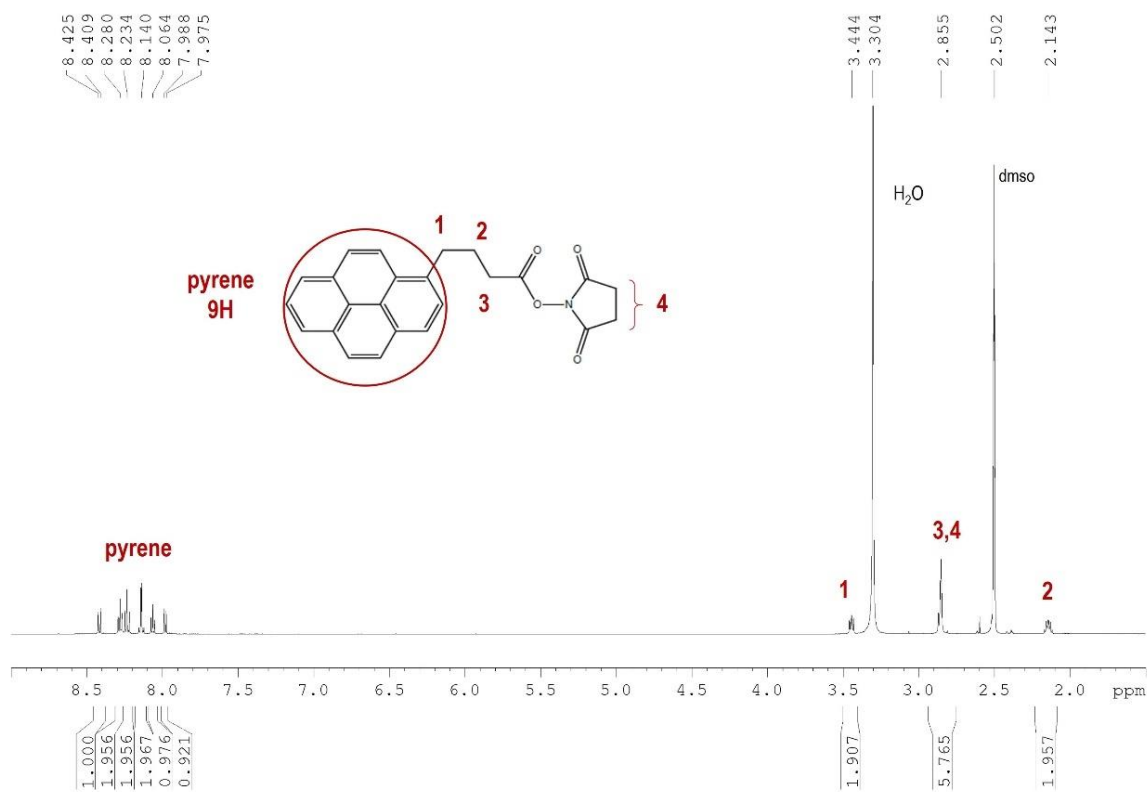


**Figure SI.III.13**  $^1\text{H}$  NMR spectrum in  $\text{DMSO-d}_6$  of PPR100K (16 scans, 308K). Traces of diethylether (t, 1.06 ppm; q & t are hidden in the background noise) are marked with an asterisk (\*).

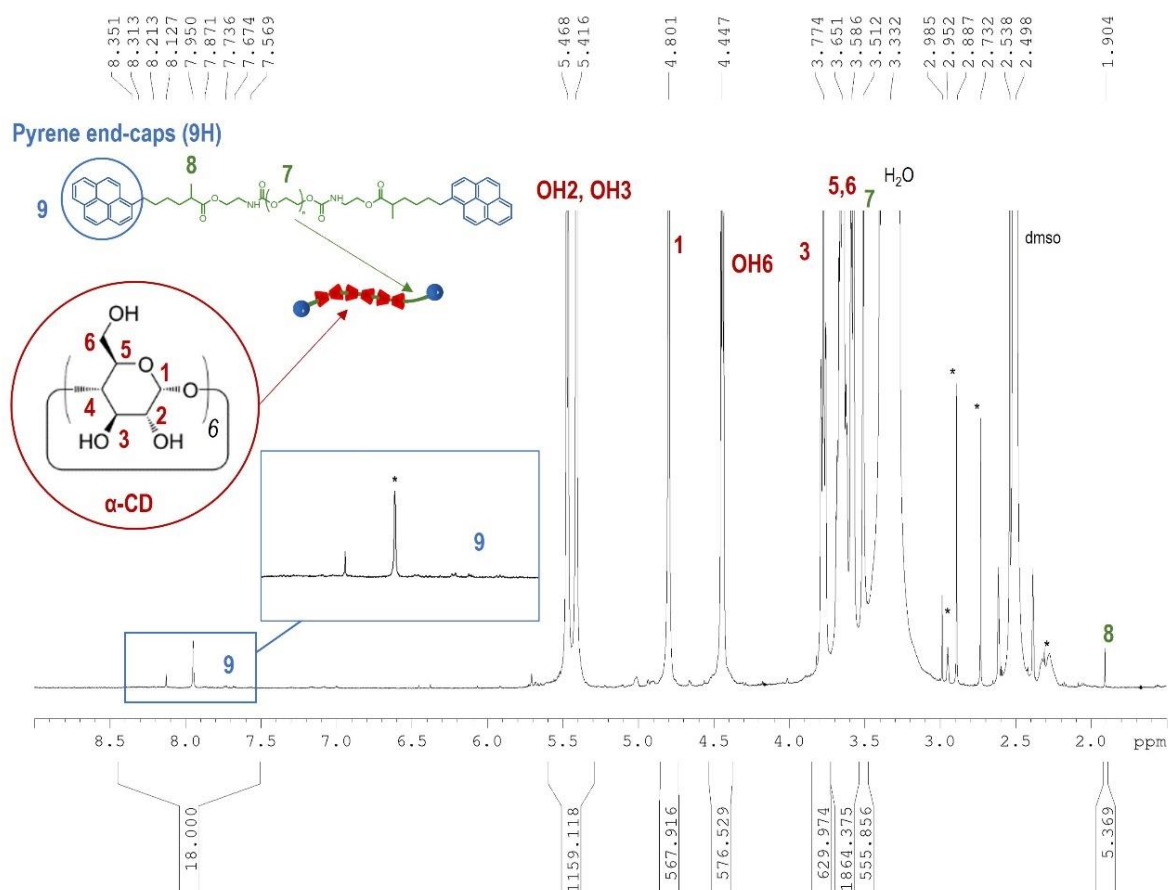
## 4. Supporting Figures: PRs characterization



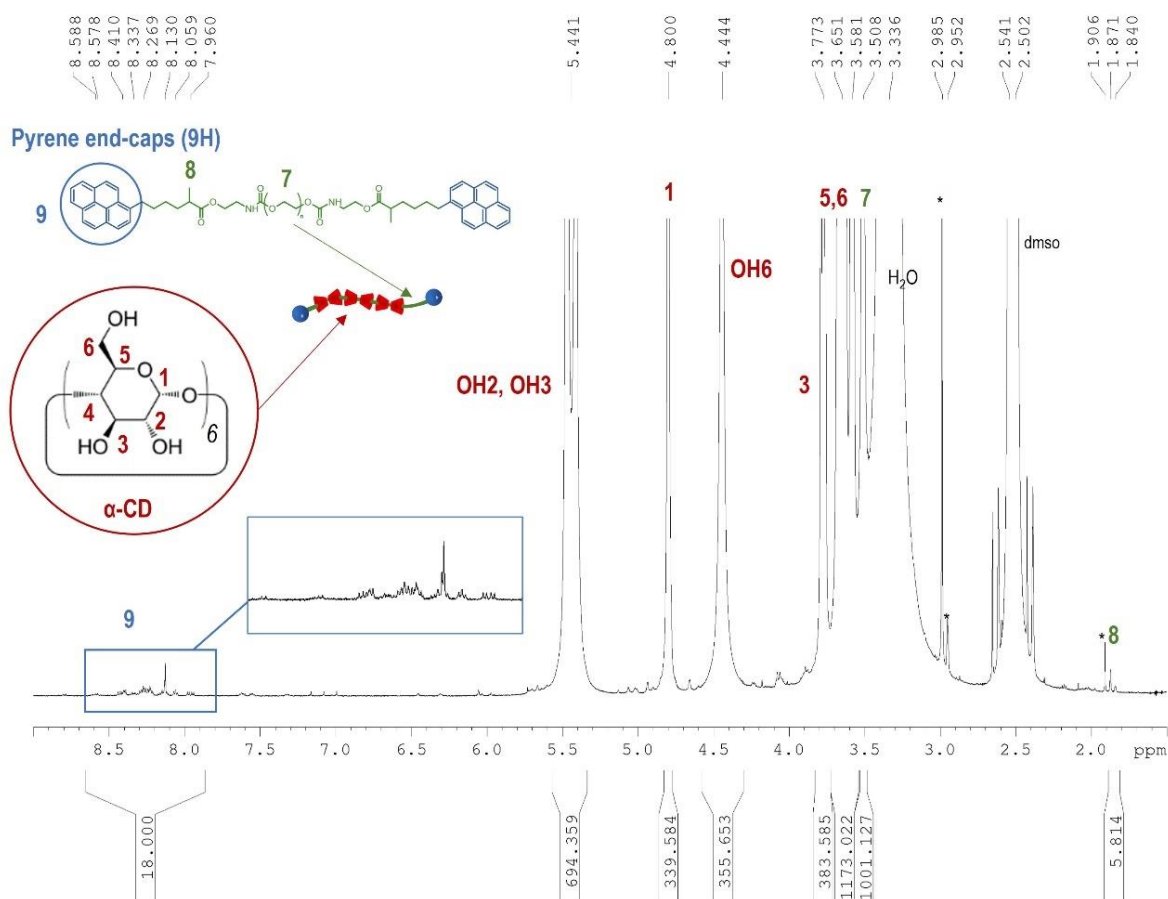
**Figure SI.III.14 Overlapped  $^1\text{H}$  NMR spectra in  $\text{DMSO-d}_6$  of PR3 before (black) and after the additional (red) purification step (16 scans, 308K).** Impurities and traces of residual DMF (s, 7.95 ppm ; s, 2.89 ppm ; s, 2.73 ppm) are marked with an asterisk (\*). Not all the protons of the polymer chain were visualized because of the poor signal to noise ratio. The vertical black dashed lines underline the different signals assigned to the protons of the threaded  $\alpha$ -CDs.



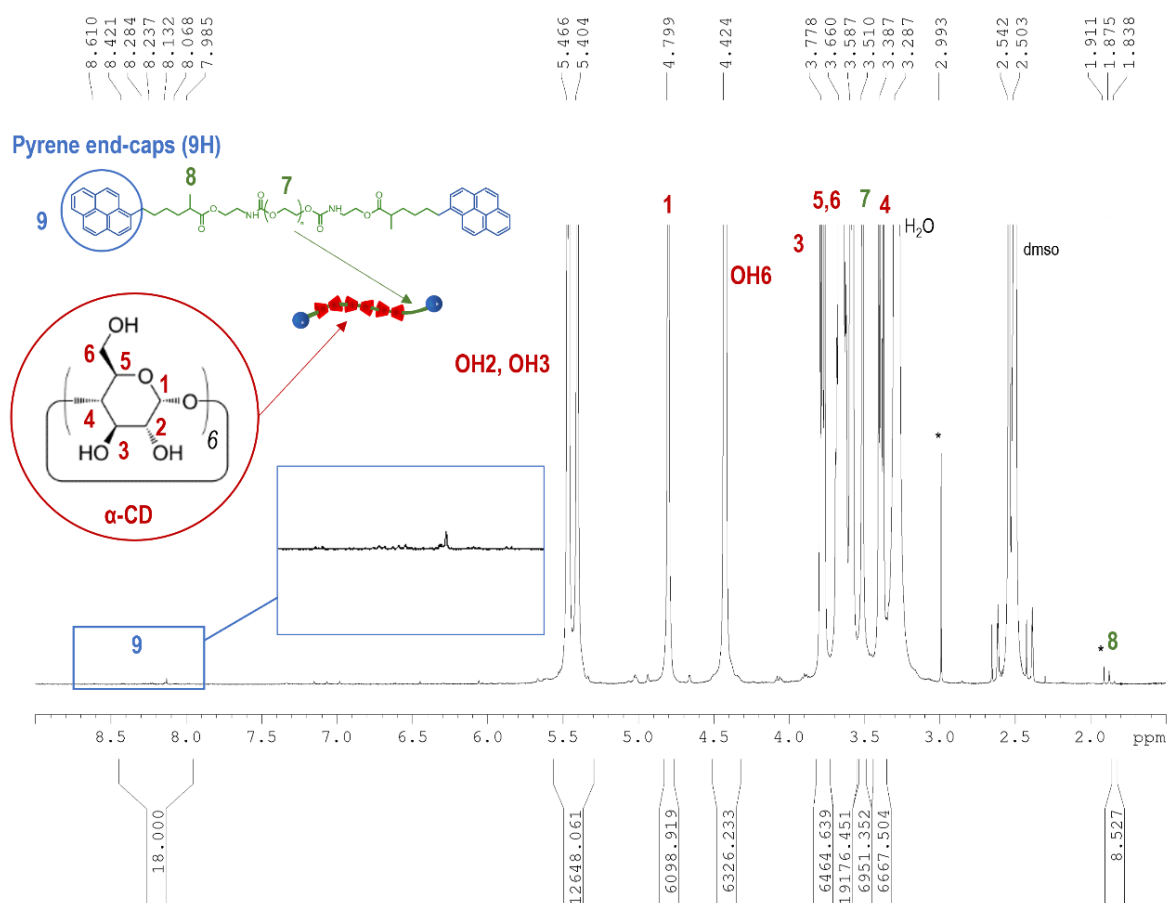
**Figure SI.III.15  $^1\text{H}$  NMR spectrum in  $\text{DMSO-d}_6$  of 1-pyrene butyric acid N- hydroxysuccinimide ester (PBS) (16 scans, 308K).**



**Figure SI.III.16**  $^1\text{H}$  NMR spectrum in  $\text{DMSO-d}_6$  of PR1 based on  $\alpha$ -CDs and PEO10K (128 scans, 308K) before the additional purification step. Impurities and traces of residual DMF (s, 7.95 ppm ; s, 2.89 ppm ; s, 2.73 ppm) are marked with an asterisk (\*). PR1 was the first batch synthesized and DMF was used as the solvent of dissolution before the PR precipitation in diethylether. This implies residual signals in the  $^1\text{H}$  NMR spectrum, one of which is superimposed with the pyrene functions signals used for quantification. That is why, from this stage, DMSO was used as an alternative solvent. Not all the protons of the polymer chain were visualized because of the poor signal to noise ratio. The integration of the protons signal of the EO units is lower than expected. This difference can be attributed to poorer mobility of such protons which are inside the  $\alpha$ -CDs cavities.

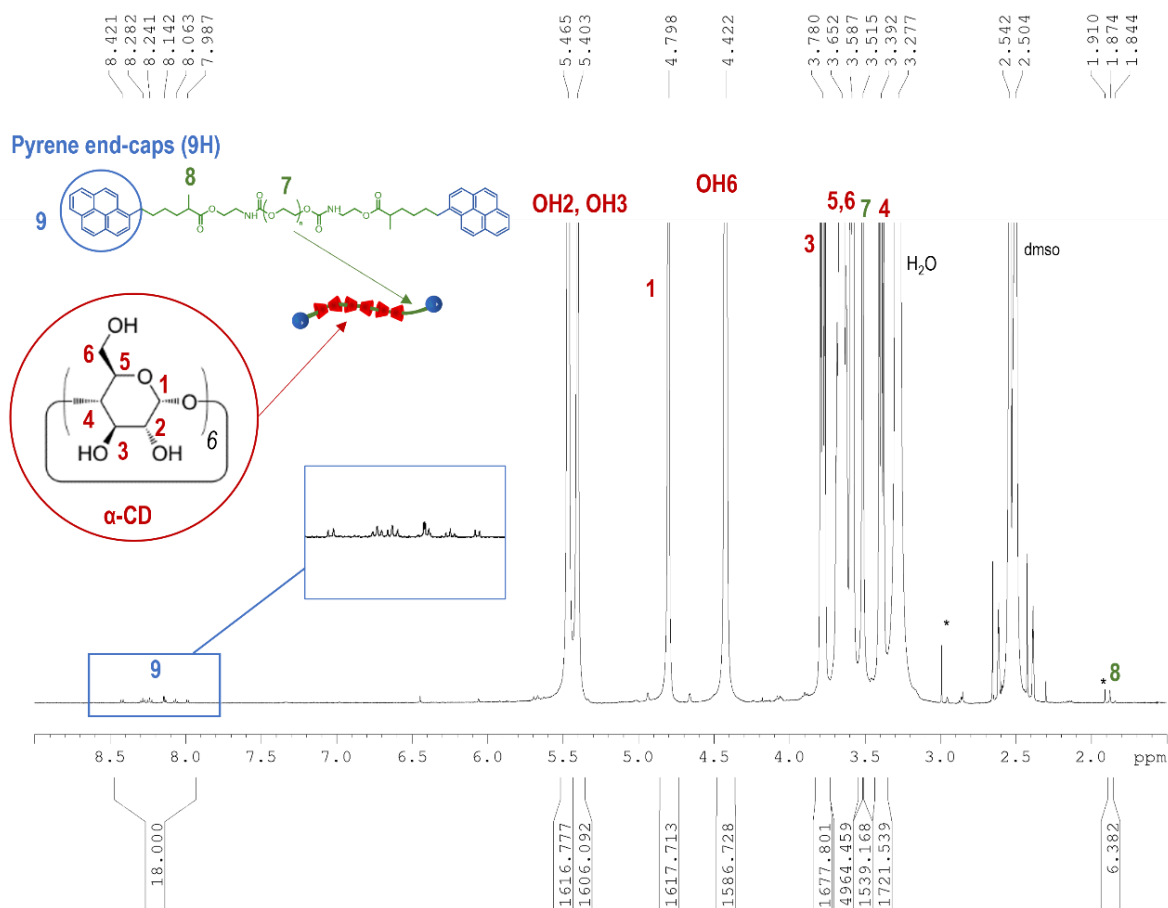


**Figure SI.III.17**  $^1\text{H}$  NMR spectrum in  $\text{DMSO-d}_6$  of PR2 based on  $\alpha$ -CDs and PEO10K (128 scans, 308K) before the additional purification step. Impurities are marked with an asterisk (\*). Not all the protons of the polymer chain were visualized because of the poor signal to noise ratio. The integration of the protons signal of the EO units is consistent with the expected one.

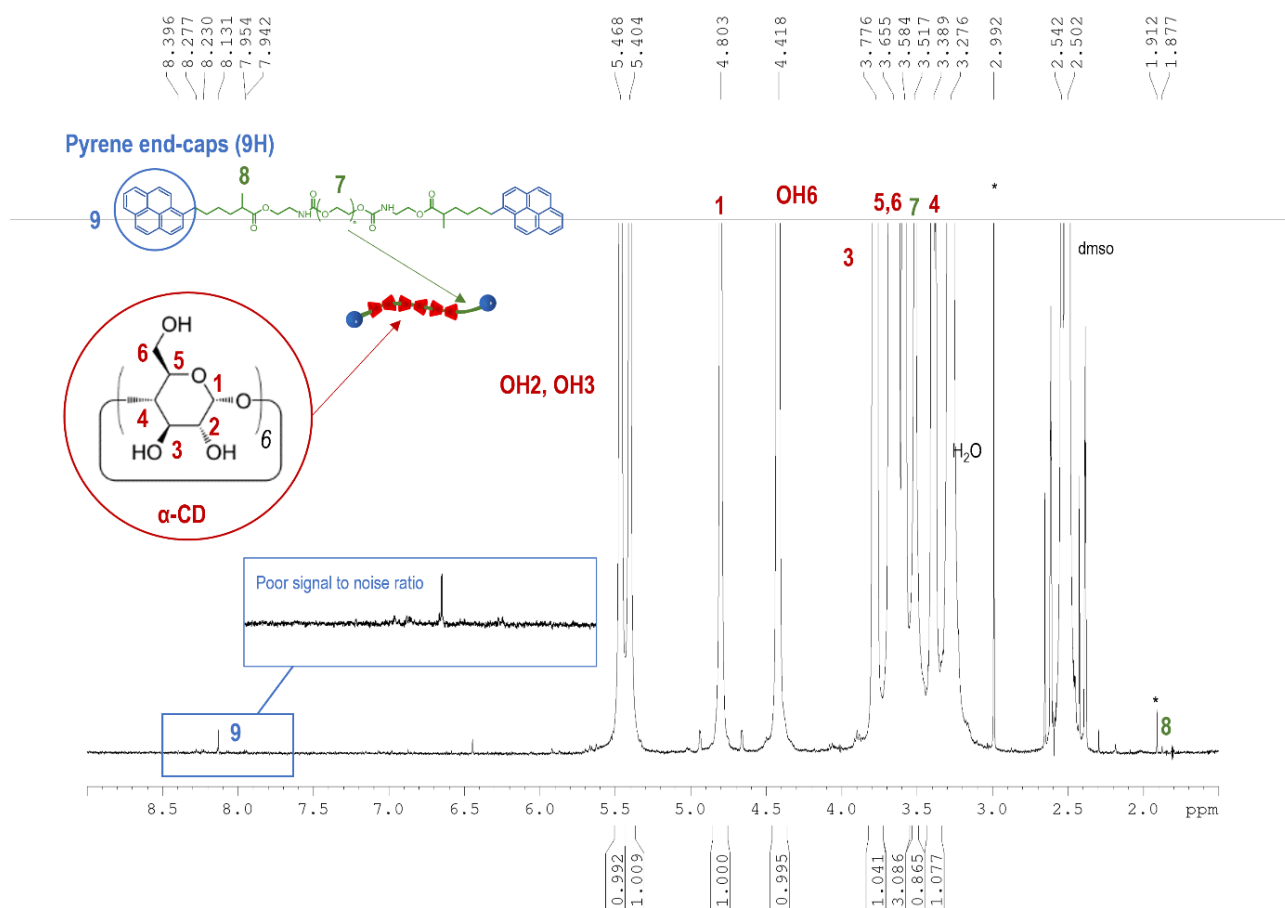


**Figure SI.III.18**  $^1\text{H}$  NMR spectrum in  $\text{DMSO-d}_6$  of PR4 based on  $\alpha$ -CDs and PEO10K (128 scans, 308K) before the additional purification step. Impurities and traces of acetone (s, 1.9 ppm) are marked with an asterisk (\*). Not all the protons of the polymer chain were visualized because of the poor signal to noise ratio. The integration of the protons signal of the EO units might be overestimated because of the broad water signal.

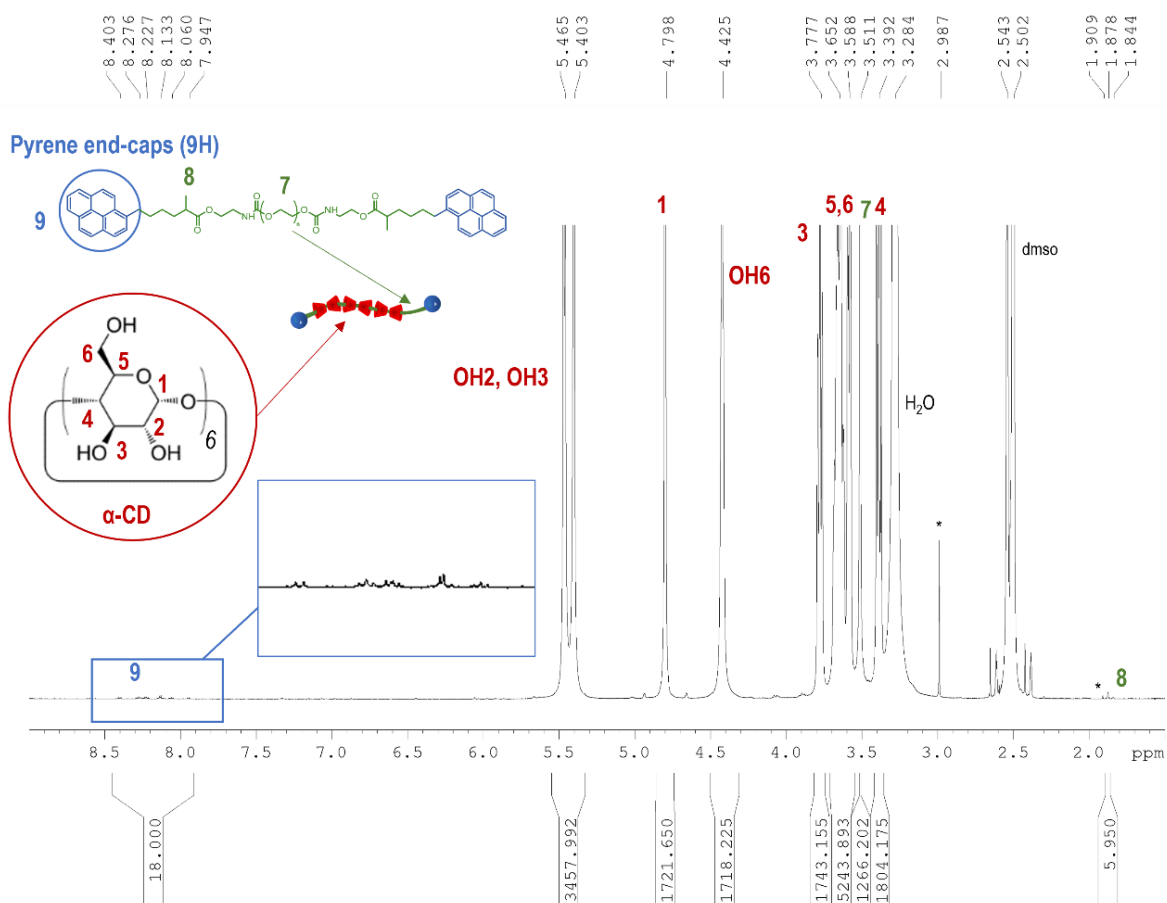




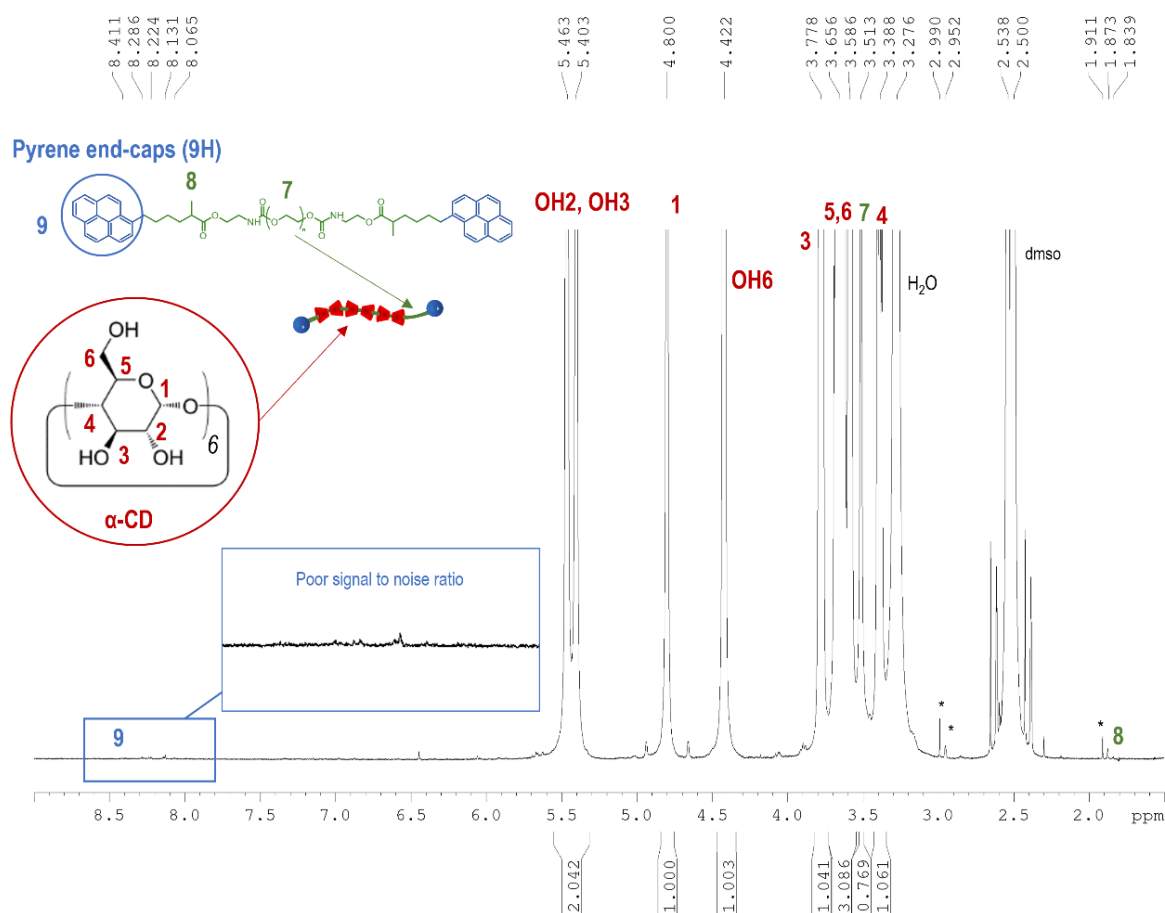
**Figure SI.III.19**  $^1\text{H}$  NMR spectrum in  $\text{DMSO-d}_6$  of PR5 based on  $\alpha$ -CDs and PEO10K (128 scans, 308K) before the additional purification step. Impurities and traces of acetone (s, 1.9 ppm) are marked with an asterisk (\*). Not all the protons of the polymer chain were visualized because of the poor signal to noise ratio. The integration of the protons signal of the EO units might be overestimated because of the broad water signal.



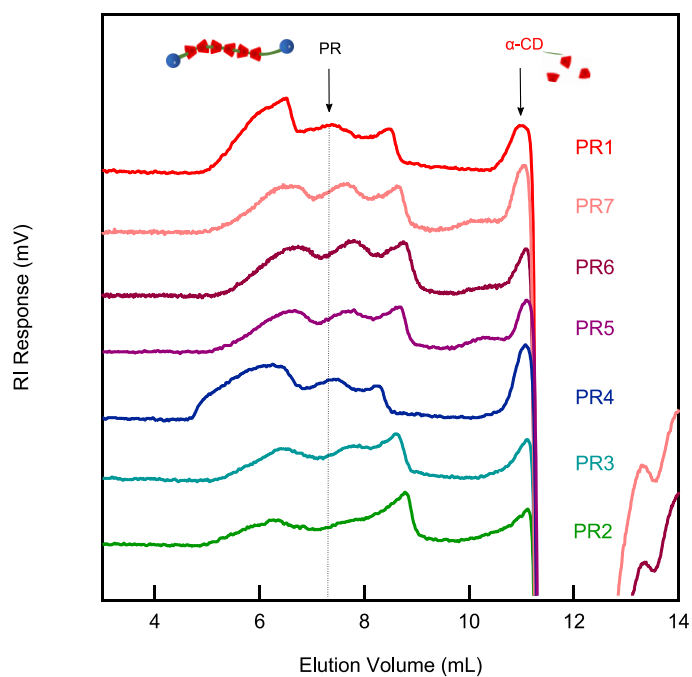
**Figure SI.III.20**  $^1\text{H}$  NMR spectrum in DMSO- $d_6$  of PR6 based on  $\alpha$ -CDs and PEO10K (128 scans, 308K) before the additional purification step. Impurities and traces of acetone (s, 1.9 ppm) are marked with an asterisk (\*). As emphasized in the insert, the signal to noise ratio of the pyrene chemical shift area was too low to carry out any quantification, even though some signal can be guessed.



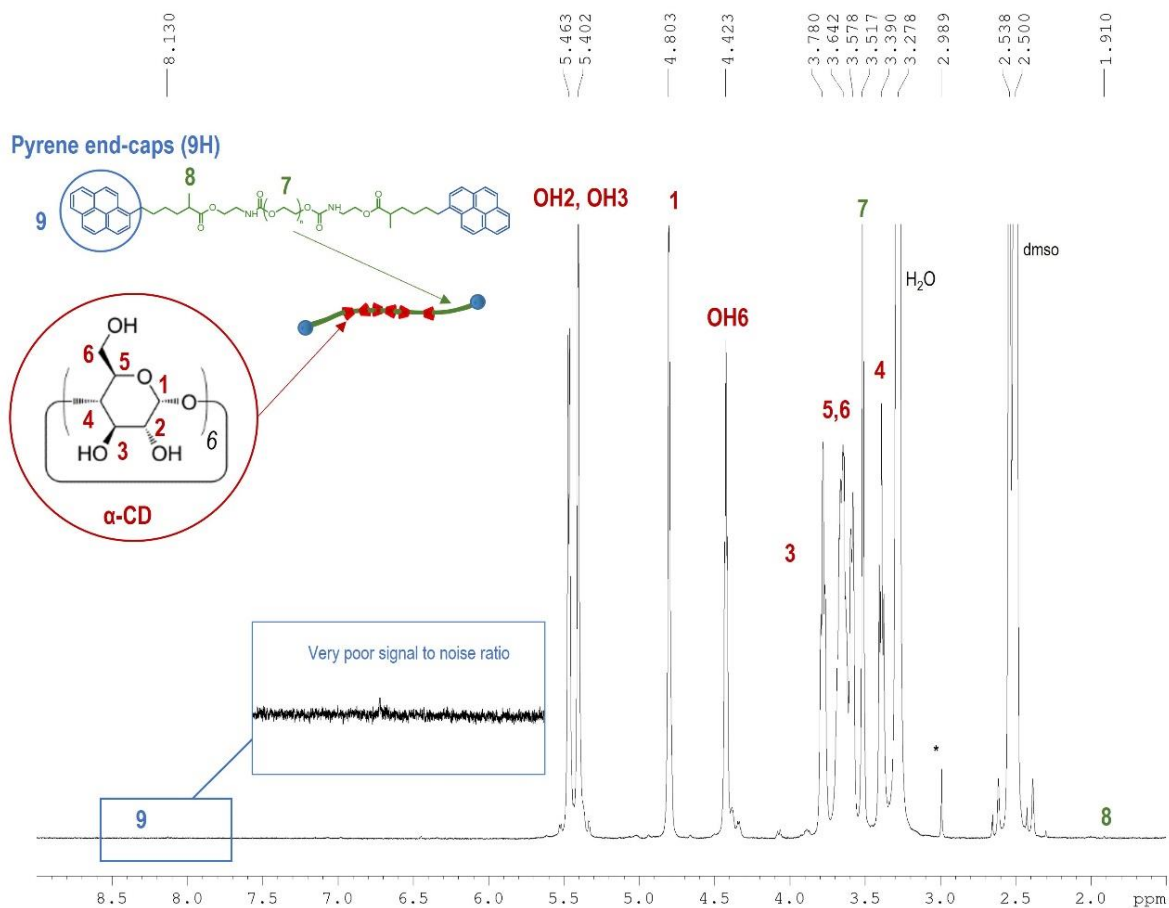
**Figure SI.III.21**  $^1\text{H}$  NMR spectrum in  $\text{DMSO-d}_6$  of PR7 based on  $\alpha\text{-CDs}$  and PEO10K (128 scans, 308K) before the additional purification step. Impurities and traces of acetone (s, 1.9 ppm) are marked with an asterisk (\*). Not all the protons of the polymer chain were visualized because of the poor signal to noise ratio. The integration of the protons signal of the EO units might be overestimated because of the broad water signal.



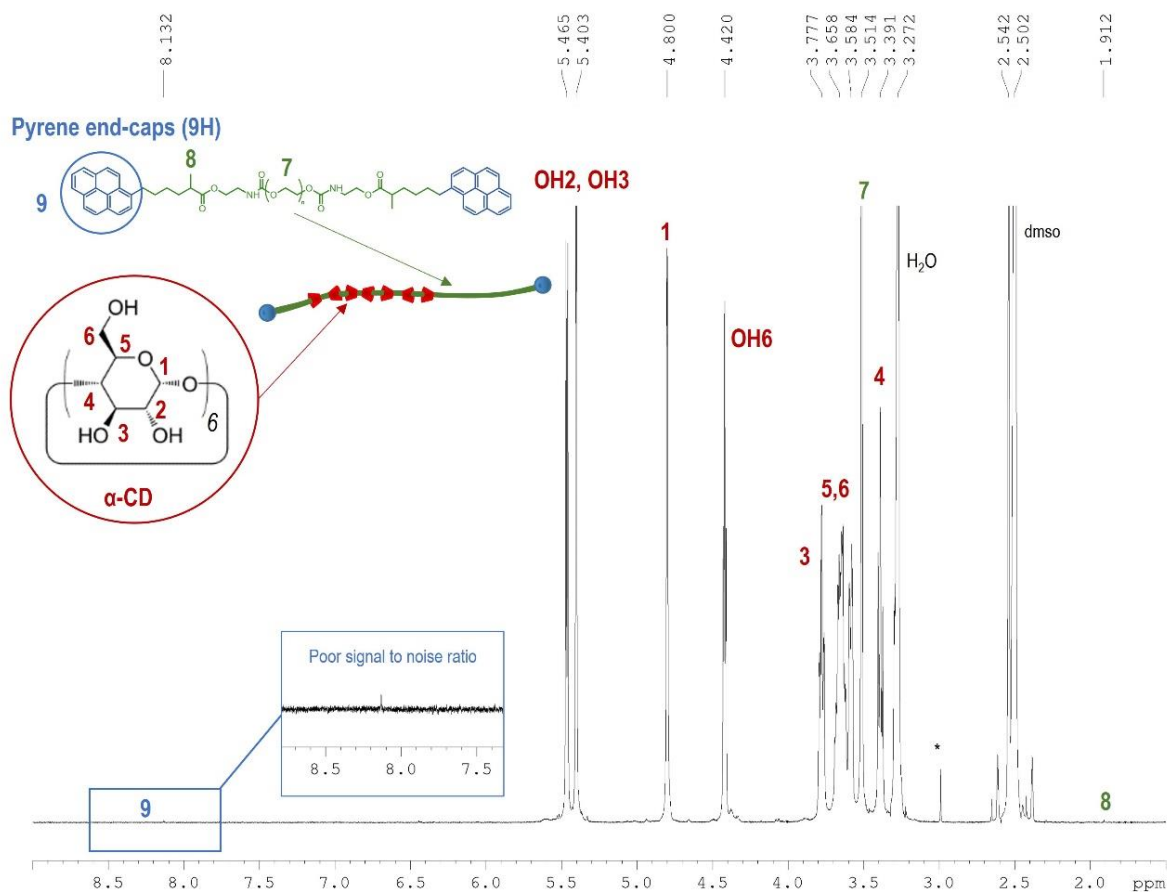
**Figure SI.III.22**  $^1\text{H}$  NMR spectrum in  $\text{DMSO-d}_6$  of PR8 based on  $\alpha$ -CDs and PEO10K (128 scans, 308K) before the additional purification step. Impurities and traces of acetone (s, 1.9 ppm) are marked with an asterisk (\*). As emphasized in the insert, the signal to noise ratio of the pyrene chemical shift area was too low to carry out any quantification, even though some signal can be guessed.



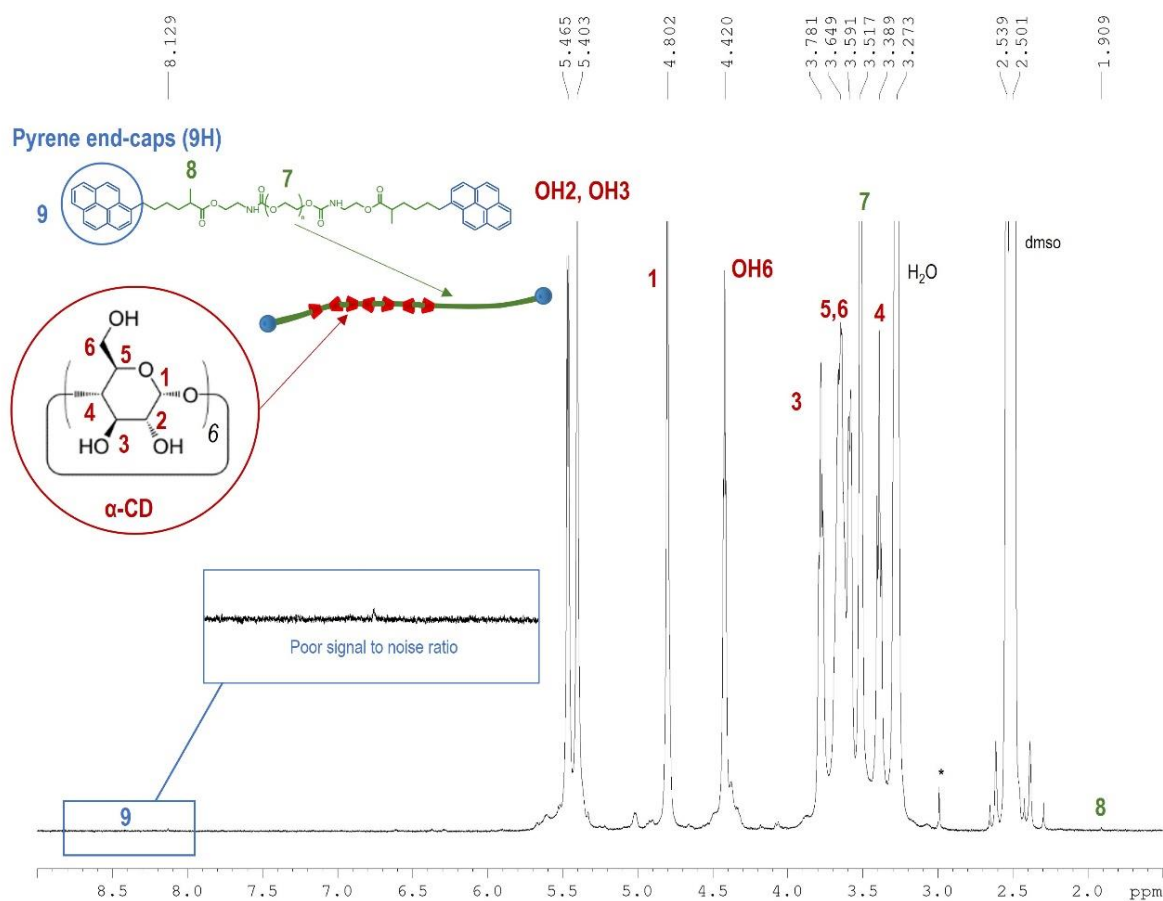
**Figure SI.III.23 Overlapped RI chromatograms of the different PR10K obtained with the Shodex KD-806M.** The evolution of the elution volumes is unscored by the vertical dashed line.



**Figure SI.III.24**  $^1\text{H}$  NMR spectrum in  $\text{DMSO-d}_6$  of PR9 based on  $\alpha$ -CDs and PEO35K (16 scans, 308K) before the additional purification step. Impurities are marked with an asterisk (\*). As emphasized in the insert, the signal to noise ratio of the pyrene chemical shift area was too low to carry out any quantification, even though some signal can be guessed.

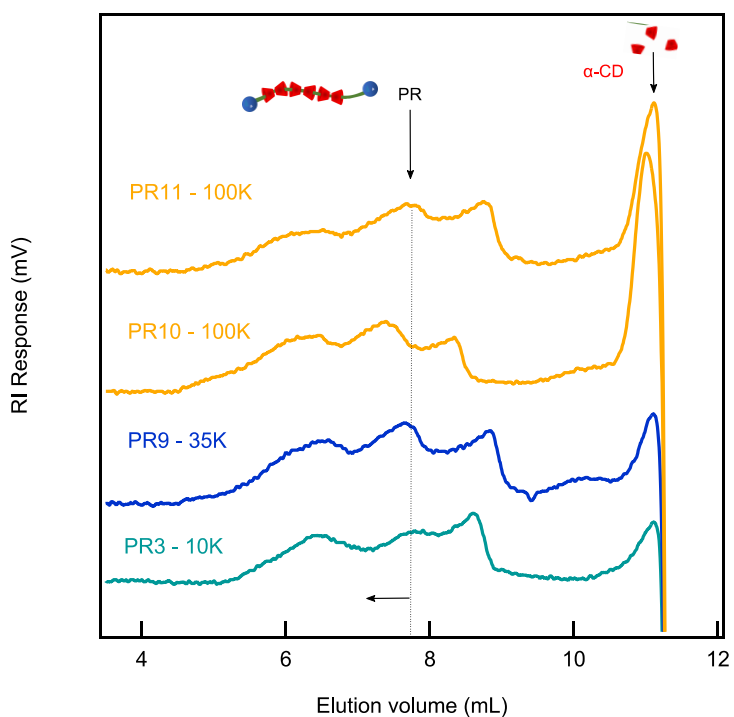


**Figure SI.III.25**  $^1\text{H}$  NMR spectrum in  $\text{DMSO-d}_6$  of PR10 based on  $\alpha$ -CDs and PEO100K (16 scans, 308K) before the additional purification step. Impurities are marked with an asterisk (\*). As emphasized in the insert, the signal to noise ratio of the pyrene chemical shift area was too low to carry out any quantification, even though some signal can be guessed.



**Figure SI.III.26**  $^1\text{H}$  NMR spectrum in  $\text{DMSO-d}_6$  of PR11 based on  $\alpha$ -CDs and PEO100K (16 scans, 308K) before the additional purification step. Impurities are marked with an asterisk (\*). As emphasized in the insert, the signal to noise ratio of the pyrene chemical shift area was too low to carry out any quantification, even though some signal can be guessed





**Figure SI.III.27 Overlapped RI chromatograms of the different PR35K and PR100K obtained with the Shodex KD-806M.** The evolution of the elution volumes is unscored by the vertical dashed line.

## 5. Supporting Figures: PR-PAA network characterization

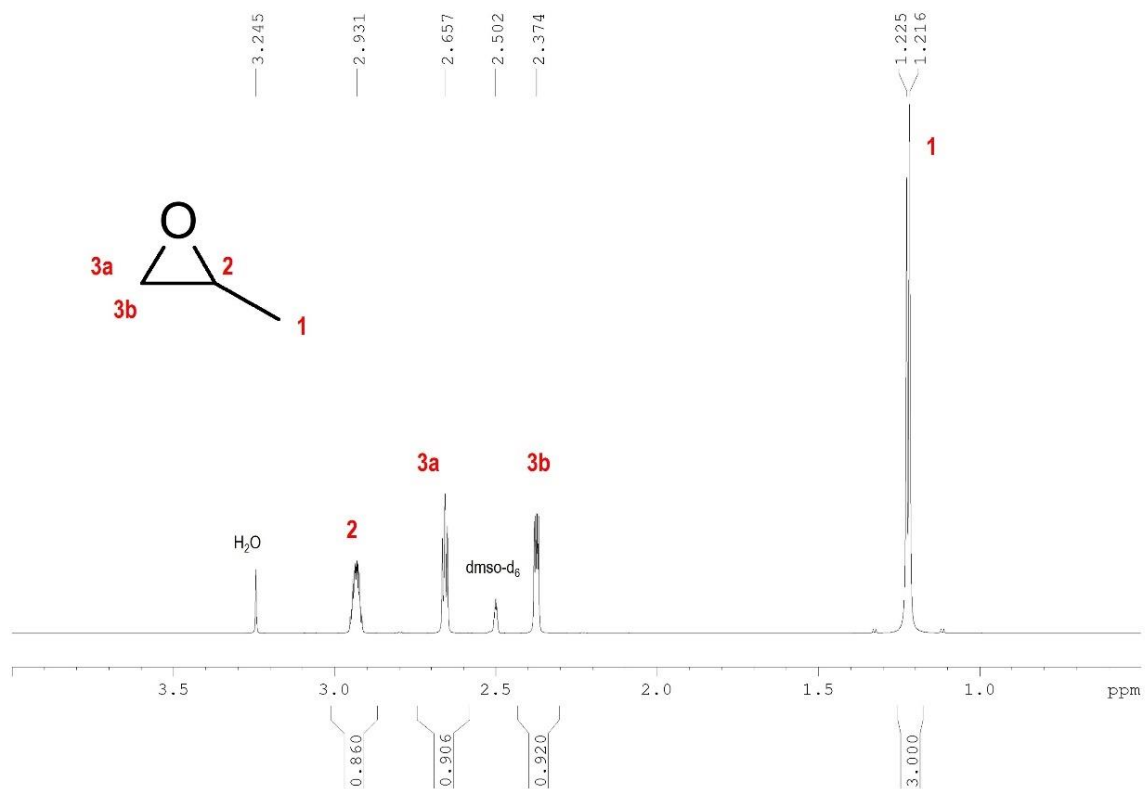
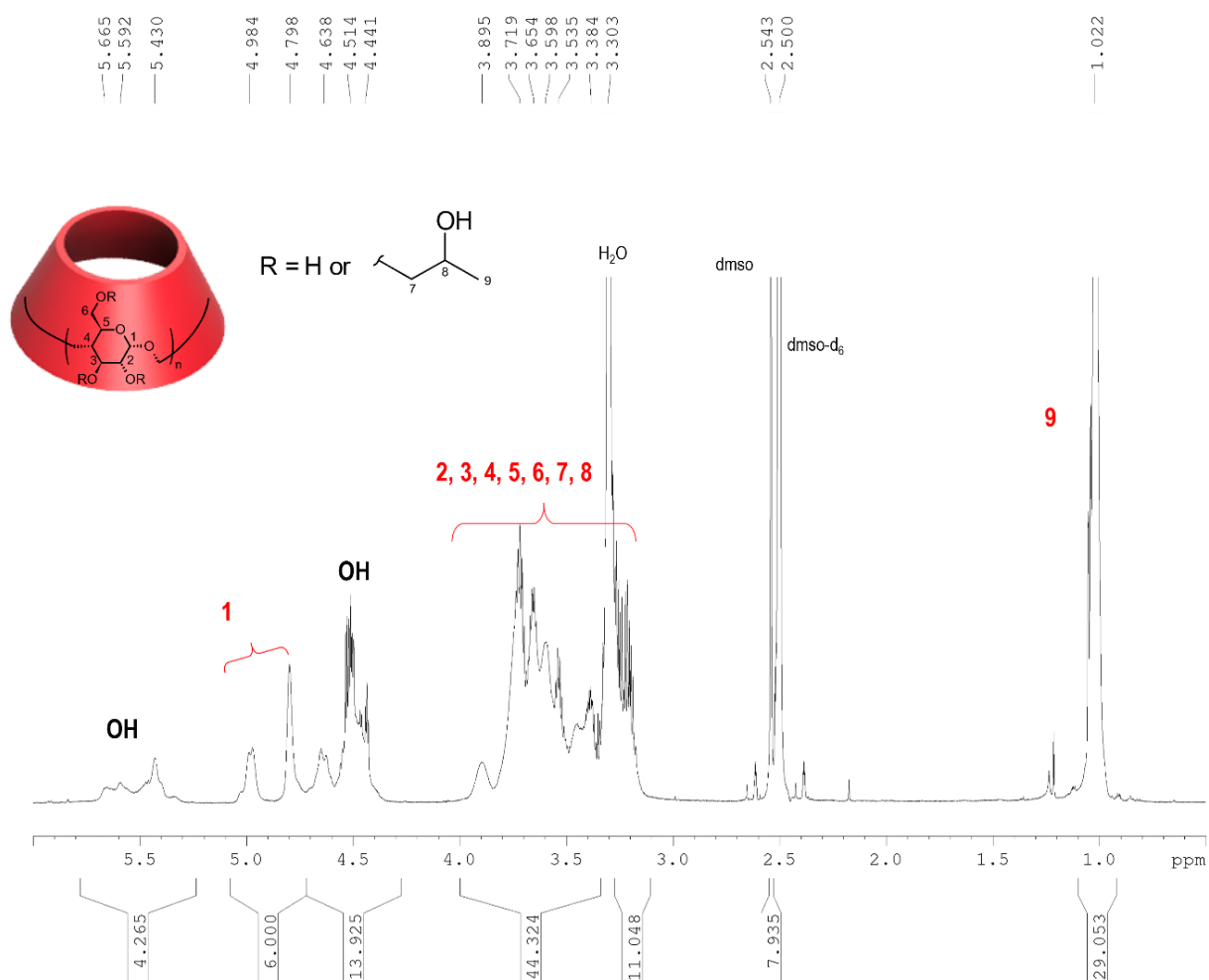
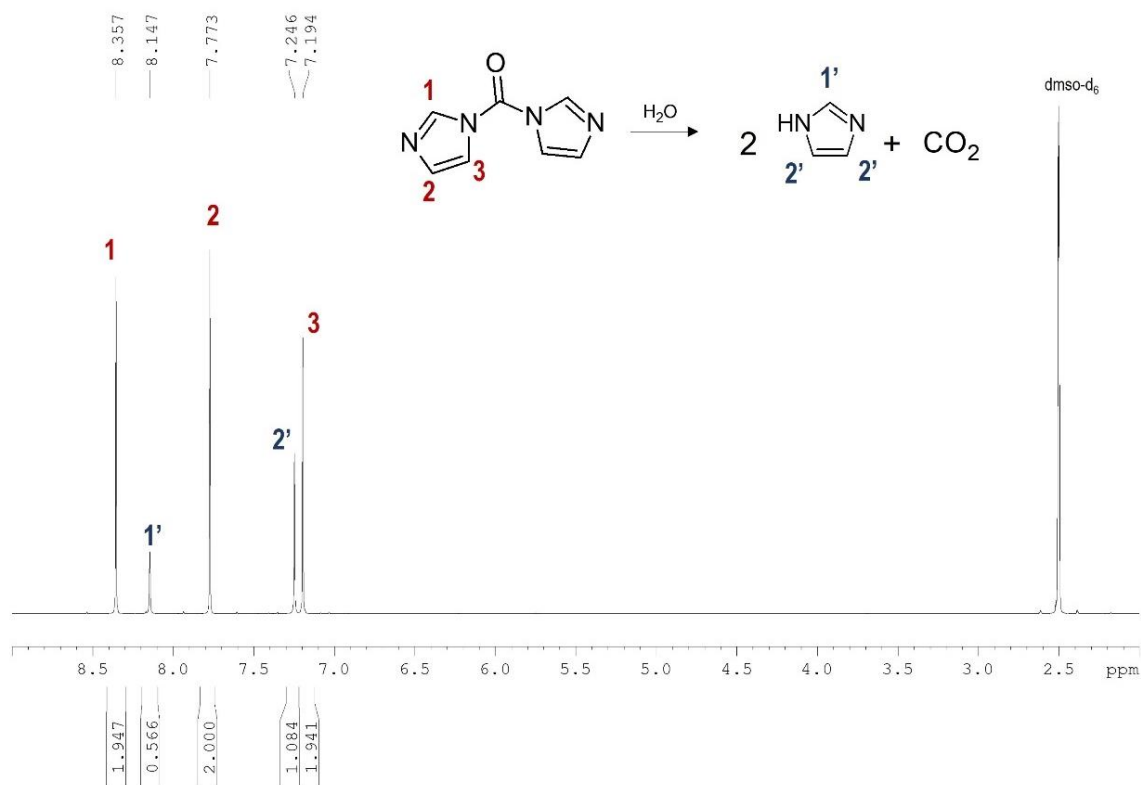


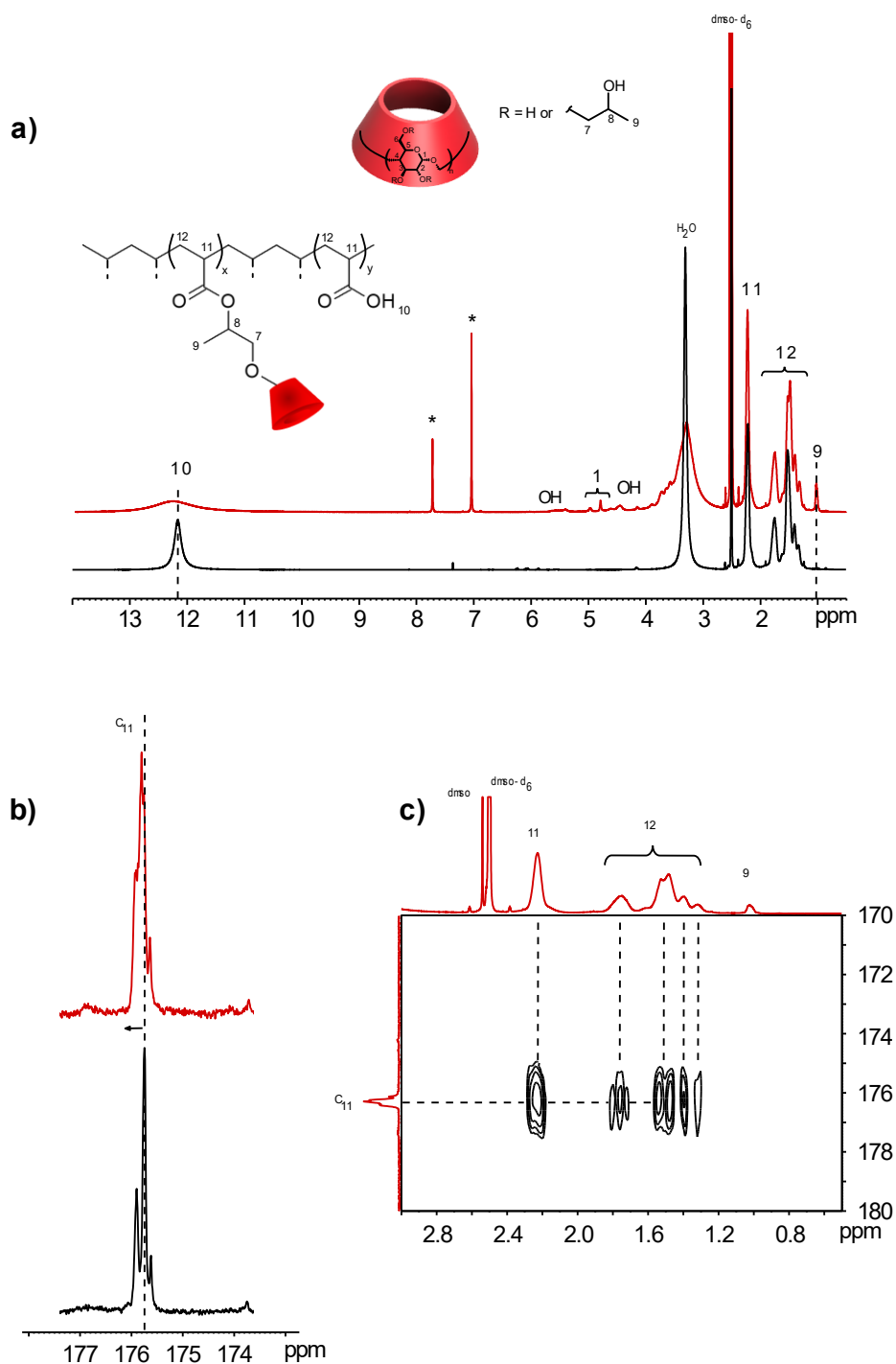
Figure SI.III.28  $^1\text{H}$  NMR spectrum in  $\text{DMSO-d}_6$  of propylene oxide (16 scans, 308K).



**Figure SI.III.29**  $^1H$  NMR spectrum in DMSO- $d_6$  of Hydroxy- $\alpha$ -CD (16 scans, 308K). According to the integration ratio between the  $\alpha$ -CD anomeric proton (1; 4.98 & 4.80 ppm) and the methyl protons (9; 1.022 ppm), it is calculated that average 53 % of hydroxyl groups of  $\alpha$ -CD are substituted with 2-hydroxypropyl groups.

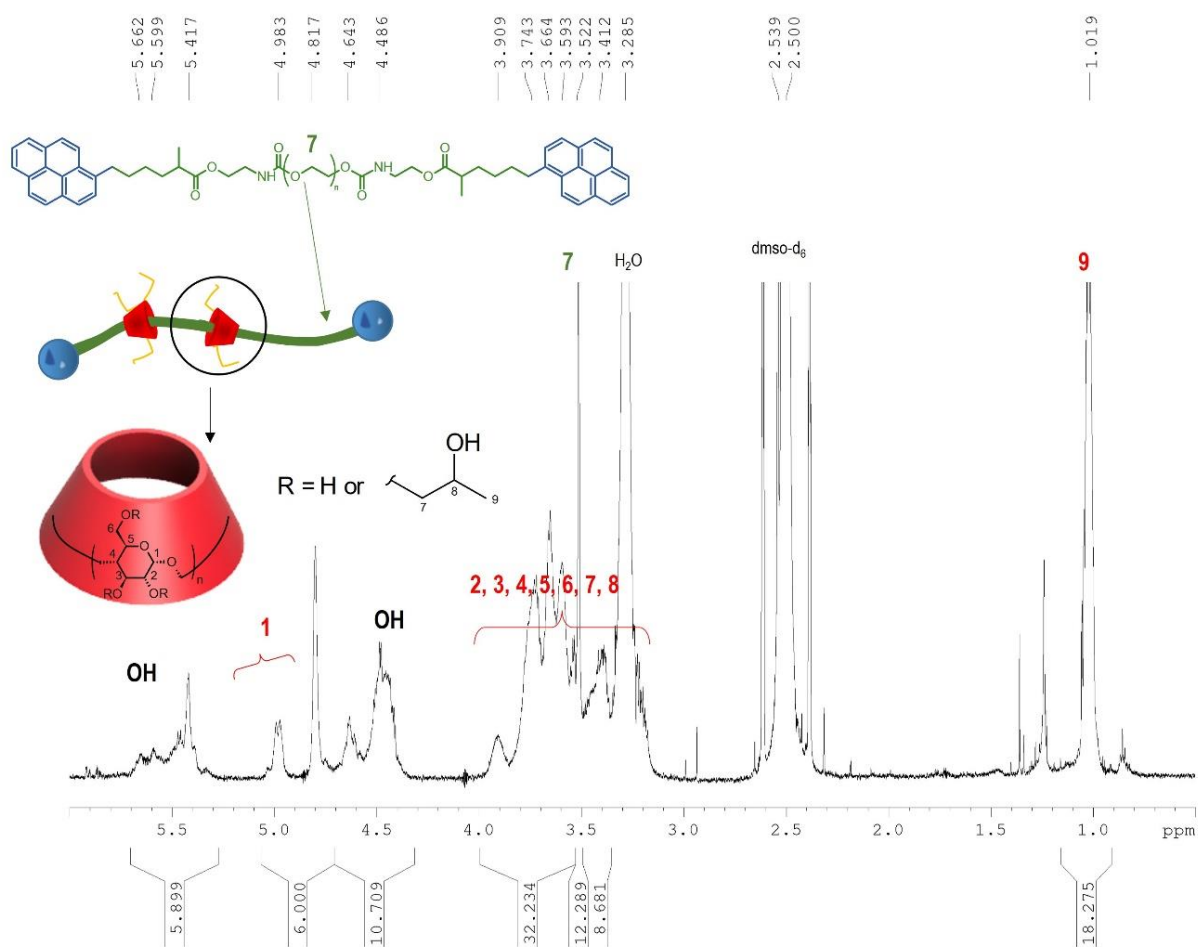


**Figure SI.III.30  $^1\text{H}$  NMR spectrum in  $\text{DMSO-d}_6$  of CDI (16 scans, 308K).** As highlighted by the presence of imidazole characteristic peaks (7.26 & 8.15 ppm), CDI is already partially hydrolysed (28%). Thus, for all the following PR-PAA network syntheses, a corresponding mass correction (+12% $_{\text{wt}}$ ) was adopted to achieve the desired CDI activation proportion.

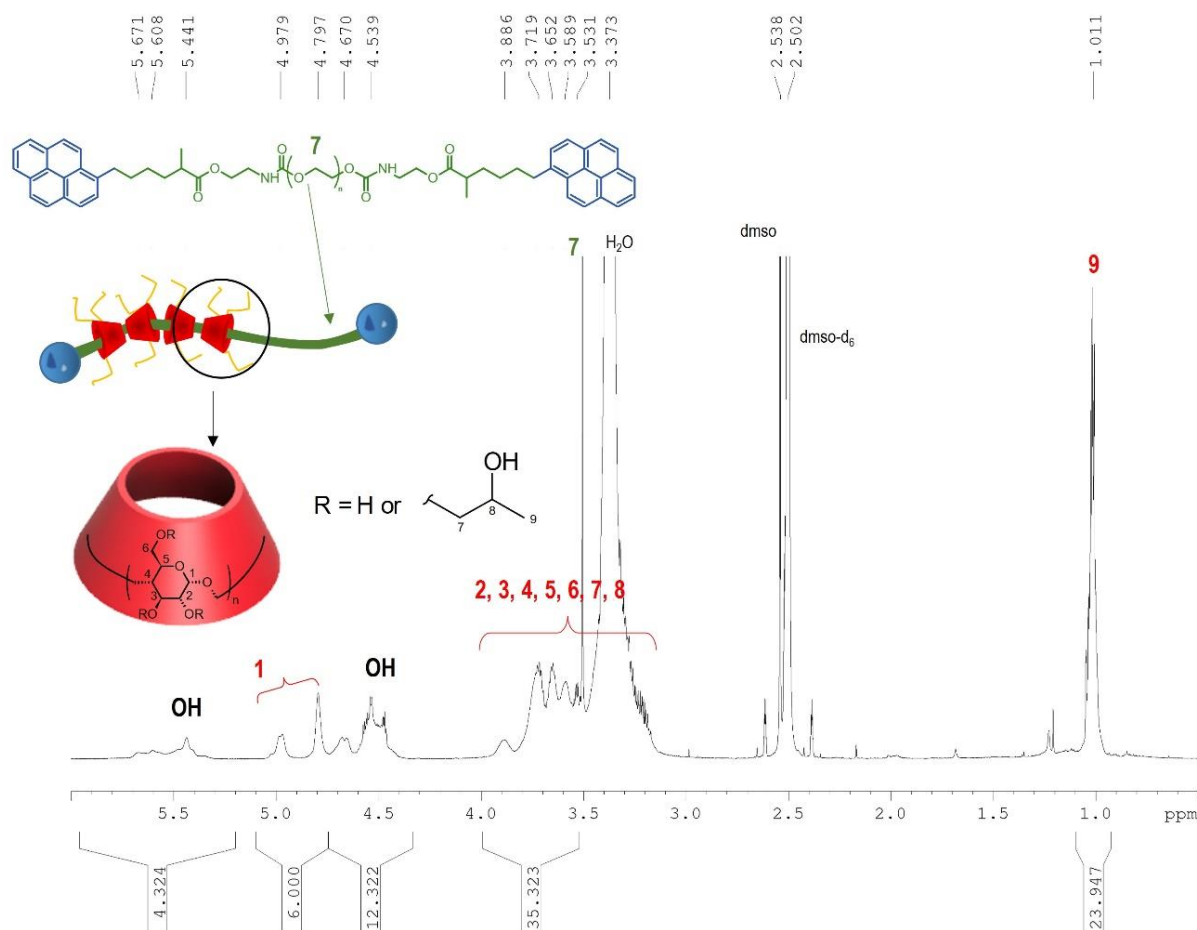


**Figure SI.III.31 NMR characterization of  $\alpha$ -CD-PAA 2 network.** As expected, clearer evidence demonstrates the esterification for  $\alpha$ -CD-PAA 2 than for  $\alpha$ -CD-PAA 1 because of the chosen experimental conditions. These conditions choice was only made to show the NMR characterization of  $\alpha$ -CD-PAA 2. Both PAA (black) and  $\alpha$ -CD-PAA 2 (red) were dissolved in DMSO- $d_6$ .  $^1\text{H}$  NMR,  $^{13}\text{C}$  NMR and HMBC spectra were acquired at 308K with 16, 4096 and 4 scans respectively. **a)** Overlapped  $^1\text{H}$  NMR spectra of PAA and  $\alpha$ -CD-PAA 2. Signals of the imidazole by-product can be seen on the  $\alpha$ -

CD-PAA 2.  $^1\text{H}$  NMR spectrum (s, 7.77 ppm and s, 7.07 ppm marked with an asterix) because it was acquired before the second precipitation in THF. The carboxylic acid proton signal is widened and shifted for  $\alpha$ -CD-PAA 2. Moreover, the 18% lower integration value suggests that the esterification reaction was efficient. **b)** Zoom in of the overlapped  $^{13}\text{C}$  NMR spectra of PAA and  $\alpha$ -CD-PAA 2 in the region of the carbonyl groups. For  $\alpha$ -CD-PAA 2, the signal is shifted towards higher chemical shift (dashed line) which is consistent with the formation of ester bonds. **c)** Zoom in of the HMBC spectrum of  $\alpha$ -CD-PAA 2. Such 2D-NMR experiment was run with the ultimate goal to confirm the ester bond formation between PAA carboxylic acids and  $\alpha$ -CD hydroxypropyl moieties. Unfortunately, no plot was seen between the carbonyl carbon (**C11**, 175.8 ppm) and the methyl protons of  $\alpha$ -CD (**9**, s, 1 ppm). Either the distance between these two atoms is too big to see any correlation plot or in proportion there is still more carboxylic acid groups than esters (max 503/6250). An idea could be to add even more CDI to generate more ester bonds.

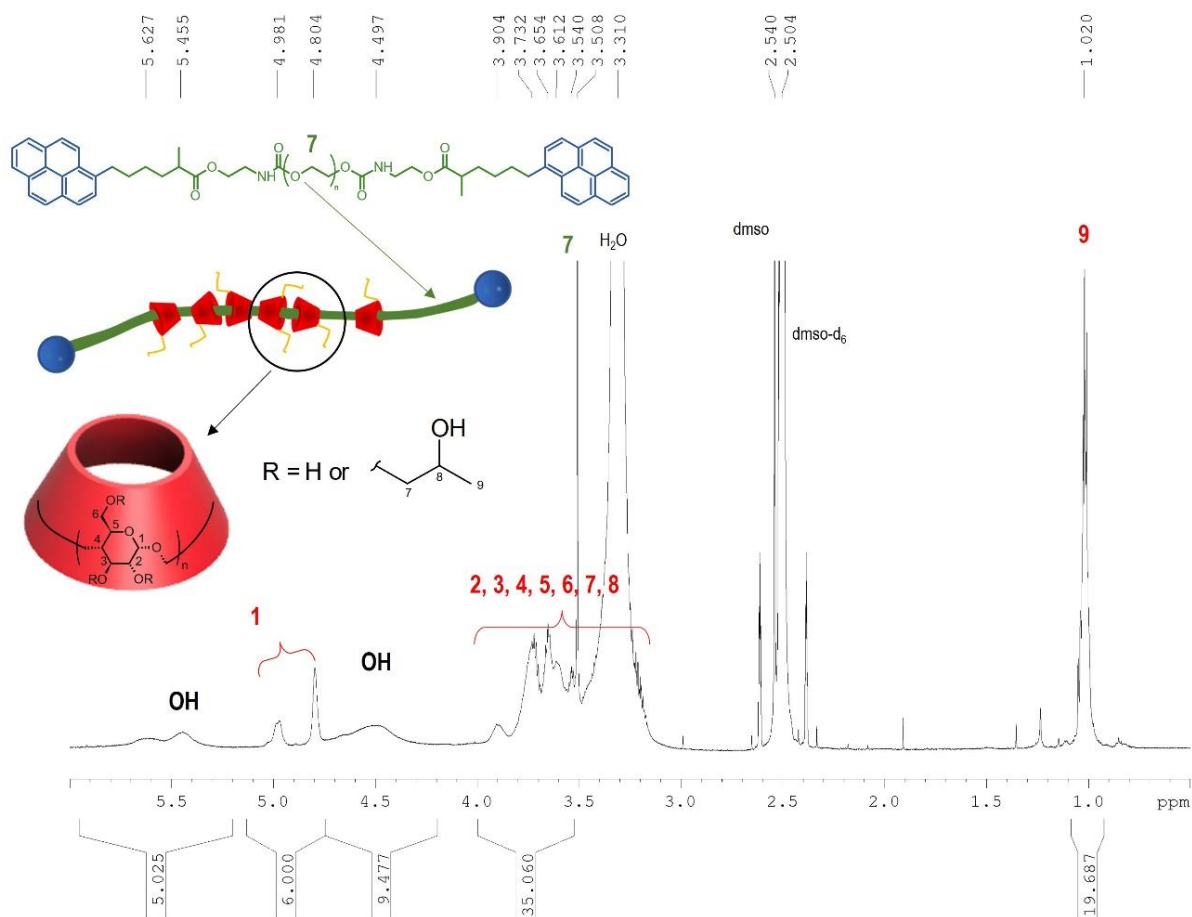


**Figure SI.III.32  $^1\text{H}$  NMR spectrum in  $\text{DMSO-d}_6$  of Hydroxy-PR3 (128 scans, 308K).** According to the integration ratio between the  $\alpha$ -CD anomeric proton (1; 4.98 & 4.80 ppm) and the methyl protons (9; 1.022 ppm), it is calculated that average 34% of hydroxyl groups of  $\alpha$ -CDs are substituted with 2-hydroxypropyl groups. Not all the protons of the polymer chain were visualized because of the poor signal to noise ratio.

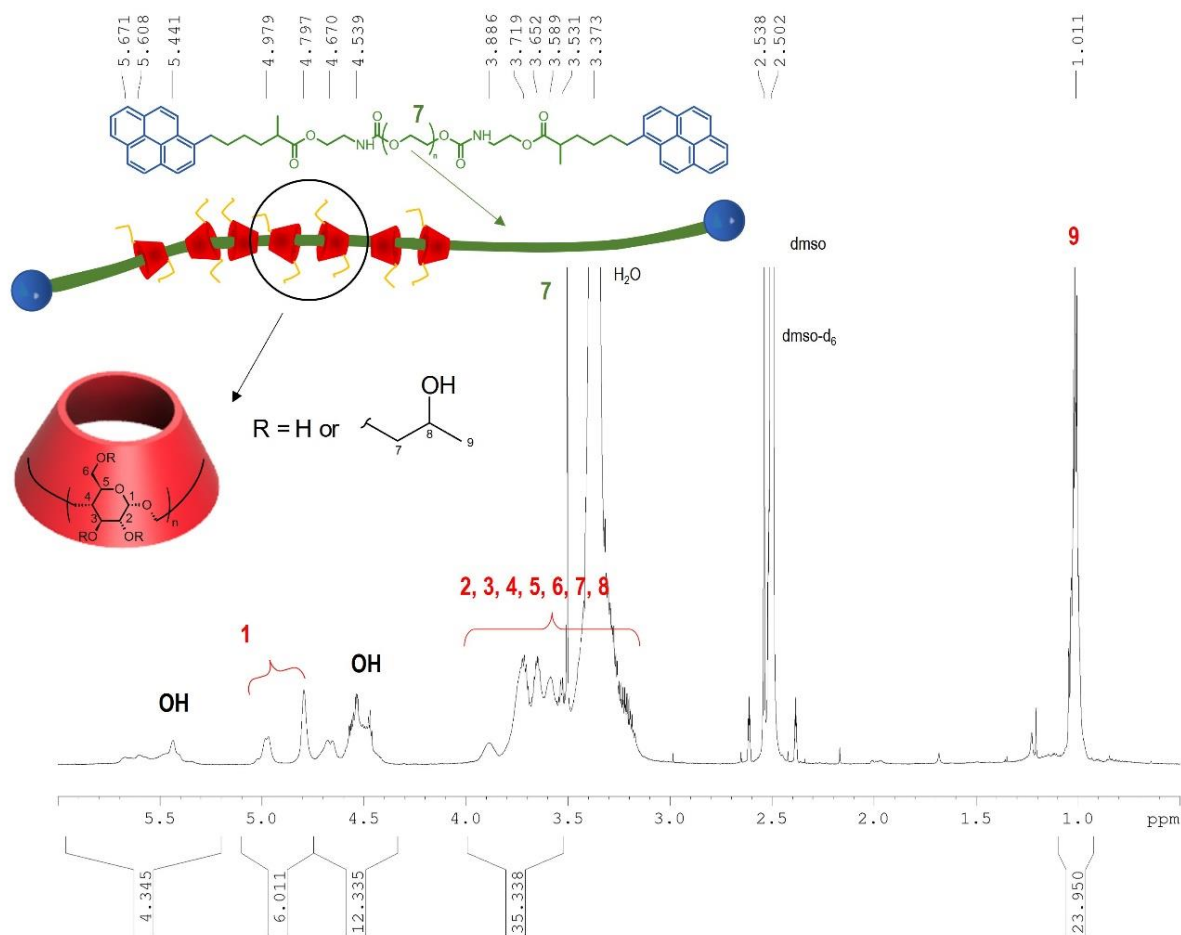


**Figure SI.III.33**  $^1\text{H}$  NMR spectrum in  $\text{DMSO-d}_6$  of Hydroxy-PR6 (128 scans, 308K). According to the integration ratio between the  $\alpha$ -CD anomeric proton (1; 4.98 & 4.80 ppm) and the methyl protons (9; 1.022 ppm), it is calculated that 49% of hydroxyl groups of  $\alpha$ -CDs are substituted with 2-hydroxypropyl groups. Not all the protons of the polymer chain were visualized because of the poor signal to noise ratio. This synthesis was performed twice leading to an average of  $47 \pm 4\%$  of hydroxypropyl groups per  $\alpha$ -CD.

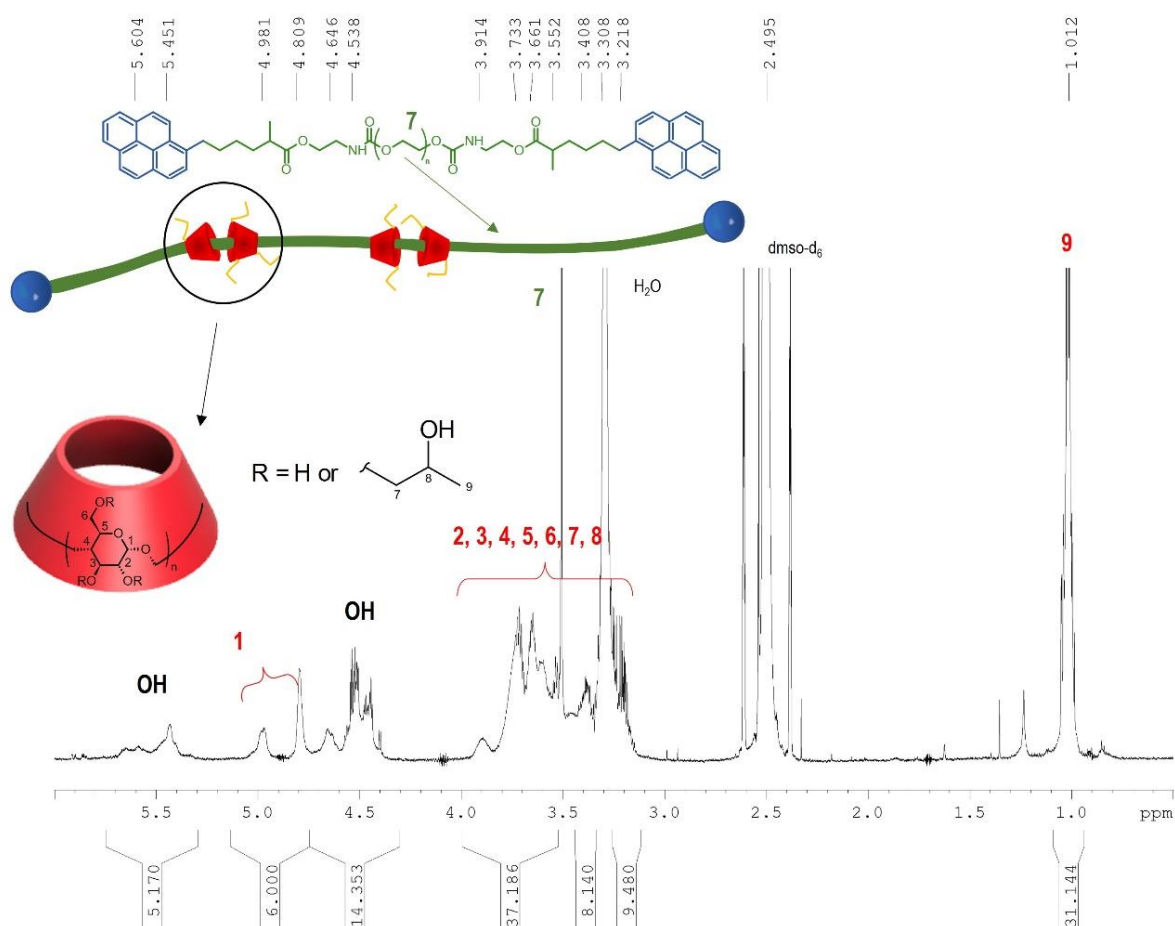




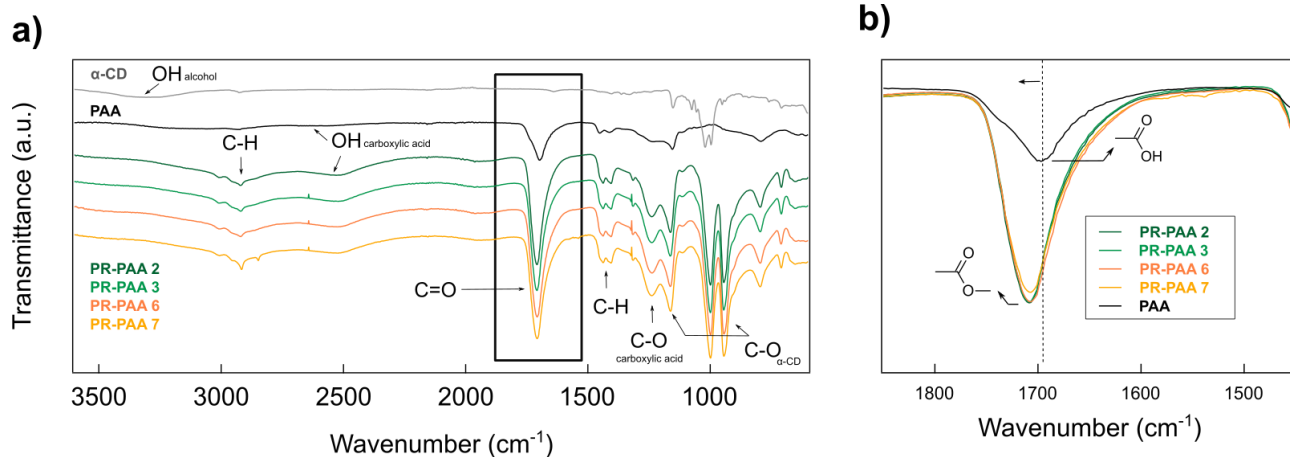
**Figure SI.III.34  $^1\text{H}$  NMR spectrum in DMSO- $\text{d}_6$  of Hydroxy-PR9 (128 scans, 308K).** According to the integration ratio between the  $\alpha$ -CD anomeric proton (1; 4.98 & 4.80 ppm) and the methyl protons (9; 1.022 ppm), it is calculated that average 36% of hydroxyl groups of  $\alpha$ -CDs are substituted with 2-hydroxypropyl groups. Not all the protons of the polymer chain were visualized because of the poor signal to noise ratio.



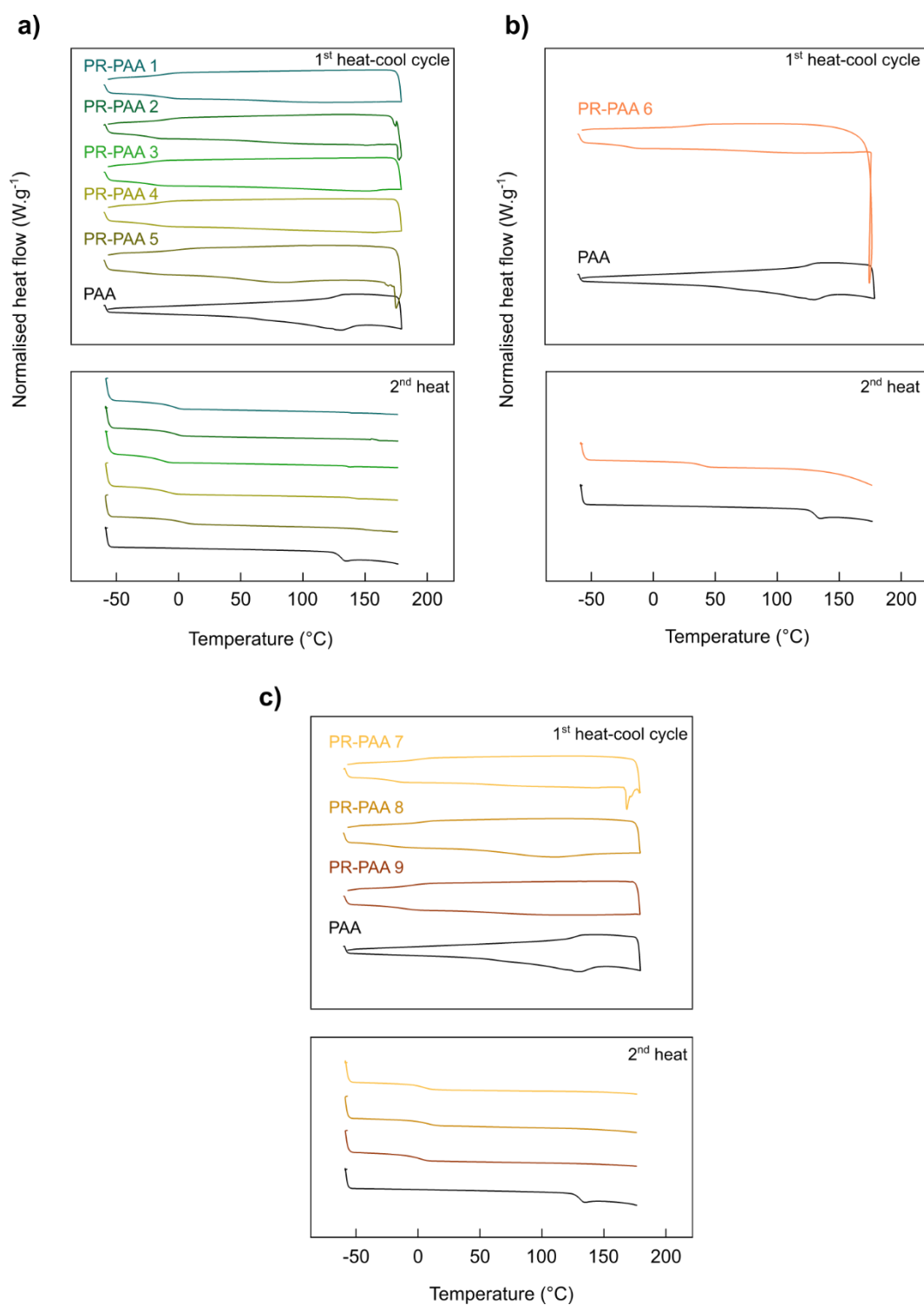
**Figure SI.III.35**  $^1\text{H}$  NMR spectrum in  $\text{DMSO-d}_6$  of Hydroxy-PR10 (128 scans, 308K). According to the integration ratio between the  $\alpha$ -CD anomeric proton (1; 4.98 & 4.80 ppm) and the methyl protons (9; 1.022 ppm), it is calculated that average 44% of hydroxyl groups of  $\alpha$ -CDs are substituted with 2-hydroxypropyl groups. Not all the protons of the polymer chain were visualized because of the poor signal to noise ratio.



**Figure SI.III.36**  $^1\text{H}$  NMR spectrum in  $\text{DMSO-d}_6$  of Hydroxy-PR11 (128 scans, 308K). According to the integration ratio between the  $\alpha$ -CD anomeric proton (1; 4.98 & 4.80 ppm) and the methyl protons (9; 1.022 ppm), it is calculated that average 58% of hydroxyl groups of  $\alpha$ -CDs are substituted with 2-hydroxypropyl groups. Not all the protons of the polymer chain were visualized because of the poor signal to noise ratio.



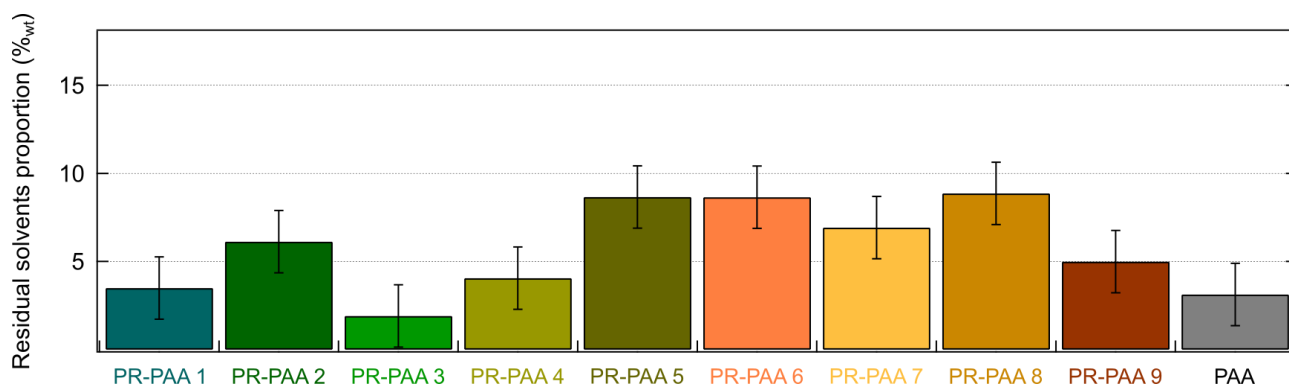
**Figure SI.III.37 ATR-FTIR spectra of PR-PAA.** Only 4 different PR-PAA networks FTIR spectra are shown here. **a)** Overlapped ATR-FTIR spectra of  $\alpha$ -CD, PAA, PR-PAA 2, PR-PAA 3, PR-PAA 6, PR-PAA 7. **b)** Zoom-in of the carbonyl groups stretching bands showing the formation of the ester bonds. The vertical dashed line underscores the band shift resulting from the appearance of this new band of higher wavenumber.



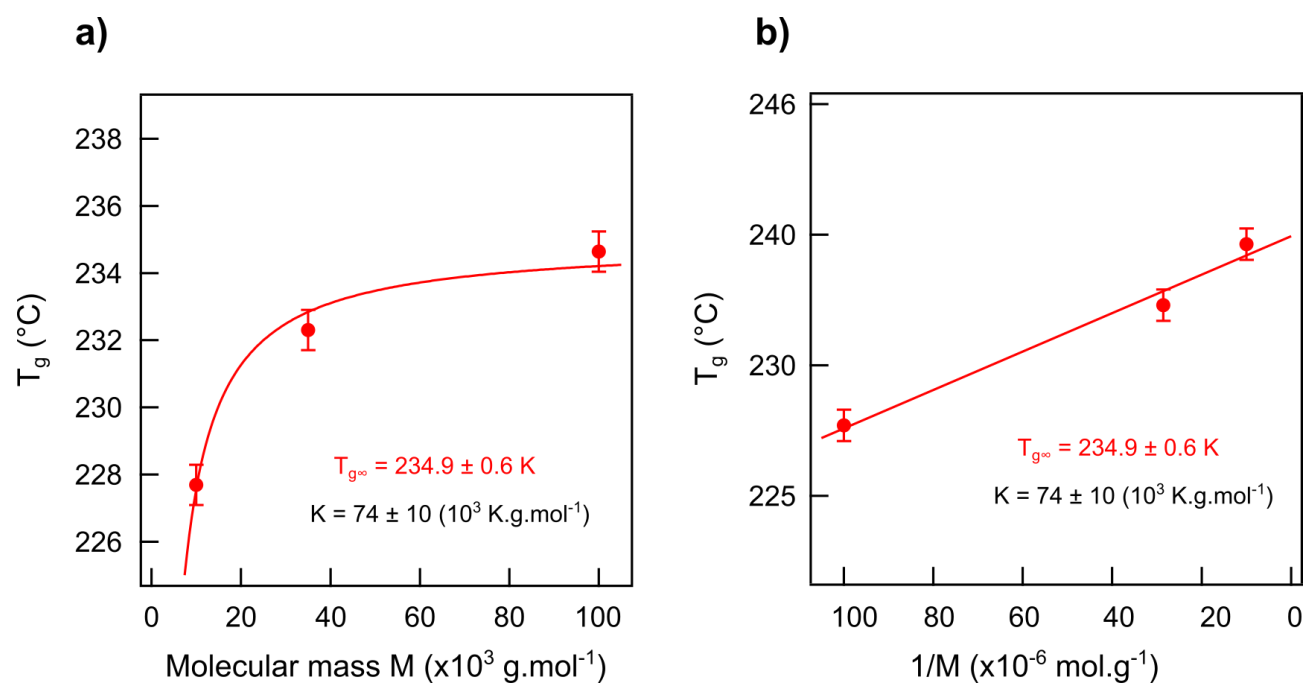
**Figure SI.III.38 DSC thermograms of PR-PAA networks.** They were recorded according to a heat-cool-heat procedure between  $-60^{\circ}\text{C}$  and  $180^{\circ}\text{C}$  at a rate of  $15^{\circ}\text{C.min}^{-1}$ . PR-PAA networks are called using their corresponding label (Table III.7). **a)** PR-PAA made of PR10K (runs 1, 2, 3, 4) **b)** PR-PAA made of PR35K (run 5). **c)** PR-PAA made of PR100K (runs 6, 7, 8).

PR-PAA sample	1 <sup>st</sup> heating ramp T <sub>g</sub> 1 (°C)	1 <sup>st</sup> cooling ramp T <sub>g</sub> 2 (°C)	2 <sup>nd</sup> heating ramp T <sub>g</sub> 3 (°C)
PR-PAA 1	-15.2	-12.2	-5.8
PR-PAA 2	-22.9	-9.6	-4.1
PR-PAA 3	-22.8	-22.4	-15.3
PR-PAA 4	-20.8	-15.5	-9.4
PR-PAA 5	-29.4	-0.9	2.2
PR-PAA 6	-19.6	31.7	38.2
PR-PAA 7	-20.6	0.0	4.3
PR-PAA 8	-23.7	2.5	5.9
PR-PAA 9	-13.3	-4.7	0.5

**Table SI.III.5 Glass transition temperatures (T<sub>g</sub>) of PR-PAA networks.** They are calculated using the TRIOS software. DSC thermograms were recorded according to a heat-cool-heat procedure between -60°C and 180°C at a rate of 15°C.min<sup>-1</sup>.



**Figure SI.III.39 Residual solvents mass proportion in PR-PAA (%wt).** PR-PAA networks are called using their corresponding label (Table III.7). The error bar of PR-PAA 2 was calculated by performing 3 times the experiment and it was extended to the other PR-PAA syntheses.



**Figure SI.III.40 Verification of the Fox and Flory's law on end-chains modified PEO.** The end-chains modified PEO10K, PEO35K and PEO100K were analysed by DSC using a heat-cool-heat procedure between  $-60^\circ\text{C}$  and  $150^\circ\text{C}$  at a rate of  $15^\circ\text{C}\cdot\text{min}^{-1}$ . The reported  $T_g$  values are the one obtained at the second heating ramp.  $T_{g\infty}$  was calculated by fitting the measured  $T_g$  values with the following equation  $T_g = T_{g\infty} - \frac{K}{M}$ .

# Supporting Information for Chapter IV

## 1. Materials & Methods

**Materials:** All materials were used as received without further purification step. Microparticle-sized silicon powder (micro-Si, 1 – 5  $\mu\text{m}$ ) was purchased from Alfa Aesar and nanoparticle-sized silicon powder (nano-Si, 40 nm) was received from Nanomakers. Super P conductive carbon black (Csp, 99 %), 4-fluoro-1,3-dioxolan-2-one (FEC 98%) were purchased from Alfa Aesar and poly(acrylic acid) (PAA,  $M_w \approx 450,000 \text{ g}\cdot\text{mol}^{-1}$ ) and lithium metal (99.9%) were obtained from Sigma Aldrich. LP30 electrolyte (99.9 %) was purchased from Solvionic. Graphite Timrex SLP50 (SLP50) was received from Imerys Graphite and Carbon®.

**Si particles characterization:** Si particles images were performed using a scanning electronic microscope (SEM-FEG Hitachi SU-70) in secondary electron mode (5kV; 50pA). Particle size distributions were obtained analysing the SEM images with ImageJ. XRD measurements were carried out with a Bruker D8 ADVANCE diffractometer operating in the Bragg–Brentano geometry with Cu  $K_\alpha$  radiation ( $\lambda(K_{\alpha 1}) = 1.54056 \text{ \AA}$ ,  $\lambda(K_{\alpha 2}) = 1.54439 \text{ \AA}$ ) and a Lynxeye XE detector. FTIR spectra were acquired in ATR mode on a Nicolet™ iS™ 5 FTIR spectrometer (Thermo Fisher Scientific) in the range of  $\sim 500$  to  $4000 \text{ cm}^{-1}$ . Thermogravimetric analysis (TGA) was performed using a Netzsch STA449C Jupiter equipped with a mass spectrometer under an air flux ( $50 \text{ ml}\cdot\text{min}^{-1}$ ) to observe the oxidation of Si particles. A heating ramp from  $25^\circ\text{C}$  to  $1400^\circ\text{C}$  with a heating rate of  $5^\circ\text{C}\cdot\text{min}^{-1}$  followed by a 2h isotherm at  $1400^\circ\text{C}$  were imposed.

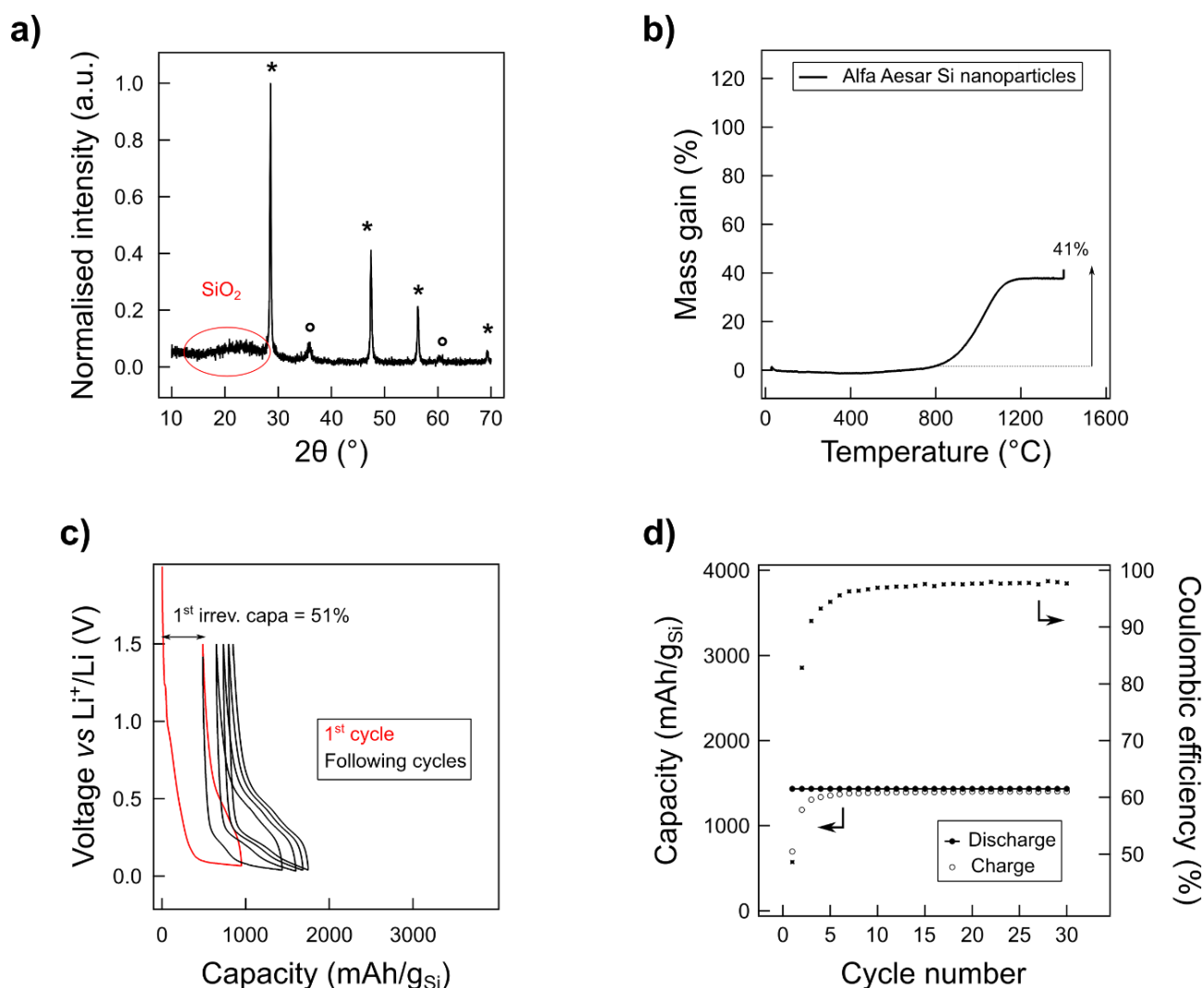
**Si electrode preparation:** The silicon anodes were prepared through a slurry coating process. Silicon active material (micro-Si or nano-Si), Csp and PAA, were first hand milled in a weight ratio of 2:1:1, and milliQ water, ethanol or DMSO was then added to the powder mix to achieve a dry mass ratio between 15 – 25 %. After 24 hours stirring, the homogeneous slurry was casted onto a copper foil (thickness of 26  $\mu\text{m}$  after heat treatment) using a doctor blade (Elcometer, 200  $\mu\text{m}$  gap,  $5 \text{ mm}\cdot\text{s}^{-1}$ ) and then dried for 24 hours in a vacuum oven at  $80^\circ\text{C}$  for the slurries prepared in water and ethanol and for 48 hours for the slurries prepared in DMSO. The dried films are stored in an argon-filled glovebox.



**Battery assembly and electrochemical tests:** Si electrodes were punched on the dried films (1.54 cm<sup>2</sup>). CR2032 coin-type half-cells were assembled in an argon-filled glove box, using lithium metal as the counter electrode. LP30 electrolyte composed of 1M Lithium hexafluorophosphate (LiPF<sub>6</sub>) in EC:DMC (1:1 by volume), was used to prepare our LP30+FEC electrolyte by adding 5%<sub>wt</sub> of 4-fluoro-1,3-dioxolan-2-one (FEC). Whatman paper was used as separator, soaked with 15 droplets of the corresponding electrolyte. The electrochemical performances of the cells were studied by galvanostatic discharge-charge cycling at constant current in the voltage range of 0.005 – 1.5 V vs. Li<sup>+</sup>/Li. The cells were cycled at 0.1C (360 mA.g<sup>-1</sup>) with a BCS-805 or MPG2 potentiostats (Bio-Logic, France) at room temperature. All specific capacities and current densities in this study are based on the mass of Si only. For each Si electrode, two duplicate cells were cycled. The variations in initial Coulombic efficiency and capacity retention are calculated as the mean values of the two testing cells. The analysis of the electrochemical data was performed on EC-Lab software.

**Electrode porosity :** The porosity of the electrodes was estimated by comparing the actual volume of an electrode (thickness measurement) to its expected volume regarding the true density of each material (here micro-Si, nano-Si, PAA, Csp). This density was measured on a helium pycnometer with a Micromeritics AccuPyc 1330 and Helium Messer gas (≥ 99.996 vol. %). One analysis is composed of 20 helium purges followed-up by 5 runs of measurements.

## 2. Supporting Figures: reference Si/PAA electrodes



**Figure SI.IV.1: Characterization of Si nanoparticles purchased from Alfa Aesar (nano-Si AA).** **a)** XRD pattern showing the presence of crystalline Si (star marker), amorphous  $\text{SiO}_2$  ( $2\theta = 23^\circ$ ) and SiC (circle marker). **b)** Thermogram obtained by TGA (heating ramp  $5^\circ\text{C}\cdot\text{min}^{-1}$  followed by a 2 hours isotherm at  $1400^\circ\text{C}$ ). From the mass increase of 41%, the proportion of pure Si is estimated to  $36\%_{\text{wt}}$  while  $\text{SiO}_2$  proportion is  $64\%_{\text{wt}}$ . Galvanostatic cycling performances of Si/Csp/PAA (2:1:1) electrode cycled vs Li metal in LP30+5FEC electrolyte at C/37.5. The cell was cycled between 0.01 V and 1.5 V in a coin cell configuration. **c)** Voltage-capacity plot of the first five cycles. The first discharge capacity reaches  $1000 \text{ mAh}\cdot\text{g}^{-1}$  supporting the presence of almost two thirds of inactive  $\text{SiO}_2$  in Si nanoparticles. **d)** Capacity retention and coulombic efficiency profiles over the first thirty cycles.

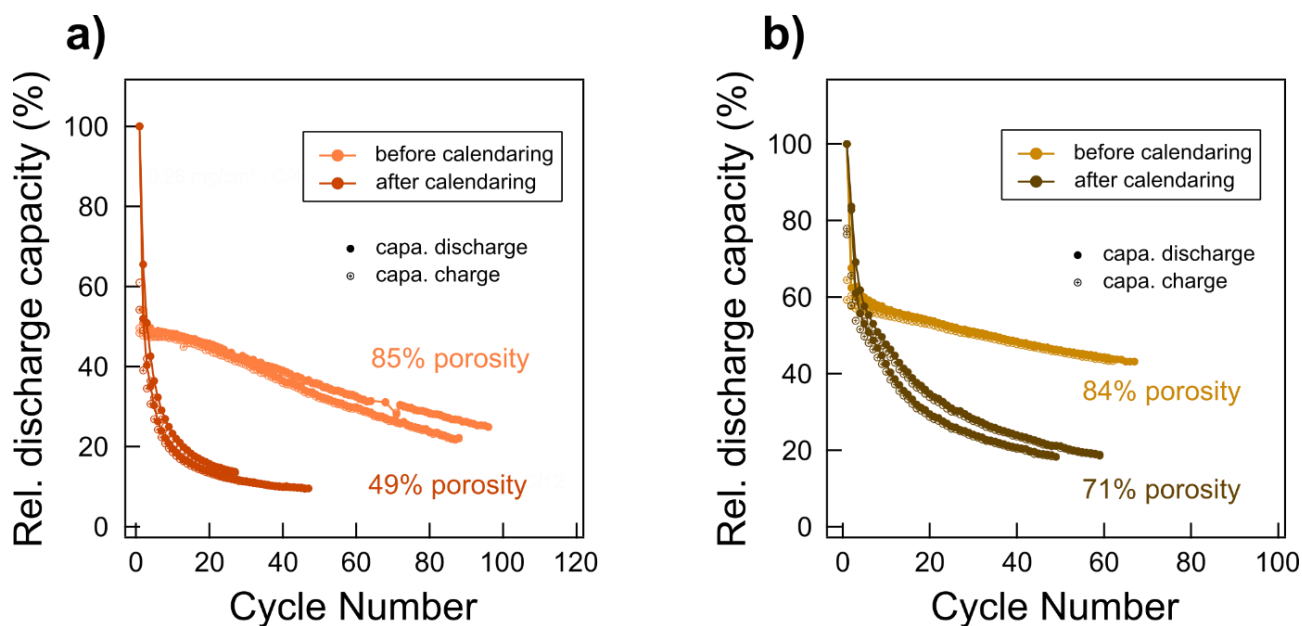
a)

micro-Si	Thickness ( $\mu\text{m}$ )	Porosity (%)	Si loading ( $\text{mg}_{\text{Si}}\cdot\text{cm}^{-2}$ )
EtOH	$20 \pm 3$	$79 \pm 4$	$0.8 \pm 0.2$
H <sub>2</sub> O	$23 \pm 1$	$75 \pm 2$	$1.1 \pm 0.1$
DMSO	38	59	1.5

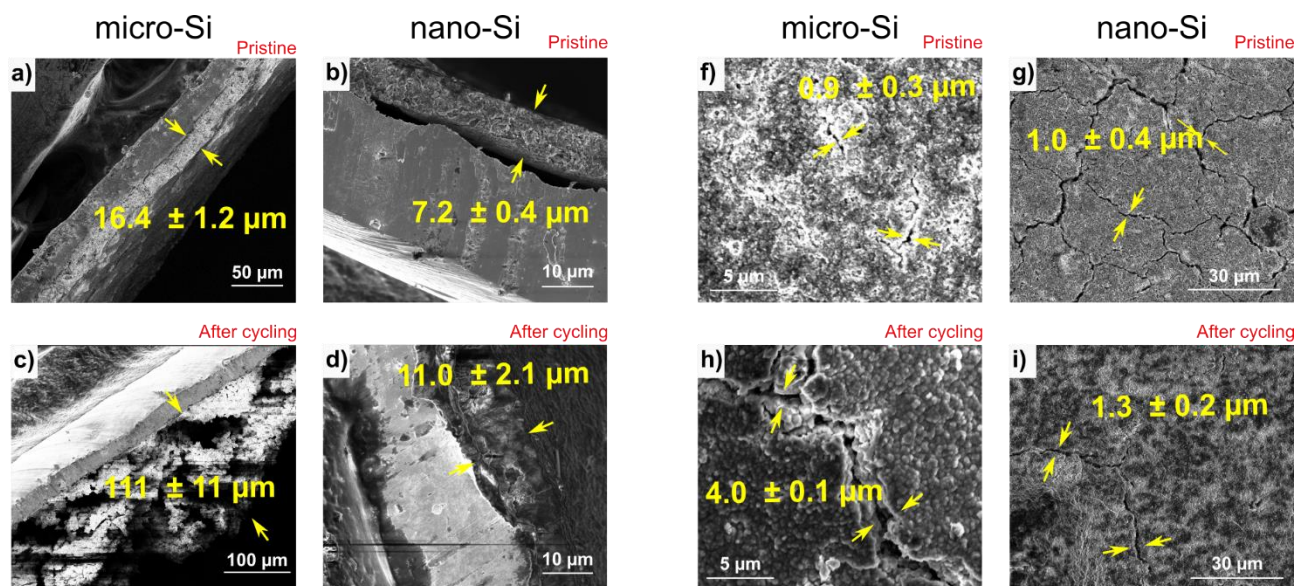
b)

nano-Si	Thickness ( $\mu\text{m}$ )	Porosity (%)	Si loading ( $\text{mg}_{\text{Si}}\cdot\text{cm}^{-2}$ )
EtOH	23	91	0.4
H <sub>2</sub> O	$12 \pm 4$	$45 \pm 3$	$0.5 \pm 0.1$
DMSO	27	76	1.2

**Table SI.IV.1: Physical characterization of Si reference electrodes.** The electrode composition is Si/Csp/PAA in a (2:1:1) weight ratio. Errors bars are calculated as standard deviations if different batches of electrodes were prepared. Two types of Si particles were investigated. **a)** Micro-Si electrodes prepared from aqueous or ethanol-based slurries show similar thickness ( $\sim 20 \mu\text{m}$ ), high porosity ( $\sim 75\text{-}80\%$ ) and relatively high Si loading ( $\sim 1 \text{ mg}\cdot\text{cm}^{-2}$ ). The thickness of DMSO-based micro-Si electrodes is doubled ( $\sim 40 \mu\text{m}$ ) and the Si loading increases to  $1.5 \text{ mg}\cdot\text{cm}^{-2}$ , resulting from the higher viscosity of DMSO. Their corresponding porosity is lowered to 60%. For nano-Si electrodes, lower Si loadings were achieved. Interestingly, they are still comparable for aqueous and ethanol-based slurries ( $\sim 0.5 \text{ mg}\cdot\text{cm}^{-2}$ ) and reach more than  $1 \text{ mg}\cdot\text{cm}^{-2}$  for DMSO-based slurries. In general, porosities are enhanced for nano Si-electrodes, which corroborates well with the micrometric size of the agglomerates of nano-Si particles (Figure IV.1.c). However, this trend is not observed for nano-Si electrodes prepared from aqueous slurry (45 vs 75% for micro-Si).

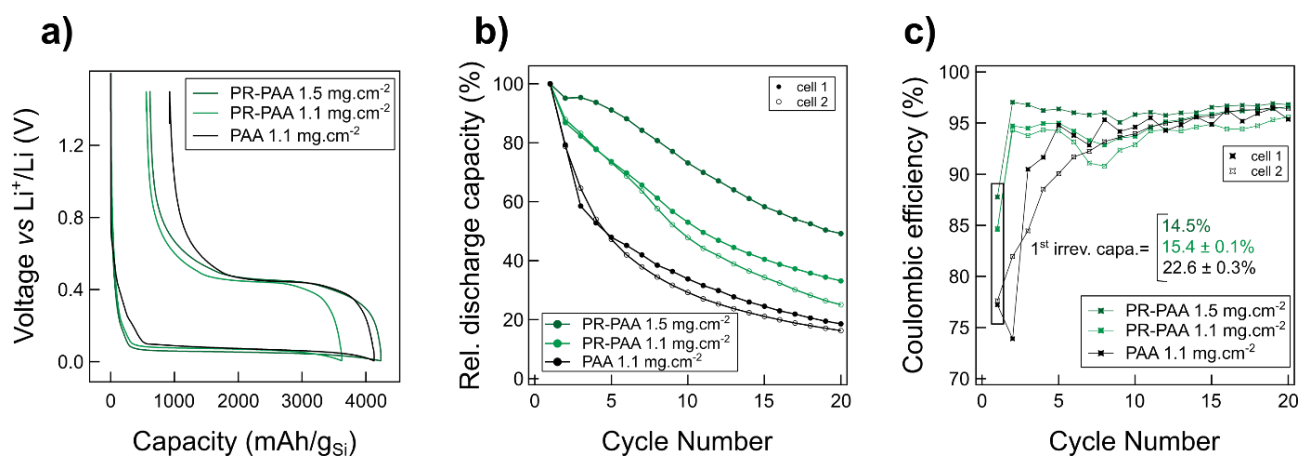


**Figure SI.IV.2: Effect of calendaring on Si electrodes cycling performances.** Nano-Si/Csp/PR-PAA (2:1:1) electrodes were cycled in duplicate vs Li metal in LP30+5FEC electrolyte at C/10 between 0.005 V and 1.5 V. Relative discharge capacity vs cycle number curves of **a)** PR-PAA 6 electrodes ( $\sim 0.32 \pm 0.02 \text{ mg}_{\text{Si}} \cdot \text{cm}^{-2}$ ) before (orange) and after (red) calendaring and **b)** PR-PAA 9 electrodes ( $\sim 0.69 \pm 0.15 \text{ mg}_{\text{Si}} \cdot \text{cm}^{-2}$ ) before (dark red) and after (brown) calendaring. The corresponding porosities are estimated assuming PR-PAA have the same density than PAA.

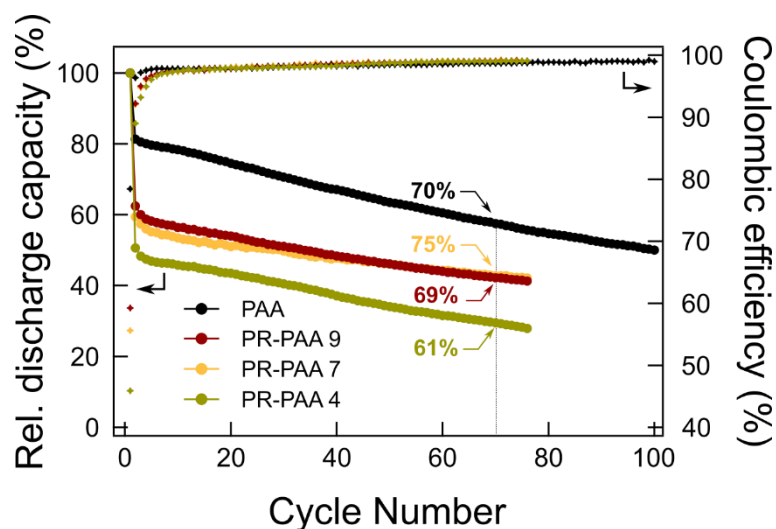


**Figure SI.IV.3: Ex situ SEM characterization of micro-Si and nano-Si AA electrodes before and after cycling.** Si/Csp/PAA (2:1:1) electrodes were cycled vs Li metal in LP30+5FEC electrolyte at C/10 between 0.01V and 1.5V. The studied Si electrodes are composed of micro-Si and nano-Si AA (Figure SI.IV.1). Micro-Si and nano-Si AA electrodes were observed after the 100<sup>th</sup> delithitation and the 26<sup>th</sup> delithitation respectively. **a) and b)** Cross-sectional images of the a) micro-Si and b) nano-Si AA electrodes before cycling. **c) and d)** Cross-sectional images of the c) micro-Si and d) nano-Si AA after cycling. **e) and f)** Top-viewed images of the e) micro-Si and f) nano-Si AA electrodes before cycling. **g) et h)** Top viewed images of the g) micro-Si and h) nano-Si electrodes after cycling. All images in this figure are obtained under secondary electron mode. The thicknesses and the sizes of the cracks are measured using ImageJ software.

## 3. Supporting Figures: Si/PR-PAA electrodes



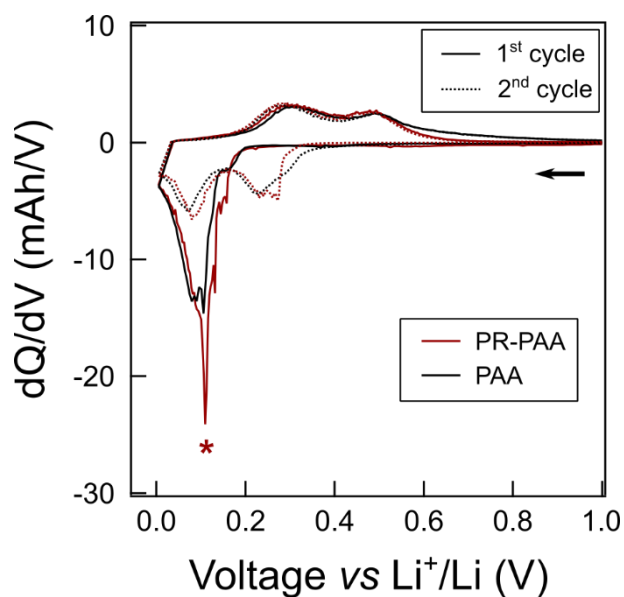
**Figure SI.IV.4: Electrochemical performances of micro-Si electrodes incorporating PAA and PR-PAA**, in LP30+5FEC electrolyte at C/10 between 0.01 V and 1.5 V vs Li. PR-PAA 2 was chosen for this study. Si electrodes are composed of micro-Si and have three different Si loading regarding the binder : PAA (1.1 mg.cm<sup>-2</sup>, black), PR-PAA (1.1 mg.cm<sup>-2</sup>, light green) and PR-PAA (1.5 mg.cm<sup>-2</sup>, dark green). **a)** Initial discharge-charge profiles of the PR-PAA and PAA Si electrodes. **b)** Relative discharge capacity vs cycle number curves. **c)** Coulombic efficiency variation upon cycling (20 first cycles) with the indication of the first irreversible capacity loss calculated as the mean value of the two duplicate cells.



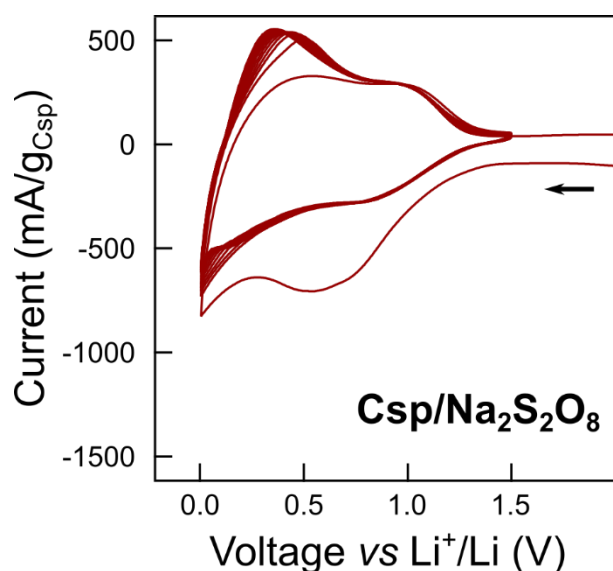
**Figure SI.IV.5: Cycling performances of aqueous nano-Si electrodes incorporating PR-PAA binders upon 80 cycles.** See Figure IV.10 for details. The capacity retentions after 70 cycles – 70<sup>th</sup> charge capacity divided by the 1<sup>st</sup> charge capacity – are reported.

Binder	Ohmic resistance ( $\Omega$ )
PAA	$22 \pm 14$
PR-PAA 2	$45 \pm 5$
PR-PAA 3	$25 \pm 7$
PR-PAA 6	$82 \pm 41$
PR-PAA 7	$62 \pm 12$

**Table SI.IV.2: Ohmic resistance of aqueous nano-Si electrodes.** Ohmic resistances were evaluated as the ratio between voltage and current, after the OCV period (10 s) following the first delithitation. The time interval of the calculations was systematically inferior to 50 ms.

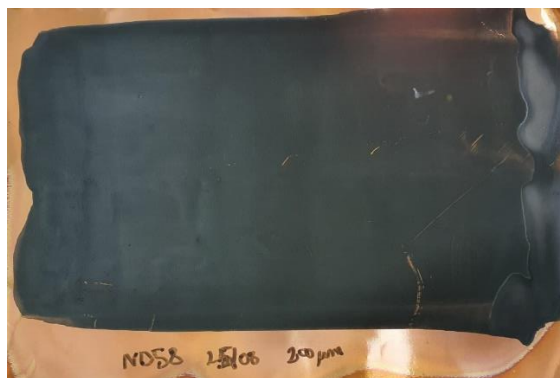


**Figure SI.IV.6: Differential capacity curves ( $dQ/dV$ ) vs voltage** of PR-PAA 7 (dark red) and PAA (black). Galvanostatic cycling was performed at C/10 in LP30+FEC vs Li metal between 0.005 V and 1.5 V. Nano-Si electrodes were made through the aqueous slurry process and consist of nano-Si/Csp/PR-PAA or PAA in weight ratio of (2:1:1).

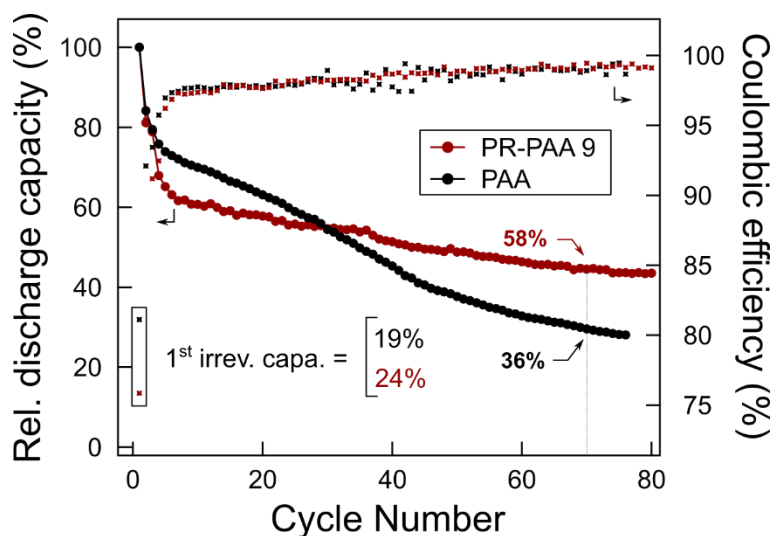


**Figure SI.IV.7: Cyclic voltammograms of Csp/( $\text{Na}_2\text{S}_2\text{O}_8$ ) (50:50) mixtures.** CV starts from open circuit voltage (OCV) and 10 cycles at a scan rate of  $1 \text{ mV}\cdot\text{s}^{-1}$  were recorded. The current is normalised with the mass of Csp.

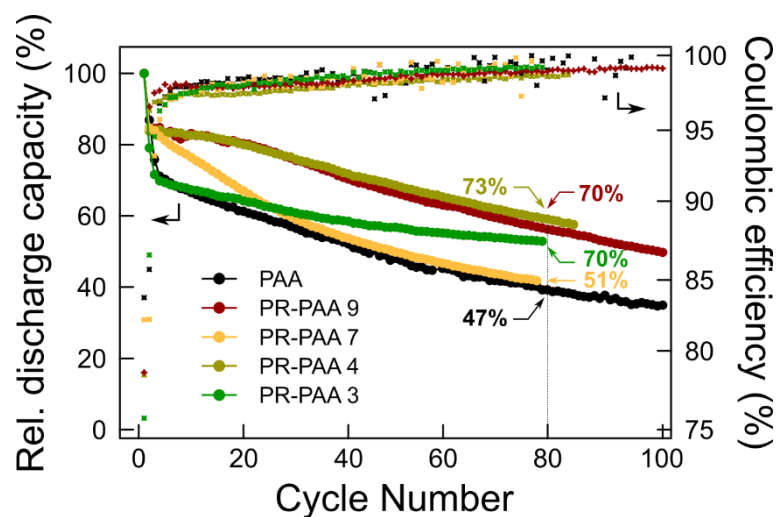




**Figure SI.IV.8: Time-controlled nano-Si electrode showing some bad adhesion**, as shown by the razor-sharp trace. The aqueous slurry nano-Si/Csp/PR-PAA 9 (2:1:1 weight ratio) was mixed for 4h before its casting.



**Figure SI.IV.9: Cycling performances of DMSO-based nano-Si electrodes incorporating PR-PAA binders upon 100 cycles**, in LP30+5FEC electrolyte at C/10 between 0.01 V and 1.5 V vs Li. Si electrodes are composed of nano-Si/Csp/binder. PR-PAA 9 ( $0.67 \text{ mg}_{\text{Si}} \cdot \text{cm}^{-2}$ , dark red) performances are compared to PAA ( $0.82 \text{ mg}_{\text{Si}} \cdot \text{cm}^{-2}$ , black). The first irreversible capacity loss and the capacity retentions after 70 cycles – 70<sup>th</sup> charge capacity divided by the 1<sup>st</sup> charge capacity – are reported. Cells were assembled in duplicate and the mean values of the first irreversible capacities are  $19 \pm 0\%$  and  $25 \pm 1\%$  for PAA and PR-PAA respectively.



**Figure SI.IV.10: Cycling performances of ethanol-based nano-Si electrodes incorporating PR-PAA binders upon 100 cycles.** See Figure IV.12 for details. The capacity retentions after 70 cycles – 70<sup>th</sup> charge capacity divided by the 1<sup>st</sup> charge capacity – are reported.



# Glossary

1D	One dimension
ADEME	French Agency for Environment and Energy Management
a-Si	Amorphous Si
CD	Cyclodextrin
CDI	N, N'-carbonyl diimidazole
CD-PAA	CD cross-linked with PAA
CE	Coulombic efficiency
CMC	Sodium carboxymethylcellulose
CO <sub>2</sub>	Carbon dioxide
cr-Si	Crystalline Si
Csp	Carbon super P
Cu	Copper
CV	Cyclic voltammetry
DEC	Diethyl carbonate
DFT	Density functional theory
DMC	Dimethyl carbonate
DME	Dimethoxyethane
DMF	Dimethyl formaldehyde
DMSO	Dimethylsulfoxide
DNA	Deoxyribonucleic acid
DNFB	Dinitrofluorobenzene
DOL	Dioxolane
dQ/dV	Differential capacity
DSC	Differential scanning calorimetry
EC	Ethylene carbonate
EMC	Ethyl methyl carbonate
EO	Ethylene oxide
EOF	Electro-osmotic flux
FEC	Fluoroethylene carbonate
FTIR	Fourier-transform infrared spectroscopy
GHG	GreenHouse Gaz
H <sub>2</sub> O	Water

HSQC	Heteronuclear single quantum coherence
IEM	2-isocyanatoethyl methacrylate
IPCC	Intergovernmental Panel of Climate Change
Li	Lithium
Li <sub>2</sub> S	Lithium sulfide
Li <sub>2</sub> S <sub>x</sub>	Lithium polysulfide
LiNO <sub>3</sub>	Lithium nitrate
LiPF <sub>6</sub>	Lithium hexafluorophosphate
Li-S	Lithium-sulfur
LiTFSI	Lithium bis(trifluoromethanesulfonyl)imide
LP30	1M LiPF <sub>6</sub> in EC/DMC
MALDI TOF	Matrix-Assisted Laser Desorption/Ionization-Time Of Flight
micro-Si	Micrometer-sized Si particles
MS	Mass spectrometry
Na <sub>2</sub> S	Sodium sulfide
Na <sub>2</sub> S <sub>2</sub> O <sub>8</sub>	Sodium persulfate
Na <sub>2</sub> S <sub>x</sub>	Sodium polysulfide
NaCl	Sodium chloride
NaHCO <sub>3</sub>	Sodium bicarbonate
Nano-Si	Nanometer-sized Si particles
NaOH	Sodium hydroxyde
NMR	Nuclear Magnetic Resonance
OE	Oligoethylene
P(ε-CL)	Poly(ε-caprolactone)
PAA	Poly(acrylic acid)
PBS	1-pyrene butyric acid N-hydroxysuccinimid ester
PC	Propylene carbonate
PDMS	Poly(dimethylsiloxane)
PE	Poly(ethylene)
PEA	Poly(alkylene adipate)
PEC	Poly(ethylene carbonate)
PEO	Poly(ethylene oxide)
PEO100K	Poly(ethylene oxide) 100 000 g.mol <sup>-1</sup>
PEO10K	Poly(ethylene oxide) 10 000 g.mol <sup>-1</sup>
PEO35K	Poly(ethylene oxide) 35 000 g.mol <sup>-1</sup>

PFPE	Perfluoropoly(ether)
PIB	Poly(isobutene)
PMVE	Poly(methyl vinyl ether)
PP	Poly(propylene)
PPG	Poly(propylene glycol)
PPO	Poly(propylene oxide)
PPR	<i>Pseudopolyrotaxane</i>
PPR100K	<i>Pseudopolyrotaxane prepared from PEO100K</i>
PPR10K	<i>Pseudopolyrotaxane prepared from PEO10K</i>
PPR35K	<i>Pseudopolyrotaxane prepared from PEO35K</i>
PR	Polyrotaxane
PR100K	Polyrotaxane prepared from PPR100K
PR10K	Polyrotaxane prepared from PPR10K
PR35K	Polyrotaxane prepared from PPR35K
PR-PAA	Polyrotaxane cross-linked with PAA
PSi	Poly(dimethylsilane)
PTFE	Poly(tetrafluoro ethylene)
PTHF	Poly(tetrahydrofuran)
PVA	Poly(vinyl alcohol)
PVCa	Poly(vinylene carbonate)
PVDF	Poly(vinylidene fluoride)
PVDF-TFE-P	Poly(vinylidene fluoride-tetrafluoroethylene-propylene)
RM $\beta$ -CD	Randomly methylated $\beta$ -cyclodextrin
RT	Room temperature
S	Sulfur
SBR	Styrene-butadiene-rubber
SEC	Size exclusion chromatography
SEI	Solid electrolyte interface
SEM	Scanning electron microscopy
Si	Silicon
SiO	Silicon monoxide
SiO <sub>2</sub>	Silicium dioxide
SLP50	Graphite
SMP	Supramolecular polymer
SPE	Solid polymer electrolyte

TFSI	Bis(trifluoromethanesulfonyl)imide
T <sub>g</sub>	Glass transition temperature
TGA	Thermal gravimetric analysis
THF	Tetrahydrofuran
UV-vis	Ultraviolet-visible
VC	Vinylene carbonate
VTF	Vogel-Tammann-Fulcher
XPS	X-ray photoelectron spectrometry
XRD	X-ray diffraction
α-HL	α-hemolysin

## Résumé détaillé

Pour sauver la planète et limiter les effets du changement climatique, l'humanité n'a pas d'autre choix que de réduire drastiquement ses émissions de gaz à effet de serre, et principalement de CO<sub>2</sub> qui représente 75% des émissions mondiales. Cet avertissement du Groupe d'Experts Intergouvernemental sur l'Evolution du Climat (GIEC) a été rappelé lors de la publication de leur rapport du 9 août 2021<sup>1</sup>. Ce dernier souligne l'influence des activités humaines sur les changements climatiques observés ces dernières décennies comme l'augmentation de la température mondiale ou les perturbations notables des conditions météorologiques. La situation est devenue tellement critique que des politiques mondiales ont été lancées, comme en témoigne l'Accord de Paris<sup>2</sup>, adopté par 196 parties le 12 décembre 2015 pour maintenir une augmentation "raisonnable" de la température à la surface du globe à 1,5°C d'ici la fin du siècle.

Par conséquent, le secteur de l'énergie connaît actuellement une mutation importante. Parmi les solutions envisagées pour décarboner notre économie, on note : (i) intégrer des énergies renouvelables dans l'approvisionnement énergétique, -par essence intermittentes-, (ii) améliorer l'efficacité énergétique de nos systèmes de production d'énergie et réduire leur consommation, (iii) électrifier le secteur des transports et (iv) développer des méthodes de capture, de stockage et valorisation du carbone. Selon l'Agence de l'environnement et de la maîtrise de l'énergie (ADEME), une telle transformation de nos méthodes de production d'énergie serait à l'origine de la réduction de près de la moitié de la consommation énergétique en France d'ici 2050 (-47%)<sup>3</sup>.

Pour atteindre ces objectifs de durabilité, les dispositifs de stockage d'énergie, en particulier les batteries rechargeables, sont devenus des acteurs essentiels et indispensables. Une batterie est une cellule électrochimique composée d'une électrode positive (cathode) et d'une électrode négative (anode), séparées par une solution ionique (électrolyte). Les électrodes sont reliées à un circuit électrique qui permet la circulation des électrons tandis que le mouvement des ions n'est possible qu'à travers l'électrolyte. Des réactions réversibles d'oxydo-réduction se produisent simultanément aux deux électrodes, conduisant à la charge (énergie stockée) ou à la décharge de la batterie (énergie fournie), selon le sens de circulation des électrons. La tension de la cellule (V) est définie comme la différence de potentiel entre les deux électrodes, tandis que la capacité de la cellule (Ah) est



intrinsèque à la nature des électrodes qui sont le siège des réactions électrochimiques. L'énergie (Wh) stockée par la batterie est calculée comme le produit de la tension de la cellule et de sa capacité (Ah).

Afin de satisfaire aux exigences du marché, les batteries rechargeables doivent répondre au cahier des charges suivant : densités d'énergie gravimétrique et volumétrique élevées ( $\text{Wh.kg}^{-1}$  et  $\text{Wh.L}^{-1}$ ), faible coût, longue durée de vie, rendement énergétique élevé et densité de puissance élevée ( $\text{W.kg}^{-1}$ ). Au cours des dernières décennies, les scientifiques se sont principalement concentrés sur l'augmentation de la densité énergétique des matériaux actifs. En raison de leur compétitivité en termes de coût, de rendement et de stockage, les batteries Li-ion ont envahi le marché et s'imposent désormais comme la technologie clé ( $< 100 \text{ \$/kWh}$ ). Omniprésentes dans les systèmes électroniques grand public, elles sont actuellement déployées dans le cadre du développement des véhicules électriques largement encouragé par les politiques gouvernementales, et sont également envisagées pour des applications de stockage stationnaire.

Les recherches en science des matériaux, associées aux efforts d'ingénierie qui ont conduit à la croissance des volumes de fabrication des batteries Li-ion, nous rendent optimistes quant au développement de prochaines générations de batteries encore plus performantes. Elles sont classées en deux catégories principales : les technologies *Li-ion avancé* et *post-Li-ion*<sup>5</sup>. Si le *Li-ion avancé* consiste à améliorer les performances des batteries Li-ion actuelles par l'optimisation des matériaux (cathode, anode), de l'électrolyte ou de la géométrie des cellules ; le *post-Li-ion* fait référence aux autres chimies de batteries telles que les batteries lithium-soufre (Li-S), lithium-air ou sodium-ion. Cette thèse s'intéresse à la fois aux batteries Li-S (*post-Li-ion*) et au développement d'anodes en silicium (Si) dans le cadre du *Li-ion avancé*, technologies connues pour présenter des mécanismes de dégradation intrinsèque les empêchant d'être commercialisées malgré leurs densités énergétiques théoriques supérieures au Li-ion actuel.

L'originalité de notre approche repose sur l'utilisation de la chimie supramoléculaire pour résoudre ces défaillances. Elle s'intègre ainsi dans le contexte de l'initiative européenne BATTERY 2030+ lancée pour réduire l'empreinte carbone des batteries<sup>6</sup>. L'un des principaux piliers de ce programme repose sur l'amélioration de la durée de vie et de la fiabilité des batteries. Ainsi, d'importants travaux de recherche sont menés pour intégrer des systèmes de détection afin de mieux comprendre et

surveiller en temps réel les mécanismes de dégradation responsables de la fin de vie prématurée des batteries<sup>7</sup>. Ces défaillances, qui sont intimement liées à la perte de cohésion entre les composants de l'électrode pendant le cyclage, se manifestent par des changements de structure et de morphologie des électrodes (gonflement, pulvérisation, microfissurations) ou des réactivités aux interfaces électrode/électrolyte, comme la formation de la SEI (film de passivation créé à cette interface), la croissance de dendrites de lithium ou la dissolution partielle des électrodes (navettes électrochimiques). Une fois le diagnostic de ces mécanismes de dégradation posé, nous proposons d'intégrer des fonctions d'auto-réparation, en s'inspirant des processus de la nature, afin d'améliorer la durée de vie des batteries. C'est ici qu'intervient la chimie supramoléculaire pour développer des systèmes adaptables aux changements locaux de structure et ayant pour but de restaurer la configuration initiale des composants de la batterie.

En s'appuyant sur les principes de la chimie supramoléculaire, (= chimie des liaisons non-covalentes et réversibles), cette thèse vise à contribuer à l'amélioration des performances des batteries au lithium. Plus spécifiquement, nous avons sélectionné la cyclodextrine (CD), molécule-cage biosourcée capable de former des complexes supramoléculaires d'inclusion de type hôte-invité. Nous avons structuré ce travail de thèse selon les quatre chapitres suivants :

Le chapitre I débute par la description des propriétés de complexation de la CD. Y est ensuite décrite la grande variété d'architectures macromoléculaires qui en résultent. Le caractère dynamique de l'interaction hôte-invité leur confère des propriétés mécaniques exceptionnelles ou adaptables comme l'auto-réparation ou encore des réactivités réversibles sous l'effet d'un stimulus externe. Ces propriétés ont déjà été mises en œuvre dans les batteries, bien que très récemment, et leur revue nous a permis d'identifier les deux applications les plus prometteuses pour la CD, à savoir les problématiques de gonflement et de dissolution d'électrodes qui se manifestent de manière exacerbée dans les anodes de Si et les batteries Li-S respectivement.

Le chapitre II s'intéresse aux batteries Li-S et se concentre sur le caractère néfaste de la dissolution des polysulfures (navette red-ox). En effet, la réduction du soufre, qui est complexe et encore peu décrite, fait intervenir des réactions en cascade au cours desquelles sont formés différents intermédiaires réactionnels composés de chaînes d'atomes de soufre de différentes tailles  $\text{Li}_2\text{S}_x$  ( $x=2-8$ ) : il s'agit des polysulfures. Ces derniers sont solubles dans l'électrolyte, la diffusion des chaînes

longues dans l'électrolyte jusqu'à l'anode de Li entraîne leur réduction en chaînes plus courtes qui migrent à nouveau vers la cathode de soufre pour y être oxydées etc... De plus, leur réduction totale en  $\text{Li}_2\text{S}$  à l'anode de Li contribue à une perte irréversible supplémentaire de matière active. Tout d'abord, nous avons étudié la complexation de la CD avec les polysulfures, en s'attachant à décrire le caractère réversible de ce processus sous l'effet d'un stimulus externe (température ou dilution), ce qui n'avait encore jamais été fait. Nous avons étudié l'influence de la taille de la cavité des CDs ainsi que la nature du polysulfure (longueur de la chaîne soufrée). Ensuite, en utilisant la complexation CD/polysulfure, nous avons utilisé la technologie nanopore, outil de caractérisation en molécule unique empruntée à la biologie, pour démontrer la possibilité de détection à l'atome de soufre près des polysulfures. Ces résultats prometteurs ouvrent la voie à l'utilisation de nanopores comme sondes ultra-sensibles des électrolytes, mais aussi au développement de nouvelles stratégies de confinement de la cathode de soufre impliquant la CD<sup>149</sup>.

Nous avons ensuite utilisé le pouvoir complexant de la CD à l'échelle macromoléculaire pour synthétiser des polyrotaxanes (PR), assemblages supramoléculaires où les CDs sont enfilées le long d'une chaîne polymère (ici poly(oxide d'éthylène) PEO) et ont l'aptitude de coulisser. Le chapitre III présente la synthèse et la caractérisation d'architectures PR-PAA qui résultent de la réticulation de l'acide poly(acrylique) sur les CDs portées par les PRs. Nous avons fait varier différents paramètres structuraux dans le but d'augmenter le mouvement de glissement des CDs, qui confère à ces architectures des propriétés mécaniques exceptionnelles. Parmi ces paramètres on note : la masse molaire du PEO, le taux de remplissage en CDs des PRs, la densité de réticulation et la proportion massique PR/PAA.

Par la suite dans le Chapitre IV, les PR-PAA sont envisagés comme nouveaux liants polymères pour anode de Si, capables de remédier aux changements de volume conséquents (~300%) dont souffrent ces électrodes au fur et à mesure des charges (lithiation) et décharges (délithiation). Ces variations de volume répétées sont à l'origine du craquellement des électrodes de Si, ce qui empêche pour l'instant qu'elles remplacent les anodes de graphite malgré leur capacité cinq fois supérieure ( $3600 \text{ mAh.g}^{-1}$ ). Le chapitre IV explore les performances électrochimiques des anodes de Si dans lesquelles sont incorporés des PR-PAA. Notre étude permet de conclure quant à l'origine de l'amélioration des performances de cette nouvelle classe de liants par rapport aux liants polymères traditionnels (ici

PAA). L'influence des paramètres structuraux des PR-PAA sur les performances en cyclage et la durée de vie des anodes en Si est enfin mise en lumière.

Ainsi, via le prisme de la CD, nous avons montré comment la chimie supramoléculaire peut être mise au service des batteries au lithium et proposer de nouveaux concepts pour augmenter leur durée de vie en se focalisant sur deux technologies : les batteries Li-S et l'anode de Si. Nous espérons que ce travail a ouvert la voie et qu'il contribuera au développement de nouvelles innovations de rupture à l'interface entre électrochimie, chimie supramoléculaire et biologie.

**Title :** Cyclodextrin : a versatile supramolecular tool to extend lithium-based batteries lifespan

**Keywords :** cyclodextrin, host-guest interaction, polyrotaxane, nanopore, lithium-sulfur battery, Si anode

**Abstract :** Our increasing dependence on lithium-ion batteries for daily energy storage applications calls for the enhancement of their performances. Research efforts, which have so far relied on increasing energy densities, have recently been focused on durability and sustainability. In this context, the inspiration of life sciences has placed great hope on supramolecular chemistry to equip batteries with some added *smart* functionalities, in order to address their inherent failures such as electrodes swelling and partial dissolution, hence enhancing their lifespan. This work aims to evaluate how relevant this new worldwide research interest is, by focusing on cyclodextrins (CDs), which are bio-sourced cage molecules that can give reversible supramolecular host-guest interactions.

We first successfully exploit the selective host-guest interaction of CDs towards polysulfides to

discriminate these soluble lithium-sulfur batteries intermediates by nanopore, with a single sulfur atom resolution. Not only this approach lays the ground to the design of powerful sensors for electrolytes, but it also confers weight to a new sulfur confinement strategy based on CD.

Next, we apply this host-guest interaction at the macromolecular scale by synthesizing mechanically interlocked architectures to be used as Si anode binders. Prepared from CDs-based polyrotaxanes (PRs) cross-linked with poly(acrylic acid), the PR-PAA prototypes disclose new routes of accommodating Si volume changes. Finally, we identify the crucial structural parameters involved in the better cyclability of Si anodes and provide an optimized design for PR-PAA binders.

**Titre :** Utilisations de la cyclodextrine pour prolonger la durée de vie des batteries au lithium

**Mots-clés :** cyclodextrine, interaction hôte-invité, polyrotaxane, nanopore, batterie lithium-soufre, anode Si

**Résumé :** Pour satisfaire aux exigences du marché, les batteries lithium-ion, devenues aujourd'hui indispensables, font l'objet d'intenses études. Cette recherche, jusqu'alors concentrée sur l'augmentation de la densité énergétique des matériaux actifs, se tourne désormais vers les problématiques de durabilité ou plus généralement liées au développement durable. En s'inspirant de la nature, la chimie supramoléculaire suscite de nombreux espoirs pour résoudre certaines défaillances intrinsèques aux batteries, comme le gonflement ou la dissolution des électrodes, ce qui permettrait une augmentation de leur durée de vie. Dans ce contexte, cette thèse s'intéresse aux cyclodextrines (CDs), molécules biosourcées capables de former des complexes supramoléculaires d'inclusion de type hôte-invité.

Tout d'abord, nous avons étudié la complexation de la CD avec les polysulfures, rendant ainsi possible la détection à l'atome de soufre près par nanopore de ces intermédiaires parasitant l'électrolyte des batteries lithium-soufre. Ces résultats prometteurs

ouvrent la voie à l'utilisation de nanopores comme sondes ultra-sensibles des électrolytes, mais aussi au développement de nouvelles stratégies de confinement de la cathode de soufre impliquant la CD.

Nous avons ensuite utilisé le pouvoir complexant de la CD à l'échelle macromoléculaire pour synthétiser des polyrotaxanes (PR), assemblages supramoléculaires où les CDs ont l'aptitude de se mouvoir le long d'une chaîne polymère. Les architectures PR-PAA, qui résultent de la réticulation de l'acide poly(acrylique) sur les CDs portées par les PRs, constituent de nouveaux liants polymères pour anode de silicium, capables de remédier à leurs changements de volume conséquents. L'étude de la relation entre structure des PR-PAA et leurs performances ont permis de nettes améliorations en cyclage.